Two-dimensional materials, correlations and topology

Yuncheng Mao

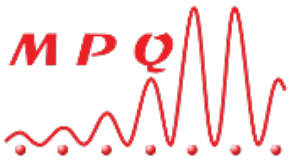

Université Paris Cité
Laboratoire Matériaux et Phénomènes Quantiques (UMR 7162)
École Doctorale de Physique en Île-de-France (ED 564)

Specialité de doctorat : Physique

Two-dimensional materials, correlations and topology

Presentée par M. Yuncheng MAO

Dirigée par M. Christophe Mora

Thèse présentée et soutenue publiquement à Université Paris Cité le 21 septembre 2023
devant un jury composé de:

M. David Carpentier	Professeur de l'École Normale Supérieure de Lyon	Rapporteur
Mme. Leni Bascones	Professeur de Instituto de Ciencia de Materiales de Madrid	Rapportrice
Mme. Cécile Repellin	Chargée de recherche d'Université Grenoble-Alpes	Examinatrice
Mme. Rebeca Ribeiro-Palau	Chargée de recherche d'Université Paris-Saclay	Examinatrice
M. Jérôme Cayssol	Professeur d'Université de Bordeaux	Examminateur
M. Christophe Mora	Professeur d'Université Paris Cité	Directeur de thèse

Contents

Table of contents iii

List of figures xii

List of tables xiii

Abstract 1

Résumé 4

Introduction 5

1 Twisted Bilayer Graphene: Flat Bands, Magic Angles and Symmetries 15
- 1.1 Bistrizer-MacDonald continuum model for TBG . . . 15
- 1.2 TBG band structure, flat bands and magic angles . . . 23
- 1.3 Analyses on typical symmetries in TBG . . . 28
- 1.4 Pseudo-Landau levels . . . 37
- 1.5 Summary . . . 38

2 Twisted trilayer graphene: model and moiré solution 41
- 2.1 Continuum model for twisted trilayer graphene . . . 41
- 2.2 Mirror-symmetrical twisted trilayer graphene . . . 43
- 2.3 Moiré staircase TTG with equal twist angles . . . 45
  - 2.3.1 Hamiltonian and wave functions . . . 45
  - 2.3.2 Band structures . . . 47
  - 2.3.3 Flat bands at chiral limit . . . 48
  - 2.3.4 Dirac cone anisotropy . . . 51
  - 2.3.5 Symmetries in staircase TTG . . . 53
  - 2.3.6 Band topology and Chern mosaic pattern . . . 58
- 2.4 Moire staircase TTG with unequal twist angles . . . 60
  - 2.4.1 Hamiltonian and band structures . . . 60
  - 2.4.2 Symmetries . . . 62
- 2.5 Summary . . . 63

3 Supermoiré effective theory: formalism, gauge, and symmetries 65
- 3.1 Symmetries of AAA-stacked exact model . . . 66
- 3.2 Separation of moiré and supermoiré scales via geometrical decomposition 67
- 3.3 Effective theory . . . 69

3.3.1 Reviewing the $\boldsymbol{k}\cdot\boldsymbol{p}$ method . . . 69
3.3.2 Ansatz wave function of the exact TTG model . . . 72
3.3.3 Effective model . . . 74
3.4 Gauge Fixing and gauge invariance . . . 78
3.4.1 General principle of fixing gauges . . . 78
3.4.2 Practical Procedures . . . 79
3.4.3 Gauge-invariance of effective model . . . 82
3.5 Symmetries of effective model . . . 83
3.5.1 Periodicity of supermoiré Hamiltonian . . . 84
3.5.2 Other important symmetries . . . 85
3.6 Computation of $|\boldsymbol{\nabla}_{\boldsymbol{R}}\psi(\boldsymbol{R})\rangle$ with gauge . . . 86
3.6.1 Gauge independent contribution from perturbation theory . . . 86
3.6.2 Gauge-dependent contribution . . . 88
3.7 Effective model on the reciprocal lattice . . . 89
3.8 Effective model at low energy in the supermoiré scale . . . 92
3.9 Summary . . . 93

4 Numerical solutions of low-energy supermoiré effective models 97
4.1 Nearly equal twist angles . . . 98
4.1.1 $\boldsymbol{\Gamma}_M$ effective model . . . 99
4.1.2 $\boldsymbol{K}_M$ effective model . . . 105
4.1.3 Evolution with different twist angles . . . 108
4.2 Effective model with $\theta_1/\theta_2 \simeq 1/2$ . . . 109
4.2.1 $\boldsymbol{\Gamma}_M$ effective model . . . 110
4.2.2 $\boldsymbol{K}_M$ effective model . . . 110
4.2.3 Evolution with different angles . . . 113
4.3 Zero-velocity singularity . . . 114
4.3.1 1D Dirac model with space-dependent velocity . . . 116
4.3.2 Explorable angles . . . 118
4.4 Summary . . . 118

5 Conclusion 121

Appendices

A Résumé substantiel en français 129
A.1 Introduction . . . 129
A.2 Travail de thèse . . . 131

A.2.1 Chapitre 1 – Graphène bicouche torsadé : bandes plates, angles magiques et symétries . . . 131
A.2.2 Chapitre 2 – Graphène tricouche torsadé : modèle et solution à l'échelle moiré . . . 132
A.2.3 Chapitre 3 – Théorie effective supermoiré : formalisme, jauge et symétries . . . 133
A.2.4 Chapitre 4 – Solution numérique du modèle supermoiré effectif à basse énergie . . . 134
A.2.5 Chapitre 5 – Conclusion . . . 136

B Gauge invariance of effective model **137**

C Symmetries of effective model **139**
C.1 General principle . . . 139
C.2 Translational symmetry . . . 141
C.3 C_{3z} symmetry . . . 147
C.4 C_{2x} symmetry. . . . 148
C.5 $C_{2z}T$ symmetry . . . 149

D Matrix elements of the 4-band K_M model **153**

Bibliography **169**

List of Figures

1 The phase diagram of magic-angle TBG, reproduced from Ref. [23]. The color plot show the longitudinal resistivity of TBG as a function of the filling factor and temperature. Various phases, such as metal, band insulator (BI), correlated states (CS) and superconductor (SC) are revealed. 6

2 Figure reproduced from Ref. [33] showing the Quantum anomalous Hall effect of TBG aligned to hBN, measured at 1.6 K. (A) The longitudinal resistance R_{xx} and the Hall resistance R_{xy} measured as functions of the density of carriers, measured with a magnetic field 150 mT. (B) The measurement of R_{xx} and R_{xy} as functions of the magnetic field at a fixed density of carriers $n = 2.37 \times 10^{12}$ cm^{-2}. (C) R_{xy} as a function of the magnetic filed and the carrier density. The hysteresis loops are shown. When ferromagnetism emerges, R_{xy} is non-zero when the magnetic field is turned off, signaling quantum anomalous Hall effect. (D) Schematic illustrations of the Chern bands with filling factors $\nu = 3$ and $\nu = 4$ (full filling of a moiré unit cell). 9

3 Schematic phase diagram of mTTG reproduced from Ref. [83]. The phase diagram is shown as a function of the displacement field D_0 and the filling factor ν. Due to the presence of particle hole symmetry in the mirror-symmetrical TTG, the phase diagram depends in fact on D_0 and $|\nu|$. At charge neutrality point ($\nu = 0$), the intervalley coherent (IVC) semimetal phase and sublattice polarized insulator phase are identified. The IVC and SPL phases coexist with spin polarization (SP) at the doping of $\nu = 2$. Three types of superconducting phases noted SC I-III are marked in the diagram. Their spin structures are also labeled in black color. The intervalley Hund's coupling J_H are shown in gray if it has opposite sign to the spin structure. 12

1.1 The real space structure of a single-layer graphene (SLG). The A- and B-sublattices are shown in blue and orange colors, respectively. 16

1.2 Real space arrangement of twisted bilayer graphene. The top and the bottom layers are rendered in orange and blue colors, respectively. Here the center is chosen to be the AA-stacking point. The recurrence of the AA points in the real space makes appear the periodicity of the moiré pattern. The AB- and BA-stacking points around a AA point defines the vertices of the Wigner-Seitz cell of the moiré lattice in real space. The top and bottom layers are rotated in the anticlockwise and the clockwise direction by an angle of $\theta/2$, respectively. 17

1.3 Left panel: The two graphene layers represented in the reciprocal space with the first Brillouin zone of each layer. The smallest possible vectors connecting the $\mathbf{K}$ points of each layer are $\boldsymbol{q}_1$, $\boldsymbol{q}_2$ and $\boldsymbol{q}_3$. Right panel: the moiré reciprocal lattice of TBG generated by $\boldsymbol{q}_1$, $\boldsymbol{q}_2$ and $\boldsymbol{q}_3$, where $\boldsymbol{G}_1$ and $\boldsymbol{G}_2$ are the bases vectors of the moiré reciprocal lattice. 20

1.4 Variation of the TBG band structure with different twist angles. The two bands closest to the zero-energy level are labeled with red color. $\theta = 1.09^\circ$ is the famous "magic angle" of TBG. The band structures are computed with the corrugation factor $r = \omega_{AA}/\omega_{AB} = 0.8$. 24

1.5 The route in the Brillouin zone along which the band structures are computed is chosen to be $\mathbf{\Gamma} \to \mathbf{K} \to \mathbf{K}' \to \mathbf{M} \to \mathbf{\Gamma}$. 24

1.6 Revival of the Fermi velocity as a function of the dimensionless coupling constant ($a \propto 1/\theta$). The velocities are calculated using $\boldsymbol{k} \cdot \boldsymbol{p}$ method near the $\mathbf{K}$ point. The angles where the Fermi velocity vanishes are the magic angles. 26

1.7 Wilson Loop computation of the middle bands. Each of the two eigenvalues accumulates $\pm 2\pi$. The total accumulated phase is however 0, giving a total Chern number $\mathcal{C} = 0$. 28

1.8 The particle hole symmetry sends an arbitrary wave vector within the TBG Brillouin zone to its counterpart symmetrical to it with respect to the $\mathbf{\Gamma}$ point. The dotted arrow show the Ukmlapp process to send $-\boldsymbol{k} + \boldsymbol{q}_1$ back inside the Brillouin zone centered at $\mathbf{\Gamma}$. 30

1.9 Transform of states under C_{3z} operation. An arbitrary wave vector $\boldsymbol{k}$, is sent to $\hat{R}_{-2\pi/3}$ under C_{3z} rotation around $\boldsymbol{k} = \mathbf{0}$ (blue color). The Ukmlapp process (dotted arrow) shifts the resulted wave vector back inside the Brillouin zone. The result is equivalent to directly rotating $\boldsymbol{k}$ around $\mathbf{\Gamma}$ point. 31

1.10 An arbitrary wave vector in the TBG Brillouin zone transformed under C_{2x} operation. 33

2.1 The approximation of moiré vectors. 45

2.2 Band structures of the zero-phase TTG with equal twist angles calculated for different twist angles. The 12 bands closest to the zero energy levels are shown. Corrugation ratio is set to $r = 0.8$. The two middle bands closest to the zero energy level are colored in red. 48

2.3 Band structures with non-zero phases. Corrugation ratio is set to $r = 0.8$. The twist angle is $1.8°$. The computation of the band structures are performed with (a) zero phases; (b) phase factors restoring C_{3z} symmetry; (c) phase factors restoring C_{2x} symmetry and (d) arbitrary phase factors breaking all of C_{2zT}, C_{3z} and C_{2x} symmetries. The particle-hole symmetry is always valid for equal twist angles despite different phase factors as will be explained later. 49

2.4 In the left panel of the figure, the completely flat bands of AAA-stacked TTG are shown. These flat bands emerge when the interlayer hopping parameter w_{AA} is set to zero, resulting in a chiral limit. The first magic angle for the AAA-stacked configuration is given by $a = 0.830$ ($\sim 0.77°$). In the right panel of the figure, the completely flat bands of ABA-stacked TTG are depicted. Similarly, these flat bands arise in the chiral limit with $w_{AA} = 0$. The first magic angle for the ABA-stacked configuration is given by $a = 0.377$ ($\sim 1.68°$). These flat bands at the chiral limit and specific twist angles are a fascinating feature of AAA and ABA-stacked TTG structures. 50

2.5 Renormalized velocity of Γ and K Dirac cones computed for AAA (left panel) and ABA (right panel) stackings, at the *chiral* limit with $w_{AA} = 0$. . 50

2.6 Renormalized velocity of Γ and K Dirac cones computed for AAA (left panel) and ABA (right panel) stackings, with $w_{AA}/w_{AB} = 0.8$. 51

2.7 Anisotroy $\mathcal{A}(\phi_2, \phi_3)$ of the Dirac cones at $\boldsymbol{\Gamma}$ (left panel) and $\boldsymbol{K}$ (right panel). Data colleted with $w_{AA}/w_{AB} = 0.8$ at $1.8°$. 53

2.8 The chern mosaic pattern computed in the phase space within a unit cell. The *periodic* boundary is highlighted in gray color. The $\mathcal{C} = \pm 1$ sections are colored in blue and orange colors respectively. The C_{3z} restoring points corresponding to AAA ($\phi_2 = 0, \phi_3 = 0$), ABA ($\phi_2 = -pi/3, \phi_3 = \pi/3$) and BAB ($\phi_2 = pi/3, \phi_3 = -\pi/3$) stackings are marked with red dots. The purple lines mark the C_{2x}-restoring phases. Data collected with corrugation factor $w_{AA}/w_{AB} = 0.8$ and equal twist angles of $1.8°$. 59

2.9 Comparison of the reciprocal moiré lattices of (a) equal twist angle TTG and (b) the double angle TTG. In the double twist TTG, the initial Dirac cones of of the top and bottom layer overlaps in the reciprocal space. 60

2.10 Band structures of AAA stacking double-angle TTG with θ_{12} being (a) $2.2°$, (b) $1.8°$ and (c) $1.4°$. Corrugation is also set to $w_{AA}/w_{AB} = 0.8$. 61

2.11 Band structures of double-angle TTG with different stackings: (a) AAA with $\boldsymbol{\phi} = (0, 0, 0)$, (b) ABA with $\boldsymbol{\phi} = (0, 2\pi/3, -2\pi/3)$ and (c) arbitrary stacking with $\boldsymbol{\phi} = (0, 0.4\pi, -0.1\pi)$. Corrugation is also set to $w_{AA}/w_{AB} = 0.8$. Twist angles are fixed at $(2^\circ, 4^\circ)$. The variation of the band structures is not as dramatic as in the equally twisted TTG. But tiny changes in the spectra are still visible due to different symmetries associated to different phases. . 61

3.1 Illustration of the geometrical decomposition of TBG moiré vectors into moiré vectors and supermoiré vectors for a pair of nearly equal twist angles. 68

4.1 The matrix elements of the $\mathbf{\Gamma}_M$ effective model computed within a supermoiré unit cell for $\Gamma_x(\boldsymbol{R})$ (first row), $\Gamma_y(\boldsymbol{R})$ (second row) and $A(\boldsymbol{R})$ (third row), with the coefficients d_0, d_x, d_y and d_z arranged in the first, second, third and fourth columns, respectively. The variation of matrix elements is confirmed to be smooth and continuous. All matrix elements return to their original value after going over a supermoiré period. Data collected with $\theta_1 = \theta_2 = 2.2^\circ$. To show more clearly the continuity and periodicity of each set of data within a supermoiré unit cell, the data in each subplot are normalized to the interval $[0, 1]$ using Eq. (4.6) so that the same color scale is employed for all color plots. 100

4.2 The absolute values of the Fourier coefficients of the data shown in Fig. 4.1. The arrangement of data in the panels corresponds to Fig. 4.1. The same normalization technique of data as in Fig. 4.1 is also performed on every set of data shwon in each subplot. 101

4.3 The supermoiré Brillouin zone. Band structure is calculated along the horizontal line $-\boldsymbol{K} - \boldsymbol{\Gamma} - \boldsymbol{K}$. The supermoiré vectors $\delta\boldsymbol{q}_j,\ j = 1, 2, 3$ are also shown. 101

4.4 In the left panel, we observe the low-energy density of states of the $\mathbf{\Gamma}_M$ effective model. The black line represents the density of states computed from the effective model, while the red line corresponds to the profile of the average density of states of the local models. It is important to note that the average local density of states has been manually shifted to align the Dirac point with that of the effective model. This comparison allows us to assess the agreement between the low-energy states of the effective model and the average behavior of the local models. In the right panel, we present the band structure computed along the path $-\boldsymbol{K} - \mathbf{\Gamma} - \boldsymbol{K}$, which traverses the supermoiré Brillouin zone. This path provides insights into the energy dispersion and the formation of bands within the effective model. By analyzing the band structure, we can identify important features such as band crossings, band gaps, and the overall behavior of the energy levels along the selected trajectory. 102

4.5 The vector field of $\boldsymbol{a}(\boldsymbol{R})$ on the $x - y$ plane. Red line depicts a supermoiré unit cell centered at $\boldsymbol{R} = \mathbf{0}$. The supermoiré coordinates restoring C_{3z} symmetry in the local models are also highlighted. The AAA stacked local model is marked with orange color, while the ABA/BAB stacked local models are shown in green. 103

4.6 The matrix elements of the $\boldsymbol{K}_M$ effective model computed within a supermoiré unit cell for $\Gamma_x(\boldsymbol{R})$ (first row), $\Gamma_y(\boldsymbol{R})$ (second row), $A(\boldsymbol{R})$ (third row) and $E(\boldsymbol{R})$ (fourth row), with the coefficients d_0, d_x, d_y and d_z arranged in the first, second, third and fourth columns, respectively. The variation of matrix elements is confirmed to be smooth and continuous. All matrix elements return to their original value after going over a supermoiré period. Data collected with $\theta_1 = \theta_2 = 2.2°$. To show more clearly the continuity and periodicity of each set of data within a supermoiré unit cell, the data in each subplot are normalized to the interval $[0, 1]$ so that the same color scale is employed for all color plots. 106

4.7 The absolute values of the Fourier coefficients of the data shown in Fig. 4.6. The arrangement of data in the panels corresponds to Fig. 4.6. All data are also normalized to $[0, 1]$ for better visibility. 107

4.8 In the left panel, we shown The low-energy density of states of the $\boldsymbol{K}_M$ effective model. Black line show the density of states computed from the effective model. The red line show profile of the average density of local models. The average local density of states is shifted by hand to make the Dirac point coincide with that of the effective model. In the right panel, we present the band structure computed along the route $-\boldsymbol{K} - \boldsymbol{\Gamma} - \boldsymbol{K}$ transversing the supermoiré Brillouin zone. 107

4.9 The vector field of $\boldsymbol{a}(\boldsymbol{R})$ on the $x - y$ plane computed for the $\boldsymbol{K}_M$ model. Red line depicts a supermoiré unit cell centered at $\boldsymbol{R} = \boldsymbol{0}$. The supermoiré coordinates restoring C_{3z} symmetry in the local models are also highlighted. The AAA stacked local model is marked with orange color, while the ABA/BAB stacked local models are shown in green. 108

4.10 Black curves show the density of states of the $\boldsymbol{\Gamma}_M$ (left) and the $\boldsymbol{K}_M$ (right) effective models computed for different values of equal twist angles. The transparent red lines show the average density of states computed with local moiré models. They are shifted by hand to superpose their Dirac points with those of the effective models. The range of twist angles are chosen to be between 2.2° and 3°. 109

4.11 The matrix elements of the $\boldsymbol{\Gamma}_M$ effective model computed within a supermoiré unit cell, for $\Gamma_x(\boldsymbol{R})$ (first row), $\Gamma_y(\boldsymbol{R})$ (second row), $A(\boldsymbol{R})$ (third row) and $E(\boldsymbol{R})$ (fourth row), with the coefficients d_0, d_x, d_y and d_z arranged in the first, second, third and fourth columns, respectively, computed for twist angles $\theta_1 = 1.8^\circ$ and $\theta_2 = 3.6^\circ$. Data are normalized to $[0, 1]$ for better visibility. We confirm the smooth and continuous variation of all data with the supermoiré coordinates $\boldsymbol{R}$ as well as their periodicity. 111

4.12 The Fourier amplitudes of all the data shown in Fig. 4.11. Every data set is normalized to $[0, 1]$. 112

4.13 The band structure (right panel) and density of states (left panel) computed from the $\boldsymbol{\Gamma}_M$ effective model with $\theta_1 = 1.8^\circ$ and $\theta_2 = 3.6^\circ$. 112

4.14 The a_x and a_y components of the gauge field extracted from the $\boldsymbol{\Gamma}_M$ effective model with $\theta_1 = 1.8^\circ$ and $\theta_2 = 3.6^\circ$. 113

4.15 Low energy density of states (left panel) and band structure (right panel) given by the 4-band $\boldsymbol{K}_M$ effective model. Data collected for twist angles $\theta_1 = 1.8^\circ$ and $\theta_2 = 3.6^\circ$. 113

4.16 The black curves show the profiles of density of states of the effective models with $\theta_1 = \frac{\theta_2}{2}$ ranging from 1.6° to 2.1°. The data of the $\boldsymbol{\Gamma}_M$ and $\boldsymbol{K}_M$ effective models are displayed in the left and right panels, respectively. Transparent red lines are the average density of states over local moiré models within a supermoiré unit cell, and are shifted by hand to align their Dirac points with those of the effective models. 114
4.17 Left: The low-energy density of states with equal twist angles of 1.8°, computed from $\boldsymbol{\Gamma}_M$ (blue curve) and $\boldsymbol{K}_M$ (orange curve) effective models. The great enhancement of density of states at low-energy is qualitatively manifested. Right: The smallest velocity found within a supermoiré cell computed at different equal twist angles, for the $\boldsymbol{\Gamma}_M$ (blue curve) and $\boldsymbol{K}_M$ (orange curve) models. 115
4.18 Left: the minimum velocity components at $\boldsymbol{\Gamma}_M$ (blue) and $\boldsymbol{K}_M$ (orange) for different values of $\theta_1 = \frac{1}{2}\theta_2$. Right: The density of states of the $\boldsymbol{K}_M$ effective model computed at several angles where the velocity of $\boldsymbol{K}_M$ does not touch zero. Comparing the plots of both sides, the remarkably high density of states emerges with small velocities. 116
4.19 Velocity components of the Dirac cone in the local models across the supermoiré coordinates. Data collected for the $\boldsymbol{\Gamma}_M$ models with equal twist angles 1.7° (blue wired surface) and 2.2° (orange wired surface). The plane of zero value is shown in gray color. 116
4.20 The maximum density of states computed for explorable angles with θ_1/θ_2 *near* 1, $1/2$ and 2, and for energy levels between -30 and 30 meV. Angles are limited between 1° and 5°. Computation were performed for angles satisfying $|\delta\boldsymbol{q}|/|\boldsymbol{q}| \leqslant 0.2$. 119

D.1 The normalized data of matrix elements $|\Gamma_{x\,i,j}(\boldsymbol{R})|$ from the $\boldsymbol{K}_M$ effective model with twist angles being 1.8° and 3.6°. 154
D.2 The normalized Fourier coefficients of $\Gamma_{x\,i,j}$ on the supermoiré reciprocal lattice from the $\boldsymbol{K}_M$ effective model with twist angles being 1.8° and 3.6°. 155
D.3 The normalized data of matrix elements $|\Gamma_{y\,i,j}(\boldsymbol{R})|$ from the $\boldsymbol{K}_M$ effective model with twist angles being 1.8° and 3.6°. 156
D.4 The normalized Fourier coefficients of $\Gamma_{y\,i,j}$ on the supermoiré reciprocal lattice from the $\boldsymbol{K}_M$ effective model with twist angles being 1.8° and 3.6°. 157
D.5 The normalized data of matrix elements $|A_{i,j}(\boldsymbol{R})|$ from the $\boldsymbol{K}_M$ effective model with twist angles being 1.8° and 3.6°. 158
D.6 The normalized Fourier coefficients of $A_{i,j}$ on the supermoiré reciprocal lattice from the $\boldsymbol{K}_M$ effective model with twist angles being 1.8° and 3.6°. 159

D.7 The normalized data of matrix elements $|E_{i,j}(\boldsymbol{R})|$ from the $\boldsymbol{K}_M$ effective model with twist angles being 1.8° and 3.6°. 160
D.8 The normalized Fourier coefficients of $E_{i,j}$ on the supermoiré reciprocal lattice from the $\boldsymbol{K}_M$ effective model with twist angles being 1.8° and 3.6°. 161

List of Tables

1.1 Character table of irreducible representations at high-symmetry points of TBG Brillouin zone, reproduced from Ref [59]. 35

Abstract

The experimental realization of twisted bilayer graphene (TBG) in 2018 marked the beginning of an active research field in physics known as “twistronics”. This field explores the remarkable tunability of electronic structures in 2D van der Waals heterostructures through relative rotations between single layers. The mismatch in periodicity between the stacked layers gives rise to a moiré pattern, and the moiré potential coupling the layers underlies the rich physics in twistronics. It has been theoretically and experimentally shown that the Dirac dispersion of graphene can completely disappear at specific rotation angles, known as "magic angles." At these angles, electrons near the graphene Fermi level experience significantly reduced mobility, leading to the emergence of exotic phases. It is fascinating to witness a single material exhibiting such a wealth of phases.

TBG has been found to exhibit superconducting phases, correlated insulating phases, strange metal phases, and more. Efforts are ongoing to fully understand the underlying mechanisms behind the rich and intricate phase diagram of this twisted 2D material.

While TBG investigations continue, attention has also turned to other similar 2D materials. Among these, twisted trilayer graphene (TTG) has emerged as a promising platform for exploring electronic structure tunability and diverse phases. With an additional layer of graphene, the complexity of TTG is significantly increased compared to TBG. The main challenge lies in the incommensurability between the two TBG patterns encoded in TTG. The mismatched TBG patterns create a secondary moiré pattern, referred to as the "supermoiré," atop them. Prior theoretical works on TTG either employed mirror-symmetrical configurations or made approximations to circumvent the supermoiré challenge. These approaches successfully elucidated the moiré band structures and topologies, identifying magic angles and the associated flat bands in TTG.

However, apart from the mirror-symmetrical TTG model, the approximate moiré TTG models assume collinear moiré vectors and rational ratios between twist angles. The incommensurability of TTG arises precisely from the deviation from collinearity and the irrationality of twist angle ratios.

This thesis is inspired by the quest to solve the incommensurate supermoiré problem. While finding a complete and general solution to the quasicrystal problem posed by incommensurability remains challenging, we aim to push the boundaries beyond the approximate periodic regime. We have developed a sophisticated theoretical framework that views the incommensurate supermoiré problem as a perturbed periodicity problem under certain con-

ditions. Specifically, our methodology examines scenarios where the ratio between twist angles is close to a rational number. In such cases, we perform a geometrical decomposition of the two sets of moiré vectors, yielding two distinct length scales: one comparable to the moiré scale and the other spanning an even longer scale, known as the supermoiré scale. We utilize the intuition that the exact solution of the TTG model should locally resemble the approximate moiré solutions, and we design an ansatz wave function for the exact solution. The ansatz wave functions can be seen as an extension of the classical k-dot-p method, involving a linear combination of local wave functions decorated by a modulation function. The modulation functions are intentionally slowly varying, nearly constant within a moiré unit cell. Consequently, the ansatz functions are locally orthonormal within each moiré unit cell. This allows us to integrate the moiré functions locally within each unit cell, resulting in an effective Schrödinger's equation that solely involves the modulation functions.

By numerically diagonalizing the effective Hamiltonian, we obtain the supermoiré states and band structure. Comparing our results to those obtained by directly averaging the local solutions, we confirm that the effective model better respects the symmetries of the original model and reveals a pseudo-magnetic field effect that cannot be captured by incoherently averaging local states.

Keywords: twistronics, twisted bilayer graphene, twisted trilayer graphene, $\boldsymbol{k}\cdot\boldsymbol{p}$ method, quasicrystal, incommensurability

Résumé en français

La réalisation expérimentale du graphène torsadé à double couche (TBG) en 2018 a marqué le début d'un domaine de recherche actif en physique connu sous le nom de "twistronics" (twistronique). Ce domaine explore la remarquable capacité d'ajustement des structures électroniques dans les hétérostructures de van der Waals en 2D grâce aux rotations relatives entre les couches individuelles. La différence de périodicité entre les couches empilées donne naissance à un motif moiré, et le potentiel moiré qui lie les couches est à la base de la physique riche de la twistronique. Il a été démontré à la fois théoriquement et expérimentalement que la dispersion de Dirac du graphène peut complètement disparaître à certains angles de rotation spécifiques, appelés "angles magiques". À ces angles, les électrons proches du niveau de Fermi du graphène connaissent une mobilité considérablement réduite, ce qui entraîne l'émergence de phases exotiques. Il est fascinant de constater qu'un seul matériau présente une telle variété de phases.

On a découvert que le TBG présente des phases supraconductrices, des phases isolantes corrélées, des phases métalliques étranges, etc. Des efforts sont en cours pour comprendre pleinement les mécanismes sous-jacents du diagramme de phase riche et complexe de ce matériau 2D torsadé.

Alors que les recherches sur le TBG se poursuivent, l'attention s'est également portée sur d'autres matériaux 2D similaires. Parmi ceux-ci, le graphène torsadé à triple couche (TTG) émerge comme une plateforme prometteuse pour explorer l'ajustabilité des structures électroniques et les différentes phases. Avec une couche supplémentaire de graphène, la complexité du TTG est considérablement accrue par rapport au TBG. Le principal défi réside dans l'incommensurabilité entre les deux motifs TBG encodés dans le TTG. Les motifs TBG non appariés créent un motif moiré secondaire, appelé "supermoiré", au-dessus d'eux. Les travaux théoriques antérieurs sur le TTG utilisaient soit des configurations symétriques par rapport à un plan miroir, soit des approximations pour contourner le défi du supermoiré. Ces approches ont permis d'élucider avec succès les structures de bande moiré et les topologies, en identifiant les angles magiques et les bandes plates associées dans le TTG.

Cependant, à l'exception du modèle symétrique par rapport à un plan miroir du TTG, les modèles moirés approximatifs du TTG supposent des vecteurs moirés colinéaires et des rapports de torsion rationnels. L'incommensurabilité du TTG provient précisément de l'écart par rapport à la colinéarité des vecteurs moirés et de l'irrationalité des rapports d'angle de torsion.

Cette thèse s'inspire de la quête visant à résoudre le problème du supermoiré incommensurable. Bien que trouver une solution complète et générale au problème du quasi-cristal posé par l'incommensurabilité reste un défi, notre objectif est de repousser les limites au-delà du régime périodique approximatif. Nous avons développé un cadre théorique sophistiqué qui considère le problème du supermoiré incommensurable comme un problème de périodicité perturbée dans certaines conditions. Plus précisément, notre méthodologie examine les scénarios où le rapport entre les angles de torsion est proche d'un nombre rationnel. Dans de tels cas, nous effectuons une décomposition géométrique des deux ensembles de vecteurs moirés, donnant ainsi deux échelles de longueur distinctes : l'une comparable à l'échelle moiré et l'autre s'étendant sur une échelle encore plus longue, appelée échelle du supermoiré. Nous utilisons l'intuition selon laquelle la solution exacte du modèle TTG devrait ressembler localement aux solutions moirées approximatives, et nous concevons une fonction d'onde ansatz pour la solution exacte. Les fonctions d'onde ansatz peuvent être considérées comme une extension de la méthode classique k-point-p, impliquant une combinaison linéaire de fonctions d'onde locales décorées par une fonction de modulation. Les fonctions de modulation varient lentement intentionnellement et sont presque constantes dans une cellule unitaire moirée. Par conséquent, les fonctions ansatz sont localement orthonormales dans chaque cellule unitaire moirée. Cela nous permet d'intégrer les fonctions moirées localement dans chaque cellule unitaire, ce qui donne une équation de Schrödinger efficace ne faisant intervenir que les fonctions de modulation.

En diagonalisant numériquement l'hamiltonien effectif, nous obtenons les états supermoirés et la structure de bande. En comparant nos résultats à ceux obtenus en moyennant directement les solutions locales, nous confirmons que le modèle effectif respecte mieux les symétries du modèle d'origine et révèle un effet de champ pseudo-magnétique qui ne peut être capturé par la moyenne incohérente des états locaux.

Mots clés: twistronique, graphènes bicouche torsadé, graphène tricouche torsadé, méthode $\boldsymbol{k} \cdot \boldsymbol{p}$, quasi-cristal, incommensurabilité

Introduction

The successful isolation of single-layer graphene marked the beginning of a fruitful era in the exploration of two-dimensional materials [1]. Graphene, with its unique properties, has captured significant attention in research. It exhibits high electron mobility across a wide temperature range [2–4], and demonstrates excellent electrical and thermal conductivity comparable to metallic materials at room temperature [5, 6]. The remarkable characteristics of graphene can be primarily attributed to its Fermi-level behavior, which features two massless Dirac cones at the $\mathbf{K}$ and $\mathbf{K}'$ points of the Brillouin zone. These cones, which are time-reversed counterparts of each other, exhibit a high dispersion velocity of approximately 10^6 m/s. Additionally, graphene displays the quantum Hall effect when subjected to a perpendicular magnetic field, resulting in quantized Hall conductivity given by $\sigma_{xy} = \pm 4(N + \frac{1}{2})\frac{e^2}{h}$, where N represents the index of the Landau levels, e is the charge of a single electron, h is the Planck constant, and B denotes the strength of the magnetic field. The Landau levels of a relativistic massless fermion can be described by the expression $E_N = \mathrm{sgn}(N)\frac{\hbar v_F}{l_B}\sqrt{2|N|}$, where l_B is the magnetic length defined by $l_B = \sqrt{\frac{\hbar}{eB}}$.

Despite the high mobility of charge carriers in graphene, achieving superconductivity in single-layer graphene is challenging. This difficulty primarily arises from the depleted density of states at the charge neutral point, resulting from the linear dispersion near the Fermi level. To overcome this limitation, researchers have explored alternative two-dimensional lattices [7]. One notable example is the *Kagome* lattice, which is known to possess completely flat bands and bands with Dirac dispersion simultaneously [8]. However, the realization of such materials in experiments and the observation of superconductivity in them have remained rare [9–12].

One natural approach to explore enhanced properties is by stacking multiple layers of graphene together. The interlayer hopping potential can potentially modify the Fermi surface and lead to interesting phenomena. In graphene stacking, two common arrangements are AA-stacking and AB-stacking (also known as Bernal stacking), depending on the relative positioning of the A- and B-sublattices of the graphene layers. Experimental observation of superconductivity in Bernal stacked graphene bilayer was recently reported [13]. It is found that the Cooper pair in this superconducting phase is the unconventional spin-triplet. Superconductivity in non-twisted trilayer graphene is also reported [14].

It was soon realized that stacked graphene layers with a twist, known as twisted bilayer graphene (TBG), exhibit a unique interlayer hopping potential due to the relative rotation

between the layers. This twist-induced effect can significantly modify the band structure of the Fermi level in a distinct way compared to direct AA or AB stackings without a twist. The non-trivial topology of the Fermi-level bands in TBG was already observed prior to the discovery of the flat bands. [15]. Subsequently, it was demonstrated that the band structure near the charge neutral point in TBG retains the Dirac dispersion, but the velocity can vary dramatically with the twist angle and even vanish at specific angles known as magic angles, leading to the emergence of the famous flat bands [16–19]. The theoretical prediction of these flat bands and the identification of magic angles in TBG sparked widespread interest in the exploration of van der Waals heterostructures based on twisted graphene layers.

The experimental discovery of superconductivity [20] and correlated insulator phases [21] in 2018 marked the beginning of a new era in the field of "twistronics". Since then, intensive investigations have been conducted to explore the exotic phases and electronic properties of van der Waals heterostructures with similar characteristics. These studies have revealed a wealth of remarkably rich physics.

The tunability of twisted bilayer graphene (TBG) is not solely dependent on the twist angle. It has been observed that hydrostatic pressure can increase the strength of interlayer coupling, leading to superconductivity at larger angles [22]. By tuning the flat-band filling factor, various phases can be frequently observed, including correlated insulator, superconducting, and ferromagnetic phases [23]. Figure 1 shows the experimentally measured phase diagram of magic angle TBG, as demonstrated by Lu et al. [23].

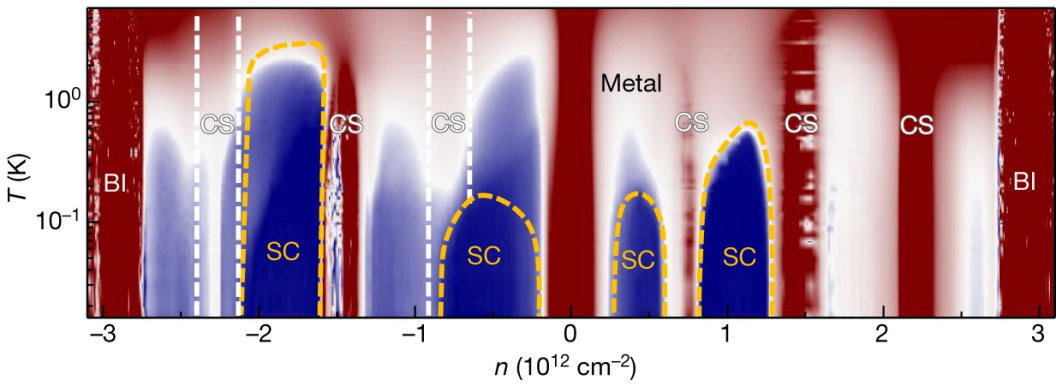

Figure 1: The phase diagram of magic-angle TBG, reproduced from Ref. [23]. The color plot show the longitudinal resistivity of TBG as a function of the filling factor and temperature. Various phases, such as metal, band insulator (BI), correlated states (CS) and superconductor (SC) are revealed.

The coexistence of correlated and superconducting phases in twisted bilayer graphene (TBG) is particularly intriguing, as it suggests intricate interplays between these phases. Experimental observations have indicated that the appearance of the superconducting phase

can be triggered upon quenching the insulating phase, indicating a competition between the two phases [24].

While fully elucidating the nature of superconductivity in magic angle TBG (MATBG) remains challenging, valuable insights have been obtained by tuning the interaction strength in MATBG and studying the behavior of the superconducting phase. It has been found that weakening the electron-electron interaction enhances superconductivity in MATBG, suggesting that electron-phonon coupling plays a stabilizing role by competing against the Coulomb interaction [25].

Experiments conducted by Arora et al. [26] have shed light on the impact of the van der Waals environment on superconductivity in TBG. The proximity effect between TBG and the substrate has been shown to be crucial in determining the phase diagram of TBG. Their measurements suggest that TBG superconductivity is consistent with a Cooper pairing mechanism that resonates with the spin-orbit interaction induced by an additional WSe_2 layer on a hexagonal boron nitride (hBN) substrate.

Similar to other unconventional superconductors, the superconducting phase in TBG exhibits nematic behavior, breaking rotational symmetry [27] and displaying anisotropic responses to in-plane magnetic fields that depend on the field direction [28].

Besides nematicity, other indications of the unconventional nature of superconductivity in twisted bilayer graphene (TBG) have been uncovered. Experimental observations have revealed that the transition temperature of TBG superconductivity deviates from the prediction of conventional s-wave superconductors. Experiments by Oh et al [29] suggested that MATBG can be a nodal superconductor with an anisotropic pairing mechanism. They found the tunneling gap Δ_T greatly exceeds the mean-field BCS ratio ($2\Delta_T/k_BT \sim 25$). Interestingly, the tunneling gap persists even when superconductivity is suppressed, suggesting its origin from a pseudogap phase [29].

The presence of flat bands in MATBG indicates strong electron-electron correlation effects. Xie et al. provided direct experimental evidence of strong correlation in MATBG [30]. Their results also demonstrated the failure of the mean-field approach in modeling the electron-electron interaction in MATBG.

The ferromagnetism observed in MATBG is another consequence of the electron-electron interaction. At approximately $3/4$ filling of the conduction band, ferromagnetic states in MATBG have been observed, accompanied by a giant anomalous Hall effect [31] (but not quantum) up to 10.4 $k\Omega$. When MATBG is placed in a finite magnetic field, a cascade of Chern insulators has also been observed [32]. The quantum anomalous Hall effect was soon confirmed in TBG by Serlin et al [33]. Depositing MATBG on a WSe_2 layer leads to a ferro-

magnetism driven by spin-orbit coupling [34]. Orbital ferromagnetism was also observed in MATBG deposited on hexagonal boron nitride (hBN) substrate [35].

Measurements of the van Hove singularity (VHS) in MATBG have suggested that correlated states in TBG are highly relevant to doping through a single VHS. The insulating gap appears at half-filling of TBG rather than at the peak of the VHS, indicating a Mott insulator picture of the correlated states.

The observed cascade of phase transitions in MATBG [36, 37] further supports the notion that the correlated insulating states and superconducting states in MATBG are ground states emerging from high-temperature parent phases characterized by broken electronic flavor symmetry and a revived Dirac-like character.

The existence of a flat electronic band in MATBG provides a unique platform for exploring strongly correlated topological phases. The discovery of the quantum anomalous Hall effect (QAH) in TBG aligned with an hBN substrate adds even more excitement to this fascinating field [33]. Interactions polarize electrons into moiré minibands with a Chern number $\mathcal{C} = 1$, resolved in terms of spin and valley. Experimental measurements confirming the QAH effect are illustrated in Fig. 2.

Experimental investigations have detected additional topological insulating phases in MATBG in the presence finite magnetic field, showing Chern numbers $\mathcal{C} = \pm 1, \pm 2$, and ± 3 at filling factors $\nu = \pm 3, \pm 2$, and ± 1 per moiré unit cell, respectively [38]. A later experimental work was able to observe a series of correlated Chern insulator phase with flavor-symmetry breaking down to zero magnetic field [39]. There are also experimental implications that fractional Chern insulator phase may also exist at zero magnetic field in MATBG [40].

When subjected to a non-zero magnetic field, MATBG exhibits distinct features compared to conventional quantum Hall ferromagnets, primarily due to the dominant Coulomb interaction that spontaneously breaks time reversal symmetry [32, 41, 42]. The Chern insulating phases possess non-trivial topological subbands and exhibit characteristics reminiscent of the Hofstadter butterfly.These new phases are accounted for in the Stoner picture.

The discovery of strange-metal behavior adds another puzzle to the already rich physical properties of TBG. This behavior is characterized by a linear dependence of resistivity ρ on temperature [43, 44], spanning a wide temperature range of over three orders of magnitude. It remains stable across various fillings leading to correlated insulators [45]. Further experimental measurements indicate that the metallic ground state is dominated by quantum fluctuations. A transition to a strange metal state is observed when the superconducting order is suppressed, shedding light on the intrinsic connection between quantum

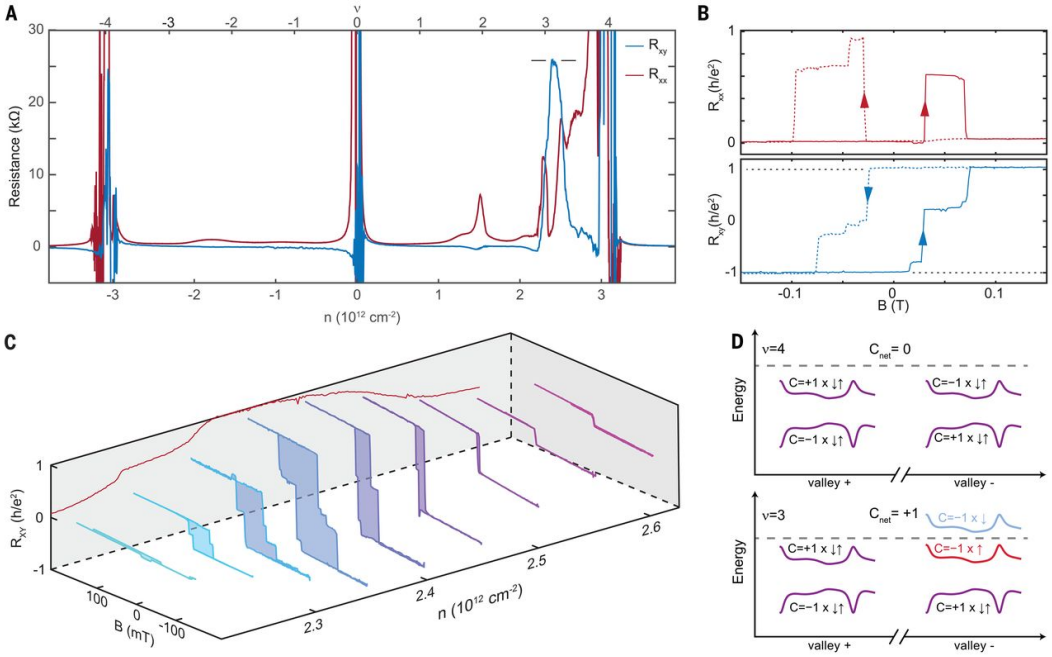

Figure 2: Figure reproduced from Ref. [33] showing the Quantum anomalous Hall effect of TBG aligned to hBN, measured at 1.6 K. (A) The longitudinal resistance R_{xx} and the Hall resistance R_{xy} measured as functions of the density of carriers, measured with a magnetic field 150 mT. (B) The measurement of R_{xx} and R_{xy} as functions of the magnetic field at a fixed density of carriers $n = 2.37 \times 10^{12}$ cm^{-2}. (C) R_{xy} as a function of the magnetic filed and the carrier density. The hysteresis loops are shown. When ferromagnetism emerges, R_{xy} is non-zero when the magnetic field is turned off, signaling quantum anomalous Hall effect. (D) Schematic illustrations of the Chern bands with filling factors $\nu = 3$ and $\nu = 4$ (full filling of a moiré unit cell).

fluctuations and superconductivity in MATBG [46].

Another intriguing phenomenon observed in TBG is the spontaneous spin/valley "flavor" polarization resulting from the breaking of flavor symmetry due to interactions [47–49].

With all these exotic and exciting physical properties listed above, twisted bilayer graphene has proven to be a versatile platform for exploring various physical phenomena, including unconventional superconductivity, correlated insulators, topological phases, and strange metals.

Significant theoretical efforts have also been devoted to understanding TBG in recent years. The Bistritzer-MacDonald model has been particularly successful in capturing the flat bands and magic angles of TBG [50]. A series of comprehensive investigations on TBG models have been presented [51–56], providing comprehensive insights into important facets of the TBG system, including electronic structures, symmetries, topologies, inter-

actions, many-body states, and correlated insulator phases, among others. Recently, the theory of topological heavy fermion models for MATBG has successfully unified different experimental observations by incorporating the Kondo effect mechanism [57, 58]. The topological nature of the flat bands and magic angles has also been emphasized [59].

TBG serves as a representative physical system for studying various two-dimensional van der Waals heterostructures with moiré structures, attracting extensive experimental and theoretical investigations. In addition to twisting two layers with the same periodicity, another approach to generate moiré structures is by overlapping and aligning two layers with slightly different periodicities. The WSe_2/WS_2 superlattice is a typical example of such a system. By tuning the filling, a transition from an antiferromagnetic Mott insulator phase to weak ferromagnetic states has been observed [60].

Inspired by TBG, other moiré structures such as twisted double bilayer graphene [61–65] and twisted monolayer-bilayer graphene [66, 67] have also been investigated. In Ref. [68], the experimental realization of twisted 4-layer and 5-layer of graphene also is reported. These systems exhibit correlated phases that can be tuned by an electric field.

A close “cousin” of TBG, twisted trilayer graphene (TTG), has recently garnered attention from the scientific community due to its structural similarities to TBG while exhibiting distinct features. Two typical configurations of TTG have been extensively studied based on the relative twist directions of the top and bottom layers: (1) mirror symmetrical TTG (mTTG), where the top and bottom layers are rotated in the same direction by the same angle relative to the middle layer, and (2) staircase TTG (sTTG), where the top and bottom layers are rotated in opposite directions.

With an additional graphene layer on top of the bilayer, TTG provides additional "knobs" to manipulate the system’s physical properties. In addition to the twist angle, the layer shifting and displacement field have been identified as channels for altering the physical properties of TTG [69, 70]. Among the experimental investigations, the mTTG configuration with vertical mirror symmetry has been the most widely studied. In this configuration, the top and bottom layers are perfectly aligned and twisted relative to the middle layer, resulting in a moiré pattern that shares the periodicity of TBG with the same twist angle. The magic-angle mTTG (MA-mTTG) with a magic angle of $\sqrt{2}$ times that of TBG has been experimentally demonstrated to exhibit strong-coupling superconductivity, which cannot be explained by the weak-coupling BCS theory [71].

The superconducting phase in MA-mTTG is characterized by flavor-polarized moiré bands [72] and persists in in-plane magnetic fields up to 10 T, violating the Pauli limit for conventional superconductors [73]. Spin locking in TTG superconductivity has been ob-

served, where the electrons forming a Cooper pair must belong to opposite valleys [74]. The Bardeen-Cooper-Schrieffer theory for superconductivity in the weak coupling limit suggests that VHS promotes superconductivity by increasing the density of states. In contrast, the superconductivity in MA-mTTG is found to be weakened when approaching VHS [69]. The VHS in MA-mTTG can also be tuned by the displacement field [69, 75–77]. Similar superconductivity phases have been experimentally observed in graphene systems with more layers stacked alternately [68]. Local spectroscopic techniques have provided evidence suggesting that the superconductivity in MA-mTTG is unconventional, exhibiting signatures similar to the superconducting phase of MATBG [78].

The relaxation of layers in MA-mTTG has been found to impact the local structure and arrangement of the system [79]. Spectroscopic observations have revealed strong moiré lattice reconstruction, with layers locked in a way that local domains exhibit structures near the magic angle of mTTG, comparable in size to the superconducting coherence length. The continuum model of mTTG indicates the coexistence of flat bands and highly dispersive Dirac cones near the magic angle of approximately 1.5°. Carr et al. further pointed out that the stability of the flat bands relies on lattice relaxation [80]. Notably, the experimental investigation of MA-mTTG has been challenging due to the mixture of flat bands and Dirac dispersion. The fully connected band structure without a gap, resulting from the $C_{2z}T$ symmetry, limits the detection of correlated insulating phases. Recent advancements in experimental techniques have successfully disentangled the intertwined bands by adding a small magnetic field and breaking the $C_{2z}T$ symmetry, facilitating the detection of correlated states in mTTG [81, 82].

In parallel with ongoing experimental research, theoretical investigations on TTG systems have been equally active. Theoretical studies on mTTG have confirmed the existence of correlated insulator, semi-metallic, and superconducting phases [83–86]. A schematic phase diagram of mTTG is shown in Fig. 3.

In addition to the mirror symmetrical arrangement, the staircase configuration of TTG has garnered considerable interest, primarily due to the presence of a supermoiré pattern, also called the "moiré of moiré" pattern. This pattern is formed by the interference between the two incommensurate TBG patterns within TTG. The staircase configuration is achieved by rotating the top and bottom layers in opposite directions relative to the middle layer. Experimental measurements have indicated the existence of superconducting and correlated insulating phases in staircase TTG (sTTG) with remarkably low carrier density [87].

Theoretical advancements in sTTG have also been made in recent years. Initially, the solution for sTTG was obtained by employing appropriate approximations to neglect the sec-

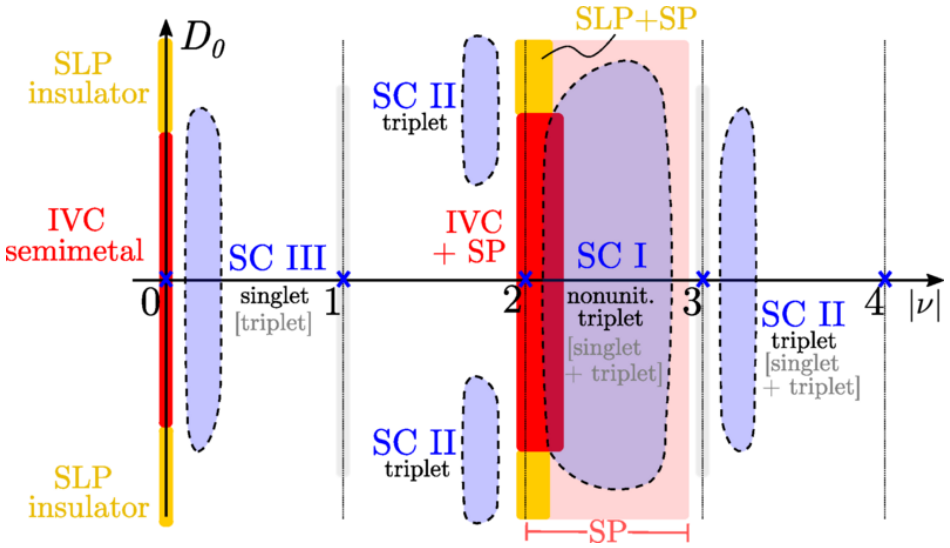

Figure 3: Schematic phase diagram of mTTG reproduced from Ref. [83]. The phase diagram is shown as a function of the displacement field D_0 and the filling factor ν. Due to the presence of particle hole symmetry in the mirror-symmetrical TTG, the phase diagram depends in fact on D_0 and $|\nu|$. At charge neutrality point ($\nu = 0$), the intervalley coherent (IVC) semimetal phase and sublattice polarized insulator phase are identified. The IVC and SPL phases coexist with spin polarization (SP) at the doping of $\nu = 2$. Three types of superconducting phases noted SC I-III are marked in the diagram. Their spin structures are also labeled in black color. The intervalley Hund's coupling J_H are shown in gray if it has opposite sign to the spin structure.

ondary supermoiré effects [88]. The results obtained in a periodic regime, similar to TBG, exhibited distinct characteristics compared to mirror symmetrical TTG. More recently, the magic angles of sTTG, which yield completely flat bands in the theoretical chiral limit, have been identified [89]. The presence of non-trivial topological bands in such models has also captured the attention of researchers [90].

The theoretical work by Zhu et al. [91] demonstrated that the supermoiré variations have significant impacts on the electronic properties of sTTG. However, a complete understanding of the supermoiré effects necessitates a comprehensive solution considering the quasicrystal structure of sTTG, which remains a major challenge in both physics and mathematics [76]. A recent experimental investigation addressed the quasi-crystal feature of TTG, and reported observations of superconductivity and interactions in the quasi-periodic regime [92].

Therefore, the main motivation of this thesis is to explore the physics of supermoiré in sTTG. Rather than attempting to tackle the complete incommensurability problem, the aim is to establish a theoretical framework that captures the supermoiré features under specific limiting conditions. Specifically, we will focus on regimes where sTTG can be treated as a

system with perturbed periodicity [93, 94]. This approach shares a similar philosophy with the so-called envelop wave function approach developed three decades ago in the semiconductor theory [95–97], and we take it further by addressing the gauge-fixing problem.

The thesis is structured as follows. Chapter 1 starts by constructing the continuum Bistrizer-MacDonaled model for TBG from fundamental principles, elucidating its band structure, magic angles, flat-band topologies, and important symmetries. Understanding TBG serves as a foundation for comprehending the TTG models. In Chapter 2, we investigate an approximate TTG model that allows for the solution on the moiré lattice. The moiré models of TTG discussed in this chapter form the basis for constructing the supermoiré effective theory presented in Chapter 3. Chapter 3 provides a detailed account of the development of the supermoiré effective theory, including discussions on symmetries and gauge invariance within the effective model. In Chapter 4, we outline the procedures for numerically solving the effective model and present the results. We showcase the supermoiré features extracted from the effective theory and compare them with results obtained through direct averaging of local models. This comparison convincingly demonstrates that the supermoiré characteristics cannot be captured by a simple incoherent average of local quantities.

Chapter 1

Twisted Bilayer Graphene: Flat Bands, Magic Angles and Symmetries

Understanding the Bistrizer-MacDonald model (BM model) of twisted bilayer graphene is a crucial aspect in comprehending the trilayer graphene model. This chapter provides a comprehensive overview of the development of the TBG BM model, beginning with the Fermi-level description of single-layer graphene. We delve into the study of the flat bands that arise in TBG and examine the corresponding magic angles at which these bands emerge. Additionally, we explore the topological properties of the flat bands and the diverse symmetries exhibited by TBG.

1.1 Bistrizer-MacDonald continuum model for TBG

We begin the construction of the TBG continuum model by examining single-layer graphene (SLG), depicted in Fig.1.1. At the charge neutrality point, the Fermi level of SLG consists of two Dirac points located at the $\boldsymbol{K}$ and $\boldsymbol{K}'$ points, often referred to as the two "valleys" of the graphene band structure, within the first Brillouin zone. The lowest-energy bands in SLG exhibit a linear dispersion forming isotropic cones. These two Dirac cones are time-reversed partners of each other. Consequently, the Fermi-level band structure of SLG effectively describes a spinless fermion, with its flavor determined by a combination of sublattice and valley indices:

$$h_{0,\eta} = (\eta \hat{k}_x - K_x^\eta)\sigma_x + \eta(\hat{k}_y - K_y^\eta)\sigma_y, \tag{1.1}$$

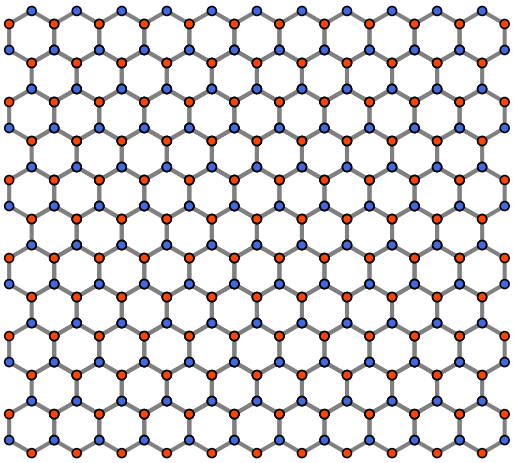

Figure 1.1: The real space structure of a single-layer graphene (SLG). The A- and B-sublattices are shown in blue and orange colors, respectively.

Here, $\eta = \pm 1$ represents the valley index for $\boldsymbol{K}$ and $\boldsymbol{K}'$ points, respectively. σ_x and σ_y are the Pauli matrices defined based on the sublattice indices, as depicted in Fig.1.1. We also used $\hat{k}_x = -i\partial_x$ and $\hat{k}_y = -i\partial_y$.

The Bistrizer-MacDonald (BM) model incorporates the near-Fermi level structure of each individual graphene layer. In the momentum space, the band structure landscape of a single-layer graphene consists of the two Dirac cones as well as their replicas resulting from translations over reciprocal lattice vectors. To construct the BM model, we focus on the cone located at the $\boldsymbol{K}$ valley of a single-layer graphene (SLG), as the cones at the two valleys are decoupled near the Fermi level. The low-energy continuum Hamiltonian for SLG is given by the Dirac Hamiltonian $\hat{h}_0 = (\hat{\boldsymbol{k}} - \boldsymbol{K}) \cdot \boldsymbol{\sigma}$, where $\hat{\boldsymbol{k}} = -i\boldsymbol{\nabla}$ represents the momentum operator.

Next, we will proceed with the construction of the TBG Hamiltonian. Usually, the derivation of the TBG Hamiltonian begins with the tight-binding model of two graphene layers. However, in this discussion, we will take an alternative approach by directly starting with the continuum Dirac Hamiltonian of each single layer.

To begin, let's write down the TBG Hamiltonian without interlayer hopping, which can be expressed as follows:

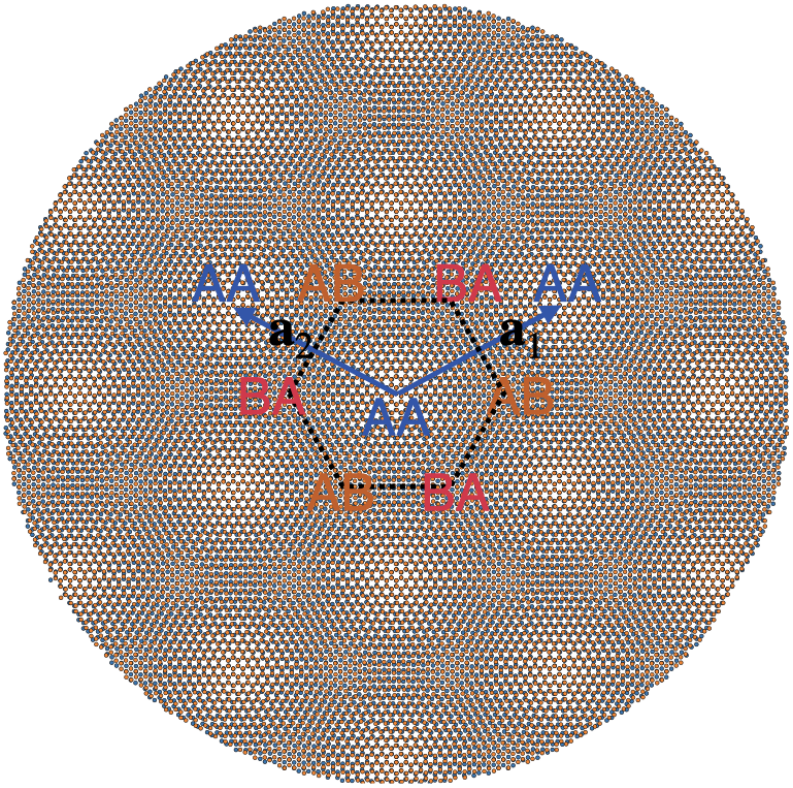

Figure 1.2: Real space arrangement of twisted bilayer graphene. The top and the bottom layers are rendered in orange and blue colors, respectively. Here the center is chosen to be the AA-stacking point. The recurrence of the AA points in the real space makes appear the periodicity of the moiré pattern. The AB- and BA-stacking points around a AA point defines the vertices of the Wigner-Seitz cell of the moiré lattice in real space. The top and bottom layers are rotated in the anticlockwise and the clockwise direction by an angle of $\theta/2$, respectively.

$$H_0(\boldsymbol{r}) = \begin{pmatrix} \hbar v_F(\hat{\boldsymbol{k}} - \hat{R}_{\theta/2}\boldsymbol{K}) \cdot \boldsymbol{\sigma} & \\ & \hbar v_F(\hat{\boldsymbol{k}} - \hat{R}_{-\theta/2}\boldsymbol{K}) \cdot \boldsymbol{\sigma} \end{pmatrix}, \tag{1.2}$$

In this expression, $\hat{R}_\alpha$ represents the operator that rotates a vector by an angle α. The two graphene layers are rotated in opposite directions by an angle of $\theta/2$. Throughout this chapter, we will adopt the convention that the top layer is rotated anticlockwise, while the bottom layer is rotated clockwise. In reciprocal space, the $\boldsymbol{K}$ point of both layers in Eq. (1.2) is rotated with respect to the $\boldsymbol{\Gamma}$ point by $\pm\theta/2$, respectively.

The layer index introduces an additional degree of freedom for the spinless fermions. To complete the model, we need to specify the interlayer hopping potential $V(\boldsymbol{r})$. This potential should be a 2×2 matrix that describes the hopping between sublattices belonging to different layers. The general form of the continuum TBG Hamiltonian is given by

$$H_{\text{TBG}}(\boldsymbol{r}) = \begin{pmatrix} \hbar v_F(\hat{\boldsymbol{k}} - \hat{R}_{\theta/2}\boldsymbol{K}) \cdot \boldsymbol{\sigma} & V(\boldsymbol{r}) \\ V^\dagger(\boldsymbol{r}) & \hbar v_F(\hat{\boldsymbol{k}} - \hat{R}_{-\theta/2}\boldsymbol{K}) \cdot \boldsymbol{\sigma} \end{pmatrix}. \tag{1.3}$$

In the following, we demonstrate that with the principles of momentum conservation during hopping, the graphene periodicity of each layer, and the inherent symmetries of the stacked graphene lattices, the expression for $V(\boldsymbol{r})$ can be determined.

We use $\boldsymbol{Q}_G$ and $\boldsymbol{Q}'_G$ to denote the reciprocal lattices of the top and bottom layers, respectively. The first constraint on $V(\boldsymbol{r})$ arises from the conservation of momentum before and after interlayer hopping. Taking into account the periodicity of each graphene layer, momentum conservation requires that:

$$V^{\alpha,\beta}_{\boldsymbol{k},\boldsymbol{k}'} = \langle \boldsymbol{k}, \alpha, l = 1 | \hat{V} | \boldsymbol{k}', \beta, l = 0 \rangle = \sum_{\boldsymbol{Q}_G, \boldsymbol{Q}'_G} \nu^{\alpha\beta}_{\boldsymbol{k},\boldsymbol{k}'}(\boldsymbol{Q}_G, \boldsymbol{Q}'_G) \delta_{\boldsymbol{k}+\boldsymbol{Q}_G, \boldsymbol{k}'+\boldsymbol{Q}'_G}, \tag{1.4}$$

where $\alpha, \beta \in \{A, B\}$ are the sublattice indices, and $l = 0, 1$ refers to the top and the bottom layers, respectively. The real-space representation of $V^{\alpha\beta}(\boldsymbol{r})$ is given by

$$V^{\alpha\beta}(\boldsymbol{r}) = \int \frac{\mathrm{d}\boldsymbol{k}^2 \mathrm{d}\boldsymbol{k}'^2}{2\pi} e^{i\boldsymbol{k}\cdot\boldsymbol{r}} V^{\alpha,\beta}_{\boldsymbol{k},\boldsymbol{k}'} e^{-i\boldsymbol{k}'\cdot\boldsymbol{r}} = \sum_{\boldsymbol{Q}_G, \boldsymbol{Q}'_G} \int \frac{\mathrm{d}\boldsymbol{k}^2}{2\pi} e^{-i(\boldsymbol{Q}_G - \boldsymbol{Q}'_G)\cdot\boldsymbol{r}} \nu^{\alpha\beta}_{\boldsymbol{k},\boldsymbol{k}+\boldsymbol{Q}_G-\boldsymbol{Q}'_G}(\boldsymbol{Q}_G, \boldsymbol{Q}'_G). \tag{1.5}$$

The Fourier coefficient $\nu^{\alpha\beta}_{\boldsymbol{k},\boldsymbol{k}'}(\boldsymbol{Q}_G, \boldsymbol{Q}'_G)$ *a priori* depends on both $\boldsymbol{k}$ and $\boldsymbol{k}'$. However, we observe that the momenta involved in the TBG Hamiltonian are restricted to the vicinity of the $\boldsymbol{K}$ points of both graphene layers, i.e., $\boldsymbol{k} \simeq \hat{R}\theta/2\boldsymbol{K}$ and $\boldsymbol{k}' \simeq \hat{R}_{-\theta/2}\boldsymbol{K}$. As a result, the coefficient $\nu^{\alpha\beta}_{\boldsymbol{k},\boldsymbol{k}'}(\boldsymbol{Q}_G, \boldsymbol{Q}'_G)$ can be approximated as $\nu^{\alpha\beta}_{\hat{R}_{\theta/2}\boldsymbol{K}, \hat{R}_{-\theta/2}\boldsymbol{K}}(\boldsymbol{Q}_G, \boldsymbol{Q}'_G) \equiv \nu^{\alpha\beta}(\boldsymbol{Q}_G, \boldsymbol{Q}'_G)$, where the dependence on $\boldsymbol{k}$ and $\boldsymbol{k}'$ is removed. This allows us to simplify the expression of $V^{\alpha\beta}(\boldsymbol{r})$ as follows:

$$V^{\alpha\beta}(\boldsymbol{r}) = \sum_{\boldsymbol{Q}_G, \boldsymbol{Q}'_G} \nu^{\alpha\beta}_{\boldsymbol{Q}_G, \boldsymbol{Q}'_G} e^{-i(\boldsymbol{Q}_G - \boldsymbol{Q}'_G)\cdot\boldsymbol{r}}. \tag{1.6}$$

This is in general *not* a periodic function unless $\boldsymbol{Q}_G$ and $\boldsymbol{Q}'_G$ are commensurate lattices.

To obtain the BM model, we need to continue the simplification of the interlayer coupling potential. We assume that $V^{\alpha\beta}(\boldsymbol{r})$ is primarily determined by $\nu^{\alpha\beta}_{\boldsymbol{Q}_G, \boldsymbol{Q}'_G}$, that gives the minimum distance between $\hat{R}_{\theta/2}\boldsymbol{K} + \boldsymbol{Q}_G$ and $\hat{R}_{-\theta/2}\boldsymbol{K} + \boldsymbol{Q}'_G$. The admissible combinations of $\boldsymbol{Q}_G$ and $\boldsymbol{Q}'_G$ are:

1. $\boldsymbol{Q}_G = \boldsymbol{Q}'_G = \boldsymbol{0}$, which yields $\hat{R}_{\theta/2}\boldsymbol{K} - \hat{R}_{-\theta/2}\boldsymbol{K} = \boldsymbol{q}_1$,
2. $\boldsymbol{Q}_G = \hat{R}_{\theta/2}\boldsymbol{b}_{G,2}$ and $\boldsymbol{Q}'_G = \hat{R}_{-\theta/2}\boldsymbol{b}_{G,2}$, resulting in $(\hat{R}_{\theta/2}\boldsymbol{K} + \boldsymbol{Q}_G) - (\hat{R}_{-\theta/2}\boldsymbol{K} + \boldsymbol{Q}'_G) = \boldsymbol{q}_2$,

3. $\boldsymbol{Q}_G = -\hat{R}_{\theta/2}\boldsymbol{b}_{G,1}$ and $\boldsymbol{Q}'_G = -\hat{R}_{-\theta/2}\boldsymbol{b}_{G,1}$, leading to $(\hat{R}_{\theta/2}\boldsymbol{K} + \boldsymbol{Q}_G) - (\hat{R}_{-\theta/2}\boldsymbol{K} + \boldsymbol{Q}'_G) = \boldsymbol{q}_3$.

Here, $\boldsymbol{b}_{G,1/2}$ represents the base vectors of the graphene reciprocal lattice, defined as:

$$\boldsymbol{b}_{G,1} = \frac{4\pi}{3d}\begin{pmatrix}\sqrt{3}/2\\ 1/2\end{pmatrix} \tag{1.7}$$

and

$$\boldsymbol{b}_{G,2} = \frac{4\pi}{3d}\begin{pmatrix}-\sqrt{3}/2\\ 1/2\end{pmatrix} \tag{1.8}$$

where d is the length of the C-C bond in the graphene layer. The vectors $\boldsymbol{q}_2$ and $\boldsymbol{q}_3$ can be generated by C_{3z} rotations of $\boldsymbol{q}_1$, as illustrated in Fig. 1.3.

Now we can apply a unitary transform to absorb the momenta $\hat{R}_{\theta/2}\boldsymbol{K}$ and $\hat{R}_{-\theta/2}\boldsymbol{K}$ on the diagonal blocks of the TBG Hamiltonian in Eq. (1.3):

$$H_{\text{BM}} = U^\dagger H_{\text{TBG}} U = \begin{pmatrix}\hbar v_F \hat{\boldsymbol{k}}\cdot\boldsymbol{\sigma} & \tilde{V}(\boldsymbol{r})\\ \tilde{V}^\dagger(\boldsymbol{r}) & \hbar v_F \hat{\boldsymbol{k}}\cdot\boldsymbol{\sigma}\end{pmatrix}, \tag{1.9}$$

where

$$U = \begin{pmatrix}e^{i\hat{R}_{\theta/2}\boldsymbol{K}\cdot\boldsymbol{r}} & \\ & e^{i\hat{R}_{-\theta/2}\boldsymbol{K}\cdot\boldsymbol{r}}\end{pmatrix}, \tag{1.10}$$

As a result, the matrix elements of the interlayer potential writes

$$\tilde{V}^{\alpha\beta}(\boldsymbol{r}) = e^{-i\hat{R}_{\theta/2}\boldsymbol{K}\cdot\boldsymbol{r}} V^{\alpha\beta}(\boldsymbol{r}) e^{i\hat{R}_{-\theta/2}\boldsymbol{K}\cdot\boldsymbol{r}} = \sum_{\boldsymbol{Q}_G,\boldsymbol{Q}'_G} V^{\alpha\beta}_{\boldsymbol{Q}_G,\boldsymbol{Q}'_G} e^{-i\left[(\hat{R}_{\theta/2}\boldsymbol{K}+\boldsymbol{Q}_G)-(\hat{R}_{-\theta/2}\boldsymbol{K}+\boldsymbol{Q}'_G)\right]\cdot\boldsymbol{r}}. \tag{1.11}$$

As explained previously, we keep only the values of $\boldsymbol{Q}_G$ and $\boldsymbol{Q}'_G$ that minimizes $(\hat{R}_{\theta/2}\boldsymbol{K}+\boldsymbol{Q}_G) - (\hat{R}_{-\theta/2}\boldsymbol{K} + \boldsymbol{Q}'_G)$ to one of the vectors among $\boldsymbol{q}_1$, $\boldsymbol{q}_2$ and $\boldsymbol{q}_3$. Finally, we can rewrite $\tilde{V}^{\alpha\beta}(\boldsymbol{r})$ as

$$\tilde{V}^{\alpha\beta}(\boldsymbol{r}) = \sum_{j=1}^{3} V_j^{\alpha\beta} e^{-i\boldsymbol{q}_j\cdot\boldsymbol{r}}. \tag{1.12}$$

We have three matrices V_j with $j = 1, 2, 3$ associated to each vector $\boldsymbol{q}_j$. The BM Hamiltonian of TBG is readily at hand.

To incorporate the C_{3z} symmetry, we consider the origin of the coordinates to be at the AA stacking point. In this case, a $120°$ rotation around an axis perpendicular to the graphene planes restores the conformation of both the top and bottom layers, preserving

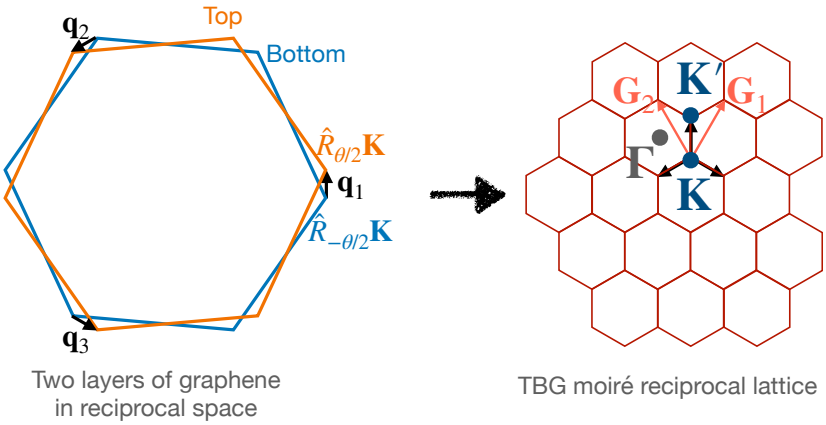

Figure 1.3: Left panel: The two graphene layers represented in the reciprocal space with the first Brillouin zone of each layer. The smallest possible vectors connecting the $\mathbf{K}$ points of each layer are $\boldsymbol{q}_1$, $\boldsymbol{q}_2$ and $\boldsymbol{q}_3$. Right panel: the moiré reciprocal lattice of TBG generated by $\boldsymbol{q}_1$, $\boldsymbol{q}_2$ and $\boldsymbol{q}_3$, where $\boldsymbol{G}_1$ and $\boldsymbol{G}_2$ are the bases vectors of the moiré reciprocal lattice.

the symmetry of the TBG system.

For the TBG Hamiltonian to respect the C_{3z} symmetry, it must satisfy the following condition before and after the C_{3z} rotation, to maintain the same physical properties:

$$C_{3z} H_{\text{TBG}}(\boldsymbol{r}) C_{3z}^{\dagger} = H_{\text{TBG}}(\hat{R}_{2\pi/3}\boldsymbol{r}), \tag{1.13}$$

Under rotation of $\boldsymbol{r}$ by $120°$, the diagonal blocks $\hat{\boldsymbol{k}} \cdot \boldsymbol{\sigma}$ transforms as $e^{2i\pi/sigma_z/3}\hat{\boldsymbol{k}} \cdot \boldsymbol{\sigma} e^{-2i\pi/sigma_z/3}$, which suggests

$$C_{3z} = e^{2i\pi\sigma_z/3}. \tag{1.14}$$

The specific form of the V_j matrices will be determined to satisfy this symmetry condition. The constraint of Eq. (1.13) imposes the following relation between V_j matrices:

$$V_{j+1} = e^{2i\pi\sigma_z/3} V_j e^{-2i\pi\sigma_z/3} \tag{1.15}$$

for Eq. (1.13) to hold.

Another symmetry to take into account is to rotate the system by $180°$ around the x-axis, noted C_{2x}. Flipping the twisted bilayer graphene around the x-axis by $180°$ exchanges

the layers and restores the original configuration of the TBG. Under the C_{2x} symmetry, the coordinates $\boldsymbol{r} = (x, y)$ are transformed to $\boldsymbol{r} = (x, -y)$. In the matrix form of $H_{\text{BM}}(x, -y)$, the diagonal blocks become $\hbar v_F \hat{\boldsymbol{k}} \cdot \boldsymbol{\sigma}^*$, where $\boldsymbol{\sigma}^*$ is the complex conjugate of the Pauli matrices $\boldsymbol{\sigma}$. The interlayer hopping potential becomes:

$$\tilde{V}(x, -y) = V_1 e^{i\boldsymbol{q}_1 \cdot \boldsymbol{r}} + V_2 e^{i\boldsymbol{q}_3 \cdot \boldsymbol{r}} + V_3 e^{i\boldsymbol{q}_2 \cdot \boldsymbol{r}}.$$

This form of the interlayer hopping potential ensures that the TBG Hamiltonian retains its symmetry under C_{2x} rotation.

To establish a unitary transformation connecting $H_{\text{BM}}(x, -y)$ with $H_{\text{BM}}(\boldsymbol{r})$ and satisfy the C_{2x} symmetry, the required unitary operation is given by:

$$C_{2x} = \tau_x \otimes \sigma_x, \tag{1.16}$$

where τ_x is a Pauli matrix defined on the *layer* indices, while σ_x is a Pauli matrix defined on the *sublattice* indices. This unitary transformation ensures that the TBG Hamiltonian exhibits the desired symmetry under C_{2x} rotation.

For C_{2x} to be valid, it is then necessary that $\sigma_x V_1 \sigma_x = V_1$, while $\sigma_x V_2 \sigma_x = V_3$ and $\sigma_x V_3 \sigma_x = V_2$. Combining the above constraints on V_j matrices imposed by C_{3z} and C_{2x} symmetries, we must have them written in the following forms:

$$\begin{aligned} V_1 &= \begin{pmatrix} w_0 & w_1 \\ w_1 & w_0 \end{pmatrix} = w_1 \begin{pmatrix} r & 1 \\ 1 & r \end{pmatrix} \\ V_2 &= \begin{pmatrix} w_0 & \omega^* w_1 \\ \omega w_1 & w_0 \end{pmatrix} = w_1 \begin{pmatrix} r & \omega^* \\ \omega & r \end{pmatrix}, \\ V_3 &= \begin{pmatrix} w_0 & \omega w_1 \\ \omega^* w_1 & w_0 \end{pmatrix} = w_1 \begin{pmatrix} r & \omega \\ \omega^* & r \end{pmatrix} \end{aligned} \tag{1.17}$$

where $\omega = \exp(2i\pi/3)$. w_0 and w_1 designate the intra-sublattice and inter-sublattice hopping energy between layers.

In typical cases, a common choice for the interlayer coupling potential is $w_1 = 110\,\text{meV}$, where w_1 represents the strength of interlayer hopping. It is also common to consider w_0 to be less than or equal to w_1, denoted as $w_0 \leqslant w_1$. The ratio $r = w_0/w_1$ is referred to as the corrugation factor of graphene.

In particular, the case of $w_0 = 0$ is known as the chiral limit, which holds special interest as it allows for analytical solutions of the flat bands. On the other hand, when $w_0 = w_1$, it

corresponds to the isotropic limit. In practical scenarios, the value of r is often around 0.8, indicating a proximity to the isotropic limit.

It is also convenient to use the T_j matrices in the following

$$T_j = \begin{pmatrix} r & \omega^{-j-1} \\ \omega^{j-1} & r \end{pmatrix} = r\sigma_0 + \cos(2(j-1)\pi/3)\sigma_x + \sin(2(j-1)\pi/3)\sigma_y, \tag{1.18}$$

where σ_0 is the identity matrix defined on the sublattice indices. We will also use $\tilde{V}(\boldsymbol{r}) = w_1 T(\boldsymbol{r})$ with

$$T(\boldsymbol{r}) = \sum_{j=1}^{3} T_j e^{-i\boldsymbol{q}_j \cdot \boldsymbol{r}}. \tag{1.19}$$

The Hamiltonian of BM TBG model finally writes

$$H_{\text{BM}} = \begin{pmatrix} \hbar v_F \hat{\boldsymbol{k}} \cdot \boldsymbol{\sigma} & w_1 T(\boldsymbol{r}) \\ w_1 T(-\boldsymbol{r}) & \hbar v_F \hat{\boldsymbol{k}} \cdot \boldsymbol{\sigma} \end{pmatrix}. \tag{1.20}$$

A little more massage of the BM TBG Hamiltonian gives:

$$H_{\text{BM}} = \hbar v_F |\boldsymbol{q}| \begin{pmatrix} \frac{\hat{\boldsymbol{k}}}{|\boldsymbol{q}|} \cdot \boldsymbol{\sigma} & \frac{w_1}{\hbar v_F |\boldsymbol{q}|} T(\boldsymbol{r}) \\ \frac{w_1}{\hbar v_F |\boldsymbol{q}|} T(-\boldsymbol{r}) & \frac{\hat{\boldsymbol{k}}}{|\boldsymbol{q}|} \cdot \boldsymbol{\sigma} \end{pmatrix}, \tag{1.21}$$

where $|\boldsymbol{q}| = |\boldsymbol{q}_j|,\ j = 1, 2, 3$. Therefore, $|\boldsymbol{q}| = \theta |\boldsymbol{K}|$. Then do the substitution

$$\hat{\boldsymbol{k}} \leftarrow \hat{\boldsymbol{k}}/|\boldsymbol{q}| \tag{1.22}$$

and we now work with dimensionless wave vectors. The ratio

$$a = \frac{w_1}{\hbar v_F |\boldsymbol{q}|} = \frac{w_1}{\hbar v_F |\boldsymbol{K}|} \frac{1}{\theta} \tag{1.23}$$

is the coupling constant. This is the unique parameter in the TBG model that controls the whole low-energy physics. It is beneficial to concentrate only on the dimensionless Hamiltonian to understand more generally the TBG physics:

$$H_{\text{BM}} \leftarrow H_{\text{BM}}/(\hbar v_F |\boldsymbol{q}|) = \begin{pmatrix} \hat{\boldsymbol{k}} \cdot \boldsymbol{\sigma} & aT(\boldsymbol{r}) \\ aT(-\boldsymbol{r}) & \hat{\boldsymbol{k}} \cdot \boldsymbol{\sigma} \end{pmatrix}. \tag{1.24}$$

Now we will examine some specific coordinates where $T(\boldsymbol{r})$ locally has some interesting

forms. First let us look at $\boldsymbol{r} = \mathbf{0}$. Obviously,

$$T(\boldsymbol{r} = \mathbf{0}) = \begin{pmatrix} 3r & 0 \\ 0 & 3r \end{pmatrix}, \tag{1.25}$$

which means at $\boldsymbol{r} = 0$, there is only AA or BB interlayer hopping. Therefore, the Hamiltonian expressed in Eq. (1.24) has chosen the AA-stacking point as the origin of coordinates.

The second special coordinate is $\boldsymbol{r} = (\boldsymbol{a}_1 - \boldsymbol{a}_2)/3$. A simple calculation gives

$$T(\frac{\boldsymbol{a}_1 - \boldsymbol{a}_2}{3}) = \begin{pmatrix} 0 & 3r \\ 0 & 0 \end{pmatrix}, \tag{1.26}$$

implying there exists only hopping between the A-sublattice of the top layer and the B-sublattice of the bottom layer at this location. Clearly, this is the AB-stacking point.

Finally one can explore another coordinate $\boldsymbol{r} = (-\boldsymbol{a}_1 + \boldsymbol{a}_2)/3$ which gives

$$T(\frac{-\boldsymbol{a}_1 + \boldsymbol{a}_2}{3}) = \begin{pmatrix} 0 & 0 \\ 3r & 0 \end{pmatrix}. \tag{1.27}$$

The hopping is between top B-sublattice and bottom A-sublattice. This is therefore a BA-stacking point of TBG.

We will see later these special coordinates are the locations of C_{3z} axes of TBG.

1.2 TBG band structure, flat bands and magic angles

The advantage of the TBG Hamiltonian given by Eq. (1.24) is that it allows us to treat non-commensurate graphene lattices at arbitrary twist angles within the periodic regime. This is made possible by considering the lowest-order terms in the interlayer coupling potential $V(\boldsymbol{r})$. The periodicity of Eq. (1.24) can be manifested by:

$$\tilde{H}_{\text{BM}}(\boldsymbol{r}) = \begin{pmatrix} e^{i\boldsymbol{q}_1\cdot\boldsymbol{r}} & \\ & 1 \end{pmatrix} H_{\text{BM}}(\boldsymbol{r}) \begin{pmatrix} e^{-i\boldsymbol{q}_1\cdot\boldsymbol{r}} & \\ & 1 \end{pmatrix} = \begin{pmatrix} (\hat{\boldsymbol{k}} - \boldsymbol{q}_1)\cdot\boldsymbol{\sigma} & \tilde{T}(\boldsymbol{r}) \\ \tilde{T}(-\boldsymbol{r}) & \hat{\boldsymbol{k}}\cdot\boldsymbol{\sigma} \end{pmatrix}. \tag{1.28}$$

$\tilde{H}_{\text{BM}}(\boldsymbol{r})$ satisfies the periodicity

$$\tilde{H}_{\text{BM}}(\boldsymbol{r} + \boldsymbol{a}_{1/2}) = \tilde{H}_{\text{BM}}(\boldsymbol{r}).$$

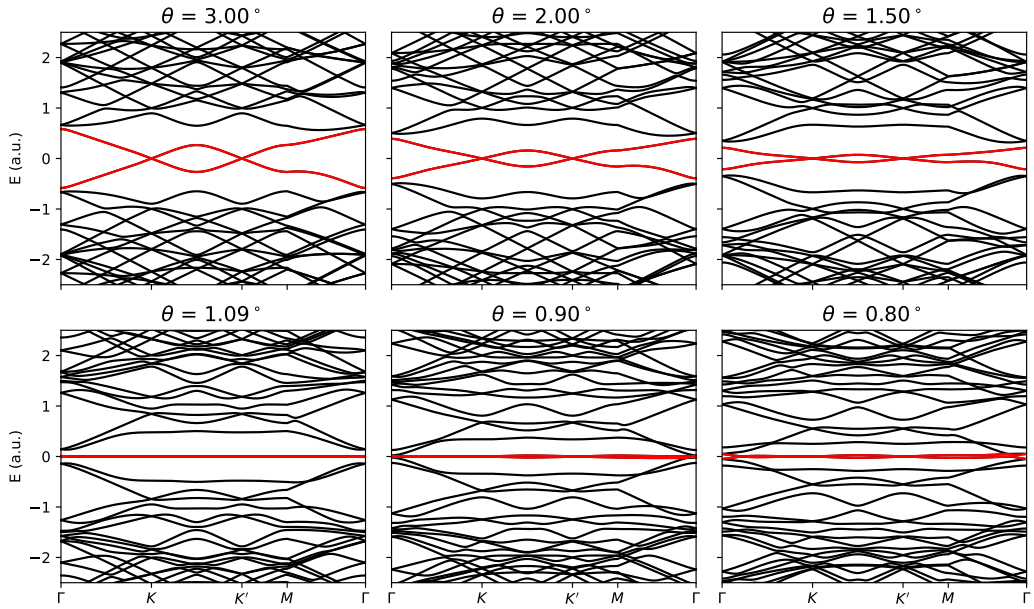

Figure 1.4: Variation of the TBG band structure with different twist angles. The two bands closest to the zero-energy level are labeled with red color. $\theta = 1.09°$ is the famous "magic angle" of TBG. The band structures are computed with the corrugation factor $r = \omega_{AA}/\omega_{AB} = 0.8$.

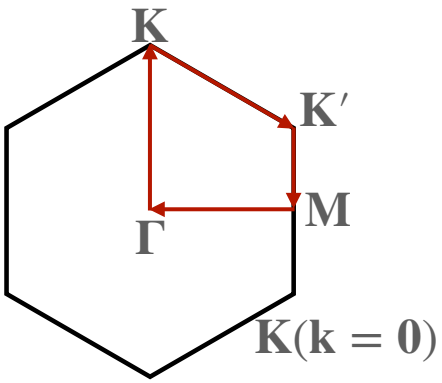

Figure 1.5: The route in the Brillouin zone along which the band structures are computed is chosen to be $\mathbf{\Gamma} \to \mathbf{K} \to \mathbf{K}' \to \mathbf{M} \to \mathbf{\Gamma}$.

with

$$\boldsymbol{a}_i \cdot \boldsymbol{G}_j = 2\pi\delta_{ij}.$$

Here $\boldsymbol{G}_1 = \boldsymbol{q}_1 - \boldsymbol{q}_2$ and $\boldsymbol{G}_2 = \boldsymbol{q}_1 - \boldsymbol{q}_3$. We have defined the potential $\tilde{T}(\boldsymbol{r})$ as

$$\tilde{T}(\boldsymbol{r}) = e^{i\boldsymbol{q}_1\cdot\boldsymbol{r}}T(\boldsymbol{r}) = T_1 + T_2 e^{i\boldsymbol{G}_1\cdot\boldsymbol{r}} + T_3 e^{i\boldsymbol{G}_2\cdot\boldsymbol{r}}. \tag{1.29}$$

According to Bloch's theorem, the eigenfunctions of $\tilde{H}_{\text{BM}}$ can be written in the form

$$\tilde{\Psi}_{n\boldsymbol{k}}(\boldsymbol{r}) = e^{i\boldsymbol{k}\cdot\boldsymbol{r}}\begin{pmatrix}\tilde{u}_{n\boldsymbol{k}}(\boldsymbol{r})\\ \tilde{v}_{n\boldsymbol{k}}(\boldsymbol{r})\end{pmatrix}, \tag{1.30}$$

where $\tilde{u}_{n\boldsymbol{k}}(\boldsymbol{r})$ and $\tilde{v}_{n\boldsymbol{k}}(\boldsymbol{r})$ are *spinor* Bloch functions that are periodic on the lattice defined by $\boldsymbol{a}_{1/2}$. Here, n is the band index and $\boldsymbol{k}$ is now a vector within the moiré Brillouin zone (mBZ).

From Eq. (1.28), the eigenfunction of H_{BM} given in Eq. (1.24) writes

$$\Psi_{n\boldsymbol{k}}(\boldsymbol{r}) = \begin{pmatrix}e^{-i\boldsymbol{q}_1\cdot\boldsymbol{r}} & \\ & 1\end{pmatrix}\tilde{\Psi}_{n\boldsymbol{k}} = e^{i\boldsymbol{k}\cdot\boldsymbol{r}}\begin{pmatrix}e^{-i\boldsymbol{q}_1\cdot\boldsymbol{r}}\tilde{u}_{n\boldsymbol{k}}(\boldsymbol{r})\\ \tilde{v}_{n\boldsymbol{k}}(\boldsymbol{r})\end{pmatrix} = e^{i\boldsymbol{k}\cdot\boldsymbol{r}}\begin{pmatrix}u_{n\boldsymbol{k}}(\boldsymbol{r})\\ v_{n\boldsymbol{k}}(\boldsymbol{r})\end{pmatrix}, \tag{1.31}$$

where $u_{n\boldsymbol{k}}(\boldsymbol{r}) = e^{-i\boldsymbol{q}_1\cdot\boldsymbol{r}}\tilde{u}_{n\boldsymbol{k}}(\boldsymbol{r})$ and $v_{n\boldsymbol{k}}(\boldsymbol{r}) = \tilde{v}_{n\boldsymbol{k}}(\boldsymbol{r})$. The Schrödinger's equation

$$H_{\text{BM}}(\boldsymbol{r})\Psi_{n\boldsymbol{k}}(\boldsymbol{r}) = \mathcal{E}_{n\boldsymbol{k}}\Psi_{n\boldsymbol{k}}(\boldsymbol{r})$$

leads to the eigenvalue equation concerning only the Bloch wave function:

$$\begin{pmatrix}(\boldsymbol{k}-i\boldsymbol{\nabla})\cdot\boldsymbol{\sigma} & aT(\boldsymbol{r})\\ aT(-\boldsymbol{r}) & (\boldsymbol{k}-i\boldsymbol{\nabla})\cdot\boldsymbol{\sigma}\end{pmatrix}\begin{pmatrix}u_{n\boldsymbol{k}}(\boldsymbol{r})\\ v_{n\boldsymbol{k}}(\boldsymbol{r})\end{pmatrix} = \mathcal{E}_{n\boldsymbol{k}}\begin{pmatrix}u_{n\boldsymbol{k}}(\boldsymbol{r})\\ v_{n\boldsymbol{k}}(\boldsymbol{r})\end{pmatrix}, \tag{1.32}$$

This equation can be solved numerically by applying Bloch's theorem and going to Fourier space. We can rewrite the Hamiltonian as a matrix defined on discrete reciprocal lattice, parameterized by a wave vector $\boldsymbol{k}$ inside the mBZ. The Hamiltonian matrix elements are given by:

$$H_{\text{BM}}{}^{\alpha\beta}_{\boldsymbol{Q},\boldsymbol{Q}'}(\boldsymbol{k}) = (\boldsymbol{k}-\boldsymbol{Q})\cdot\boldsymbol{\sigma}^{\alpha\beta}\delta_{\boldsymbol{Q},\boldsymbol{Q}'} + \sum_{j=1}^{3} T_j^{\alpha\beta}(\delta_{\boldsymbol{Q},\boldsymbol{Q}'+\boldsymbol{q}_j} + \delta_{\boldsymbol{Q},\boldsymbol{Q}'-\boldsymbol{q}_j}), |\boldsymbol{Q}|, |\boldsymbol{Q}'| < Q_{\text{max}}, \tag{1.33}$$

where we use $\boldsymbol{Q}$ to denote the reciprocal lattice sites. The values of $\boldsymbol{Q}$ are given by

$$\boldsymbol{Q}(n_1, n_2, l) = n_1\boldsymbol{G}_1 + n_2\boldsymbol{G}_2 + l\boldsymbol{q}_1,\ n_1, n_2 \in \mathbb{Z}. \tag{1.34}$$

where $l = 0, 1$ is the layer index for bottom and top layers, respectively. We also use $\alpha, \beta \in \{A, B\}$ to denote the sublattice degree of freedom. The parameter Q_{max} represents the cutoff of the reciprocal lattice vectors included in the computation. By setting an upper limit for Q_{max}, one restricts the range of reciprocal lattice vectors that are considered in the calculation of the Bloch functions. Reference [51] provides further details and anal-

ysis regarding the numerical convergence and the choice of $Q_{\max}$ in the context of TBG calculations.

In Fig. 1.4, the band structures of twisted bilayer graphene (TBG) at various twist angles are presented. It is observed that regardless of the twist angle, there are two Dirac cones located at the $\boldsymbol{K}$ and $\boldsymbol{K}'$ points of the moiré Brillouin zone. These Dirac cones correspond to the low-energy excitations in the system and are reminiscent of the Dirac cones in pristine graphene. However, in TBG, the dispersion velocity of these cones is renormalized compared to graphene due to the interlayer coupling.

As the twist angle decreases (or the interlayer coupling constant increases), the renormalized velocity of the Dirac cones decreases. At the magic angle, the renormalized velocity vanishes completely, leading to the emergence of flat bands. The magic angle is a special twist angle where the interplay between lattice moiré pattern and the electronic structure results in the formation of a narrow energy band with suppressed dispersion. It is interesting to note that as the twist angle continues to decrease from the magic angle, the velocity of the Dirac cones revives and disappears repeatedly.

In the mBZ of TBG, it is mentioned that the origin of the k-space coordinates $\boldsymbol{k} = \mathbf{0}$ is set at the $\boldsymbol{K}$ point rather than the $\boldsymbol{\Gamma}$ point. This choice is made to fix the symmetry center at the $\boldsymbol{\Gamma}$ point, which simplifies the analysis of the system's symmetries and facilitates the description of its electronic properties.

Further explanations and analysis regarding the band structures and the mBZ of TBG are likely provided in the corresponding figures and accompanying text.

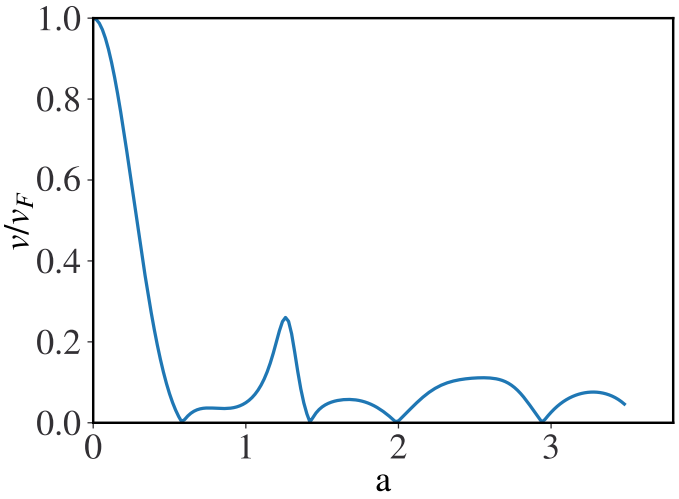

Figure 1.6: Revival of the Fermi velocity as a function of the dimensionless coupling constant ($a \propto 1/\theta$). The velocities are calculated using $\boldsymbol{k} \cdot \boldsymbol{p}$ method near the $\mathbf{K}$ point. The angles where the Fermi velocity vanishes are the magic angles.

Fig. 1.6 displays the renormalized Fermi velocity of twisted bilayer graphene (TBG) as a function of the dimensionless coupling constant, which is proportional to $1/\theta$, where θ is the twist angle. The renormalized Fermi velocity provides insight into the behavior of the electronic bands and can offer a simplified understanding of the emergence of flat bands in TBG.

The renormalized Fermi velocity is computed using the $\boldsymbol{k} \cdot \boldsymbol{p}$ method, which enables a degenerate perturbative calculation near the TBG $\boldsymbol{K}$ point. By analyzing the behavior of the Fermi velocity, important information about the electronic properties and the emergence of flat bands can be obtained.

The plot in Fig. 1.6 demonstrates that as the dimensionless coupling constant (related to $1/\theta$) increases, the renormalized Fermi velocity decreases until the first magic angle met. This behavior is in line with the observation that the dispersion velocity of the Dirac cones in TBG is renormalized compared to pristine graphene. As the Fermi velocity decreases, it approaches zero at the magic angle, where the flat bands emerge.

It is important to note that the plot provides an incomplete understanding of the flat bands and should be complemented with a more comprehensive analysis of the electronic structure and band dispersions. However, this simplified approach can serve as a useful starting point to gain insight into the emergence of flat bands in TBG.

The flat bands in twisted bilayer graphene (TBG) exhibit a non-trivial topology known as fragile topology. This characterization was first established in a study by Song et al. [59]. Although the total Chern number of the two detached middle bands is zero, an interesting phenomenon occurs at the chiral limit.

In the chiral limit, the two flat bands can be isolated based on sublattice polarization. Each of these chiral bands possesses an individual Chern number equal to ± 1. This implies that each chiral band exhibits a non-zero Chern number, indicating a non-trivial topological nature. However, when these two bands are considered together, their topological properties combine, resulting in a cancellation of their Chern numbers. As a result, the total Chern number for the combined bands becomes zero, signifying a trivial overall topology.

This delicate interplay between individual non-trivial Chern numbers and their cancellation when combined leads to the concept of fragile topology in TBG. It highlights the sensitivity of the topological properties to band crossings and the intricate nature of the electronic structure in this system. The fragile topology of TBG adds to its rich and fascinating physics, making it a subject of significant research interest.

We have carried out a Wilson Loop calculation for the two middle bands away from the

chiral limit, as shown in Fig. 1.7. A two band Wilson loop is a 2×2 matrix given by

$$W(k_2) = \Psi^{\dagger}_{0,k_2} \prod_{n=0}^{N-1} P_{\frac{n}{N},k_2} \Psi_{0,k_2}, \tag{1.35}$$

where $0 \leqslant k_{1/2} \leqslant 1$ and $\Psi_{k_1,0} = [|\psi_{1,k_1\boldsymbol{G}_1}\rangle, |\psi_{2,k_1\boldsymbol{G}_1}\rangle]$ is a two-column matrix with $|\psi_{1/2,k_2\boldsymbol{G}_2}\rangle$ being the two states of the middle bands computed at $\boldsymbol{k} = k_1\boldsymbol{G}_1$. P_{k_1,k_2} is a projector

$$P_{k_1,k_2} = \sum_{m=1,2} |\psi_{m,k_1\boldsymbol{G}_1+k_2\boldsymbol{G}_2}\rangle\langle\psi_{m,k_1\boldsymbol{G}_1+k_2\boldsymbol{G}_2}| \,. \tag{1.36}$$

The two eigenvalues of the Wilson loop accumulates $\pm 2\pi$ when the Wilson loop swipes over the moire reciprocal unit cell, giving a total Chern number equal to 0.

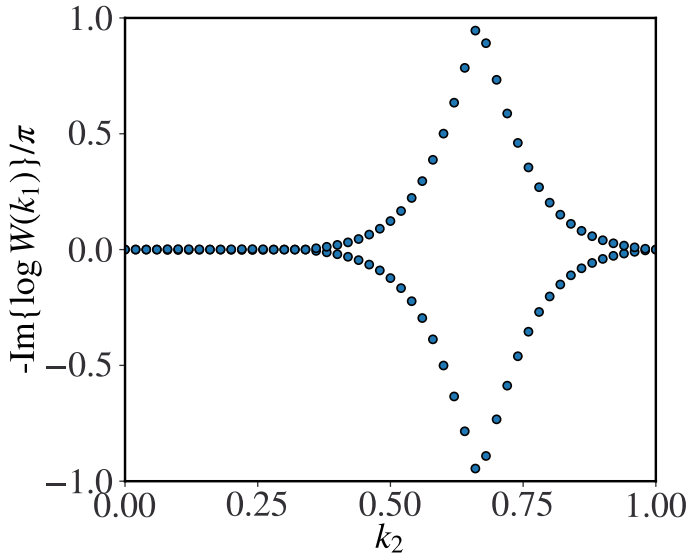

Figure 1.7: Wilson Loop computation of the middle bands. Each of the two eigenvalues accumulates $\pm 2\pi$. The total accumulated phase is however 0, giving a total Chern number $\mathcal{C} = 0$.

1.3 Analyses on typical symmetries in TBG

The BM TBG model incorporates various symmetries that play a crucial role in determining the system's topology. Understanding these symmetries and their effect on the wave functions is essential for characterizing the properties of TBG.

Translational symmetry. As has been discussed in Eq. (1.28), the invariance of translation is the prerequisite for the application of the Bloch's theorem. Another way to show it

is to start directly from Eq. (1.24) and show that $H_{\mathrm{BM}}(\boldsymbol{r}+\boldsymbol{a}_{1/2})$ and $H_{\mathrm{BM}}(\boldsymbol{r})$ can be related by a unitary transform on the other degrees of freedom other than $\boldsymbol{r}$. Indeed, one has

$$H_{\mathrm{BM}}(\boldsymbol{r}+\boldsymbol{a}_{1/2}) = \mathcal{T}_{\boldsymbol{a}_{1/2}} H_{\mathrm{BM}}(\boldsymbol{r}) \mathcal{T}^{\dagger}_{\boldsymbol{a}_{1/2}}, \tag{1.37}$$

with

$$\mathcal{T}_{\boldsymbol{a}_{1/2}} = \begin{pmatrix} \omega & 0 \\ 0 & \omega^* \end{pmatrix}_{\text{layer}} \otimes \sigma_0, \tag{1.38}$$

with $\omega = \exp(2i\pi/3)$.

Invariance of phase factors. If we parameterize the interlayer hopping potential by three phase factors, i.e.

$$T_{[\phi_1,\phi_2,\phi_3]}(\boldsymbol{r}) = T_1 e^{-i\boldsymbol{q}_1\cdot\boldsymbol{r}+\phi_1} + T_2 e^{-i\boldsymbol{q}_2\cdot\boldsymbol{r}+\phi_2} + T_3 e^{-i\boldsymbol{q}_3\cdot\boldsymbol{r}+\phi_3}, \tag{1.39}$$

A Hamiltonian equipped with $T_{[\phi_1,\phi_2,\phi_3]}(\boldsymbol{r})$ is noted $H_{\mathrm{BM}[\phi_1,\phi_2,\phi_3]}(\boldsymbol{r})$. It is always possible to restored it to the form of Eq. (1.24) up to a gauge change without any phase factors. This is done by a simple shift of the origin of the coordinates. To be precise, we have

$$\begin{pmatrix} e^{-i\phi_1/2} & \\ & e^{i\phi_1/2} \end{pmatrix} H_{\mathrm{BM}[\phi_1,\phi_2,\phi_3]}(\boldsymbol{r}+\boldsymbol{r}_0) \begin{pmatrix} e^{i\phi_1/2} & \\ & e^{-i\phi_1/2} \end{pmatrix} = H_{\mathrm{BM}[0,0,0]}(\boldsymbol{r}) \tag{1.40}$$

where $\boldsymbol{r}_0$ satisfies $\boldsymbol{G}_1\cdot\boldsymbol{r}_0 = \phi_2-\phi_1$ and $\boldsymbol{G}_2\cdot\boldsymbol{r}_0 = \phi_3-\phi_1$, or more explicitly

$$\boldsymbol{r}_0 = \frac{\phi_2-\phi_1}{2\pi}\boldsymbol{a}_1 + \frac{\phi_3-\phi_1}{2\pi}\boldsymbol{a}_2. \tag{1.41}$$

The consequence of the invariance of phases is that all TBGs with the same twist angles are identical up to a translation, irrespective of the rotation center of the twist.

Particle-Hole symmetry. The particle-hole symmetry (PHS) in the BM model of TBG originates from the Dirac Hamiltonian inherited from the low-energy band structure of each graphene single layer. It would be broken if the precise band structure of graphene is taken into consideration. Strictly speaking, the unitary transform of the particle-hole symmetry, $\mathcal{P}$, is not a "symmetry", as it does *anticommutes* with the Hamiltonian. Commutation is only possible when limited to the zero-energy subspace. The PHS is manifested by

$$\mathcal{P} H_{\mathrm{BM}}(\boldsymbol{r}) \mathcal{P}^{\dagger} = -H_{\mathrm{BM}}(-\boldsymbol{r}). \tag{1.42}$$

It is not hard to find a unitary transform satisfying the above condition is

$$\mathcal{P} = \tau_y, \tag{1.43}$$

with τ_y being a Pauli matrix acting on the layer indices. This choice of $\mathcal{P}$ is obviously a unitary Hermitian matrix and squares to 1. Often in literature a different choice $\mathcal{P} = i\tau_y$ may be adopted [52], which is an anti-Hermitian operator and squares to -1.

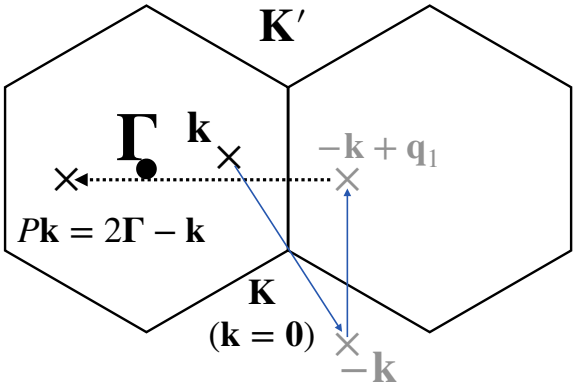

Figure 1.8: The particle hole symmetry sends an arbitrary wave vector within the TBG Brillouin zone to its counterpart symmetrical to it with respect to the $\mathbf{\Gamma}$ point. The dotted arrow show the Ukmlapp process to send $-\boldsymbol{k} + \boldsymbol{q}_1$ back inside the Brillouin zone centered at $\mathbf{\Gamma}$.

One thing particular about the PHS of TBG is that it sends a momentum $\boldsymbol{k}$ to $-\boldsymbol{k} + \boldsymbol{q}_1$ instead of $-\boldsymbol{k}$. This can be understood from Eq. (1.31):

$$\mathcal{P}\Psi_{n\boldsymbol{k}}(-\boldsymbol{r}) = e^{-i\boldsymbol{k}\cdot\boldsymbol{r}} \begin{pmatrix} -i\tilde{v}_{n\boldsymbol{k}}(-\boldsymbol{r}) \\ ie^{i\boldsymbol{q}_1\cdot\boldsymbol{r}}\tilde{u}_{n\boldsymbol{k}}(-\boldsymbol{r}) \end{pmatrix} = e^{i(-\boldsymbol{k}+\boldsymbol{q}_1)\cdot\boldsymbol{r}} \begin{pmatrix} e^{-i\boldsymbol{q}_1\cdot\boldsymbol{r}}\tilde{u}'(\boldsymbol{r}) \\ \tilde{v}'(\boldsymbol{r}) \end{pmatrix} = \Psi_{\bar{n},(-\boldsymbol{k}+\boldsymbol{q}_1)}(\boldsymbol{r}), \tag{1.44}$$

where $\tilde{u}(\boldsymbol{r})$, $\tilde{v}(\boldsymbol{r})$, $\tilde{u}'(\boldsymbol{r})$ and $\tilde{v}'(\boldsymbol{r})$ are all *periodic* functions over the moiré Bravais lattice. $\bar{n}$ indicates the index of the PHS counterpart of the band n. In fact, the wave vector $-\boldsymbol{k} + \boldsymbol{q}_1$ can be shifted back inside the Brillouin zone by a vector $\boldsymbol{Q}$ belonging to the TBG reciprocal lattice. One of the choices is $\boldsymbol{Q} = \boldsymbol{G}_2 - \boldsymbol{G}_1$, so that the two wave vectors related by PHS are symmetrical with respect to the point $(\boldsymbol{q}_1 + \boldsymbol{G}_2 - \boldsymbol{G}_1)/2 = -\boldsymbol{G}_1/3 + 2\boldsymbol{G}_2/3$. If we choose this symmetry center to be the center of the Brillouin zone, i.e. the $\mathbf{\Gamma}$ point, then we will find the two Dirac cones are located at the vertices of the hexagon, similar to the case of graphene. All states within the TBG Brillouin zone are particle-hole symmetrical

with respect to $\mathbf{\Gamma}$ point. A graphical representation of how a wave vector is transformed is shown in Fig. 1.8.

C_{3z} symmetry. In development of the continuum TBG model, we have utilized the C_{3z} symmetry as a rotation around $\boldsymbol{r} = 0$. Here we explore further if there exist other C_{3z} center within a moiré unit cell. If such a coordinate exists, we can shift the origin of coordinates to this symmetry point by a translation. The shifted Hamiltonian now has phase factors as shown in Eq. (1.45). The search of new rotation centers becomes the investigation of the phase factors in the shifted Hamiltonian to see if they satisfy the C_{3z} symmetry.

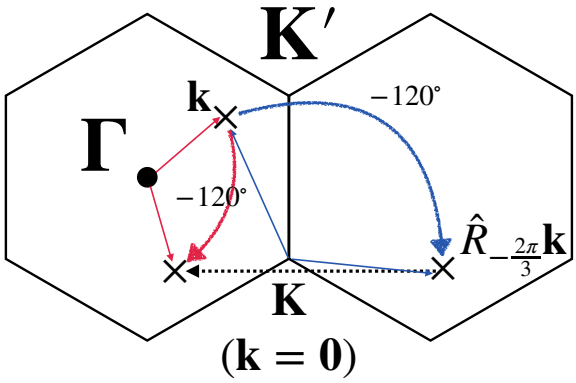

Figure 1.9: Transform of states under C_{3z} operation. An arbitrary wave vector $\boldsymbol{k}$, is sent to $\hat{R}_{-2\pi/3}$ under C_{3z} rotation around $\boldsymbol{k} = \mathbf{0}$ (blue color). The Ukmlapp process (dotted arrow) shifts the resulted wave vector back inside the Brillouin zone. The result is equivalent to directly rotating $\boldsymbol{k}$ around $\mathbf{\Gamma}$ point.

One notices first that

$$\begin{aligned} T_{[\phi_1,\phi_2,\phi_3]}(\hat{R}_{2\pi/3}\boldsymbol{r}) &= T_2 e^{-i\boldsymbol{q}_1\cdot\boldsymbol{r}} e^{i\phi_2} + T_3 e^{-i\boldsymbol{q}_2\cdot\boldsymbol{r}} e^{i\phi_3} + T_1 e^{-i\boldsymbol{q}_3\cdot\boldsymbol{r}} e^{i\phi_1} \\ &= e^{\frac{2i\pi\sigma_z}{3}} T_{[\phi_2,\phi_3,\phi_1]}(\boldsymbol{r}) e^{\frac{-2i\pi\sigma_z}{3}}. \end{aligned} \tag{1.45}$$

The unitary transform is coherent with $-i\boldsymbol{\nabla}_{\hat{R}_{2\pi/3}\boldsymbol{r}}\cdot\boldsymbol{\sigma} = e^{\frac{2i\pi\sigma_z}{3}} - i\boldsymbol{\nabla}\cdot\boldsymbol{\sigma} e^{\frac{-2i\pi\sigma_z}{3}}$. To validate the C_{3z} symmetry, the only extra requirement is to impose

$$\begin{aligned} \phi_3 - \phi_2 &= \phi_2 - \phi_1 + 2N\pi; \\ \phi_1 - \phi_3 &= \phi_3 - \phi_2 + 2M\pi, \end{aligned} \tag{1.46}$$

with $N, M \in \mathbb{Z}$. The above condition tells that $\phi_1,\ \phi_2$ and ϕ_3 are equidistantly distributed along a unit sphere. Therefore we have three cases that verifies C_{3z} symmetry:

- $\phi_1 = \phi_2 = \phi_3$;
- $\phi_2 = \phi_1 + 2\pi/3,\ \phi_3 = \phi_2 + 2\pi/3$;
- $\phi_2 = \phi_1 - 2\pi/3,\ \phi_3 = \phi_2 - 2\pi/3$.

Since ϕ_1 can always be gauged out so that $\phi_1 = 0$, it suffices to say we have three C_{3z} axes located differently:

- $\phi_1 = \phi_2 = \phi_3 = 0$ is the AA-stacking point;
- $\phi_j = 2(j-1)\pi/3,\ j = 1, 2, 3$ is the AB-stacking point;
- $\phi_j = -2(j-1)\pi/3,\ j = 1, 2, 3$ is the BA-stacking point.

As a summary, the C_{3z} operator writes

$$C_{3z} = e^{2i\pi\sigma_z/3} \otimes \begin{pmatrix} e^{-i\phi_2} & \\ & 1 \end{pmatrix}_{\text{layer}}, \tag{1.47}$$

under which the Hamiltonian transforms as

$$C_{3z} H_{\text{BM}}(\boldsymbol{r}) C_{3z}^\dagger = H_{\text{BM}}(\hat{R}_{2\pi/3}\boldsymbol{r}) \tag{1.48}$$

Now we examine how the wave functions are related by C_{3z} operation. Without loss of generality, one needs only to look at the case where $\phi_1 = \phi_2 = \phi_3 = 0$. First we write

$$H_{\text{BM}}(\hat{R}_{2\pi/3}\boldsymbol{r})\Psi_{n\boldsymbol{k}}(\hat{R}_{2\pi/3}\boldsymbol{r}) = C_{3z} H_{\text{BM}}(\boldsymbol{r}) C_{3z}^\dagger \Psi_{n\boldsymbol{k}}(\hat{R}_{2\pi/3}\boldsymbol{r}) = \mathcal{E}_{n\boldsymbol{k}}\Psi_{n\boldsymbol{k}}(\hat{R}_{2\pi/3}\boldsymbol{r}), \tag{1.49}$$

and therefore we have

$$H_{\text{BM}}(\boldsymbol{r}) C_{3z}^\dagger \Psi_{n\boldsymbol{k}}(\hat{R}_{2\pi/3}\boldsymbol{r}) = \mathcal{E}_{n\boldsymbol{k}} C_{3z}^\dagger \Psi_{n\boldsymbol{k}}(\hat{R}_{2\pi/3}\boldsymbol{r}). \tag{1.50}$$

It is clear that under C_{3z} a wave function $\Psi_{n\boldsymbol{k}}(\boldsymbol{r})$ is sent to $C_{3z}^\dagger \Psi_{n\boldsymbol{k}}(\hat{R}_{2\pi/3}\boldsymbol{r})$. With

$$\begin{aligned} C_{3z}^\dagger \Psi_{n\boldsymbol{k}}(\hat{R}_{2\pi/3}\boldsymbol{r}) = e^{i\hat{R}_{2\pi/3}^{-1}\boldsymbol{k}\cdot\boldsymbol{r}} \begin{pmatrix} e^{-i\boldsymbol{q}_3\cdot\boldsymbol{r}}\tilde{u}'(\boldsymbol{r})\omega^* \\ \tilde{v}'(\boldsymbol{r})\omega \end{pmatrix} &= e^{i\hat{R}_{2\pi/3}^{-1}\boldsymbol{k}\cdot\boldsymbol{r}} \begin{pmatrix} e^{-i\boldsymbol{q}_1\cdot\boldsymbol{r}} e^{i\boldsymbol{G}_2\cdot\boldsymbol{r}}\tilde{u}'(\boldsymbol{r})\omega^* \\ \tilde{v}'(\boldsymbol{r})\omega \end{pmatrix} \\ &\equiv \Psi_{n,\hat{R}_{2\pi/3}^{-1}\boldsymbol{k}}(\boldsymbol{r}), \end{aligned} \tag{1.51}$$

where $\tilde{u}'(\boldsymbol{r}) = \tilde{u}(\hat{R}_{2\pi/3}\boldsymbol{r})$ and $\tilde{v}'(\boldsymbol{r}) = \tilde{v}(\hat{R}_{2\pi/3}\boldsymbol{r})$. Since $\tilde{u}(\boldsymbol{r})$ and $\tilde{v}(\boldsymbol{r})$ are periodic functions on a triangular lattice, rotating $\boldsymbol{r}$ by 120° also gives periodic functions on the same lattice. We confirm that $C_{3z}^\dagger \Psi_{n\boldsymbol{k}}(\hat{R}_{2\pi/3}\boldsymbol{r})$ is a state whose wave vector is $\hat{R}_{2\pi/3}^{-1}\boldsymbol{k}$.

However, direct computation of $\hat{R}_{2\pi/3}^{-1}\boldsymbol{k}$ is a clockwise rotation of $\boldsymbol{k}$ around $\boldsymbol{K}$ point. Therefore $\hat{R}_{2\pi/3}^{-1}\boldsymbol{k}$ is out of the Brillouin zone centered at $\boldsymbol{\Gamma}$. It should be mapped to a wave vector inside the Brillouin zone via the Ukmlapp process:

$$\begin{aligned} C_{3z}^\dagger \Psi_{n\boldsymbol{k}}(\hat{R}_{2\pi/3}\boldsymbol{r}) &= e^{i(\hat{R}_{2\pi/3}^{-1}\boldsymbol{k}+\boldsymbol{G}_2-\boldsymbol{G}_1)\cdot\boldsymbol{r}} \begin{pmatrix} e^{-i\boldsymbol{q}_1\cdot\boldsymbol{r}} e^{i\boldsymbol{G}_1\cdot\boldsymbol{r}}\tilde{u}'(\boldsymbol{r})\omega^* \\ \tilde{v}'(\boldsymbol{r})\omega \end{pmatrix} \\ &= \Psi_{n,\hat{R}_{2\pi/3}^{-1}\boldsymbol{k}+\boldsymbol{G}_2-\boldsymbol{G}_1}(\boldsymbol{r}) \equiv \Psi_{n,\hat{R}_{2\pi/3}^{-1}(\boldsymbol{k}-\boldsymbol{\Gamma})+\boldsymbol{\Gamma}}(\boldsymbol{r}). \end{aligned} \tag{1.52}$$

Sending $\boldsymbol{k}$ to $\hat{R}_{2\pi/3}^{-1}(\boldsymbol{k}-\boldsymbol{\Gamma})+\boldsymbol{\Gamma}$ is a clockwise rotation around $\boldsymbol{\Gamma}$ point, the center of the Brillouin zone. The transform of wave vectors under C_{3z} can be understood easily from the graphical representation in Fig. 1.9.

C_{2x} symmetry. In the matrix of $H_{\mathrm{BM}[\phi_1,\phi_2,\phi_3]}(x,-y)$, the diagonal blocks writes $\hat{k}_x\sigma_x - \hat{k}_y\sigma_y = \sigma_x\hat{\boldsymbol{k}}\cdot\boldsymbol{r}\sigma_x$. The transform of $T_{[\phi_1,\phi_2,\phi_3]}(\boldsymbol{r})$ goes as

$$T_{[\phi_1,\phi_2,\phi_3]}(x,-y) = T_1 e^{i\phi_1}e^{i\boldsymbol{q}_1\cdot\boldsymbol{r}} + T_3 e^{i\phi_3}e^{i\boldsymbol{q}_2\cdot\boldsymbol{r}} + T_2 e^{i\phi_2}e^{i\boldsymbol{q}_3\cdot\boldsymbol{r}} = \sigma_x T^\dagger_{[-\phi_1,-\phi_3,-\phi_2]}(\boldsymbol{r})\sigma_x \tag{1.53}$$

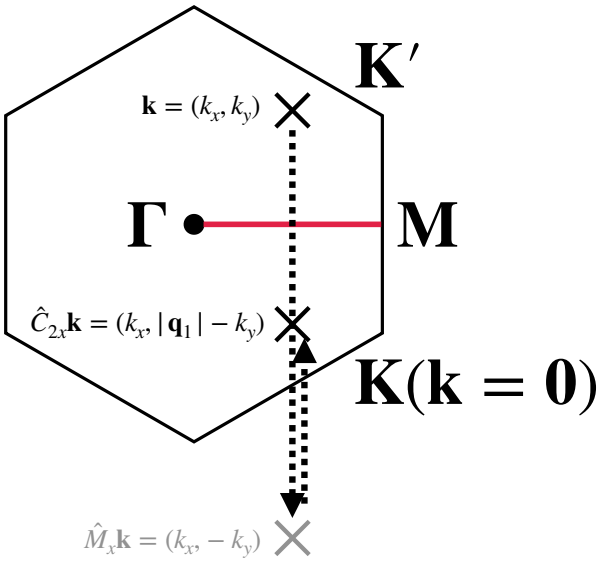

Figure 1.10: An arbitrary wave vector in the TBG Brillouin zone transformed under C_{2x} operation.

To make the C_{2x} of Eq. (1.16) hold, one needs only $\phi_2 = -\phi_3$, while ϕ_1 can be set to 0

by a gauge change. Such a condition implies an axis parallel to the x-axis going through any point $\boldsymbol{r}_0 = \xi\boldsymbol{a}_1 - \xi\boldsymbol{a}_2,\ \xi \in \mathbb{R}$ is a valid C_{2x} axis. Not surprisingly, it is not hard to see such a $\boldsymbol{r}_0$ is any point on the x-axis.

Since C_{2x} does not commute with C_{3z}, two other two-fold rotation operations can be generated by $C_{3z}C_{2x}C_{3z}^{-1}$ and $C_{3z}^{-1}C_{2x}C_{3z}$.

A wave function transforms under C_{2x} as

$$\begin{aligned}\tau_x \otimes \sigma_x \Psi_{n\boldsymbol{k}}(\hat{M}_x\boldsymbol{r}) = e^{\hat{M}_x\boldsymbol{k}\cdot\boldsymbol{r}}\begin{pmatrix}\sigma_x\tilde{v}(\boldsymbol{r})\\ e^{i\boldsymbol{q}_1\cdot\boldsymbol{r}\sigma_x}\sigma_x\tilde{u}(\boldsymbol{r})\end{pmatrix} &= e^{(\hat{M}_x\boldsymbol{k}+\boldsymbol{q}_1)\cdot\boldsymbol{r}}\begin{pmatrix}e^{-i\boldsymbol{q}_1\cdot\boldsymbol{r}}\sigma_x\tilde{v}(\boldsymbol{r})\\ \sigma_x\tilde{u}(\boldsymbol{r})\end{pmatrix} \\ &\equiv \Psi_{n,\hat{M}_x\boldsymbol{k}+\boldsymbol{q}_1}(\boldsymbol{r}) = \Psi_{\hat{C}_{2x}\boldsymbol{k}}(\boldsymbol{r})\end{aligned} \tag{1.54}$$

One notices that the wave vectors $\boldsymbol{k}$ and $\hat{C}_{2x}\boldsymbol{k} + \boldsymbol{q}_1$ are symmetrical to each other with respect to the $\mathbf{\Gamma}$–$\mathbf{M}$ line, i.e. the horizontal line $k_y = |\boldsymbol{q}_1|/2$, as illustrated in Fig. 1.10.

$C_{2z}T$ symmetry. $C_{2z}T$ is an important symmetry of TBG in terms of its profound relation to the topology in this system. This is a space-time inversion operation sending $\boldsymbol{r} \to -\boldsymbol{r}$ and $i \to -i$. Therefore, any momentum is kept unchanged. The diagonal block of $H^*_{\mathrm{BM}[\phi_1,\phi_2,\phi_3]}(-\boldsymbol{r})$ writes $\hat{\boldsymbol{k}}\cdot\boldsymbol{\sigma}^* = \sigma_x\hat{\boldsymbol{k}}\cdot\boldsymbol{\sigma}\sigma_x$. And

$$T^*_{[\phi_1,\phi_2,\phi_3]}(-\boldsymbol{r}) = T_1e^{-i\phi_1}e^{-i\boldsymbol{q}_1\cdot\boldsymbol{r}} + T_3e^{-i\phi_2}e^{-i\boldsymbol{q}_2\cdot\boldsymbol{r}} + T_2e^{-i\phi_3}e^{-i\boldsymbol{q}_3\cdot\boldsymbol{r}} = \sigma_x T_{[-\phi_1,-\phi_2,-\phi_3]}(\boldsymbol{r})\sigma_x \tag{1.55}$$

As ϕ_1 can be gauged out, for the relation $H^*_{\mathrm{BM}[\phi_1,\phi_2,\phi_3]}(-\boldsymbol{r}) = \sigma_x H_{\mathrm{BM}[\phi_1,\phi_2,\phi_3]}(\boldsymbol{r})\sigma_x$ to be valid, it is necessary that $\phi_2 = \phi_3 = 0$. It is clear that the $C_{2z}T$ axis only goes through the AA-stacking point. The $C_{2z}T$ symmetry operator is expressed as

$$C_{2z}T = \sigma_x\mathcal{K}, \tag{1.56}$$

where $\mathcal{K}$ is the complex conjugation operator. $C_{2z}T$ symmetry in TBG is manifested by

$$\sigma_x H^*(\boldsymbol{r})\sigma_x = H(-\boldsymbol{r}). \tag{1.57}$$

The wave function transformed under $C_{2z}T$ is then

$$\sigma_x\Psi^*_{n\boldsymbol{k}}(-\boldsymbol{r}) = e^{i\boldsymbol{k}\cdot\boldsymbol{r}}\begin{pmatrix}e^{-i\boldsymbol{q}_1\cdot\boldsymbol{r}}\sigma_x\tilde{u}^*(-\boldsymbol{r})\\ \sigma_x\tilde{v}^*(-\boldsymbol{r})\end{pmatrix} \equiv \Psi_{n\boldsymbol{k}}(\boldsymbol{r}) \tag{1.58}$$

Protection of two Dirac cones at K and K′. Here we show an important consequence of the symmetries of TBG is that the existence of zero-energy states is always true regardless

	Γ_1	Γ_2	Γ_3		M_1	M_2		K_1	K_2K_3
E	1	1	2	E	1	1	E	1	2
$2C_3$	1	1	-1	C_2'	1	-1	C_3	1	-1
$3C_2'$	1	-1	0				C_3^{-1}	1	-1

Table 1.1: Character table of irreducible representations at high-symmetry points of TBG Brillouin zone, reproduced from Ref [59].

of the twist angle. And the they must be at $\mathbf{K}$ and $\mathbf{K}'$ points separately.

First we notice another operator that anticommutes with the TBG Hamiltonian:

$$M_y = \tau_z \otimes \sigma_x. \tag{1.59}$$

It is a mirror operator, with the mirror along the y-direction and perpendicular to the graphene plane. Under M_y, the TBG Hamiltonian is transformed as

$$M_y H(x, y) M_y = -H(-x, y). \tag{1.60}$$

A state with wave vector $\boldsymbol{k} = (k_x, k_y)$ is send to another state with $\boldsymbol{k} = (-k_x, k_y)$ of opposite energy level.

Due to the presence of C_{3z} symmetry, the mirror rotated by $\pm 120°$ around the z-axis is also a valid mirror symmetry. As a result, there are 3 mirrors going through the z-axis. All of the three mirrors transformed by C_{2x} will create 3 new symmetry mirrors passing through the axis locate at $\boldsymbol{k} = \boldsymbol{q}_1$ and perpendicular to the graphene plane. In short, all of the 6 mirror symmetry operators can be obtained from:

$$M_{y,(n,m)} = C_{2x}^m C_{3z}^n M_y C_{3z}^{-n} C_{2x}^{-m}, \tag{1.61}$$

where n and m are integers, with $n = 0, 1, 2$ and $m = 0, 1$.

Then let us turn off the interlayer coupling by setting $a = 0$. The band structure now consists of the intersection of all the replicas of the Dirac cones at $\mathbf{K}$ and $\mathbf{K}'$ with the mBZ. Under C_{3z} operation, all momenta are send to different positions except for momenta at *three* high-symmetry points: $\mathbf{\Gamma}$, $\mathbf{K}$ and $\mathbf{K}'$. All states not located at these points contribute 0 to the total trace of C_{3z}.

Then, we compute the contribution of the states at $\mathbf{\Gamma}$, $\mathbf{K}$, and $\mathbf{K}'$ points to the trace of C_{3z}. At every point of the band structure at $\mathbf{\Gamma}$, there is a 6-fold degeneracy, which can be divided into 2 triplets: three states originating from the replica of the $\mathbf{K}$ Dirac cone and the other three from the replica of the $\mathbf{K}'$ Dirac cone. The C_{3z} operation permutes the states

within each triplet, resulting in a matrix without diagonal entries when projected onto the bases of each triplet. Consequently, the matrix is zero-traced.

Now let's examine the **K** point. All non-zero-energy states are either 3-fold degenerate or 6-fold degenerate. The 3-fold degeneracy arises from the 3 Dirac cones originating from the 3 replicas of the $\mathbf{K}'$ point on the reciprocal lattice around the **K** point. The 6-fold degeneracy comes from the replica of the Dirac cone at the **K** point. The C_{3z} operation permutes the states within each degeneracy point, resulting in a zero contribution to the trace for these non-zero states at the **K** point. The only non-zero contribution comes from the double degenerate zero-energy states. The contribution to the trace of these two zero-energy states is given by:

$$\sum_{\alpha=A,B} \langle K, l=0, \alpha | e^{2i\pi\sigma_z/3} | K, l=0, \alpha \rangle = -1.$$

The same computation is performed for the states at the $\mathbf{K}'$ point. Only the double degenerate zero-energy states at $\mathbf{K}'$ contribute -1 to the total trace of C_{3z}. This result can also be directly obtained from the fact that the states at $\mathbf{K}'$ are **K**-states transformed by C_{2x}. Thus, we have:

$$\mathrm{Tr}[C_{3z}] = -2. \tag{1.62}$$

The only non-zero contributions to $\mathrm{Tr}[C_{3z}]$ are from the **K** and $\mathbf{K}'$ points, each contributing -1. Turning on the interlayer hopping in TBG Hamiltonian does not break the C_{3z} symmetry. As this is a continuous process from $a = 0$ to $a \neq 0$, $\mathrm{Tr}[C_{3z}]$ can only acquire -1 from states at **K** and $\mathbf{K}'$ points.

This is a direct consequence of the irreducible representations of the states at **K** or $\mathbf{K}'$ point, as shown in Table 1.1. $\mathrm{Tr}[C_{3z}]$ evaluated at the **K** states gives -1, indicating that a 2-fold degeneracy, i.e. the Dirac point, is protected.

Due to the mirror-like particle hole symmetry, M_y, the two states of the Dirac point must be at zero-energy level. If not, there must be another 2 states at opposite energy level and $\mathrm{Tr}[C_{3z}]$ over the **K** states would become -2.

States at $\mathbf{K}'$ are the C_{2x}-transformed **K** states. As a consequence, a Dirac point is also protected at zero-energy level at $\mathbf{K}'$ point.

1.4 Pseudo-Landau levels

To understand the nature of the flat bands is not an easy task. In this section, we expand the interlayer hopping potential to lowest order in $\boldsymbol{r}$ near $\boldsymbol{r} = \boldsymbol{0}$ (AA-stacking point) at the *chiral limit*. This will give an potential that acts as a pseudo-magnetic field.

The expansion of $T(\boldsymbol{r})$ to lowest order in $\boldsymbol{r}$ near $\boldsymbol{r} = \boldsymbol{0}$ gives:

$$T(\boldsymbol{r}) = -i\left(\frac{3}{2}\boldsymbol{q}_1 \cdot \boldsymbol{r}\sigma_x - \frac{\sqrt{3}}{2}(\boldsymbol{q}_3 - \boldsymbol{q}_2) \cdot \boldsymbol{r}\sigma_y\right). \tag{1.63}$$

Given that $\boldsymbol{q}_1 = \boldsymbol{e}_y$ and $\boldsymbol{q}_3 - \boldsymbol{q}_2 = \sqrt{3}\boldsymbol{e}_x$ where $\boldsymbol{e}_{x/y}$ is the unit vector along the x/y direction. Therefore

$$T(\boldsymbol{r}) \equiv T(x, y) = -i\frac{3}{2}(y\sigma_x - x\sigma_y). \tag{1.64}$$

The TBG Hamiltonian now writes

$$H_{\text{BM}} = \hat{\boldsymbol{k}} \cdot \boldsymbol{\sigma} \otimes \tau_0 + \boldsymbol{A} \cdot \boldsymbol{\sigma} \otimes \tau_y \tag{1.65}$$

where $\boldsymbol{A}$ is an effective vector potential

$$\boldsymbol{A} = \frac{3a}{2}\begin{pmatrix} y \\ -x \end{pmatrix}. \tag{1.66}$$

The unitary transform Y acting only on the layer indices diagonalizes τ_y

$$Y = \frac{1}{\sqrt{2}}\begin{pmatrix} 1 & -i \\ i & 1 \end{pmatrix}_{\text{layer}}. \tag{1.67}$$

The transformed Hamiltonian $YH_{\text{BM}}Y$ is block-diagonal:

$$YH_{\text{BM}}Y = \begin{pmatrix} H_+ & \\ & H_- \end{pmatrix}, \tag{1.68}$$

where

$$H_\pm = (\hat{\boldsymbol{k}} \pm \boldsymbol{A}) \cdot \boldsymbol{\sigma}. \tag{1.69}$$

It is then obvious that $H_\pm$ each describes a free Fermion in a uniform magnetic field perpendicular to the graphene plane described by a vector potential equipped with symmetrical

gauge. The strength of the magnetic field is given by

$$B = \frac{3w_1}{2|e|v_F} \tag{1.70}$$

where e is the charge of an electron, and accordingly the "magnetic" length is

$$l_B = \sqrt{\frac{\hbar}{|e|B}}. \tag{1.71}$$

Following the textbook steps, the pseudo-Landau levels can be solved as in the regime of a Dirac Fermion in uniform magnetic field. The energy levels in *both* $H_\pm$ are given by the following formula,

$$\mathcal{E}_{\lambda,n} = \lambda \frac{\hbar v_F}{l_B} \sqrt{2n}, \tag{1.72}$$

where $\lambda = \pm 1$, designating the branch in each diagonal block.

Mapping the TBG model to the Landau level problem explains, at least partially, why we can obtain the flat bands in TBG. The Landau levels have non-zero Chern numbers, signaling the quantum anomalous Hall effect in TBG as no magnetic field is actually applied.

The chiral limit allows us to obtain the analytical solutions of the flat bands polarized on the sublattices [98]. This is also important in the many-body physics context, as the sublattice polarized states maximize the exchange energy. In the presence of *short-range* interaction, the overlap integral between wave functions from difference sublattices is zero. Therefore, to maximize the interaction, it is favorable that electrons maximize the total pseudo-spin.

1.5 Summary

In this chapter, we have developed the continuum BM model of TBG, taking into account the essential symmetries inherited from graphene. This model allows us to treat TBG in the periodic regime for arbitrary twist angles, providing a powerful framework for understanding its properties.

We have shown the emergence of the famous flat bands in TBG and their connection to the magic angles. The numerical solutions of the model reveal the existence of these flat bands and their dependence on the twist angle. This provides important insights into the unique electronic structure of TBG.

Furthermore, we have investigated the symmetries of the TBG model and analyzed the

transformation of the eigenstates under symmetry operators. This detailed analysis helps us understand the symmetries and their role in shaping the electronic properties of TBG.

In addition, we briefly reviewed the pseudo-Landau levels in TBG by expanding the model around the AA-stacking point. This expansion allows us to study the low-energy physics and reveals the presence of the quantum anomalous Hall effect in TBG. It also provides a partial explanation for the emergence of the flat bands in the system.

Overall, the continuum BM model and the analytical and numerical tools developed in this chapter provide a solid foundation for further research on twisted trilayer graphene in the subsequent chapters.

Chapter 2

Twisted trilayer graphene: model and moiré solution

The twisted trilayer graphene (TTG) exhibits distinct characteristics compared to TBG, including differences in band structures, symmetries, and topology. In this chapter, we construct a continuum model for TTG based on the BM description of TBG. We begin by briefly discussing the simplest TTG with mirror symmetry before delving into the analysis of staircase TTG.

A notable feature of staircase TTG is the emergence of a supermoiré pattern, also known as the second moiré or moiré-of-moiré pattern. This pattern arises from the interference between two TBG moiré patterns. In this chapter, we will analyze the physics at the moiré scale, employing appropriate approximations to gain insights into the system.

2.1 Continuum model for twisted trilayer graphene

The continuum model for twisted trilayer graphene can be obtained straightforwardly from the TBG model. To define the model, we arrange the three layers such that the middle layer remains fixed, while only the top and bottom layers are rotated. This configuration allows us to define two sets of moiré vectors for each TBG moiré pattern. We denote the difference between the graphene $\boldsymbol{K}$ points in reciprocal space as $\boldsymbol{q}_j^{l_1 l_2} = \boldsymbol{K}^{l_1} - \boldsymbol{K}^{l_2}$, where l_1 and $l_2 \in 1, 2, 3$ represent the layer indices. It is important to note that $\boldsymbol{q}_j^{l_1 l_2} = -\boldsymbol{q}_j^{l_2 l_1}$ by definition.

Therefore, the continuum model for TTG can be expressed as follows:

$$H_{\mathrm{TTG}}(\boldsymbol{r}) = \begin{pmatrix} \hbar v_F \hat{\boldsymbol{k}} \cdot \boldsymbol{\sigma} & aT_{12}(\boldsymbol{r}; \boldsymbol{\phi}^{12}) & \varnothing \\ aT_{12}^{\dagger}(\boldsymbol{r}; \boldsymbol{\phi}^{12}) & \hbar v_F \hat{\boldsymbol{k}} \cdot \boldsymbol{\sigma} & aT_{23}(\boldsymbol{r}; \boldsymbol{\phi}^{23}) \\ \varnothing & aT_{23}^{\dagger}(\boldsymbol{r}; \boldsymbol{\phi}^{23}) & \hbar v_F \hat{\boldsymbol{k}} \cdot \boldsymbol{\sigma} \end{pmatrix}. \tag{2.1}$$

where a represents the interlayer hopping amplitude, $\hat{\boldsymbol{k}}$ is the momentum operator, $\boldsymbol{\sigma}$ denotes the Pauli matrices, and $T_{12}(\boldsymbol{r}; \boldsymbol{\phi}^{12})$ and $T_{23}(\boldsymbol{r}; \boldsymbol{\phi}^{23})$ are the moiré potential terms that depend on the relative rotation angles $\boldsymbol{\phi}^{12}$ and $\boldsymbol{\phi}^{23}$, respectively.

The interlayer hopping potentials in the form of phase factors are given by:

$$T_{l_1 l_2}(\boldsymbol{r}; \boldsymbol{\phi}) = \sum_{j=1}^{3} e^{i\phi_j^{l_1 l_2}} T_j e^{-i\boldsymbol{q}_j^{l_1 l_2} \cdot \boldsymbol{r}}. \tag{2.2}$$

where $\boldsymbol{\phi}$ represents the set of phase factors, and $\boldsymbol{q}_j^{l_1 l_2}$ is the difference between the graphene $\boldsymbol{K}$ points of two neighboring layers.

As discussed in the TBG model, the phase factors $e^{i\phi_j^{l_1 l_2}}$ describe the stacking of two adjacent layers at the origin of coordinates. In general, it is not possible to choose a gauge that eliminates all the phases simultaneously in $T_{12}(\boldsymbol{r}; \boldsymbol{\phi}^{12})$ and $T_{23}(\boldsymbol{r}; \boldsymbol{\phi}^{23})$. Therefore, the band structure and symmetries of TTG are dependent on the phase factors. Different phase factors lead to distinct TTG Hamiltonian matrices, which cannot be connected by unitary operators in general.

Before delving into the treatment of the TTG model, it is essential to clarify two distinctive features of TTG in comparison to TBG: incommensurability and stacking configurations.

The approach used to restore periodicity in the TBG model, as demonstrated in the previous chapter, does not apply to the TTG Hamiltonian. Thus, it becomes crucial to address how to treat the TTG model as a periodic system through appropriate approximations. The interference between two TBG moiré patterns gives rise to two length scales of periodicity: the moiré periodicity, comparable to that of TBG, and an additional supermoiré periodicity that significantly exceeds the TBG moiré scale. This supermoiré scale physics will be explored in the subsequent chapter, while this chapter focuses on the moiré-scale TTG.

The stacking of the trilayer under BM description can always be represented by "AXA," which is distinct from the untwisted trilayer model that typically exhibits AAA, ABA, ABC stacking configurations, among others. Here, "C" refers to the center of the hexagonal lattice. In twisted trilayer graphene, we can envision a moiré potential between the top and

bottom layers, and the origin of coordinates can always be chosen as the AA-stacking point of the top-bottom moiré pattern, as explained in TBG. By fixing the stacking between the top and middle layers as "AX" at the origin, the stacking between the middle and bottom layers is constrained to be "XA." The phase factors in $T_{12}(\boldsymbol{r})$ and $T_{23}(\boldsymbol{r})$ are derived from the TBG "AX" stacking and "XA" stacking, respectively.

In other words, ϕ_j^{12} and ϕ_j^{23} are not entirely independent of each other. Once ϕ_j^{12} determines the "AX" stacking between the top and middle layers, ϕ_j^{23} is immediately determined with respect to the "XA" stacking between the middle and bottom layers, and vice versa. After careful consideration, one realizes that the phase factors in $T_{12}(\boldsymbol{r};\boldsymbol{\phi}^{12})$ and $T_{23}^{\dagger}(\boldsymbol{r},\boldsymbol{\phi}^{23})$ must be the same to satisfy the "AXA" stacking condition. Hence, it is necessary that

$$\boldsymbol{\phi}^{12} = -\boldsymbol{\phi}^{23} \equiv \boldsymbol{\phi}.$$

A TTG model is thus characterized by a single phase triplet $\boldsymbol{\phi} = (\phi_1, \phi_2, \phi_3)$. Similarly to TBG, it is possible to gauge out ϕ_1, leading to the consideration of only $\boldsymbol{\phi} = (0, \phi_2, \phi_3)$. The TTG Hamiltonian can be expressed as follows:

$$H_{\mathrm{TTG}}(\boldsymbol{r};\boldsymbol{\phi}) = \begin{pmatrix} \hbar v_F \hat{\boldsymbol{k}}\cdot\boldsymbol{\sigma} & aT_{12}(\boldsymbol{r};\boldsymbol{\phi}) & \varnothing \\ aT_{12}(-\boldsymbol{r};-\boldsymbol{\phi}) & \hbar v_F \hat{\boldsymbol{k}}\cdot\boldsymbol{\sigma} & aT_{23}(\boldsymbol{r};-\boldsymbol{\phi}) \\ \varnothing & aT_{23}(-\boldsymbol{r};\boldsymbol{\phi}) & \hbar v_F \hat{\boldsymbol{k}}\cdot\boldsymbol{\sigma} \end{pmatrix}, \tag{2.3}$$

It is evident that $T_{l_1 l_2}^{\dagger}(\boldsymbol{r};\boldsymbol{\phi}) = T_{l_1 l_2}(-\boldsymbol{r};-\boldsymbol{\phi})$.

2.2 Mirror-symmetrical twisted trilayer graphene

A particularly simple case of the TTG model arises when the top and bottom layers perfectly overlap and are rotated in the same direction relative to the middle layer by the same angle. This configuration exhibits symmetry with respect to the mirror plane passing through the middle layer.

In this case, it is evident that the $\boldsymbol{K}$ points of the top and bottom graphene layers perfectly coincide in reciprocal space. Consequently, we have $\boldsymbol{q}_j^{12} = -\boldsymbol{q}_j^{23} = \boldsymbol{q}_j$. To simplify notation, we can align $\boldsymbol{q}_1$ along the vertical y-direction, and its rotation by C_{3z} generates $\boldsymbol{q}_2$ and $\boldsymbol{q}_3$ vectors. The relation between interlayer hopping potentials in the mirror-symmetrical TTG (mTTG) model can be expressed as:

$$T_{23}(\pm\boldsymbol{r};\pm\boldsymbol{\phi}) = T_{12}(\mp\boldsymbol{r};\pm\boldsymbol{\phi}). \tag{2.4}$$

The Hamiltonian of the mTTG model takes the following form:

$$H_{\text{mTTG}}(\boldsymbol{r}) = \begin{pmatrix} \hbar v_F \hat{\boldsymbol{k}} \cdot \boldsymbol{\sigma} & w_1 T(\boldsymbol{r}; \boldsymbol{\phi}) & \varnothing \\ w_1 T(-\boldsymbol{r}; -\boldsymbol{\phi}) & \hbar v_F \hat{\boldsymbol{k}} \cdot \boldsymbol{\sigma} & w_1 T(-\boldsymbol{r}; -\boldsymbol{\phi}) \\ \varnothing & w_1 T(\boldsymbol{r}; \boldsymbol{\phi}) & \hbar v_F \hat{\boldsymbol{k}} \cdot \boldsymbol{\sigma} \end{pmatrix}. \tag{2.5}$$

Interestingly, the mTTG model allows for the complete elimination of *all* phase factors in $\boldsymbol{\phi}$ through a shift of origin, similar to TBG. Therefore, when discussing the mTTG model, we can disregard the phase factors and express it as:

$$H_{\text{mTTG}}(\boldsymbol{r}) = \begin{pmatrix} \hbar v_F \hat{\boldsymbol{k}} \cdot \boldsymbol{\sigma} & w_1 T(\boldsymbol{r}) & \varnothing \\ w_1 T(-\boldsymbol{r}) & \hbar v_F \hat{\boldsymbol{k}} \cdot \boldsymbol{\sigma} & w_1 T(-\boldsymbol{r}) \\ \varnothing & w_1 T(\boldsymbol{r}) & \hbar v_F \hat{\boldsymbol{k}} \cdot \boldsymbol{\sigma} \end{pmatrix}, \tag{2.6}$$

where we define $T(\boldsymbol{r}) \equiv T(\boldsymbol{r}; \boldsymbol{0})$.

The mirror symmetry operation in the mirror-symmetrical TTG (mTTG) model is a simple exchange of the top and bottom layers given by:

$$\hat{M} = \begin{pmatrix} & & 1 \\ & 1 & \\ 1 & & \end{pmatrix}_{\text{layer}}. \tag{2.7}$$

To work with eigenstates of the mirror symmetry, it is convenient to transform the mTTG Hamiltonian as follows:

$$U_M^\dagger H_{\text{mTTG}}(\boldsymbol{r}) U_M = \begin{pmatrix} \hbar v_F \hat{\boldsymbol{k}} \cdot \boldsymbol{\sigma} & \sqrt{2} w_1 T(\boldsymbol{r}) & \varnothing \\ \sqrt{2} w_1 T(-\boldsymbol{r}) & \hbar v_F \hat{\boldsymbol{k}} \cdot \boldsymbol{\sigma} & \varnothing \\ \varnothing & \varnothing & \hbar v_F \hat{\boldsymbol{k}} \cdot \boldsymbol{\sigma} \end{pmatrix}, \tag{2.8}$$

with

$$U_M = \begin{pmatrix} 1/\sqrt{2} & 0 & 1/\sqrt{2} \\ 0 & 1 & 0 \\ 1/\sqrt{2} & 0 & -1/\sqrt{2} \end{pmatrix}. \tag{2.9}$$

The mirror symmetry isolates two subspaces with eigenvalues of $\hat{M}$ being +1 and -1, respectively, and the Hamiltonian in these subspaces decouples. Equation (2.8) describes a structure $H_{\text{TBG}} \oplus \hbar v_F \hat{\boldsymbol{k}} \cdot \boldsymbol{\sigma}$. Solving the TBG part is exactly the same as in the previous chapter. It is worth noting that the effective TBG Hamiltonian in the mTTG model has the interlayer hopping amplitude exaggerated by $\sqrt{2}$, resulting in the magic angles being $\sqrt{2}$ times those of real TBG, i.e. 1.54° for the mirror symmetrical TTG compared to 1.09° of

TBG.

A notable characteristic of mirror-symmetrical TTG is its $C_{2z}T$ symmetry, which imposes a *fully connected* spectrum [88, 99]. The full connectivity in mTTG is trivially true due to the presence of the bare Dirac cone.

2.3 Moiré staircase TTG with equal twist angles

2.3.1 Hamiltonian and wave functions

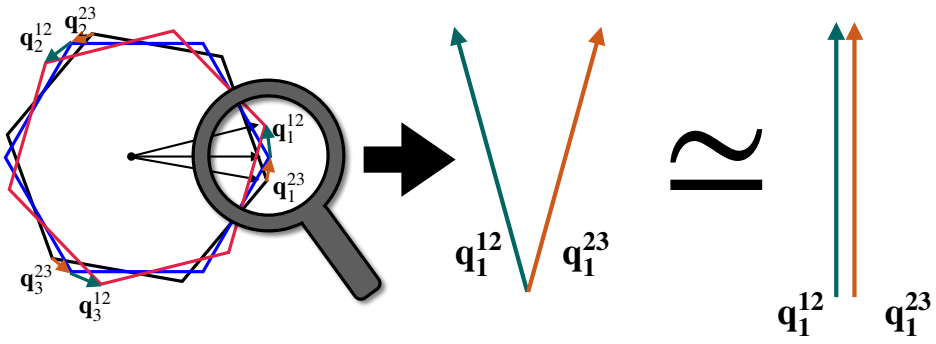

Figure 2.1: The approximation of moiré vectors.

In general, when there are relative rotations between the top and bottom layers, the TTG model does not exhibit two sets of colinear moiré vectors. However, due to the small deviation from colinearity (on the order of $\theta_{1/2}^2$), it is tempting to approximate the TTG model by neglecting the non-colinearity. Under this assumption, the two moiré lattices become commensurate again when the ratio θ_1/θ_2 is a rational number. The colinearity assumption can lead to a reciprocal lattice with the same periodicity as TBG, as illustrated in Fig. 2.1.

In this section, we investigate staircase twisted trilayer graphene, where the top and bottom layers are twisted in opposite directions with respect to the middle layer, both by the same angle θ. The Hamiltonian matrix for this system is given by:

$$H_M(\boldsymbol{r};\boldsymbol{\phi}) = \begin{pmatrix} \hbar v_F \hat{\boldsymbol{k}}\cdot\boldsymbol{\sigma} & w_1 T(\boldsymbol{r};\boldsymbol{\phi}) & \varnothing \\ w_1 T(-\boldsymbol{r};-\boldsymbol{\phi}) & \hbar v_F \hat{\boldsymbol{k}}\cdot\boldsymbol{\sigma} & w_1 T(\boldsymbol{r};-\boldsymbol{\phi}) \\ \varnothing & w_1 T(-\boldsymbol{r};\boldsymbol{\phi}) & \hbar v_F \hat{\boldsymbol{k}}\cdot\boldsymbol{\sigma} \end{pmatrix}. \tag{2.10}$$

Despite its similarities to mirror-symmetrical TTG, the staircase TTG exhibits two profound differences:

1. The phase factors cannot be completely eliminated by a gauge transformation;
2. The Hamiltonian no longer commutes with the mirror symmetry operator.

These differences distinguish the staircase TTG from the mirror-symmetrical TTG.

To simplify the analysis, we can work with the dimensionless Hamiltonian by dividing Eq. (2.10) by $\hbar v_F q$, where $q = |\boldsymbol{q}_j|$. We also introduce the dimensionless wave vector operator $\hat{\boldsymbol{k}} := -i\frac{1}{|\boldsymbol{q}|}\boldsymbol{\nabla}$. This yields the following form for the Hamiltonian:

$$H_M(\boldsymbol{r};\boldsymbol{\phi}) = \begin{pmatrix} \boldsymbol{k}\cdot\boldsymbol{\sigma} & aT(\boldsymbol{r};\boldsymbol{\phi}) & \varnothing \\ aT(-\boldsymbol{r};-\boldsymbol{\phi}) & \hat{\boldsymbol{k}}\cdot\boldsymbol{\sigma} & aT(\boldsymbol{r};-\boldsymbol{\phi}) \\ \varnothing & aT(-\boldsymbol{r};\boldsymbol{\phi}) & \hat{\boldsymbol{k}}\cdot\boldsymbol{\sigma} \end{pmatrix}, \tag{2.11}$$

where the interlayer hopping amplitude is given by:

$$a = \frac{w_1}{\hbar v_F q} = \frac{w_1}{\hbar v_F |\boldsymbol{K}_G|}\frac{1}{\theta}.$$

The periodicity of the Hamiltonian expressed in Eq. (2.11) is not affected by the phase factors. The reciprocal lattice structure is generated by two base vectors defined as $\boldsymbol{G}_1 = \boldsymbol{q}_1 - \boldsymbol{q}_2$ and $\boldsymbol{G}_2 = \boldsymbol{q}_1 - \boldsymbol{q}_3$. The corresponding real-space Bravais lattice is generated by $\boldsymbol{A}_1$ and $\boldsymbol{A}_2$, satisfying $\boldsymbol{A}_i \cdot \boldsymbol{G}_j = 2\pi\delta_{ij}$.

Following the procedures outlined in the previous chapter on TBG, we find that Bloch's theorem limits the eigenfunctions of Eq. (2.11) to the form:

$$\Psi_{n\boldsymbol{k}}(\boldsymbol{r}) = e^{i\boldsymbol{k}\cdot\boldsymbol{r}} u_{n\boldsymbol{k}}(\boldsymbol{r}), \tag{2.12}$$

where n denotes the band index and $\boldsymbol{k}$ is a wave vector within the first moiré Brillouin zone. The function $u_{n\boldsymbol{k}}(\boldsymbol{r})$ can be expressed as:

$$u_{n\boldsymbol{k}}(\boldsymbol{r}) = \begin{pmatrix} e^{-i\boldsymbol{q}_1\cdot\boldsymbol{r}} & & \\ & 1 & \\ & & e^{i\boldsymbol{q}_1\cdot\boldsymbol{r}} \end{pmatrix}_{\text{layer}} \tilde{u}_{n\boldsymbol{k}}(\boldsymbol{r}). \tag{2.13}$$

where $\tilde{u}_{n\boldsymbol{k}}(\boldsymbol{r}) = [\cdots, \tilde{u}^{l\alpha}_{n\boldsymbol{k}}(\boldsymbol{r}), \cdots]^T$, $l = 1, 2, 3$, and $\alpha \in$ A,B is a completely periodic Bloch function with respect to translations by $\boldsymbol{A}_{1/2}$ vectors, i.e., $\tilde{u}_{n\boldsymbol{k}}(\boldsymbol{r} + \boldsymbol{A}_{1/2}) = \tilde{u}_{n\boldsymbol{k}}(\boldsymbol{r})$. It is a 6-component "spinor" wavefunction, with its "flavor" determined by the combination of layer and sublattice indices.

The components of $u_{n\boldsymbol{k}}$ can be expanded like a Fourier series:

$$u_{n\boldsymbol{k}}^{l\alpha}(\boldsymbol{r}) = \sum_{\boldsymbol{Q}^l} u_{n\boldsymbol{k},\boldsymbol{Q}}^{l\alpha} e^{-i\boldsymbol{Q}^l\cdot\boldsymbol{r}}, \tag{2.14}$$

where

$$\boldsymbol{Q}(x,y,l) = x\boldsymbol{G}_1 + y\boldsymbol{G}_2 + l\boldsymbol{q}_1,\ x,y\in\mathbb{Z} \text{ and } l=0,\pm1. \tag{2.15}$$

It is evident that the Hamiltonian couples three different sets of reciprocal lattices from the three graphene layers, forming a hexagonal lattice, as shown in Fig. 2.1. The Hamiltonian, in second-quantized form, can be written as:

$$\begin{aligned}\hat{H}_M = &\sum_{ll'}\sum_{\alpha\beta}\sum_{\boldsymbol{Q},\boldsymbol{Q}'}(\boldsymbol{k}-\boldsymbol{Q})\cdot\boldsymbol{\sigma}^{\alpha\beta}\delta_{\boldsymbol{Q},\boldsymbol{Q}'}c^\dagger_{\boldsymbol{Q},\alpha,l}c_{\boldsymbol{Q}',\beta,l'}\\ &+\sum_{l=\pm1}\sum_{\alpha\beta}\sum_{\boldsymbol{Q},\boldsymbol{Q}'}\sum_{j=0}^{3}[T_j^{\alpha\beta}e^{i\phi_j}\delta_{\boldsymbol{Q},\boldsymbol{Q}'+\boldsymbol{q}_j}c^\dagger_{\boldsymbol{Q},\alpha,l}c_{\boldsymbol{Q}',\beta,0}+\text{h.c.}].\end{aligned} \tag{2.16}$$

In the following sections, we will demonstrate that the band structure of the system varies significantly with different phase factors. The phase factors have a significant impact on the symmetries of the system.

2.3.2 Band structures

The staircase TTG model with $\boldsymbol{\phi} = (0,0,0)$ exhibits rich symmetries, the most notable of which is the space-time inversion symmetry $C_{2z}T$. This symmetry ensures that the single-particle band structure remains gapless and fully connected. In Figure 2.2, we present the band structures for different twist angles. Despite the significant variations in the band structures as the twist angles decrease, the full connectivity of the bands is always preserved due to the $C_{2z}T$ symmetry. A detailed discussion of the full connectivity protected by $C_{2z}T$ will be provided in Chapter 2.3.5.

None zero phase factors will bring in significant modifications to the band structures. In Fig. 2.3, the twist angle is fixed to be 1.8° and the spectra resulted from different combinations of phase factors are presented. The variation of the band structure is remarkable with different phase factors, as the symmetries present in the model is profoundly altered. In Fig. 2.3(b) and (d), the full connectivity of the spectrum is gone as an expected consequence of breaking $C_{2z}T$ symmetry. While in Fig. 2.3(c), the band is again connected albeit with broken $C_{2z}T$. More profound reasons will be discussed later.

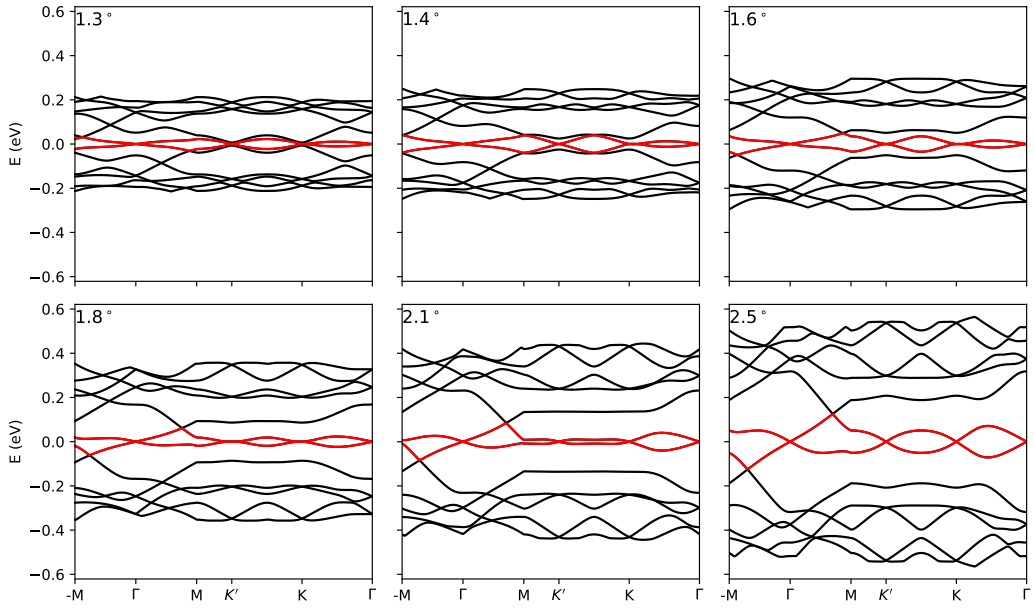

Figure 2.2: Band structures of the zero-phase TTG with equal twist angles calculated for different twist angles. The 12 bands closest to the zero energy levels are shown. Corrugation ratio is set to $r = 0.8$. The two middle bands closest to the zero energy level are colored in red.

2.3.3 Flat bands at chiral limit

The presence of exactly flat bands is a special feature that occurs only in certain cases. Specifically, it occurs in the chiral limit where the interlayer hopping parameter w_{AA} is set to zero, and in the case of AAA- or ABA-stacked TTG configurations. In Figure 2.4, it is illustrated that the middle bands can indeed become completely flat for AAA and ABA stacked TTG structures.

The appearance of completely flat bands requires the velocities of all three Dirac cones at $\boldsymbol{\Gamma}$, $\boldsymbol{K}$, and $\boldsymbol{K}'$ to simultaneously vanish. However, since the cones at $\boldsymbol{K}$ and $\boldsymbol{K}'$ are particle-hole symmetric (PHS) counterparts of each other, it is sufficient to examine the dispersion velocities at $\boldsymbol{\Gamma}$ and $\boldsymbol{K}$. Such conditions can be satisfied in the chiral limit.

The computation of the velocity is based on degenerate perturbation theory at the Dirac point. Suppose $|n\rangle$ and $|m\rangle$ are the two degenerate zero-energy states at $\boldsymbol{\Gamma}$ or $\boldsymbol{K}$. The velocity is obtained by diagonalizing the perturbation Hamiltonian:

$$\delta W^{nm}(\delta\boldsymbol{k}) = \langle n|\delta\boldsymbol{k}\cdot\boldsymbol{\sigma}|m\rangle\,. \tag{2.17}$$

where $\delta\boldsymbol{k}$ represents a small perturbation in the wave vector. For an isotropic cone, the

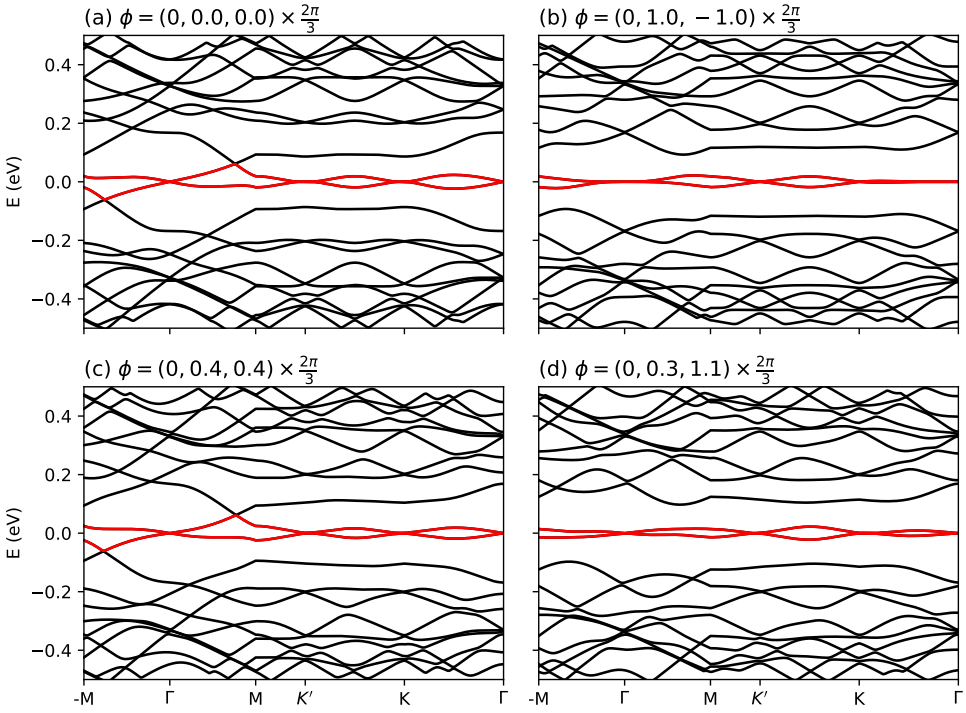

Figure 2.3: Band structures with non-zero phases. Corrugation ratio is set to $r = 0.8$. The twist angle is $1.8°$. The computation of the band structures are performed with (a) zero phases; (b) phase factors restoring C_{3z} symmetry; (c) phase factors restoring C_{2x} symmetry and (d) arbitrary phase factors breaking all of C_{2zT}, C_{3z} and C_{2x} symmetries. The particle-hole symmetry is always valid for equal twist angles despite different phase factors as will be explained later.

dispersion takes the form:

$$\delta E(\delta \boldsymbol{k}) = v^* |\delta \boldsymbol{k}| \tag{2.18}$$

where v^* is the renormalized velocity, given by $v^* = v/v_F$. The vanishing of the velocities at the $\boldsymbol{\Gamma}$ and $\boldsymbol{K}$ points is a condition for the appearance of completely flat bands in the chiral limit of AAA and ABA-stacked TTG.

In Fig. 2.5, we compute the velocities of each Dirac cone at the $\boldsymbol{\Gamma}$ and $\boldsymbol{K}$ points for AAA ($\boldsymbol{\phi} = [0, 0, 0]^T$) and ABA ($\boldsymbol{\phi} = [0, 2\pi/3, -2\pi/3]$) TTGs, respectively. The magic angle is expected to occur when both velocities vanish simultaneously.

However, when deviating from the chiral limit, it is not always possible to find an ideal angle where both velocities vanish simultaneously. This is demonstrated in Fig. 2.6.

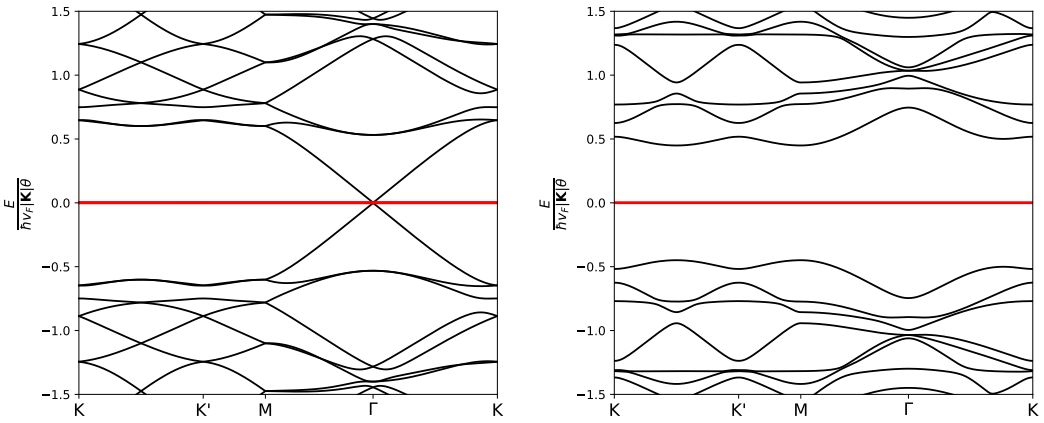

Figure 2.4: In the left panel of the figure, the completely flat bands of AAA-stacked TTG are shown. These flat bands emerge when the interlayer hopping parameter w_{AA} is set to zero, resulting in a chiral limit. The first magic angle for the AAA-stacked configuration is given by $a = 0.830$ ($\sim 0.77°$). In the right panel of the figure, the completely flat bands of ABA-stacked TTG are depicted. Similarly, these flat bands arise in the chiral limit with $w_{AA} = 0$. The first magic angle for the ABA-stacked configuration is given by $a = 0.377$ ($\sim 1.68°$). These flat bands at the chiral limit and specific twist angles are a fascinating feature of AAA and ABA-stacked TTG structures.

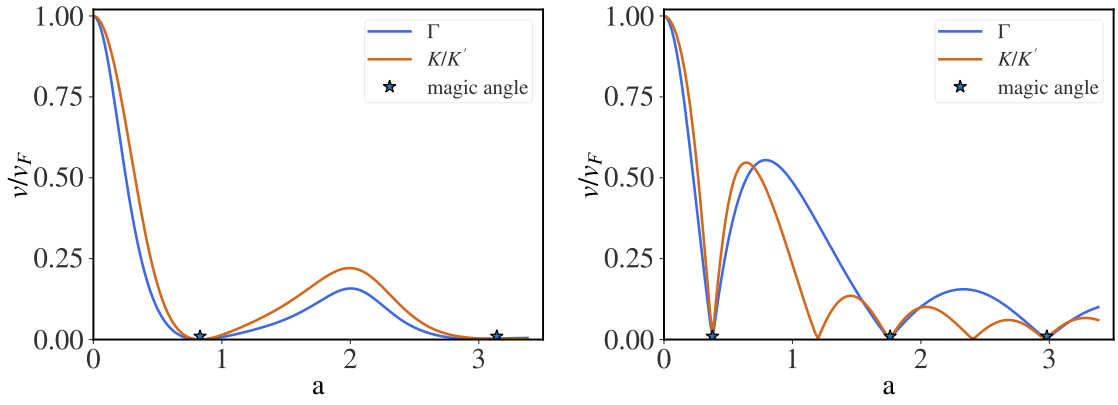

Figure 2.5: Renormalized velocity of Γ and K Dirac cones computed for AAA (left panel) and ABA (right panel) stackings, at the *chiral* limit with $w_{AA} = 0$.

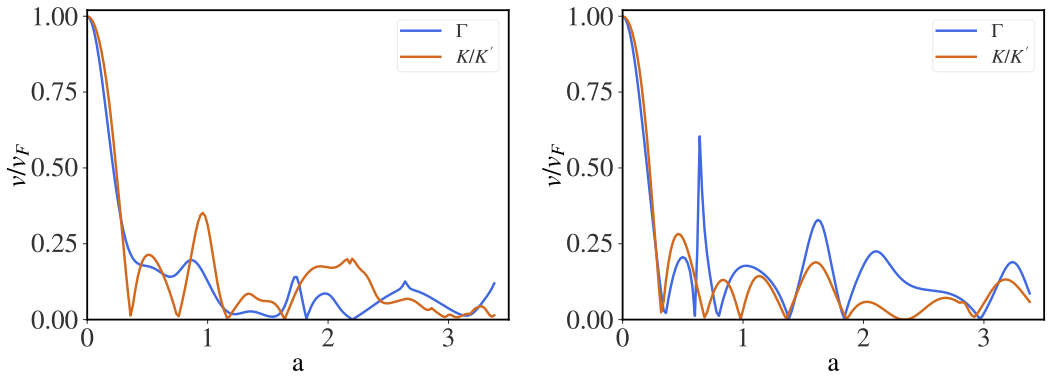

Figure 2.6: Renormalized velocity of Γ and K Dirac cones computed for AAA (left panel) and ABA (right panel) stackings, with $w_{AA}/w_{AB} = 0.8$.

2.3.4 Dirac cone anisotropy

When the stacking is neither AAA nor ABA/BAB, the Dirac cones in twisted trilayer graphene (TTG) become anisotropic. In this section, we aim to characterize this anisotropy and understand why achieving flat bands with anisotropic cones is more challenging compared to isotropic cones.

We can rewrite the $\boldsymbol{k} \cdot \boldsymbol{p}$ Hamiltonian near a Dirac point, as given in Eq. (2.17), in the following form:

$$\delta W_{nm} = \delta k_x \langle n|\sigma_x|m\rangle + \delta k_y \langle n|\sigma_y|m\rangle = \delta k_x \Gamma_x^{nm} + \delta k_y \Gamma_y^{nm}, \tag{2.19}$$

with the 2×2 Hermitian matrices $\Gamma_{x/y}^{nm} = \langle n|\sigma_{x/y}|m\rangle$. These matrices can be decomposed into linear combinations of Pauli matrices defined on the *band indices*, denoted as τ_i, where $i = x, y, z$, as follows:

$$\Gamma_i = \sum_j \gamma_{ij} \tau_j, \ i, j = x, y, z. \tag{2.20}$$

Using the tensor γ, we can rewrite δW as:

$$\delta W = \sum_{i,j \in \{x,y,z\}} \delta k_i \gamma_{ij} \Gamma_j. \tag{2.21}$$

Since γ is a 2×3 *real* matrix, it can be decomposed using the *singular value decomposition* (SVD) as:

$$\gamma = U^T S V \tag{2.22}$$

where U and V are *orthogonal* matrices, and S is a 2×3 diagonal matrix with positive

diagonal entries denoted as s_x and s_y. We define:

$$\delta k_i' = \sum_j U_{ij} \delta k_j, \tag{2.23}$$

and

$$\tau_i' = \sum_j V_{ij} \tau_j. \tag{2.24}$$

The new matrices τ_i' also satisfy the relation:

$$\tau_i' \tau_j' = \delta_{ij} \mathbb{1} + i\varepsilon_{ijk} \tau_k', \tag{2.25}$$

due to the orthogonality of the matrix V. Here, εijk represents the completely antisymmetric tensor. Notably, the matrices τ_j' form a distinct set of generators for SU(2) that are different from the Pauli matrices.

Proof of Eq. (2.24): The original Pauli matrices satisfy the relation $\tau_i \tau_j = \delta_{ij}\mathbb{1} + \sum_{jk} i\varepsilon_{ijk}\tau_k$, where $i, j, k \in x, y, z$. Using this relation, we can compute the product of the new Pauli matrices as follows:

$$\begin{aligned} \tau_i' \tau_j' &= V_{il} V_{jm} \tau_l \tau_k = V_{il} V_{jm} (i\varepsilon_{lmp} \tau_p + \delta_{lm} \mathbb{1}) \\ &= i\varepsilon_{lmp} V_{il} V_{jm} \tau_p + V_{il} V_{jm} \delta_{lm} \mathbb{1} \\ &= i\varepsilon_{ijk} V_{kp} \tau_p + \delta_{ij} \mathbb{1} \\ &= i\varepsilon_{ijk} \tau_k' + \delta_{ij} \mathbb{1} \end{aligned} \quad . \tag{2.26}$$

Now, the expression for δW becomes:

$$\delta W = \sum_l \sum_{ij} \delta k_i U_{il}^T s_l V_{lj} \tau_j = \sum_l s_l k_l' \tau_l'. \tag{2.27}$$

The dispersion relation is then given by $\delta E(\boldsymbol{k}') = \pm\sqrt{(s_x k_x')^2 + (s_y k_y')^2}$. Only when $s_x = s_y = s$, the Dirac cone is isotropic and the renormalized velocity is equal to the singular value.

We define the anisotropy function as:

$$\mathcal{A}(\phi_2, \phi_3) = 1 - \min(s_x, s_y)/\max(s_x, s_y). \tag{2.28}$$

The value of $\mathcal{A}$ is maximum at 1 when one of the velocity components vanishes, and minimum at 0 when the Dirac cone is isotropic. In Fig. 2.7, we show the anisotropy of the Dirac cones at $\boldsymbol{\Gamma}$ and $\boldsymbol{K}$ as a function of (ϕ_2, ϕ_3). The isotropy of both Dirac cones is restored at

the C_{3z} symmetrical phases, specifically at $(\phi_2, \phi_3) = (0, 0)$ and $(\pm\pi/3, \mp\pi/3)$.

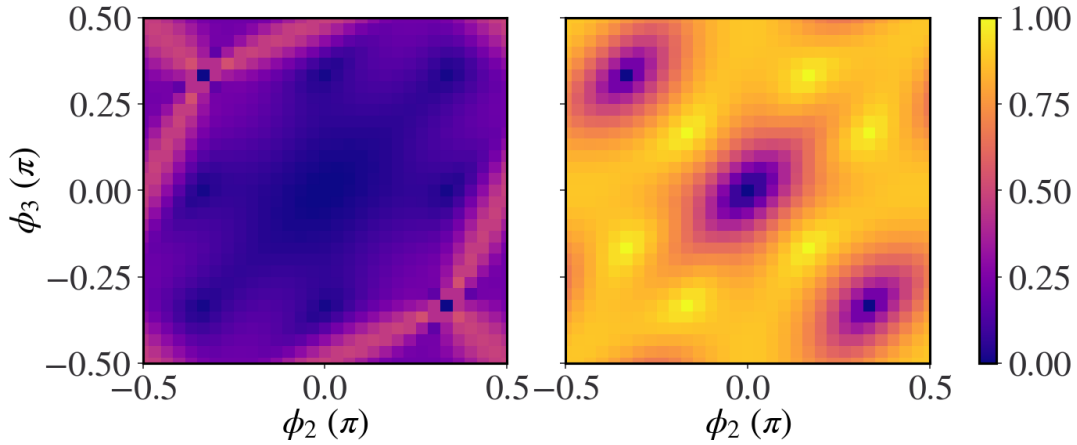

Figure 2.7: Anisotroy $\mathcal{A}(\phi_2, \phi_3)$ of the Dirac cones at $\boldsymbol{\Gamma}$ (left panel) and $\boldsymbol{K}$ (right panel). Data colleted with $w_{AA}/w_{AB} = 0.8$ at $1.8°$.

For a TTG model with anisotropic cones to have completely flat bands, it would require all four singular values to vanish simultaneously, which is much more difficult to achieve compared to isotropic cones. The latter only requires the suppression of two singular values.

2.3.5 Symmetries in staircase TTG

It is crucial to examine the symmetries present in the staircase TTG, as they have important impacts on the band structures and more profoundly on the topology. Since the phases cannot be gauged out as was in TBG, different phases have important impacts on the symmetries. Or otherwise said, for certain symmetries to be valid, there must be constraints on the phase factors. In the following, we explore the conditions on phase factors imposed by desired symmetries and the consequences of symmetries on the states.

Periodicity of phase factors

It is evident that when one of the phase factors is changed by 2π, the model remains invariant. However, this does not represent the smallest periodicity in phase factors. To determine the minimum period in phase, denoted as $\boldsymbol{\varphi} = (0, \varphi_2, \varphi_3)$, we need to find a specific vector $\boldsymbol{r}_0$ that satisfies the following condition:

$$H_M(\boldsymbol{r}; \boldsymbol{\phi} + \boldsymbol{\varphi}_0) = U H_M(\boldsymbol{r} + \boldsymbol{r}_0; \boldsymbol{\phi}) U^\dagger, \tag{2.29}$$

where the change in phase factors can be entirely compensated by shifting the origin of coordinates.

The unitary matrix U is given by:

$$U = \begin{pmatrix} 1 & & \\ & e^{-i\boldsymbol{q}_1\cdot\boldsymbol{r}_0} & \\ & & 1 \end{pmatrix}_{\text{layer}}. \tag{2.30}$$

where U eliminates the additional phase in front of the T_1 matrix.

Let's explicitly write the right-hand side of Eq.(2.29) as follows:

$$\begin{aligned} &UH_M(\boldsymbol{r}+\boldsymbol{r}_0;\boldsymbol{\phi})U^\dagger \\ &= \begin{pmatrix} \hat{\boldsymbol{k}}\cdot\boldsymbol{r} & T(\boldsymbol{r};\boldsymbol{\phi}+(0,\boldsymbol{b}_1\cdot\boldsymbol{r}_0,\boldsymbol{b}_2\cdot\boldsymbol{r}_0)) & \varnothing \\ h.c. & \hat{\boldsymbol{k}}\cdot\boldsymbol{r} & T(\boldsymbol{r};-\boldsymbol{\phi}+(0,\boldsymbol{b}_1\cdot\boldsymbol{r}_0,\boldsymbol{b}_2\cdot\boldsymbol{r}_0)) \\ \varnothing & h.c. & \hat{\boldsymbol{k}}\cdot\boldsymbol{r} \end{pmatrix}. \end{aligned} \tag{2.31}$$

The validity of Eq. (2.29) is verified only when the following conditions are satisfied simultaneously:

$$\begin{matrix} \boldsymbol{\varphi}_0 = (0,\boldsymbol{b}_1\cdot\boldsymbol{r}_0,\boldsymbol{b}_2\cdot\boldsymbol{r}_0) \\ \boldsymbol{\varphi}_0 = (0,-\boldsymbol{b}_1\cdot\boldsymbol{r}_0+2N\pi,-\boldsymbol{b}_2\cdot\boldsymbol{r}_0+2M\pi) \end{matrix},\ N,M\in\mathbb{Z}. \tag{2.32}$$

The smallest vector $\boldsymbol{r}_0$ is either $\boldsymbol{a}_1/2$ or $\boldsymbol{a}_2/2$, shifting ϕ_2 or ϕ_3 by π, respectively.

Therefore, the period in phase factors is π instead of the trivial value 2π.

Particle-Hole symmetry and the protection of Dirac cone at Γ

A strong implication arising from the band structures is the presence of particle-hole symmetry. The band structures exhibit symmetry with respect to the zero-energy level at the $\boldsymbol{\Gamma}$ point of the moiré Brillouin zone. To capture this symmetry, we seek an operator $\mathcal{P}$ that *anticommutes* with the Hamiltonian. In other words, if there exists a state $|\psi\rangle$ satisfying $\hat{H}|\psi\rangle = E|\psi\rangle$, then $\hat{H}\mathcal{P}|\psi\rangle = -E\mathcal{P}|\psi\rangle$.

We can observe the following relation:

$$-H_M(-\boldsymbol{r};\boldsymbol{\phi}) = \begin{pmatrix} \hat{\boldsymbol{k}}\cdot\boldsymbol{\sigma} & -aT(-\boldsymbol{r},\boldsymbol{\phi}) & \varnothing \\ -aT(\boldsymbol{r},-\boldsymbol{\phi}) & \hat{\boldsymbol{k}}\cdot\boldsymbol{\sigma} & -aT(-\boldsymbol{r},-\boldsymbol{\phi}) \\ \varnothing & -aT^(\boldsymbol{r},\boldsymbol{\phi}) & \hat{\boldsymbol{k}}\cdot\boldsymbol{\sigma} \end{pmatrix} = \mathcal{P}H_M(\boldsymbol{r};\boldsymbol{\phi})\mathcal{P}, \tag{2.33}$$

where

$$\mathcal{P} = \begin{pmatrix} & & 1 \\ & -1 & \\ 1 & & \end{pmatrix}_{\text{layer}} . \tag{2.34}$$

If we have a wave function $\Psi n\boldsymbol{k}(\boldsymbol{r})$ satisfying $H_M(\boldsymbol{r})\Psi_{n\boldsymbol{k}}(\boldsymbol{r}) = E_{n\boldsymbol{k}}\Psi_{n\boldsymbol{k}}(\boldsymbol{r})$, then we also have

$$H(\boldsymbol{r})\mathcal{P}\Psi_{n\boldsymbol{k}}(-\boldsymbol{r}) = -E_{n\boldsymbol{k}}\mathcal{P}\Psi_{n\boldsymbol{k}}(-\boldsymbol{r}). \tag{2.35}$$

The state $\mathcal{P}\Psi_{n\boldsymbol{k}}(-\boldsymbol{r})$ corresponds to an eigenstate with energy $-E_{n\boldsymbol{k}}$. Using the notation

$$\mathcal{P}\Psi_{n\boldsymbol{k}}(-\boldsymbol{r}) = e^{-i\boldsymbol{k}\cdot\boldsymbol{r}} \begin{pmatrix} u^1(-\boldsymbol{r}) \\ u^2(-\boldsymbol{r}) \\ u^3(-\boldsymbol{r}) \end{pmatrix} \equiv \Psi_{\bar{n},-\boldsymbol{k}}(\boldsymbol{r}), \tag{2.36}$$

where $u^l(\boldsymbol{r})$ is a shorthand for the spinor wave function belonging to layer l, written as $u^l(\boldsymbol{r}) = \binom{u^{l\alpha}(\boldsymbol{r})}{u^{l\beta}(\boldsymbol{r})}$, we can confirm that $\mathcal{P}$ maps the state $|\Psi_{n,\boldsymbol{k}}\rangle$ to $|\Psi_{\bar{n},-\boldsymbol{k}}\rangle$. Particle-hole symmetry connects two momenta in the Brillouin zone that are symmetric with respect to $\boldsymbol{\Gamma} = \boldsymbol{0}$. The symmetry center of TTG is regular, unlike TBG.

Protection of the Dirac cone at Γ point. In the limit $a \to 0$ of Eq.(2.11), the spectrum consists of three bare Dirac cones located at the $\boldsymbol{\Gamma}$, $\boldsymbol{K}$, and $\boldsymbol{K}'$ points. There are only two states invariant under the operator $\mathcal{P}$, which are $|0, \alpha, l = 0\rangle$, and they transform as

$$\mathcal{P}\,|0, \alpha, l = 0\rangle = -\,|0, \alpha/\beta, l = 0\rangle\,. \tag{2.37}$$

For the other states, the transformation is given by

$$\mathcal{P}\,|k, \alpha, l\rangle = \eta_l\,\left|-k, \alpha, \bar{l}\right\rangle, \tag{2.38}$$

where

$$\eta = \begin{cases} 1 & \text{if } l = \pm 1 \\ -1 & \text{if } l = 0 \end{cases}, \tag{2.39}$$

and

$$\bar{l} = \begin{cases} -1 & \text{if } l = 1 \\ 0 & \text{if } l = 0 \\ 1 & \text{if } l = -1 \end{cases}. \tag{2.40}$$

The *total* trace of $\mathcal{P}$ is given by

$$\operatorname{Tr}\mathcal{P} = \sum_{\boldsymbol{k}} \sum_{\alpha\in\{A,B\}} \sum_{l=0,\pm 1} \langle \boldsymbol{k}, \alpha, l|\mathcal{P}|\boldsymbol{k}, \alpha, l\rangle = -2. \tag{2.41}$$

Since the trace of an operator is invariant under changes of basis, it is also true that when computed in the eigenbasis of the Hamiltonian with the interlayer hopping turned on,

$$\operatorname{Tr}\mathcal{P} = \sum_{k\in \mathrm{BZ}} \sum_{n} \langle \boldsymbol{k}, n|\mathcal{P}|\boldsymbol{k}, n\rangle = -2, \tag{2.42}$$

where n runs over the band indices. Given that $\mathcal{P}\,|\boldsymbol{k}, n\rangle = |-\boldsymbol{k}, \bar{n}\rangle$, only two states at $\boldsymbol{k} = \boldsymbol{0}$ and at zero energy can contribute a nonzero value to the trace.

C_{3z} Symmetry

The relation

$$H_M(\hat{R}_{2\pi/3}\boldsymbol{r}; [\phi_1, \phi_2, \phi_3]) = e^{2i\pi\sigma_z/3} H_M(\boldsymbol{r}, [\phi_2, \phi_3, \phi_1]) e^{-2i\pi\sigma_z/3}, \tag{2.43}$$

implies that the phase factors satisfying C_{3z} symmetry must either be the same or uniformly distributed on a unit circle, corresponding to three different stacking configurations. By a gauge transformation, we can always choose ϕ_1 to be zero. Therefore, the configuration $\boldsymbol{\phi} = (0, 0, 0)$ corresponds to AAA stacking at the origin, $\boldsymbol{\phi} = (0, \omega, \omega^*)$ corresponds to ABA stacking, and $\boldsymbol{\phi} = (0, \omega^*, \omega)$ corresponds to BAB stacking. The ABA and BAB stacked models are related by the C_{2x} operation and therefore have the same band structure.

With the convention that $\phi_1 \equiv 0$, the C_{3z} operator is expressed as

$$C_{3z} = e^{i\frac{2\pi}{3}\sigma_z} \otimes \begin{pmatrix} 1 & & \\ & e^{i\phi_2} & \\ & & 1 \end{pmatrix}_{\text{layer}}, \tag{2.44}$$

so that the Hamiltonian satisfying C_{3z} symmetry obeys

$$C_{3z} H_M(\boldsymbol{r}; \boldsymbol{\phi}) C_{3z}^\dagger = H_M(\hat{R}_{2\pi/3}\boldsymbol{r}; \boldsymbol{\phi}). \tag{2.45}$$

For an arbitrary eigenstate satisfying $H(\boldsymbol{r})\Psi_{n\boldsymbol{k}}(\boldsymbol{r}) = E_{n\boldsymbol{k}}\Psi_{n\boldsymbol{k}}(\boldsymbol{r})$, $C_{3z}\Psi_{n\boldsymbol{k}}(\hat{R}_{-2\pi/3}\boldsymbol{r})$ is also an eigenstate. Using $e^{i\boldsymbol{k}\cdot\hat{R}_{-2\pi/3}\boldsymbol{r}} = e^{i(\hat{R}_{-2\pi/3}\boldsymbol{k})\cdot\boldsymbol{r}}$, it is clear that

$$C_{3z}\Psi_{n\boldsymbol{k}}(\hat{R}_{-2\pi/3}\boldsymbol{r}) \equiv \Psi_{n\hat{R}_{2\pi/3}\boldsymbol{k}}(\boldsymbol{r}), \tag{2.46}$$

i.e., C_{3z} maps a state with momentum $\boldsymbol{k}$ to $\hat{R}_{2\pi/3}\boldsymbol{k}$, which corresponds to a rotation by $2\pi/3$ around the $\boldsymbol{\Gamma}$ point.

C_{3z} center displaced from origin. Previous discussions have revealed that the model remains invariant under phase shifts of $\pm\pi$. Consequently, we can always confine the phase factors to the interval $[-\pi/2, \pi/2[$. Without loss of generality, let's consider the ABA stacking configuration with phase factors $\boldsymbol{\phi} = (0, 2\pi/3, -2\pi/3)$ as an example, which can be expressed as $\boldsymbol{\phi} = (0, -\pi/3, \pi/3)$. Initially, the wrapped phase factors may not satisfy the C_{3z} symmetry requirement. This implies that the model describes a configuration where the rotation center of C_{3z} is not located at the origin of the $\boldsymbol{r}$ coordinates. However, by shifting $\boldsymbol{r}$ to $\boldsymbol{r} - \boldsymbol{r}_0$ with $\boldsymbol{r}_0 = -\boldsymbol{a}_1/2 + \boldsymbol{a}_2/2$, we can restore the C_{3z} center to the origin of the coordinates. Consequently, the phase factors revert back to $(0, 2\pi/3, -2\pi/3)$.

C_{2x} symmetry

Similar to TBG, we can identify the C_{2x} symmetry in this TTG model by examining the following relation:

$$H_M(x, -y; [0, \phi_2, \phi_3]) = \sigma_x \otimes \begin{pmatrix} & & 1 \\ & 1 & \\ 1 & & \end{pmatrix}_{\text{layer}} H_M(x, y, [0, \phi_3, \phi_2]) \begin{pmatrix} & & 1 \\ & 1 & \\ 1 & & \end{pmatrix}_{\text{layer}} \otimes \sigma_x. \tag{2.47}$$

For the C_{2x} symmetry to hold, it is necessary that $\phi_2 = \phi_3$.

Furthermore, we can explore additional candidate symmetries by considering the rotation of the C_{2x} axis by $\pm 120°$ and the combinations $C_{3z}C_{2x}C_{3z}^{-1}$ and $C_{3z}^{-1}C_{2x}C_{3z}$ as potential symmetries. These symmetries require $\phi_3 = 0$ and $\phi_2 = 0$, respectively (while ϕ_1 is always taken as zero by convention).

$C_{2z}T$ and full connectivity

The $C_{2z}T$ symmetry in TTG can be examined by analyzing $H^*(-\boldsymbol{r}, \boldsymbol{\phi})$. When we send $\boldsymbol{r} \to -\boldsymbol{r}$ and take the complex conjugate, $\hat{\boldsymbol{k}} \cdot \boldsymbol{\sigma}$ is transformed into $\hat{\boldsymbol{k}} \cdot \boldsymbol{\sigma}^* = \sigma_x \hat{\boldsymbol{k}} \cdot \boldsymbol{\sigma} \sigma_x$. The interlayer potential undergoes the transformation:

$$T^*(-\boldsymbol{r}; [0, \phi_2, \phi_3]) = T_1 e^{-i\boldsymbol{q}_1 \cdot \boldsymbol{r}} + e^{-i\phi_2} T_3 e^{-i\boldsymbol{q}_2 \cdot \boldsymbol{r}} + e^{-i\phi_3} T_2 e^{-i\boldsymbol{q}_3 \cdot \boldsymbol{r}} \equiv \sigma_x T(\boldsymbol{r}; [0, -\phi_2, -\phi_3]) \sigma_x.$$

Therefore, we find that

$$H_M^*(-\boldsymbol{r}; \boldsymbol{\phi}) = \sigma_x H_M(\boldsymbol{r}; -\boldsymbol{\phi}) \sigma_x. \tag{2.48}$$

For this relation to hold, it is necessary that $\boldsymbol{\phi} = -\boldsymbol{\phi} = \boldsymbol{0}$. Thus, a unitary transformation, σ_x, can relate $H_M^*(-\boldsymbol{r})$ and $H_M(\boldsymbol{r})$, validating the $C_{2z}T$ symmetry.

In conclusion, the $C_{2z}T$ symmetry is only valid for the AAA-stacked TTG configuration.

The significance of the $C_{2z}T$ symmetry is evident in the full connectivity of the band structure, which has a topological origin related to an odd number of Dirac cones coupled by a potential. Here is a detailed explanation:

Firstly, $C_{2z}T$ symmetry includes a time-reversal operation and leads to zero Berry curvature everywhere in each band. When the interlayer potential is introduced, the Dirac cones must either merge or appear in pairs. Consequently, the total number of Dirac cones in the band structure must always be an odd number.

A Wilson Loop traversing from one side to the other of the Brillouin zone must accumulate a phase that is a multiple of 2π. Since the Berry curvature is zero everywhere, this phase can only be acquired by crossing Dirac points. As each Dirac point contributes $\pm\pi$, every band must have an even number of Dirac crossings with neighboring bands.

Suppose there is a gap in the band structure. The first band has an even number of Dirac crossings with the second band. The second band has an even number of Dirac crossings with the third band. By induction, the number of Dirac crossings between the i-th and $(i+1)$-th bands is always an even number. This implies that the total number of Dirac cones is even, contradicting the requirement of an odd number of Dirac cones.

Therefore, by contradiction, we can conclude that the band structure must be fully connected to satisfy the $C_{2z}T$ symmetry.

2.3.6 Band topology and Chern mosaic pattern

By breaking both the C_{2x} and C_{3z} symmetries simultaneously, the two middle bands become detached from the others. This provides an opportunity to study the topology of these bands through the calculation of Wilson loops. In this section, we demonstrate that the two middle bands exhibit non-trivial topology, which is characterized by a non-zero total Chern number $\mathcal{C} = \pm 1$.

In Fig.2.8, we compute the total Chern number of the two middle bands as a function of (ϕ_2, ϕ_3) in the phase space. When crossing the domain wall defined by the C_{2x} symmetry lines, a topological phase transition occurs, resulting in the closure of the spectral gap. This explains the observation of fully connected spectra in Fig.2.3 (bottom left panel) where $C_{2z}T$ is broken but C_{2x} is preserved. The Chern numbers in each section remain stable as they represent continuous variations from the ABA/BAB points until they reach the C_{2x} domain wall.

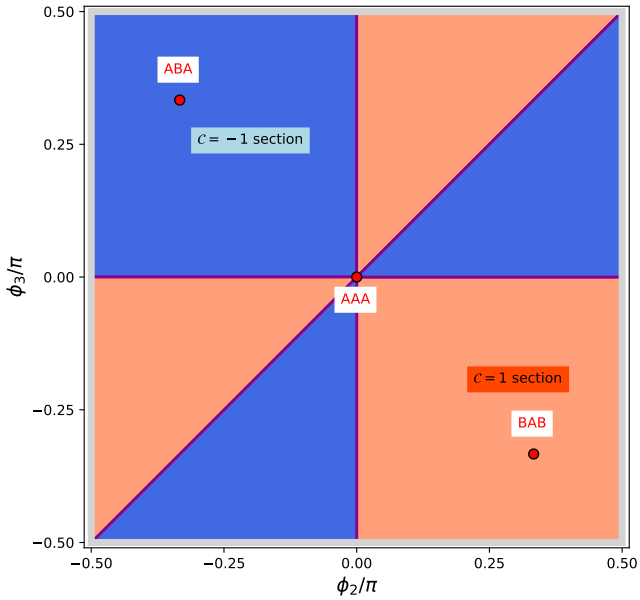

Figure 2.8: The chern mosaic pattern computed in the phase space within a unit cell. The *periodic* boundary is highlighted in gray color. The $\mathcal{C} = \pm 1$ sections are colored in blue and orange colors respectively. The C_{3z} restoring points corresponding to AAA ($\phi_2 = 0, \phi_3 = 0$), ABA ($\phi_2 = -pi/3, \phi_3 = \pi/3$) and BAB ($\phi_2 = pi/3, \phi_3 = -\pi/3$) stackings are marked with red dots. The purple lines mark the C_{2x}-restoring phases. Data collected with corrugation factor $w_{AA}/w_{AB} = 0.8$ and equal twist angles of $1.8°$.

The presence of two middle bands with a non-zero total Chern number is a notable distinction between TTG and TBG. As shown in the previous chapter, TBG has middle bands with a total Chern number of zero.

To further investigate the Chern number of the middle bands, we can examine the chiral limit where analytical solutions are available for the flat bands at the magic angle. The zero-energy model in the chiral limit corresponds to sublattice-polarized states, allowing us to compute the Chern number for each flat band. For ABA-stacked TTG, the explicit computation yields $\mathcal{C}_A^{\mathrm{ABA}} = -2$ for the A-polarized band and $\mathcal{C}_B^{\mathrm{ABA}} = 1$ for the B-polarized band. Therefore, the total Chern number for the ABA middle bands is -1. Introducing corrugation is a continuation from the chiral limit and does not change the total Chern number. However, with finite corrugation, the two middle bands can no longer be separated by sublattice polarization, and only the total Chern number can be considered.

Similarly, for BAB-stacked TTG in the chiral limit, the Chern number of the A-polarized band is $\mathcal{C}_A^{\mathrm{BAB}} = -1$, while $\mathcal{C}_B^{\mathrm{BAB}} = 2$ for the B-polarized band. Consequently, the BAB middle bands have a total Chern number of 1. For a more detailed discussion on the analytical

solutions, please refer to Ref. [90].

2.4 Moire staircase TTG with unequal twist angles

The colinear approximation of moiré vectors enables us to study the periodic regime of equal-twist angle TTG. Following the same approach, we can also investigate other TTG models where the ratio of twist angles is a rational number. In this section, we focus on the TTG model with $\theta_1/\theta_2 = 1/2$ and compare its symmetries with those of the equally twisted TTG. For consistency, we adopt the convention where the top layer is rotated counterclockwise by an angle θ, and the bottom layer is rotated clockwise by 2θ.

2.4.1 Hamiltonian and band structures

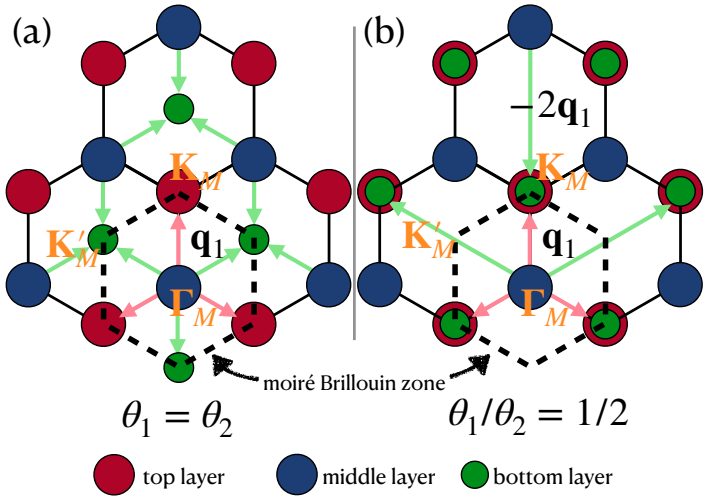

Figure 2.9: Comparison of the reciprocal moiré lattices of (a) equal twist angle TTG and (b) the double angle TTG. In the double twist TTG, the initial Dirac cones of of the top and bottom layer overlaps in the reciprocal space.

Assuming that the top-middle moiré vectors $\boldsymbol{q}_j^{12} = \boldsymbol{q}_j$ are colinear with the middle-bottom moiré vectors $\boldsymbol{q}_j^{23} = 2\boldsymbol{q}_j$, the interlayer hopping potentials can be expressed as follows:

$$T_{12}(\boldsymbol{r};\boldsymbol{\phi}) = \sum_{j=1}^{3} T_j e^{i\phi_j} e^{-i\boldsymbol{q}_j\cdot\boldsymbol{r}}, \tag{2.49}$$

and

$$T_{23}(\boldsymbol{r};-\boldsymbol{\phi}) = \sum_{j=1}^{3} T_j e^{-i\phi_j} e^{-2i\boldsymbol{q}_j\cdot\boldsymbol{r}}. \tag{2.50}$$

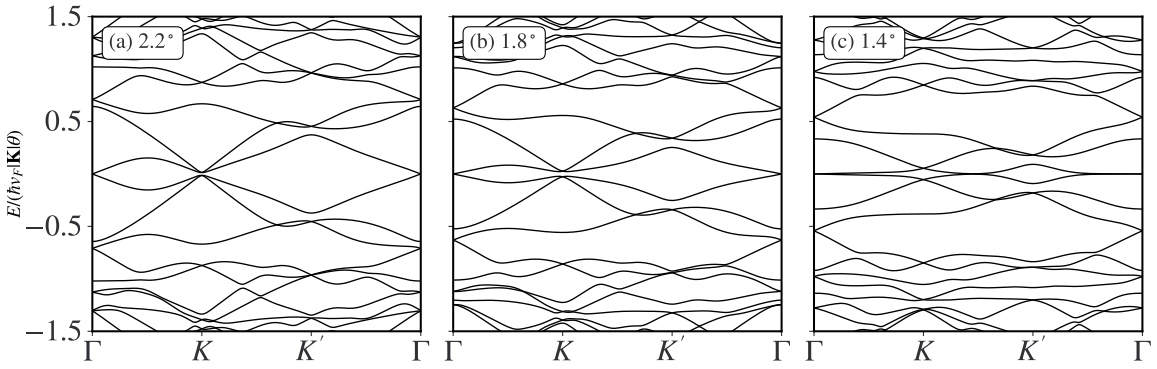

Figure 2.10: Band structures of AAA stacking double-angle TTG with θ_{12} being (a) $2.2°$, (b) $1.8°$ and (c) $1.4°$. Corrugation is also set to $w_{AA}/w_{AB} = 0.8$.

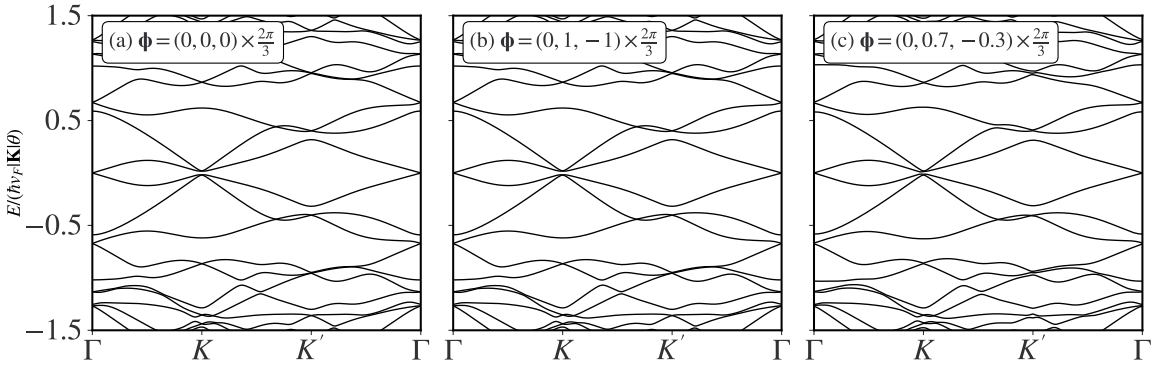

Figure 2.11: Band structures of double-angle TTG with different stackings: (a) AAA with $\boldsymbol{\phi} = (0, 0, 0)$, (b) ABA with $\boldsymbol{\phi} = (0, 2\pi/3, -2\pi/3)$ and (c) arbitrary stacking with $\boldsymbol{\phi} = (0, 0.4\pi, -0.1\pi)$. Corrugation is also set to $w_{AA}/w_{AB} = 0.8$. Twist angles are fixed at $(2°, 4°)$. The variation of the band structures is not as dramatic as in the equally twisted TTG. But tiny changes in the spectra are still visible due to different symmetries associated to different phases.

It is important to note that the middle-bottom moiré vectors have twice the length of the top-middle moiré vectors, which fundamentally changes the structure of the reciprocal lattice and the symmetries, as explained in Figure 2.9. Consequently, the band structure is distinct from that of the equal twist angles case.

Figure 2.10 illustrates the band structures for different twist angles in the AAA-stacked double-angle TTG. The appearance of *four* low-energy states near the zero-energy level at the $\boldsymbol{K}$ point is a direct consequence of the overlapping Dirac cones from the top and bottom layers at the $\boldsymbol{K}$ point.

In Figure 2.11, we display different spectra with varying phase factors. The impact of the phase factors on the band structures is not as drastic as in the equally twisted TTG case. However, the symmetries in the model are still modified by the phase factors, leading to

slight but noticeable modifications in the band structures when different phase factors are applied.

2.4.2 Symmetries

Based on the same reasoning as before, we can verify the presence of symmetries with different phases.

Phase period. In the double-angle TTG, the phase factors have a period of $2\pi/3$ instead of π. This can be observed in the equation:

$$H_M(\boldsymbol{r};\boldsymbol{\phi}+\boldsymbol{\phi}_T) = UH_M(\boldsymbol{r}-\boldsymbol{r}_0;\boldsymbol{\phi})U^\dagger, \tag{2.51}$$

where $\boldsymbol{\phi}_T = (0, 2\pi/3, 0)$ or $(0, 0, 2\pi/3)$, and correspondingly $\mathbf{r}_0 = \mathbf{a}_1/3$ or $\mathbf{a}_2/3$ respectively. The unitary matrix U compensates for the extra phase in ϕ_1 resulting from the shift of the origin:

$$U = \begin{pmatrix} e^{2i\pi/9} & & \\ & 1 & \\ & & e^{4i\pi/9} \end{pmatrix}. \tag{2.52}$$

$C_{2z}T$ symmetry. $C_{2z}T$ symmetry is valid when all phase factors are zero, and is manifested by the same expression as Eq. (2.48).

C_{2x} symmetry. C_{2x} does *not* exist any more, regardless of the phases. Different twist angles makes it impossible to restore the original trilayer by flipping the system around the x-axis.

C_{3z} symmetry. The analysis of the C_{3z} symmetry in the double-angle TTG model follows a similar approach as in the equally twisted TTG. We find that the phase factors that restore the C_{3z} symmetry are $\boldsymbol{\phi} = (0, 0, 0)$ and $\boldsymbol{\phi} = (0, \pm 2\pi/3, \mp 2\pi/3)$. Shifting ϕ_2 or ϕ_3 by $2\pi/3$ also leads to phases that restore the C_{3z} symmetry. An interesting observation is that the AAA, ABA ($\boldsymbol{\phi} = (0, 2\pi/3, -2\pi/3)$), and BAB ($\boldsymbol{\phi} = (0, -2\pi/3, 2\pi/3)$) stacked double-angle TTG models are *exactly the same* because the phase differences are multiples of $2\pi/3$.

In contrast, the AAA, ABA, and BAB stacked equally twisted TTG models are *different*. The ABA and BAB models in the equal-angle TTG have the same band structures, as they are related by a C_{2x} transformation, but they have opposite Chern numbers for the middle band.

Particle-hole symmetry. The double-angle TTG model exhibits a distinct particle-hole symmetry compared to the equal-angle TTG. In this case, particle-hole symmetry acts as a mirror operator perpendicular to the graphene plane, passing through the y-axis. The manifestation of particle-hole symmetry is given by the equation:

$$-H_M(-x,y) = \mathcal{P}_M H_M(x,y)\mathcal{P}_M, \tag{2.53}$$

where

$$\mathcal{P}_M = \sigma_x \otimes \begin{pmatrix} 1 & & \\ & -1 & \\ & & 1 \end{pmatrix}_{\text{layer}}. \tag{2.54}$$

It is evident that $\mathcal{P}_M$ exchanges the two phases ϕ_2 and ϕ_3, therefore requiring $\phi_2 = \phi_3$ for particle-hole symmetry to be valid. This is in stark contrast to the case with $\theta_1 = \theta_2$, where particle-hole symmetry is always valid regardless of the phases.

By employing similar reasoning as in the equal-angle case, it can be shown that particle-hole symmetry gives rise to two zero-energy states in the mirror plane. To localize these states at the $\mathbf{\Gamma}$ point, C_{3z} symmetry is required to generate two additional mirror planes along the y-axis and its C_{3z}-rotated counterparts. The zero-energy states must exist in all three mirrors simultaneously and are thus pinned at $\boldsymbol{k} = \mathbf{0}$, corresponding to the $\mathbf{\Gamma}$ point.

2.5 Summary

This chapter explores the solution of the moiré TTG models with twist angle ratios of $\theta_1/\theta_2 = 1$ and $1/2$. The band structures of these models can undergo dramatic variations with changes in the twist angles, and flat bands occurs when the velocities of all three Dirac cones simultaneously vanish.

The trilayer system exhibits high tunability, not only in terms of the twist angles but also in the phase factors that describe the horizontal displacement of the middle layer relative to the top and bottom layers. The phase factors provide an additional avenue for tuning the electronic properties of TTG, setting it apart from TBG, which is invariant under changes in the phases. In both TTG models, with and without equal twist angles, the phase factors play a crucial role in defining the symmetries and modifying the band structures, including their topology.

Moreover, the phase factors exhibit a periodicity that restores the Hamiltonian to its original form up to a gauge change. This periodicity is closely related to the rational ratio

of the twist angles, which has significant implications for the subsequent chapter.

By assuming colinearity of the two sets of moiré vectors, we are able to solve the TTG model within the moiré periodic regime, similar to TBG. However, finding a general solution for arbitrary pairs of twist angles remains a challenging task. The next chapter aims to extend the analysis beyond colinear moiré vectors and rational twist angle ratios.

Chapter 3

Supermoiré effective theory: formalism, gauge, and symmetries

In this chapter, we aim to develop an analytical framework for treating the quasicrystalline structure of the exact TTG model described by Eq. (2.3). Unlike the TBG model, the TTG model incorporates two moiré periodicities that are generally incommensurate, resulting in an overall quasi-crystalline structure. This poses challenges in applying the conventional Bloch's theorem directly.

Previous approximate treatments of the TTG model assumed colinearity between the two sets of moiré vectors and employed rational ratios between the twist angles, allowing for solutions in the periodic regime similar to TBG. However, these treatments completely ignored the secondary moiré pattern that arises from the mismatched TBG periodicities.

Our approach in this chapter aims to develop an analytical framework that considers the non-colinearity of the moiré vectors and takes into account small deviations from rational ratios between the twist angles. We leverage the moiré TTG solutions discussed in the previous chapter, which serve as "local" wave functions that vary slowly over the supermoiré length scale. Based on these local solutions, we construct a supermoiré effective model. It is important to note that our objective is not to provide a comprehensive solution to the entire quasicrystal problem, but rather to access the low-energy features of the supermoiré pattern.

In this chapter, we begin by examining the symmetries in the exact TTG model described by Eq. (2.3). Subsequently, we demonstrate the development of the effective theory. The construction of the effective theory starts with a geometrical decomposition that separates the moiré and supermoiré scales. This decomposition allows us to leverage the ap-

proximate solutions obtained in the previous chapter as local solutions within the effective model. By applying the ansatz wave function to the Schrödinger's equation of the exact Hamiltonian, we derive the supermoiré effective model by integrating out the fast-varying moiré details. We thoroughly examine the gauge invariance and symmetries of the effective Hamiltonian. Additionally, we discuss the principles and practical algorithms of gauge fixing in detail.

3.1 Symmetries of AAA-stacked exact model

Before delving into the development of the effective theory for the TTG model, it is important to conduct a symmetry analysis of the full TTG model. This analysis will help us understand the symmetries present in the original model and guide us in ensuring that the effective model we construct captures these symmetries to some extent.

Perodicity. The TTG Hamiltonian defined in Eq. (2.3) is in general *not* periodic, due to the incommensurability of the two moiré patterns between top and middle layers and between middle and bottom layers. This lack of periodicity poses a challenge in applying traditional Bloch's theorem and treating the system within a periodic framework. As a result, alternative approaches are required to effectively analyze and understand the properties of the TTG model.

Particle-Hole symmetry. In the TTG model, the non-colinearity between the two sets of TBG moiré vectors leads to the permanent breaking of particle-hole symmetry (PHS), even when the twist angles between the layers are strictly equal. In the presence of non-colinear moiré vectors, the system lacks the necessary symmetry operations to preserve PHS. This non-colinearity introduces additional complexity to the TTG model and requires alternative methods to study its properties and phenomena.

$C_{2z}T$ **symmetry.** The exact model with AAA stacking still preserves $C_{2z}T$ symmetry and also acts on the Hamiltonian as

$$C_{2z}T = \sigma_x K,$$

where K is the complex conjugation operator.

C_{3z} **symmetry.** C_{3z} is still preserved and is still manifested by

$$C_{3z} = e^{2i\pi\sigma_z/3}.$$

C_{2x} symmetry. C_{2x} is only valid when the two twist angles are *strictly* equal. It acts on the Hamiltonian as

$$C_{2x} = \sigma_x \begin{pmatrix} & & 1 \\ & 1 & \\ 1 & & \end{pmatrix}_{\text{layer}} .$$

3.2 Separation of moiré and supermoiré scales via geometrical decomposition

For a pair of twist angles $\theta_{12}/\theta_{23} \simeq p/q$, where p and q are *coprime* positive integers, the moiré vectors of the top-middle and the middle-bottom TBG patterns are generated by the C_{3z} rotated partners of the moiré vectors

$$\boldsymbol{q}_1^{12} = \hat{R}_{\theta_{12}}\boldsymbol{K} - \boldsymbol{K}, \tag{3.1}$$

and

$$\boldsymbol{q}_1^{23} = \boldsymbol{K} - \hat{R}_{-\theta_{23}}\boldsymbol{K}, \tag{3.2}$$

respectively, with the convention that the middle layer remains unrotated. The other moiré vectors are generated by $\boldsymbol{q}_j^{l,l+1} = \hat{R}_{2(j-1)\pi/3}\boldsymbol{q}_1^{l,l+1}$, with $l = 1, 2$ and $j = 1, 2, 3$.

Although the lengths of these moiré vectors satisfy $|\boldsymbol{q}_j^{12}| \simeq \theta 12|\boldsymbol{K}|$ and $|\boldsymbol{q}_j^{23}| \simeq \theta 23|\boldsymbol{K}|$, making the ratio $|\boldsymbol{q}_j^{12}|/|\boldsymbol{q}_j^{23}|$ approximately equal to $\theta 12/\theta 23 \simeq p/q$, the non-colinearity between the moiré vectors makes the two TBG moiré patterns incommensurate. Therefore, it is natural to seek sets of colinear moiré vectors that are as close as possible to the original vectors while still respecting the rational ratio.

To achieve this, we solve the linear equations:

$$\begin{aligned} \boldsymbol{q}_j^{12} &= p\boldsymbol{q}_j + \delta\boldsymbol{q}_j/(p+q), \\ \boldsymbol{q}_j^{23} &= q\boldsymbol{q}_j - \delta\boldsymbol{q}_j/(p+q). \end{aligned} \tag{3.3}$$

The solutions for $\boldsymbol{q}_j$ and $\delta\boldsymbol{q}_j$ define two sets of vectors with distinct length scales. The vector $\boldsymbol{q}_j$,

$$\boldsymbol{q}_j = \frac{\boldsymbol{q}_j^{12} + \boldsymbol{q}_2^{23}}{p+q} \tag{3.4}$$

is of the same order of magnitude as the original moiré vectors. On the other hand, the vector $\delta\boldsymbol{q}_j$,

$$\delta\boldsymbol{q}_j = q\boldsymbol{q}_j^{12} - p\boldsymbol{q}_j^{23} \tag{3.5}$$

is much smaller compared to $\boldsymbol{q}_j^{12}$, $\boldsymbol{q}_j^{23}$ or $\boldsymbol{q}_j$, i.e. $|\delta\boldsymbol{q}_j| \ll |\boldsymbol{q}_j|$. The triplet $\{\boldsymbol{q}_j, j = 1, 2, 3\}$ defines a moiré periodic structure. The smaller triplet $\{\delta\boldsymbol{q}_j, j = 1, 2, 3\}$ corresponds to a supermoiré modulation, which defines the periodicity over the supermoiré length scale.

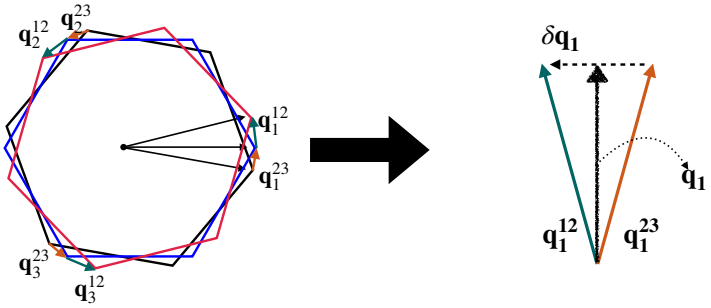

Figure 3.1: Illustration of the geometrical decomposition of TBG moiré vectors into moiré vectors and supermoiré vectors for a pair of nearly equal twist angles.

An intuitive example is the case with $p = q = 1$, which corresponds to *nearly* equal twist angles, as illustrated in Fig. 3.1. It is important to note that strict equality between the twist angles is not necessary. With nearly equal angles, the new moiré vectors are given by $\boldsymbol{q}_j = (\boldsymbol{q}_j^{12} + \boldsymbol{q}_j^{23})/2$, which are simply the average of the two sets of TBG moiré vectors. The supermoiré vectors are obtained by taking the difference between the TBG vectors, $\delta\boldsymbol{q}_j = \boldsymbol{q}_j^{12} - \boldsymbol{q}_j^{23}$.

The geometrical decomposition discussed above allows us to express the exact TTG Hamiltonian in a rewritten form:

$$H(\boldsymbol{r}) = \begin{pmatrix} \hat{\boldsymbol{k}} \cdot \boldsymbol{r} & aT_{12}(\boldsymbol{r}, -\boldsymbol{\phi}(\boldsymbol{r})) & \varnothing \\ aT_{12}(-\boldsymbol{r}, \boldsymbol{\phi}(\boldsymbol{r})) & \hat{\boldsymbol{k}} \cdot \boldsymbol{r} & aT_{23}(\boldsymbol{r}, \boldsymbol{\phi}(\boldsymbol{r})) \\ \varnothing & aT_{23}(-\boldsymbol{r}, -\boldsymbol{\phi}(\boldsymbol{r})) & \hat{\boldsymbol{k}} \cdot \boldsymbol{r} \end{pmatrix} \tag{3.6}$$

with

$$T_{12}(\boldsymbol{r}, \boldsymbol{\phi}(\boldsymbol{r})) = \sum_j T_j e^{-ip\boldsymbol{q}_j \cdot \boldsymbol{r}} e^{i\delta\boldsymbol{q}_j \cdot \boldsymbol{r}/(p+q)} \equiv \sum_j T_j e^{-ip\boldsymbol{q}_j \cdot \boldsymbol{r}} e^{i\phi_j(\boldsymbol{r})}, \tag{3.7}$$

and

$$T_{23}(\boldsymbol{r}, \boldsymbol{\phi}(\boldsymbol{r})) = \sum_j T_j e^{-iq\boldsymbol{q}_j \cdot \boldsymbol{r}} e^{i\delta\boldsymbol{q}_j \cdot \boldsymbol{r}/(p+q)} \equiv \sum_j T_j e^{-iq\boldsymbol{q}_j \cdot \boldsymbol{r}} e^{i\phi_j(\boldsymbol{r})}, \tag{3.8}$$

where

$$\boldsymbol{\phi}(\boldsymbol{r}) = [\phi_1(\boldsymbol{r}), \phi_2(\boldsymbol{r}), \phi_3(\boldsymbol{r})]^T, \tag{3.9}$$

and

$$\phi_j(\boldsymbol{r}) = \frac{\delta\boldsymbol{q}_j \cdot \boldsymbol{r}}{p+q}. \tag{3.10}$$

Indeed, Eq.(3.6) represents the exact model of TTG without any approximation. How-

ever, it can also be interpreted as an approximate moiré TTG model with a phase modulation that spans the supermoiré length scale. Locally, Eq.(3.6) describes differently stacked moiré TTG models.

The models discussed in Chapter 2 can be understood as different local solutions of the exact AAA-stacking models. Due to the small magnitude of $\delta\boldsymbol{q}_j$ compared to $\boldsymbol{q}_j$, the phases $\phi_j(\boldsymbol{r})$ vary slowly in space compared to $\boldsymbol{q}_j \cdot \boldsymbol{r}$. Consequently, it is reasonable to assume that $\boldsymbol{\phi}(\boldsymbol{r})$ remains nearly constant within the length scale of a moiré unit cell. In this case, Eq. (3.6) locally approximates moiré TTG models with constant phase factors, which can be solved straightforwardly. To reflect this, we introduce the supermoiré coordinates denoted as $\boldsymbol{R}$, and parameterize the phase factors of the local moiré models as $\boldsymbol{\phi}(\boldsymbol{R})$.

3.3 Effective theory

In this section, we will develop the effective theory for the TTG model based on the geometric decomposition of the TBG moiré vectors, which allows us to separate the system into two distinct length scales. We will begin by reviewing the conventional $\boldsymbol{k}\cdot\boldsymbol{p}$ method, which provides us with the intuition necessary to construct an ansatz for the full TTG model. Subsequently, we will build the effective Hamiltonian by solving the Schrödinger's equation for the ansatz wave functions.

3.3.1 Reviewing the $\boldsymbol{k}\cdot\boldsymbol{p}$ method

Let us consider a *periodic* Hamiltonian in a simplified way as $H(\boldsymbol{r}) = \hat{\boldsymbol{k}}\cdot\boldsymbol{\sigma} + V(\boldsymbol{r})$ with $V(\boldsymbol{r}+\boldsymbol{a}_{1/2}) = UV(\boldsymbol{r})U^\dagger$. U is a unitary matrix acting on the *other* degrees of freedom than $\boldsymbol{r}$.

According to Bloch's theorem, the eigenfunctions of the periodic Hamiltonian at any point $\boldsymbol{\kappa}$ inside the first Brillouin zone can be written as $\Psi_{n\boldsymbol{\kappa}}(\boldsymbol{r}) = e^{i\boldsymbol{\kappa}\cdot\boldsymbol{r}}u_{n\boldsymbol{\kappa}}(\boldsymbol{r})$ where $u_{n\boldsymbol{\kappa}}(\boldsymbol{r})$ is the Bloch function defined on the reciprocal lattice and satisfies the eigenvalue equation:

$$[\boldsymbol{\kappa}\cdot\boldsymbol{\sigma} - i\boldsymbol{\nabla}\cdot\boldsymbol{\sigma} + V(\boldsymbol{r})]u_{n\boldsymbol{\kappa}}(\boldsymbol{r}) = E_{n\boldsymbol{\kappa}}u_{n\boldsymbol{\kappa}}(\boldsymbol{r}). \tag{3.11}$$

The area of the Bravais unit cell in real space is denoted by S. The periodicity of the Bloch functions is expressed as:

$$u_{n\boldsymbol{\kappa}}(\boldsymbol{r}+\boldsymbol{a}_{1/2}) = Uu_{n\boldsymbol{\kappa}}(\boldsymbol{r}). \tag{3.12}$$

The Bloch functions satisfy the orthonormal condition:

$$\int_S \mathrm{d}\boldsymbol{r}^2\, u^*_{n\boldsymbol{\kappa}}(\boldsymbol{r}) u_{n'\boldsymbol{\kappa}}(\boldsymbol{r}) = \delta_{nn'}. \tag{3.13}$$

Introducing a new set of states $|n, \boldsymbol{k}\rangle$ defined as $\langle \boldsymbol{r}|n, \boldsymbol{k}\rangle = e^{i\boldsymbol{k}\cdot\boldsymbol{r}} u_{n\boldsymbol{\kappa}}(\boldsymbol{r})$, we have a complete set of orthonormal bases satisfying:

$$\langle n, \boldsymbol{k}|n', \boldsymbol{k}'\rangle = \int_S \mathrm{d}\boldsymbol{r}^2\, e^{-i(\boldsymbol{k}-\boldsymbol{k}')\cdot\boldsymbol{r}} u^*_{n\boldsymbol{\kappa}}(\boldsymbol{r}) u_{n'\boldsymbol{\kappa}}(\boldsymbol{r}) = \delta(\boldsymbol{k}-\boldsymbol{k}')\delta_{nn'}. \tag{3.14}$$

Without loss of generality, we can choose $\boldsymbol{\kappa}$ to be the $\boldsymbol{\Gamma}$ point who are the eigenfunctions of the equation:

$$[-i\boldsymbol{\nabla}\cdot\boldsymbol{\sigma} + V(\boldsymbol{r})] u_{n\boldsymbol{\Gamma}}(\boldsymbol{r}) = E_{n\boldsymbol{\Gamma}} u_{n\boldsymbol{\Gamma}}(\boldsymbol{r}). \tag{3.15}$$

In the subsequent analysis, we will omit the subscript $\boldsymbol{\Gamma}$ for simplicity. The $\boldsymbol{k}\cdot\boldsymbol{p}$ method is essentially a procedure to solve the Hamiltonian in the new basis $|n, \boldsymbol{k}\rangle$ at a different point in the Brillouin zone.

As a consequence of Bloch's theorem, an eigenstate can be expressed as:

$$\Psi(\boldsymbol{r}) = e^{i\boldsymbol{k}\cdot\boldsymbol{r}} \sum_n f_n u_n(\boldsymbol{r}). \tag{3.16}$$

Substituting this expression into the Schrödinger's equation, we obtain:

$$[\boldsymbol{k}\cdot\boldsymbol{\sigma} - i\boldsymbol{\nabla} + V(\boldsymbol{r})] \sum_{n'} f_{n'} u_{n'}(\boldsymbol{r}) = \mathcal{E} \sum_{n'} f_{n'} u_{n'}(\boldsymbol{r}). \tag{3.17}$$

Since $u_n(\boldsymbol{r})$ are eigenstates of $-i\boldsymbol{\nabla} + V(\boldsymbol{r})$ with eigenvalue E_n, the equation simplifies to:

$$\sum_{n'} (\boldsymbol{k}\cdot\boldsymbol{\sigma} + E_{n'}) f_{n'} u_{n'}(\boldsymbol{r}) = \mathcal{E} \sum_{n'} f_{n'} u_{n'}(\boldsymbol{r}). \tag{3.18}$$

Multiplying both sides by $u^*_n(\boldsymbol{r})$ and integrating over the Bravais unit cell, we obtain:

$$\int_S \mathrm{d}\boldsymbol{r}^2\, u^*_n(\boldsymbol{r}) \sum_{n'} (\boldsymbol{k}\cdot\boldsymbol{\sigma} + E_{n'}) f_{n'} u_{n'}(\boldsymbol{r}) = \int_S \mathrm{d}\boldsymbol{r}^2\, u^*_n(\boldsymbol{r}) \mathcal{E} \sum_{n'} f_{n'} u_{n'}(\boldsymbol{r}). \tag{3.19}$$

Using the orthonormal condition in Eq. (3.13), we can rewrite the equation as an eigenvalue equation for a matrix:

$$\sum_{n'}(E_n\delta_{nn'} + \mathbf{\Gamma}_{nn'}\cdot\boldsymbol{k})f_{n'} = \mathcal{E}f_n, \tag{3.20}$$

where

$$\mathbf{\Gamma}_{nn'} = \int_S \mathrm{d}\boldsymbol{r}^2\, u_n^*(\boldsymbol{r})\boldsymbol{\sigma}u_{n'}(\boldsymbol{r}). \tag{3.21}$$

Solving Eq. (3.20) gives the complete spectrum of the system without any approximation. In particular, if we want to focus on states at a specific energy level, the coefficients f_n will be dominated by contributions from wavefunctions at the $\mathbf{\Gamma}$ point whose energy levels are closest to $\mathcal{E}$.

From Eq. (3.20) we can write the equation for the coefficient f_n as:

$$f_n = \frac{1}{\mathcal{E}-E_n}\sum_{n'}\boldsymbol{k}\cdot\mathbf{\Gamma}_{nn'}f_{n'}, \tag{3.22}$$

This equation indicates that the coefficient f_n is proportional to $\frac{1}{\mathcal{E}-E_n}$. Therefore, if we are interested in states at a specific energy level $\mathcal{E}$, the dominant contribution to the resulting eigenstate(s) will come from the wavefunctions at the $\mathbf{\Gamma}$ point whose energy levels E_n are closest to $\mathcal{E}$. This observation allows us to focus on the wavefunctions and energy levels near the $\mathbf{\Gamma}$ point when studying specific energy levels in the system.

Fall back to the degenerate perturbation theory. If we are interested in the energy levels $\mathcal{E}$ near the zero-energy level at a specific $\boldsymbol{k}$ point, the dominant contribution will come from the two degenerate states at the $\mathbf{\Gamma}$ Dirac point. In this case, we can restrict the indices n and n' in Eq.(3.20) to the two zero-energy states at the $\mathbf{\Gamma}$ Dirac point. As a result, the matrix $\mathbf{\Gamma}_{nn'}$ becomes a 2×2 matrix, and Eq.(3.20) reduces to the first-order degenerate perturbation theory for two states. This allows us to analyze the effects of perturbations and obtain an effective Hamiltonian for the low-energy states near the zero-energy level.

Higher order expansion. By separating the subspace into two parts, one with energy levels close to $\mathcal{E}$ and the other with energy levels far away, we can obtain higher-order corrections to the low-energy states.

In the subspace with energy close to $\mathcal{E}$, the coefficients f_α can be expressed in terms of the matrix elements $\mathbf{\Gamma}_{\alpha\beta}$ and $\mathbf{\Gamma}_{\alpha m}$ as given in Eq. (3.23). Here, α and β are Greek in-

dices representing states in the subspace with energy close to $\mathcal{E}$, while m is a Latin index representing states in the subspace with energy far away from $\mathcal{E}$.

$$f_\alpha = \frac{1}{\mathcal{E} - E_\alpha}(\sum_\beta \boldsymbol{k}\cdot\boldsymbol{\Gamma}_{\alpha\beta} f_\beta + \sum_m \boldsymbol{k}\cdot\boldsymbol{\Gamma}_{\alpha m} f_m) \tag{3.23}$$

On the other hand, for the subspace with energy levels far away from $\mathcal{E}$, we can approximate $\frac{1}{\mathcal{E}-E_m}$ as $-\frac{1}{E_m}(1+\mathcal{O}(\frac{\mathcal{E}}{E_m^2}))$. This allows us to write the coefficients f_m in terms of the matrix elements $\boldsymbol{\Gamma}_{m\beta}$ and $\boldsymbol{\Gamma}_{ml}$, as shown in Eq. (3.24).

$$f_m = -\frac{1}{E_m}(\sum_\beta \boldsymbol{k}\cdot\boldsymbol{\Gamma}_{m\beta} + \sum_l \boldsymbol{k}\cdot\boldsymbol{\Gamma}_{ml} f_l). \tag{3.24}$$

By substituting Eq.(3.24) into Eq.(3.23) iteratively, we can generate an expansion in orders of $\boldsymbol{k}$. The expansion includes terms involving multiple matrix elements and allows us to obtain higher-order corrections to the coefficients f_α:

$$\begin{aligned} f_\alpha = \frac{1}{\mathcal{E}-E_\alpha}\times\{ & \\ & \sum_\beta \boldsymbol{k}\cdot\boldsymbol{\Gamma}_{\alpha\beta} f_\beta \\ & -\sum_{m,\beta} \boldsymbol{k}\cdot\boldsymbol{\Gamma}_{\alpha m}\frac{1}{E_m}\boldsymbol{k}\cdot\boldsymbol{\Gamma}_{m\beta} f_\beta \\ & +\sum_{m,l,\beta} \boldsymbol{k}\cdot\boldsymbol{\Gamma}_{\alpha m}\frac{1}{E_m}\boldsymbol{k}\cdot\boldsymbol{\Gamma}_{ml}\frac{1}{E_l}\boldsymbol{k}\cdot\boldsymbol{\Gamma}_{l\beta} f_\beta \\ & +\cdots \\ & \} \end{aligned} \tag{3.25}$$

3.3.2 Ansatz wave function of the exact TTG model

The $\boldsymbol{k}\cdot\boldsymbol{p}$ method demonstrated above applies to any model with well defined periodicity, which requires solving the model at one specific point first. The exact model of the twisted trilayer graphene, however, does not offer such a facility due to its quasi-crystal nature. To circumvent this difficulty, we will find a way to construct the wave functions based on the "local" solutions from Chapter 2. Our intuition of the technique originates from the notion that the exact wave functions should share certain similarities with the local solutions. If

the local solutions are given by

$$H_{\text{local}}(\boldsymbol{r};\boldsymbol{\phi}(\boldsymbol{R}))u_{n\boldsymbol{k}}(\boldsymbol{r};\boldsymbol{\phi}(\boldsymbol{R})) = E_{n\boldsymbol{k}}(\boldsymbol{\phi}(\boldsymbol{R}))u_{n\boldsymbol{k}}(\boldsymbol{r};\boldsymbol{\phi}(\boldsymbol{R})), \tag{3.26}$$

then we propose the *ansatz* wave functions for the exact solution as

$$\varphi(\boldsymbol{r}) = \sum_n f_n(\boldsymbol{r})u_{n\boldsymbol{\kappa}}(\boldsymbol{r};\boldsymbol{\phi}(\boldsymbol{r})), \tag{3.27}$$

where $\boldsymbol{\kappa}$ belongs to the *local moiré Brillouin zone*. It should be emphasized that in Eq. (3.26) $\boldsymbol{r}$ and $\boldsymbol{R}$ are decoupled coordinates and $\boldsymbol{R}$ is parameter controlling the phases. In the ansatz given in Eq. (3.27) $\phi(\boldsymbol{r})$ also varies with $\boldsymbol{r}$. The modulation functions $f_n(\boldsymbol{r})$ are assumed to be slowly varying over the supermoiré length scale, such that $f_n(\boldsymbol{r})$, similar to $\boldsymbol{\phi}(\boldsymbol{r})$, is almost invariant within a moiré unit cell. The validity of Eq. (3.27) also requires $\boldsymbol{\phi}(\boldsymbol{r})$ to be a smooth and continuous function of $\boldsymbol{r}$. Consequently, gauge-fixing is implied for $u_{n\boldsymbol{\kappa}}(\boldsymbol{r};\boldsymbol{\phi}(\boldsymbol{r}))$ to vary smoothly and continuously. For clarity, the formalism of the TTG effective theory will be established first, while the discussion of the gauge-fixing procedures will be addressed subsequently.

Let us write down the Schrödinger's equation for the exact TTG model using the ansatz wave function. To simplify the notation, we use $H(\boldsymbol{r}) = -i\boldsymbol{\nabla}\cdot\boldsymbol{\sigma} + V(\boldsymbol{r},\boldsymbol{\phi}(\boldsymbol{r}))$ to represent the exact TTG Hamiltonian. Since $[-i\boldsymbol{\nabla}\cdot\boldsymbol{\sigma}+V(\boldsymbol{r},\boldsymbol{\phi}(\boldsymbol{R}))]u_{n\boldsymbol{\kappa}}(\boldsymbol{r};\boldsymbol{\phi}(\boldsymbol{R})) = E_{n\boldsymbol{\kappa}}(\boldsymbol{R})u_{n\boldsymbol{\kappa}}(\boldsymbol{r};\boldsymbol{\phi}(\boldsymbol{R}))$, the action of the exact Hamiltonian on the ansatz wave function yields:

$$\begin{aligned}\sum_{n'}\{&f_{n'}(\boldsymbol{r})(-i\boldsymbol{\sigma}\cdot\boldsymbol{\nabla}_{\boldsymbol{r}}\boldsymbol{\phi}\boldsymbol{\nabla}_{\boldsymbol{\phi}}u_{n'\boldsymbol{\kappa}}(\boldsymbol{r};\boldsymbol{\phi}(\boldsymbol{r}))\\ &+ u_{n'\boldsymbol{\kappa}}(\boldsymbol{r};\boldsymbol{\phi}(\boldsymbol{r}))(-i\boldsymbol{\sigma}\cdot\boldsymbol{\nabla}f_{n'}(\boldsymbol{r})\\ &+ E_{n\boldsymbol{\kappa}}(\boldsymbol{\phi}(\boldsymbol{r}))f_{n'}(\boldsymbol{r})u_{n'\boldsymbol{\kappa}}(\boldsymbol{r};\boldsymbol{\phi}(\boldsymbol{r}))\} = \mathcal{E}\sum_{n'} f_{n'}(\boldsymbol{r})u_{n'\boldsymbol{\kappa}}(\boldsymbol{r};\boldsymbol{\phi}(\boldsymbol{r})).\end{aligned} \tag{3.28}$$

So far, no further approximations have been made except for the form of the ansatz.

We then proceed by multiplying $u^*_{n\boldsymbol{\kappa}}(\boldsymbol{r},\boldsymbol{\phi}(\boldsymbol{r}))$ on both sides and integrating over the *moiré unit cell* (MUC). Since $f_n(\boldsymbol{r})$ is a slowly varying function that is almost constant within a moiré unit cell, we can take it out of the integral. The right-hand side then becomes:

$$RHS \simeq \mathcal{E}\sum_{n'} f_{n'}(\boldsymbol{r})\int_{\text{MUC}} \mathrm{d}\boldsymbol{r}^2\; u^*_{n\boldsymbol{\kappa}}(\boldsymbol{r};\boldsymbol{\phi}(\boldsymbol{r}))u_{n'\boldsymbol{\kappa}}(\boldsymbol{r};\boldsymbol{\phi}(\boldsymbol{r})) = \mathcal{E}\sum_{n'} f_{n'}(\boldsymbol{r})\delta_{nn'} = \mathcal{E}f_n(\boldsymbol{r}). \tag{3.29}$$

Applying the same orthonormal relation to the left-hand side gives:

$$\begin{aligned} LHS \simeq \sum_{n'} \{ & \int_{\text{MUC}} \mathrm{d}\boldsymbol{r}^2 \; u^*_{n\boldsymbol{\kappa}}(\boldsymbol{r};\boldsymbol{\phi}(\boldsymbol{r}))(-i\boldsymbol{\sigma}\cdot\boldsymbol{\nabla}_{\boldsymbol{r}})\boldsymbol{\phi}\boldsymbol{\nabla}_{\boldsymbol{\phi}} u_{n'\boldsymbol{\kappa}}(\boldsymbol{r};\boldsymbol{\phi}(\boldsymbol{r})) \\ & + \int_{\text{MUC}} \mathrm{d}\boldsymbol{r}^2 \; u^*_{n\boldsymbol{\kappa}}(\boldsymbol{r};\boldsymbol{\phi}(\boldsymbol{r})\boldsymbol{\sigma} u_{n'\boldsymbol{\kappa}}(\boldsymbol{r};\boldsymbol{\phi}(\boldsymbol{r}))(-i\boldsymbol{\nabla}) \\ & + E_{nn'}(\boldsymbol{r})\} f_{n'}(\boldsymbol{r}) \end{aligned} \tag{3.30}$$

Note that $E_{nn'}$ is not necessarily a diagonal matrix since the gauge-fixing procedures mix the eigenstates of local models. Within the moiré unit cell, we can treat $\boldsymbol{\phi}(\boldsymbol{r})$ as constant, allowing us to compute the integrals using local states. By integrating out the variations within the moiré scale, we obtain a new equation that describes the physics on the supermoiré scale. To emphasize the difference in length scales between the effective equation and the original model, we change the notation from $\boldsymbol{r}$ to $\boldsymbol{R}$ to represent the supermoiré coordinates.

To simplify the notation, we introduce the quantities:

$$\begin{aligned} A(\boldsymbol{R}) = & \; \langle u_{n\boldsymbol{\kappa}}(\boldsymbol{R})| -i\boldsymbol{\nabla}_{\boldsymbol{R}}\cdot\boldsymbol{\sigma}| u_{n'\boldsymbol{\kappa}}(\boldsymbol{R})\rangle \\ = & \sum_{\alpha\alpha'}\sum_{l}\int_{\text{MUC}} \mathrm{d}\boldsymbol{r}^2 \; u^{\alpha l *}_{n\boldsymbol{\kappa}}(\boldsymbol{r};\boldsymbol{\phi}(\boldsymbol{R}))(-i\boldsymbol{\sigma}\cdot\boldsymbol{\nabla}_{\boldsymbol{R}}) u^{\alpha' l}_{n'\boldsymbol{\kappa}}(\boldsymbol{r};\boldsymbol{\phi}(\boldsymbol{R})), \end{aligned} \tag{3.31}$$

which will later prove to be a non-Abelian gauge field acting as a pseudo-magnetic field, and

$$\boldsymbol{\Gamma}_{nn'}(\boldsymbol{R}) = \langle u_{n\boldsymbol{\kappa}}(\boldsymbol{R})|\boldsymbol{\sigma}|u_{n'\boldsymbol{\kappa}}(\boldsymbol{R})\rangle = \sum_{\alpha\alpha'}\sum_{l}\int_{\text{MUC}} \mathrm{d}\boldsymbol{r}^2 \; u^{\alpha l *}_{n\boldsymbol{\kappa}}(\boldsymbol{r};\boldsymbol{\phi}(\boldsymbol{R})\boldsymbol{\sigma} u^{\alpha' l}_{n'\boldsymbol{\kappa}}(\boldsymbol{r};\boldsymbol{\phi}(\boldsymbol{R})). \tag{3.32}$$

$E_{nn'}(\boldsymbol{R})$ is simply given by

$$E_{nn'}(\boldsymbol{R}) = \langle u_{n\boldsymbol{\kappa}}(\boldsymbol{R})|H(\boldsymbol{\phi}(\boldsymbol{R}))|u_{n'\boldsymbol{\kappa}}(\boldsymbol{R})\rangle \, . \tag{3.33}$$

3.3.3 Effective model

Combining the results in Chapter 3.3.2,we obtain a new effective Hamiltonian $H_{\text{eff}}(\boldsymbol{R})$ that only concerns the modulation functions:

$$H_{\text{eff}}(\boldsymbol{R}) = -i\boldsymbol{\Gamma}(\boldsymbol{R})\cdot\boldsymbol{\nabla}_{\boldsymbol{R}} \circ + A(\boldsymbol{R}) + E(\boldsymbol{R}), \tag{3.34}$$

where the matrices, $\mathbf{\Gamma}(\boldsymbol{R})$, $A(\boldsymbol{R})$, and $E(\boldsymbol{R})$ are given by Eqs. (3.32), (3.31), and (3.33), respectively. Here, we use $\boldsymbol{\nabla}_{\boldsymbol{R}}\circ$ to indicate that the gradient operator acts *only* on the modulation functions to avoid confusion in later discussions. The Schrödinger's equation for the effective Hamiltonian can be written as:

$$\sum_m H_{\text{eff},nm}(\boldsymbol{R}) f_m(\boldsymbol{R}) = \mathcal{E} f_n(\boldsymbol{R}). \tag{3.35}$$

where $H_{\text{eff},nm}(\boldsymbol{R})$ are the matrix elements of the effective Hamiltonian.

Before attempting to solve the effective mode, we will first analyze the hermiticity of the effective Hamiltonian given in Eq. (3.34). To facilitate the subsequent computations, it is convenient to expand the *local* wave functions as follows:

$$u^{\alpha,l}_{n\boldsymbol{k}}(\boldsymbol{r};\boldsymbol{\phi}(\boldsymbol{R})) = \sum_{\boldsymbol{Q}} u^{\alpha,l}_{n\boldsymbol{k}}(\boldsymbol{Q};\boldsymbol{\phi}(\boldsymbol{R})) e^{-i\boldsymbol{Q}\cdot\boldsymbol{r}}. \tag{3.36}$$

where the expansion is possible due to the fact that gauge-fixed states are linear combinations of the eigenstates of the local Hamiltonian with the same periodicity. Therefore, the resulting gauge-fixed local wave functions share the periodicity of the eigenstates of the local Hamiltonians.

To check the hermiticity of $E_{nn'}(\boldsymbol{R})$, we need to evaluate its explicit form:

$$E_{nn'}(\boldsymbol{R}) = \sum_{\alpha\alpha'}\sum_{ll'}\int_{\text{MUC}} \mathrm{d}\boldsymbol{r}^2 u^{\alpha l*}_{n\boldsymbol{k}}(\boldsymbol{r};\boldsymbol{\phi}(\boldsymbol{R}))(-i\boldsymbol{\nabla}_{\boldsymbol{r}}\cdot\boldsymbol{\sigma}^{\alpha\alpha'}\delta_{ll'} + V^{\alpha\alpha'}_{ll'}(\boldsymbol{r})) u^{\alpha' l'}_{n'\boldsymbol{k}}(\boldsymbol{r};\boldsymbol{\phi}(\boldsymbol{R})) \tag{3.37}$$

We can compute this expression in two parts:

$$\begin{aligned} E_{nn'}(\boldsymbol{R}) = &\sum_{\alpha\alpha'}\sum_{ll'}\int_{\text{MUC}} \mathrm{d}\boldsymbol{r}^2 u^{\alpha l*}_{n\boldsymbol{k}}(\boldsymbol{r};\boldsymbol{\phi}(\boldsymbol{R}))(-i\boldsymbol{\nabla}_{\boldsymbol{r}}\cdot\boldsymbol{\sigma}^{\alpha\alpha'}\delta_{ll'} u^{\alpha' l'}_{n'\boldsymbol{k}}(\boldsymbol{r};\boldsymbol{\phi}(\boldsymbol{R})) \\ &+ \sum_{\alpha\alpha'}\sum_{ll'}\int_{\text{MUC}} \mathrm{d}\boldsymbol{r}^2 u^{\alpha l*}_{n\boldsymbol{k}}(\boldsymbol{r};\boldsymbol{\phi}(\boldsymbol{R})) V^{\alpha\alpha'}_{ll'}(\boldsymbol{r}) u^{\alpha' l'}_{n'\boldsymbol{k}}(\boldsymbol{r};\boldsymbol{\phi}(\boldsymbol{R})) \end{aligned}. \tag{3.38}$$

The hermiticity of the first term is not immediately apparent if we want to apply the integration by parts. However, it becomes more convenient to use the expression given in

Eq. (3.36):

$$\begin{aligned}
&\sum_{\alpha\alpha'}\sum_{ll'}\int_{\mathrm{MUC}}\mathrm{d}\boldsymbol{r}^2 u^{\alpha l*}_{n\boldsymbol{k}}(\boldsymbol{r};\boldsymbol{\phi}(\boldsymbol{R}))(-i\boldsymbol{\nabla}_{\boldsymbol{r}}\cdot\boldsymbol{\sigma}^{\alpha\alpha'}\delta_{ll'}u^{\alpha' l'}_{n'\boldsymbol{k}}(\boldsymbol{r};\boldsymbol{\phi}(\boldsymbol{R}))\\
&=\sum_{\alpha\alpha'}\sum_{ll'}\sum_{\boldsymbol{Q},\boldsymbol{Q}'}\frac{1}{S}\int_{\mathrm{MUC}}\mathrm{d}\boldsymbol{r}^2 u^{\alpha l*}_{n\boldsymbol{k}}(\boldsymbol{Q};\boldsymbol{\phi}(\boldsymbol{R}))e^{i\boldsymbol{Q}\cdot\boldsymbol{r}}(-i\boldsymbol{\nabla}_{\boldsymbol{r}}\cdot\boldsymbol{\sigma}^{\alpha\alpha'}\delta_{ll'}u^{\alpha' l'}_{n'\boldsymbol{k}}(\boldsymbol{Q}';\boldsymbol{\phi}(\boldsymbol{R}))e^{-i\boldsymbol{Q}'\cdot\boldsymbol{r}}\\
&=\sum_{\alpha\alpha'}\sum_{ll'}\sum_{\boldsymbol{Q}}u^{\alpha l*}_{n\boldsymbol{k}}(\boldsymbol{Q};\boldsymbol{\phi}(\boldsymbol{R}))(-\boldsymbol{Q}\cdot\boldsymbol{\sigma}^{\alpha\alpha'})u^{\alpha' l'}_{n'\boldsymbol{k}}(\boldsymbol{Q};\boldsymbol{\phi}(\boldsymbol{R}))
\end{aligned}\tag{3.39}$$

Now let's evaluate the matrix element of the Hermitian conjugate of $E_{nn'}(\boldsymbol{R})$:

$$\begin{aligned}
(E(\boldsymbol{R}))^\dagger_{nn'}=E^*_{n'n}(\boldsymbol{R})&=\sum_{\alpha\alpha'}\sum_{ll'}\sum_{\boldsymbol{Q}}u^{\alpha l}_{n'\boldsymbol{k}}(\boldsymbol{Q};\boldsymbol{\phi}(\boldsymbol{R}))(-\boldsymbol{Q}\cdot\boldsymbol{\sigma}^{*,\alpha\alpha'})u^{\alpha' l',*}_{n\boldsymbol{k}}(\boldsymbol{Q};\boldsymbol{\phi}(\boldsymbol{R}))\\
&+\sum_{\alpha\alpha'}\sum_{ll'}\int_{\mathrm{MUC}}\mathrm{d}\boldsymbol{r}^2\, u^{\alpha l}_{n'\boldsymbol{k}}(\boldsymbol{r};\boldsymbol{\phi}(\boldsymbol{R}))V^{*\alpha\alpha'}_{ll'}(\boldsymbol{r};\boldsymbol{\phi}(\boldsymbol{R}))u^{\alpha' l',*}_{n\boldsymbol{k}}(\boldsymbol{r};\boldsymbol{\phi}(\boldsymbol{R}))\\
&=\sum_{\alpha\alpha'}\sum_{ll'}\sum_{\boldsymbol{Q}}u^{\alpha' l',*}_{n\boldsymbol{k}}(\boldsymbol{Q};\boldsymbol{\phi}(\boldsymbol{R}))(-Q\cdot\boldsymbol{\sigma}^{\alpha'\alpha})u^{\alpha l}_{n'\boldsymbol{k}}\\
&+\sum_{\alpha\alpha'}\sum_{ll'}\int_{\mathrm{MUC}}\mathrm{d}\boldsymbol{r}^2\, u^{\alpha' l'}_{n\boldsymbol{k}}(\boldsymbol{r};\boldsymbol{\phi}(\boldsymbol{R}))V^{\alpha'\alpha}_{l'l}(\boldsymbol{r};\boldsymbol{\phi}(\boldsymbol{R}))u^{\alpha l}_{n'\boldsymbol{k}}(\boldsymbol{r};\boldsymbol{\phi}(\boldsymbol{R}))\\
&=E_{nn'}(\boldsymbol{R}).
\end{aligned}\tag{3.40}$$

Therefore the matrix $E(\boldsymbol{R})$ is explicitly confirmed to be Hermitian.

Although the velocity term $\boldsymbol{\Gamma}(\boldsymbol{R})$ is Hermitian, verifying

$$\begin{aligned}
\boldsymbol{\Gamma}^*_{n'n}(\boldsymbol{R})&=\sum_{\alpha\alpha'}\sum_{ll'}\int_{\mathrm{MUC}}\mathrm{d}\boldsymbol{r}^2\, u^{\alpha l}_{n'\boldsymbol{k}}(\boldsymbol{r};\boldsymbol{\phi}(\boldsymbol{R}))\boldsymbol{\sigma}^{\alpha\alpha'*}u^{\alpha' l'}_{n\boldsymbol{k}}(\boldsymbol{r};\boldsymbol{\phi}(\boldsymbol{R}))\\
&=\sum_{\alpha\alpha'}\sum_{ll'}\int_{\mathrm{MUC}}\mathrm{d}\boldsymbol{r}^2\, u^{\alpha' l'}_{n\boldsymbol{k}}(\boldsymbol{r};\boldsymbol{\phi}(\boldsymbol{R}))\boldsymbol{\sigma}^{\alpha'\alpha}u^{\alpha l}_{n'\boldsymbol{k}}(\boldsymbol{r};\boldsymbol{\phi}(\boldsymbol{R}))\\
&=\boldsymbol{\Gamma}_{nn'}(\boldsymbol{R}),
\end{aligned}\tag{3.41}$$

the entire kinetic energy term $-i\boldsymbol{\Gamma}(\boldsymbol{R})\cdot\boldsymbol{\nabla}$ is not Hermitian because of

$$\begin{aligned}
(-i\boldsymbol{\Gamma}(\boldsymbol{R})\cdot\boldsymbol{\nabla}_{\boldsymbol{R}}\circ)^\dagger&=i\boldsymbol{\nabla}_{-\boldsymbol{R}}\cdot\boldsymbol{\Gamma}(\boldsymbol{R})+i\boldsymbol{\nabla}_{-\boldsymbol{R}}\circ\\
&=-i\boldsymbol{\nabla}_{\boldsymbol{R}}\cdot\boldsymbol{\Gamma}(\boldsymbol{R})-i\boldsymbol{\Gamma}(\boldsymbol{R})\cdot\boldsymbol{\nabla}_{\boldsymbol{R}}\circ\neq-i\boldsymbol{\Gamma}(\boldsymbol{R})\cdot\boldsymbol{\nabla}_{\boldsymbol{R}}\circ,
\end{aligned}\tag{3.42}$$

with the inequality caused by the extra term $-i(\boldsymbol{\nabla}_{\boldsymbol{R}}\cdot\boldsymbol{\Gamma}(\boldsymbol{R}))$ which is generally non-zero.

The Hermitian conjugate of the gauge field term $A(\boldsymbol{R})$ is given by

$$\begin{aligned}
A^*_{n'n}(\boldsymbol{R}) &= \sum_{\alpha\alpha'}\sum_{l}\int_{\mathrm{MUC}} \mathrm{d}\boldsymbol{r}^2\; u^{\alpha l}_{n'\boldsymbol{k}}(\boldsymbol{r};\boldsymbol{\phi}(\boldsymbol{R}))(i\boldsymbol{\sigma}^{\alpha\alpha'*}\cdot\boldsymbol{\nabla}_{\boldsymbol{R}})u^{\alpha' l*}_{n\boldsymbol{k}}(\boldsymbol{r};\boldsymbol{\phi}(\boldsymbol{R})) \\
&= \sum_{\alpha\alpha'}\sum_{l}\int_{\mathrm{MUC}} \mathrm{d}\boldsymbol{r}^2\; [\boldsymbol{\nabla}_{\boldsymbol{R}} u^{\alpha' l*}_{n\boldsymbol{k}}(\boldsymbol{r};\boldsymbol{\phi}(\boldsymbol{R}))]\cdot i\boldsymbol{\sigma}^{\alpha'\alpha} u^{\alpha l}_{n'\boldsymbol{k}}(\boldsymbol{r};\boldsymbol{\phi}(\boldsymbol{R})) \\
&= i\boldsymbol{\nabla}_{\boldsymbol{R}}\cdot\sum_{\alpha\alpha'}\sum_{l}\int_{\mathrm{MUC}} \mathrm{d}\boldsymbol{r}^2\; u^{\alpha' l*}_{n\boldsymbol{k}}(\boldsymbol{r};\boldsymbol{\phi}(\boldsymbol{R}))\boldsymbol{\sigma}^{\alpha'\alpha} u^{\alpha l}_{n'\boldsymbol{k}}(\boldsymbol{r};\boldsymbol{\phi}(\boldsymbol{R})) \\
&+ \sum_{\alpha\alpha'}\sum_{l}\int_{\mathrm{MUC}} \mathrm{d}\boldsymbol{r}^2\; u^{\alpha' l*}_{n\boldsymbol{k}}(\boldsymbol{r};\boldsymbol{\phi}(\boldsymbol{R}))(-i\boldsymbol{\sigma}^{\alpha'\alpha}) u^{\alpha l}_{n'\boldsymbol{k}}(\boldsymbol{r};\boldsymbol{\phi}(\boldsymbol{R})) \\
&= i(\boldsymbol{\nabla}_{\boldsymbol{R}}\cdot\boldsymbol{\Gamma}_{nn'}(\boldsymbol{R})) + A_{nn'}(\boldsymbol{R}) \neq A_{nn'}(\boldsymbol{R}).
\end{aligned} \tag{3.43}$$

In general there is no constraint to impose that the term $i(\boldsymbol{\nabla}_{\boldsymbol{R}}\cdot\boldsymbol{\Gamma}_{nn'}(\boldsymbol{R}))$ is zero. Therefore the gauge field term $A(\boldsymbol{R})$ is not Hermitian either.

Upon closer examination, it becomes evident that in the sum $-i\boldsymbol{\Gamma}(\boldsymbol{R})\cdot\boldsymbol{\nabla}_{\boldsymbol{R}}\circ + A(\boldsymbol{R})$, the additional terms in the Hermitian conjugates of $-i\boldsymbol{\Gamma}(\boldsymbol{R})\cdot\boldsymbol{\nabla}_{\boldsymbol{R}}\circ$ and $A(\boldsymbol{R})$ will cancel out, resulting in the hermiticity of the entire equation.

Although the non-symmetrized operators preserve the hermiticity of the equation, it is advantageous to symmetrize each part to facilitate numerical solutions. The symmetrization process allows for a more straightforward implementation and computational efficiency in practical calculations. To symmetrize the operators, we apply the following transformations. For $-i\boldsymbol{\Gamma}(\boldsymbol{R})\cdot\boldsymbol{\nabla}_{\boldsymbol{R}}\circ$, we symmetrize it as follows:

$$\begin{aligned}
-i\boldsymbol{\Gamma}(\boldsymbol{R})\cdot\boldsymbol{\nabla}_{\boldsymbol{R}}\circ &\to \frac{1}{2}[-i\boldsymbol{\Gamma}(\boldsymbol{R})\cdot\boldsymbol{\nabla}_{\boldsymbol{R}}\circ + (-i\boldsymbol{\Gamma}(\boldsymbol{R})\cdot\boldsymbol{\nabla}_{\boldsymbol{R}}\circ)^\dagger] \\
&= -i\boldsymbol{\Gamma}(\boldsymbol{R})\cdot\boldsymbol{\nabla}_{\boldsymbol{R}}\circ - \frac{i}{2}\boldsymbol{\nabla}_{\boldsymbol{R}}\cdot\boldsymbol{\Gamma}(\boldsymbol{R}),
\end{aligned} \tag{3.44}$$

Similarly, $A(\boldsymbol{R})$ is symmetrized as follows:

$$A(\boldsymbol{R}) \to \frac{1}{2}\{A(\boldsymbol{R}) + A^\dagger(\boldsymbol{R})\}. \tag{3.45}$$

It is important to note that although we use the symmetrized operators in the treatment of the effective model, for clarity, we maintain the non-symmetrized notations in Eq. (3.34).

3.4 Gauge Fixing and gauge invariance

3.4.1 General principle of fixing gauges

As mentioned earlier, the ansatz for the wave function relies on selecting a set of "local" states that exhibit smooth and continuous variations with respect to the supermoiré coordinate $\boldsymbol{R}$. Achieving this requires fixing two key aspects:

- Continuous evolution of states: The chosen ensemble of local states should evolve continuously as a function of $\boldsymbol{R}$. This means that as $\boldsymbol{R}$ changes, the local states smoothly transition from one configuration to another, maintaining a coherent and gradual evolution throughout the supermoiré lattice.
- Continuous evolution of the global phases: In addition to the continuous evolution of states, it is crucial to ensure the continuous evolution of the global phases associated with the local wave functions. The global phase refers to the overall phase factor of the wave function, which can vary as a function of $\boldsymbol{R}$. To achieve a smooth and continuous variation, the global phase of the local wave functions must be properly accounted for and preserved throughout the supermoiré lattice.

By addressing both the continuous evolution of states and the continuous evolution of global phases, the gauge-fixing algorithm ensures that the ensemble of local states exhibits the desired smooth and continuous variation with respect to the supermoiré coordinate $\boldsymbol{R}$. This enables a consistent and accurate description of the system within the framework of the ansatz for the wave function.

Assuming that a set of N states $\{|\psi_n(\boldsymbol{R})\rangle, n = 1, 2, \cdots, N\}$, has been obtained through numerical diagonalization of the local Hamiltonian $\hat{H}(\boldsymbol{R})$ at each coordinate $\boldsymbol{R}$, these states can be referred to as “wild-gauge” states since they inherently carry an implicit random gauge. In the process of gauge-fixing, it is important to ensure that none of the states are projected out of the subspace spanned by the wild-gauge states. Consequently, gauge fixing can be understood as a rotation within the same subspace. In general, the gauge-fixed states can be expressed as:

$$|\varphi_n(\boldsymbol{R})\rangle = \sum_m |\psi_m(\boldsymbol{R})\rangle \, \chi_{mn}(\boldsymbol{R}), \; n, m = 1, 2, \cdots, N \tag{3.46}$$

where $|\varphi_n(\boldsymbol{R})\rangle$ represents the gauge-fixed states, and $\chi(\boldsymbol{R})$ is a *unitary* matrix. The unitarity of $\chi(\boldsymbol{R})$ guarantees that the gauge-fixed states remain within the same subspace

spanned by the wild-gauge states. By applying this gauge-fixing transformation, the wild-gauge states are rotated to yield the gauge-fixed states, resulting in a consistent and controlled gauge choice for the ensemble of local wave functions.

The first requirement for gauge-fixing is achieved by selecting states that satisfy the same constraint at all positions $\boldsymbol{R}$. For instance, one can choose the states $|\varphi_n\rangle$ in such a way that the expectation value $\langle\varphi_n|\hat{O}|\varphi_m\rangle$ is proportional to the Kronecker delta δ_{nm}, where $\hat{O}$ is typically a Hermitian operator.

To address the global phase fixing, a set of "reference" states $|g_n\rangle$ is chosen, which are independent of $\boldsymbol{R}$. These reference states are selected in a manner such that $\langle g_n|\varphi_n(\boldsymbol{R})\rangle$ always lies in the positive real domain.

Therefore, the objective of gauge fixing is to determine a unitary matrix $\chi(\boldsymbol{R})$ at each position $\boldsymbol{R}$, such that the overlap matrix between the reference states and the gauge-fixed states has only positive diagonal elements. In other words, the gauge-fixing process seeks to establish a consistent phase convention by appropriately adjusting the phases of the states within the chosen subspace.

3.4.2 Practical Procedures

In principle, there are infinite possibilities for choosing the unitary matrix $\chi(\boldsymbol{R})$ at each point $\boldsymbol{R}$. The gauge of the states needs to be fixed at every point in $\boldsymbol{R}$, and for clarity, we will denote the unitary matrix as simply χ. To simplify the discussion, we can employ linear algebra notations. The wild-gauge states can be arranged in a matrix $\Psi = [|\psi_1\rangle, \cdots, |\psi_N\rangle]$, where each column represents a state vector. Similarly, the reference states can be collected in a matrix $G = [|g_1\rangle, \cdots, |g_N\rangle]$. The resulting gauge-fixed states are stored in $\Phi = [|\varphi_1\rangle, \cdots, |\varphi_N\rangle]$. The goal is to devise an algorithm that generates the desired unitary matrix χ, which gives the gauge-fixed states

$$\Phi = \Psi\chi. \tag{3.47}$$

Gauge fixing with an operator specified. In many cases, it is desirable for the gauge-fixed states to be maximally aligned with the eigenstates of a Hermitian operator $\hat{O}$, as this facilitates the physical interpretation of the model using the gauge-fixed states. To achieve this, we first project the operator $\hat{O}$ onto the subspace spanned by the wild-gauge states by

computing $\Psi^\dagger O \Psi$. It can be diagonalized using

$$U^\dagger \Psi^\dagger O \Psi U = D, \tag{3.48}$$

where U is a unitary matrix whose columns represent the eigenvectors of the projected operator, and D is a diagonal matrix whose diagonal entries are the eigenvalues. At this step ΨU gives the new states that are maximally aligned with the true eigenstates of $\hat{O}$. It remains to fix the global gauge using

$$\Phi = \Psi U V, \tag{3.49}$$

where V is a diagonal unitary matrix whose diagonal entries fix the global phase of the gauge-fixed states. The diagonal entries of V are given by

$$V_{nn} = \frac{(G^\dagger \Psi U)^*_{nn}}{|G^\dagger \Psi U|}. \tag{3.50}$$

As a result, the gauge-fixing matrix χ is given by

$$\chi = UV. \tag{3.51}$$

This last step ensures that $\langle g_n | \varphi_n \rangle$ is real and positive.

Gauge-fixing based on a specific Hermitian operator is intuitive and straightforward. It works efficiently for a small number of wild-gauge states. However, when dealing with a large number of states, finding N reference states that have non-zero overlap with the gauge-fixed states is not always easy.

Fast gauge-fixing algorithm. The gauge-fixing algorithm based on the singular value decomposition (SVD) provides a fast and efficient way to accomplish gauge fixing, simultaneously addressing both the alignment of states and the fixing of global phases [100]. We start by testing the matrix $\chi = \Psi^\dagger G$, which ensures that the diagonal matrix elements of $G^\dagger \Psi \chi = G^\dagger \Psi \Psi^\dagger G$ are real and positive due to the product of a matrix with its adjoint. However, $\Psi^\dagger G$ is not unitary because $|g_n\rangle$ and $|\psi_n\rangle$ do not live in completely overlapping subspaces. The size of the $|\psi_n\rangle$ vectors shrinks when multiplied by $\Psi^\dagger U$. To restore unitarity, we apply the correction:

$$\chi = \Psi^\dagger G (G^\dagger \Psi \Psi^\dagger G)^{-\frac{1}{2}}. \tag{3.52}$$

To demonstrate the unitarity of χ, we perform the SVD of $\Psi^\dagger G$:

$$\Psi^\dagger G = ZSW \tag{3.53}$$

where Z and W are unitary matrices, and S is a *real* and diagonal matrix with *positive* diagonal entries called singular values. We solve Eq. (3.53) to determine the matrices Z and W. Later we will realize that the gauge-fixing states is directly given by

$$\Phi = \Psi ZW, \tag{3.54}$$

which means the gauge-fixing matrix χ is simply

$$\chi = ZW. \tag{3.55}$$

To prove this , we compute first

$$(G^\dagger \Psi \Psi^\dagger G)^{-\frac{1}{2}} = (W^\dagger S Z^\dagger Z S W)^{\frac{1}{2}} = W^\dagger S^{-1} W. \tag{3.56}$$

As a result, Eq. (3.52) is rewritten as

$$\chi = ZSWW^\dagger S^{-1} W = ZW, \tag{3.57}$$

which is unitary as it is a product of two unitary matrices. The gauge fixing is accomplished through a single step of SVD. There is no need to explicitly diagonalize the projector $\sum_n |g_n\rangle\langle g_n| \equiv GG^\dagger$ within the subspace of $\{|\psi_n\rangle\}$, as it is implicitly fulfilled by the SVD.

Now let's explicitly demonstrate that Z fixes the states, and W fixes the global phases. The matrix form of $GG^\dagger$ projected into the subspace spanned by $|\psi_n\rangle$ is given by

$$\Psi^\dagger G G^\dagger \Psi = ZSWW^\dagger S Z^\dagger = ZS^2 Z^\dagger. \tag{3.58}$$

which implies that

$$Z^\dagger \Psi^\dagger G G^\dagger \Psi Z = S^2, \tag{3.59}$$

yielding a diagonal matrix. The unitary matrix Z registers all the eigenvectors of the projected operator as its column vectors.

The global phases are given by the diagonal elements of the following matrix:

$$G^\dagger \Psi \chi = W^\dagger S Z^\dagger Z W = W^\dagger S W. \tag{3.60}$$

Since S is a diagonal matrix with positive values, the product $W^\dagger SW$ must have positive diagonal entries. Hence, the global phases are fixed by the W matrix. In fact, the overlap between the n-th reference state and the n-th gauge-fixed state is given by

$$\langle g_n|\varphi_n\rangle = (W^\dagger SW)_{nn} = \sum_l W^*_{ln} s_l W_{ln} = \sum_l s_l |W_{ln}|^2 > 0, \tag{3.61}$$

where s_l denotes the l-th singular value.

The fast gauge-fixing algorithm leverages the singular value decomposition to simultaneously accomplish both aspects of gauge fixing. Since the Hermitian operator is inherently chosen as the projector onto the reference states, the non-zero overlap of the eigenstates of the operator with the reference states is trivially guaranteed. In practical applications, it suffices to check that the overlap matrix of the reference states and the wild-gauge states has a rank equal to the dimension of the subspace of the reference states, and the gauge fixing will succeed.

3.4.3 Gauge-invariance of effective model

The formalism of the effective Hamiltonian depends on the choice of gauge. As a valid physical theory should give gauge-independent measurement, we expect the effective theory to have gauge-invariant spectra. In other words, it is expected that the effective models produced in two different gauges should be able to be connected by a unitary transform. This section demonstrates explicitly the unitary transform upon a change of gauge.

The passage from one set of gauge-fixed states to another can be described as a unitary rotation within the same subspace. The gauge change of local states is expressed as:

$$|\varphi'_n(\boldsymbol{R})\rangle = \sum_m |\varphi_m(\boldsymbol{R})\rangle\, \xi_{mn}(\boldsymbol{R}), \tag{3.62}$$

where $\xi(\boldsymbol{R})$ is a unitary matrix that performs the rotation of states. This unitary matrix is a smooth and continuous function of $\boldsymbol{R}$ because the gauge-fixed states $|\varphi'_n(\boldsymbol{R})\rangle$ and $|\varphi_m(\boldsymbol{R})\rangle$ are continuous functions of $\boldsymbol{R}$.

In fact, under a gauge change, the effective Hamiltonian undergoes the following unitary transformation:

$$H'_{nm}(\boldsymbol{R}) = \sum_{n'm'} \xi^\dagger_{nn'}(\boldsymbol{R}) H_{n'm'}(\boldsymbol{R}) \xi_{m'm}(\boldsymbol{R}), \tag{3.63}$$

where $H'(\boldsymbol{R})$ represents the effective Hamiltonian obtained using the gauge-transformed local states $|\varphi'_n(\boldsymbol{R})\rangle$.

The detailed computations, which demonstrate the gauge invariance, are provided in Appendix B.

3.5 Symmetries of effective model

This section explores the symmetries of the effective model, which are closely related to the transformation of local states under symmetry operations. Let's consider a symmetry operator S that transforms a local Hamiltonian at a supermoiré coordinate $\boldsymbol{R}$, denoted as $\hat{H}_{\text{local}}(\boldsymbol{R})$, to another local Hamiltonian at a different supermoiré coordinate $\hat{H}_{\text{local}}(\boldsymbol{s}(\boldsymbol{R}))$:

$$S\hat{H}_{\text{local}}(\boldsymbol{R})S^{\dagger} = \hat{H}_{\text{local}}(\boldsymbol{s}(\boldsymbol{R})), \tag{3.64}$$

This transformation implies that $\hat{H}_{\text{local}}(\boldsymbol{R})$ and $\hat{h}\text{loc}(\boldsymbol{s}(\boldsymbol{R}))$ share the same spectrum. In other words, if $\hat{H}_{\text{local}}(\boldsymbol{R})\,|\psi(\boldsymbol{R})\rangle = E(\boldsymbol{R})\,|\psi(\boldsymbol{R})\rangle$, then $\hat{H}_{\text{local}}(\boldsymbol{s}(\boldsymbol{R}))S\,|\psi(\boldsymbol{R})\rangle = E(\boldsymbol{R})S\,|\psi(\boldsymbol{R})\rangle$. However, it is important to note that Eq. (3.64) is *not* a symmetry of the local Hamiltonian because $\boldsymbol{R}$ is a parameter rather than the moiré coordinate of the local model. The *gauge-fixed* eigenfunctions at $\boldsymbol{R}$ and at $\boldsymbol{s}(\boldsymbol{R})$ are related by the equation:

$$|\psi_n(\boldsymbol{s}(\boldsymbol{R}))\rangle = \sum_m S\,|\psi_m(\boldsymbol{R})\rangle\,\zeta_{mn}(\boldsymbol{R}), \tag{3.65}$$

where $\zeta(\boldsymbol{R})$ is a unitary matrix that remedies the gauge-fixing conditions potentially broken by the direct application of S and may depend on $\boldsymbol{R}$. Once the choice of gauge is determined, $\zeta(\boldsymbol{R})$ is also fixed.

For a symmetry to be present in the effective model, it is required that

$$S^{\dagger}(\boldsymbol{\nabla}_{\boldsymbol{s}(\boldsymbol{R})}) \cdot \boldsymbol{\sigma} S = S^{\dagger}\boldsymbol{\sigma}S \cdot \boldsymbol{\nabla}_{\boldsymbol{s}(\boldsymbol{R})} = \boldsymbol{\sigma} \cdot \boldsymbol{\nabla}_{\boldsymbol{R}}. \tag{3.66}$$

The symmetry is then manifested by:

$$H_{\text{eff}}(\boldsymbol{s}(\boldsymbol{R})) = \zeta^{\dagger}(\boldsymbol{R})H_{\text{eff}}(\boldsymbol{R})\zeta(\boldsymbol{R}). \tag{3.67}$$

The detailed computation proving the symmetries in the effective model is provided in Appendix. C.1.

Diagonal condition of ζ. Ideally, one would expect that the action of the symmetry operator S on the state $|\psi_n(\boldsymbol{R})\rangle$ is equivalent, up to a global phase, to the gauge-fixed state $|\psi_n(\boldsymbol{s}(\boldsymbol{R}))\rangle$. This can be expressed as:

$$\langle\psi_n(s(\boldsymbol{R}))|S|\psi_m(\boldsymbol{R})\rangle = e^{i\phi_n}\delta_{nm}. \tag{3.68}$$

If this condition holds, the matrix ζ becomes diagonal with elements given by $\zeta_{nm} = e^{i\phi_n}\delta_{nm}$. Since the gauge-fixed states satisfy $\langle\psi_n(\boldsymbol{R})|\hat{O}|\psi_m(\boldsymbol{R})\rangle \propto \delta_{nm}$ for all $\boldsymbol{R}$, where $\hat{O}$ is a Hermitian operator, it follows directly from Eq. (3.68) that:

$$\langle\psi_n(\boldsymbol{R})|S^\dagger\hat{O}S|\psi_m(\boldsymbol{R})\rangle \propto \delta_{nm}. \tag{3.69}$$

A situation that naturally satisfies Eq. (3.69) is when the operators S and $\hat{O}$ commute with each other:

$$[S,\hat{O}] = 0, \tag{3.70}$$

which implies that

$$\langle\psi_n(\boldsymbol{R})|S^\dagger\hat{O}S|\psi_m(\boldsymbol{R})\rangle = \langle\psi_n(\boldsymbol{R})|\hat{O}|\psi_m(\boldsymbol{R})\rangle \propto \delta_{nm}.$$

3.5.1 Periodicity of supermoiré Hamiltonian

The effective theory offers the advantage of solving the TTG model in a periodic regime once again. In order to demonstrate the supermoiré periodicity of the effective model, it is necessary to first examine the periodic recurrence of the local models on the supermoiré coordinates.

As demonstrated in Chapter 2, the phase factors in the moiré TTG models have a period of π for equal twist angles and $2\pi/3$ for $\theta_1/\theta_2 = 1/2$ or 2. The periodicity of phase factors reflects a corresponding periodicity on the supermoiré coordinates. Here, we generalize the discussion of the phase period and deduce the size of the supermoiré periodic unit cell. The periodicity of the phase factors can be generalized for any ratio between twist angles $\theta_1/\theta_2 = p/q$, where p and q are coprime integers. As demonstrated in the computations presented in Appendix C.2, the phase in the local moiré model exhibits a period of $2\pi/(p+q)$. In the local model, increasing ϕ_2 (ϕ_3) by $2\pi/(p+q)$ corresponds to shifting the supermoiré coordinates by $\boldsymbol{a}_1^{MM}$ ($\boldsymbol{a}_2^{MM}$), where $\boldsymbol{a}_{1/2}^{MM}$ are the generating vectors of the supermoiré Bravais lattice satisfying $\boldsymbol{a}_i^{MM}\cdot\boldsymbol{b}_j^{MM} = 2\pi\delta_{ij}$, with $\boldsymbol{b}_{1/2}^{MM}$ being the base vectors of the supermoiré reciprocal lattice. The periodicity of the effective Hamiltonian is

manifested by

$$H_{\text{eff}}(\boldsymbol{R} + \boldsymbol{a}_{1/2}^{mm})) = \zeta_{\mathcal{T}}^{\dagger} H_{\text{eff}}(\boldsymbol{R}) \zeta_{\mathcal{T}}, \tag{3.71}$$

where $\zeta_{\mathcal{T}}$ is a unitary matrix that ensures the translational symmetry of the effective model.

This property allows for the application of Bloch's theorem to the effective model. However, in order to write down the Bloch function, the explicit form of $\zeta_{\mathcal{T}}$ is required. In Appendix C.2, we provide the detailed steps to obtain a simple and diagonal form of $\zeta_{\mathcal{T}}$ by carefully choosing reference states during gauge fixing.

3.5.2 Other important symmetries

Unlike the discussions on translational symmetry, we will not look for the explicit form ζ for the other symmetries discussed below. Confirming the presence of ζ is sufficient to validate the symmetry. In the previous chapter, it was demonstrated that the local symmetries may differ for $\theta_1/\theta_2 \simeq 1$ or $1/2$. The verification of potential symmetries in the effective model will be addressed separately for both cases. To confirm the symmetries in the effective model, as explained earlier, we examine the validity of Eqs. (3.64) and (3.66) for the local Hamiltonian. The following symmetries will be discussed: particle-hole symmetry (PHS), C_{3z}, C_{2x}, and $C_{2z}T$.

Particle-hole symmetry is absent. The exact TTG model described by Eq. (3.6) has been shown to lack particle-hole symmetry (PHS) for any ratio between the twist angles. In Chapter 2.3.5, it was explained that local models with $\theta_1/\theta_2 \simeq 1$ exhibit PHS for any combination of phase factors, while local models with $\theta_1/\theta_2 \simeq 1/2$ can restore PHS only for specific phase factors, i.e. particular supermoiré coordinates. However, in both cases, the criterion outlined in Eq. (3.64) cannot be satisfied by the PHS operator. Therefore, PHS does not exist in the effective model.

It is noteworthy that the equal-twist TTG model possesses local PHS "everywhere" but globally breaks PHS.

C_{3z} symmetry. We find that C_{3z} can be locally broken, but is globally restored in the effective model. The C_{3z} symmetry of the effective model is verified by satisfying the criterion of Eq. (3.66). More precisely, the C_{3z} acts on the local Hamiltonian as $e^{2i\pi\sigma_z/3}$, and satisfies:

$$e^{2i\pi\sigma_z/3} \boldsymbol{\nabla}_{\hat{R}_{2\pi/3}\boldsymbol{R}} \cdot \boldsymbol{\sigma} e^{-2i\pi\sigma_z/3} = \boldsymbol{\sigma} \cdot \boldsymbol{\nabla}_{\boldsymbol{R}}. \tag{3.72}$$

The detailed computations are presented in Appendix C.3.

C_{2x} symmetry. C_{2x} symmetry, as shown in the previous chapter, is only present in

local models for $\theta_1 \simeq \theta_2$. After careful analyses, we find that for C_{2x} to be present in the effective model, the strict equality between the twist angles is required.

C_{2x} acts on the local Hamiltonian as

$$C_{2x} = \sigma_x \otimes \begin{pmatrix} & & 1 \\ & 1 & \\ 1 & & \end{pmatrix}_{\text{layer}},$$

and it satisfies the criterion of Eq. (3.66) *only if* the two twist angles are exactly equal, so that

$$C_{2x}\boldsymbol{\sigma} \cdot \boldsymbol{\nabla}_{\hat{M}_y \boldsymbol{R}} \circ \cdot C_{2x} = \sigma_x \boldsymbol{\sigma} \sigma_x \cdot \hat{M}_y^{-1} \boldsymbol{\nabla}_{\boldsymbol{R}} \circ = \boldsymbol{\sigma} \cdot \boldsymbol{\nabla}_{\boldsymbol{R}} \circ.$$

Therefore C_{2x} exists in the effective model only when we exactly have $\theta_1 = \theta_2$. We present the detailed computation of C_{2x} symmetry in Appendix C.4.

$C_{2z}T$ **symmetry.** Interestingly, $C_{2z}T$ symmetry is locally broken every where except for $\boldsymbol{R} = \boldsymbol{0}$, but is globally restored in the effective model. It acts on the local models as $C_{2z}T = \sigma_x K$ where K is the complex conjugation. The $C_{2z}T$ symmetry in the effective model is valid by satisfying the criterion of Eq. (3.66), i.e.

$$\sigma_x K \boldsymbol{\sigma} \cdot \boldsymbol{\nabla}_{-\boldsymbol{R}} \circ K \sigma_x = \boldsymbol{\sigma} \cdot \boldsymbol{\nabla}_{\boldsymbol{R}} \circ . \tag{3.73}$$

We demonstrated the detailed computation of $C_{2z}T$ symmetry for the effective model in Appendix C.5.

3.6 Computation of $|\boldsymbol{\nabla}_{\boldsymbol{R}} \psi(\boldsymbol{R})\rangle$ with gauge

In order to numerically solve effective model, all matrix elements must be computed with gauge-fixed local states. The calculation of the kinetic energy term $-i\boldsymbol{\Gamma}_(\boldsymbol{R}) \cdot \boldsymbol{\nabla}_{\boldsymbol{R}}$ and the onsite potential $E(\boldsymbol{R})$ are direct with gauge-fixed states. It then remains to derive the gauge-fixed local states with respect to $\boldsymbol{R}$ to calculate the non-Abelian gauge field $A(\boldsymbol{R})$.

3.6.1 Gauge independent contribution from perturbation theory

First we review the text-book computation of $|\boldsymbol{\nabla}_{\boldsymbol{R}} \psi(\boldsymbol{R})\rangle$ from the perturbation theory. We can always suppose that we are working under a specific gauge so that all gauge-fixed states are the eigenstates of the local Hamiltonians. The passage to other desired gauge

choice can be achieved by an additional unitary transform on the effective model, as has been discussed in the gauge-invariance of the effective model. Throughout this section, we will implicitly adopt such a gauge choice to facilitate the demonstration. To simplify the analysis, we can initially ignore the degeneracy without loss of generality.

Let's suppose we have a local state described by the equation:

$$\hat{H}_{\text{local}}(\boldsymbol{R})\left|\psi_n(\boldsymbol{R})\right\rangle = E_n(\boldsymbol{R})\left|\psi_n(\boldsymbol{R})\right\rangle,$$

where n represents the state index. Applying $\boldsymbol{\nabla}_{\boldsymbol{R}}$ to both sides of the equation yields:

$$\boldsymbol{\nabla}_{\boldsymbol{R}}\hat{H}_{\text{local}}(\boldsymbol{R})\left|\psi_n(\boldsymbol{R})\right\rangle+\hat{H}_{\text{local}}(\boldsymbol{R})\left|\boldsymbol{\nabla}_{\boldsymbol{R}}\psi_n(\boldsymbol{R})\right\rangle = \boldsymbol{\nabla}_{\boldsymbol{R}}E_n(\boldsymbol{R})\left|\psi_n(\boldsymbol{R})\right\rangle+E_n(\boldsymbol{R})\left|\boldsymbol{\nabla}_{\boldsymbol{R}}\psi_n(\boldsymbol{R})\right\rangle. \tag{3.74}$$

Taking the inner product with $\langle\psi_m(\boldsymbol{R})|$, where $m \neq n$, on both sides of the equation above, we obtain:

$$\langle\psi_m(\boldsymbol{R})|\nabla_{\boldsymbol{R}}\hat{H}_{\text{local}}(\boldsymbol{R})|\psi_n(\boldsymbol{R})\rangle+E_m(\boldsymbol{R})\left\langle\psi_m(\boldsymbol{R})\middle|\boldsymbol{\nabla}_{\boldsymbol{R}}\psi_n(\boldsymbol{R})\right\rangle = E_n(\boldsymbol{R})\left\langle\psi_m(\boldsymbol{R})\middle|\boldsymbol{\nabla}_{\boldsymbol{R}}\psi_n(\boldsymbol{R})\right\rangle. \tag{3.75}$$

Simplifying further, we find:

$$\left\langle\psi_m(\boldsymbol{R})\middle|\boldsymbol{\nabla}_{\boldsymbol{R}}\psi_n(\boldsymbol{R})\right\rangle = \frac{\left|\psi_m(\boldsymbol{R})\right\rangle\left\langle\psi_m(\boldsymbol{R})\right|\boldsymbol{\nabla}_{\boldsymbol{R}}\hat{H}_{\text{local}}(\boldsymbol{R})\left|\psi_n(\boldsymbol{R})\right\rangle}{E_n(\boldsymbol{R})-E_m(\boldsymbol{R})}. \tag{3.76}$$

According to perturbation theory, we consider only the contributions to $|\boldsymbol{\nabla}_{\boldsymbol{R}}\psi_n(\boldsymbol{R})\rangle$ that are orthogonal to $|\psi_n(\boldsymbol{R})\rangle$, and we can write:

$$\left|\boldsymbol{\nabla}_{\boldsymbol{R}}\psi_n(\boldsymbol{R})\right\rangle = \sum_{m\neq n}\frac{\left|\psi_m(\boldsymbol{R})\right\rangle\left\langle\psi_m(\boldsymbol{R})\right|\boldsymbol{\nabla}_{\boldsymbol{R}}\hat{H}_{\text{local}}(\boldsymbol{R})\left|\psi_n(\boldsymbol{R})\right\rangle}{E_n(\boldsymbol{R})-E_m(\boldsymbol{R})}. \tag{3.77}$$

This formula leads to $\langle\psi_n(\boldsymbol{R})|\boldsymbol{\nabla}_{\boldsymbol{R}}\psi_n(\boldsymbol{R})\rangle = \mathbf{0}$.

It is important to note that the operator:

$$\sum_{m\neq n}\frac{\left|\psi_m(\boldsymbol{R})\right\rangle\left\langle\psi_m(\boldsymbol{R})\right|\boldsymbol{\nabla}_{\boldsymbol{R}}\hat{H}_{\text{local}}(\boldsymbol{R})}{E_n(\boldsymbol{R})-E_m(\boldsymbol{R})}$$

in Eq. (3.77) is gauge-invariant. Therefore, the contribution to $|\boldsymbol{\nabla}_{\boldsymbol{R}}\psi_n(\boldsymbol{R})\rangle$ for an arbitrary state $|\psi_n(\boldsymbol{R})\rangle$ calculated using Eq.(3.77) is independent of the gauge choice for the states $|\psi_m(\boldsymbol{R})\rangle$.

Consequently, the value of $\langle g_n|\boldsymbol{\nabla}_{\boldsymbol{R}}\psi_n(\boldsymbol{R})\rangle$, where $|g_n\rangle$ is the reference state used for

gauge-fixing, is predetermined once $|g_n\rangle$ and $|\psi_n(\boldsymbol{R})\rangle$ are chosen. The value is a priori a complex number and not necessarily real and positive. This leads to contradiction with $\langle g_n|\boldsymbol{\psi}_n(\boldsymbol{R})\rangle \in \mathbb{R}^+$, which imposes

$$\boldsymbol{\nabla}_{\boldsymbol{R}} \langle g_n|\boldsymbol{\psi}_n(\boldsymbol{R})\rangle = \langle g_n|\boldsymbol{\nabla}_{\boldsymbol{R}}\psi_n(\boldsymbol{R})\rangle \in \mathbb{R}^+. \tag{3.78}$$

To obtain a derivative of states respecting the gauge-fixing conditions, a missing puzzle must be added back to the calculation of $|\boldsymbol{\nabla}_{\boldsymbol{R}}\psi_n(\boldsymbol{R})\rangle$.

3.6.2 Gauge-dependent contribution

To obtain the derivative of states respecting the gauge-fixing conditions, we need to consider the missing puzzle, which is the contribution along $|\psi_n(\boldsymbol{R})\rangle$ that was initially ignored in the perturbation theory formalism. We start by writing the expression for $|\boldsymbol{\nabla}_{\boldsymbol{R}}\psi_n(\boldsymbol{R})\rangle$ as follows:

$$\begin{aligned}
&|\boldsymbol{\nabla}_{\boldsymbol{R}}\psi_n(\boldsymbol{R})\rangle = \mathbb{1}\,|\boldsymbol{\nabla}_{\boldsymbol{R}}\psi_n(\boldsymbol{R})\rangle \\
&= \sum_{m\neq n} |\psi_m(\boldsymbol{R})\rangle\langle\psi_m(\boldsymbol{R})|\,\boldsymbol{\nabla}_{\boldsymbol{R}}\psi_n(\boldsymbol{R})\rangle + |\psi_n(\boldsymbol{R})\rangle\langle\psi_n(\boldsymbol{R})|\,\boldsymbol{\nabla}_{\boldsymbol{R}}\psi_n(\boldsymbol{R})\rangle \\
&= |\psi_n(\boldsymbol{R})\rangle\,\langle\psi_n(\boldsymbol{R})|\boldsymbol{\nabla}_{\boldsymbol{R}}\psi_n(\boldsymbol{R})\rangle + \sum_{m\neq n} \frac{|\psi_m(\boldsymbol{R})\rangle\langle\psi_m(\boldsymbol{R})|\,\boldsymbol{\nabla}_{\boldsymbol{R}}\hat{H}_{\text{local}}(\boldsymbol{R})\,|\psi_n(\boldsymbol{R})\rangle}{E_n(\boldsymbol{R}) - E_m(\boldsymbol{R})}.
\end{aligned} \tag{3.79}$$

To determine the value of the Berry connection $\langle\psi_n(\boldsymbol{R})|\boldsymbol{\nabla}_{\boldsymbol{R}}\psi_n(\boldsymbol{R})\rangle$, we attempt to apply $\langle\psi_n(\boldsymbol{R})|$ to both sides of Eq. (3.74). However, in this case, the Berry connection term cancels out, and we are left with:

$$\boldsymbol{\nabla}_{\boldsymbol{R}} E_n(\boldsymbol{R}) = \langle\psi_n(\boldsymbol{R})|\boldsymbol{\nabla}_{\boldsymbol{R}}\hat{H}_{\text{local}}(\boldsymbol{R})|\psi_n(\boldsymbol{R})\rangle\,. \tag{3.80}$$

This implies the Berry connection is purely a gauge-dependent term, which needs to be deduced from the gauge-fixing condition. By considering the gauge-fixing condition $\langle g_n|\boldsymbol{\nabla}_{\boldsymbol{R}}\psi_n(\boldsymbol{R})\rangle \in \mathbb{R}^+$, we find that

$$\begin{aligned}
&\langle g_n|\boldsymbol{\nabla}_{\boldsymbol{R}}\psi_n(\boldsymbol{R})\rangle \\
&= \langle g_n|\psi_n(\boldsymbol{R})\rangle\,\langle\psi_n(\boldsymbol{R})|\boldsymbol{\nabla}_{\boldsymbol{R}}\psi_n(\boldsymbol{R})\rangle + \sum_{m\neq n} \frac{\langle g_n\,|\psi_m(\boldsymbol{R})\rangle\langle\psi_m(\boldsymbol{R})|\,\boldsymbol{\nabla}_{\boldsymbol{R}}\hat{H}_{\text{local}}(\boldsymbol{R})\,|\psi_n(\boldsymbol{R})\rangle}{E_n(\boldsymbol{R}) - E_m(\boldsymbol{R})} \in \mathbb{R}^+.
\end{aligned} \tag{3.81}$$

For $\langle g_n|\boldsymbol{\nabla}_{\boldsymbol{R}}\psi_n(\boldsymbol{R})\rangle$ to be real and positive, its imaginary part must be zero. Given that the Berry connection term, $\langle\psi_n(\boldsymbol{R})|\boldsymbol{\nabla}_{\boldsymbol{R}}\psi_n(\boldsymbol{R})\rangle$, is purely imaginary, while $\langle g_n|\boldsymbol{\nabla}_{\boldsymbol{R}}\psi_n(\boldsymbol{R})\rangle$ is a positive real number guaranteed by gague fixing, we have

$$\begin{aligned}
&\mathrm{Im}\left\{\langle g_n|\boldsymbol{\nabla}_{\boldsymbol{R}}\psi_n(\boldsymbol{R})\rangle\right\} \\
&= -i\,\langle g_n|\psi_n(\boldsymbol{R})\rangle\,\langle\psi_n(\boldsymbol{R})|\boldsymbol{\nabla}_{\boldsymbol{R}}\psi_n(\boldsymbol{R})\rangle + \mathrm{Im}\left\{\sum_{m\neq n}\frac{\langle g_n\,|\psi_m(\boldsymbol{R})\rangle\langle\psi_m(\boldsymbol{R})|\,\boldsymbol{\nabla}_{\boldsymbol{R}}\hat{H}_{\text{local}}(\boldsymbol{R})\,|\psi_n(\boldsymbol{R})\rangle}{E_n(\boldsymbol{R})-E_m(\boldsymbol{R})}\right\} \\
&= 0
\end{aligned} \tag{3.82}$$

$$\langle\psi_n(\boldsymbol{R})|\boldsymbol{\nabla}_{\boldsymbol{R}}\psi_n(\boldsymbol{R})\rangle = -\frac{i}{\langle g_n|\psi_n(\boldsymbol{R})\rangle}\mathrm{Im}\left\{\sum_{m\neq n}\frac{\langle g_n\,|\psi_m(\boldsymbol{R})\rangle\langle\psi_m(\boldsymbol{R})|\,\boldsymbol{\nabla}_{\boldsymbol{R}}\hat{H}_{\text{local}}(\boldsymbol{R})\,|\psi_n(\boldsymbol{R})\rangle}{E_n(\boldsymbol{R})-E_m(\boldsymbol{R})}\right\}, \tag{3.83}$$

which allows for the computation of Berry connections everywhere with gauge-fixed states. Let us denote the Berry connection $\boldsymbol{A}_n(\boldsymbol{R}) = \langle\psi_n(\boldsymbol{R})|\boldsymbol{\nabla}_{\boldsymbol{R}}\psi_n(\boldsymbol{R})\rangle$, then the derivative of a state that respects the gauge-fixing condition is given by

$$|\boldsymbol{\nabla}_{\boldsymbol{R}}\psi_n(\boldsymbol{R})\rangle = \boldsymbol{A}_n(\boldsymbol{R})\,|\psi_n(\boldsymbol{R})\rangle + \sum_{m\neq n}\frac{\langle\psi_m(\boldsymbol{R})|\boldsymbol{\nabla}_{\boldsymbol{R}}\hat{H}_{\text{local}}(\boldsymbol{R})|\psi_n(\boldsymbol{R})\rangle}{E_n(\boldsymbol{R})-E_m(\boldsymbol{R})}\,|\psi_m(\boldsymbol{R})\rangle\,. \tag{3.84}$$

3.7 Effective model on the reciprocal lattice

Having obtained all the matrix elements of the effective Hamiltonian, we can now proceed with solving the effective model. In Chapter 3.5.1, the form of the Bloch functions for the effective Hamiltonian was established. However, it is important to note that although the effective Hamiltonian possesses a gauge-invariant spectrum, different gauge choices can introduce different challenges in obtaining solutions.

By carefully selecting the gauge-fixing operator and the reference states, it is possible to simplify the expression of the wave function. This can be achieved by ensuring that the transformation operator $\mathcal{T}(\boldsymbol{R})$ becomes a diagonal matrix with straightforward diagonal entries that can be easily determined.

To proceed with the solution of the effective model, we utilize Bloch's theorem by substituting the wave function given in Eq. (C.33) into the Schrödinger's equation of the effective Hamiltonian. This yields the equation:

$$[\boldsymbol{\Gamma}(\boldsymbol{R})\cdot(\boldsymbol{k}-i\boldsymbol{\nabla}_{\boldsymbol{R}}) + A(\boldsymbol{R}) + E(\boldsymbol{R})]\mathcal{T}(\boldsymbol{R})\boldsymbol{f}_{\boldsymbol{k}}(\boldsymbol{R}) = \mathcal{E}_{\boldsymbol{k}}\mathcal{T}(\boldsymbol{R})\boldsymbol{f}_{\boldsymbol{k}}(\boldsymbol{R}), \tag{3.85}$$

where $\boldsymbol{k}$ represents a wave vector within the supermoiré Brillouin zone. Here, we omit the band index of the effective spectrum for clarity of notation. Since $\mathcal{T}(\boldsymbol{R})$ is a unitary operator, applying $\mathcal{T}^\dagger(\boldsymbol{R})$ from the left on both sides of the equation gives:

$$\tilde{H}^{\text{eff}}_{\boldsymbol{k}}(\boldsymbol{R})\boldsymbol{f}_{\boldsymbol{k}}(\boldsymbol{R}) = \mathcal{E}_{\boldsymbol{k}}\boldsymbol{f}_{\boldsymbol{k}}(\boldsymbol{R}), \tag{3.86}$$

where

$$\tilde{H}^{\text{eff}}_{\boldsymbol{k}}(\boldsymbol{R}) = \mathcal{T}^\dagger(\boldsymbol{R})[\boldsymbol{\Gamma}(\boldsymbol{R})\cdot(\boldsymbol{k} - i\boldsymbol{\nabla}_{\boldsymbol{R}}) + A(\boldsymbol{R}) + E(\boldsymbol{R})]\mathcal{T}(\boldsymbol{R}). \tag{3.87}$$

$\tilde{H}^{\text{eff}}_{\boldsymbol{k}}(\boldsymbol{R})$ is a perfectly periodic Hamiltonian satisfying $\tilde{H}^{\text{eff}}_{\boldsymbol{k}}(\boldsymbol{R} + \boldsymbol{a}^{MM}_{1/2}) = \tilde{H}^{\text{eff}}_{\boldsymbol{k}}(\boldsymbol{R})$ for *arbitrary* choice of gauge. In practice, numerical solutions are typically obtained by working with the Fourier-transformed Hamiltonian, whose matrix elements are given by:

$$\tilde{H}^{\text{eff}}_{\boldsymbol{k}}(\boldsymbol{Q}, \boldsymbol{Q}') = \int \frac{\mathrm{d}\boldsymbol{R}^2}{S} e^{i\boldsymbol{Q}\cdot\boldsymbol{R}} \tilde{H}^{\text{eff}}_{\boldsymbol{k}}(\boldsymbol{R}) e^{-i\boldsymbol{Q}'\cdot\boldsymbol{R}}. \tag{3.88}$$

where the Fourier transform must be computed for each term in

- $\mathcal{T}^\dagger(\boldsymbol{R})\boldsymbol{\Gamma}(\boldsymbol{R})\mathcal{T}(\boldsymbol{R})$,
- $\mathcal{T}^\dagger(\boldsymbol{R})(-i\boldsymbol{\nabla}_{\boldsymbol{R}}\mathcal{T}(\boldsymbol{R}))$,
- $\mathcal{T}^\dagger(\boldsymbol{R})A(\boldsymbol{R})\mathcal{T}(\boldsymbol{R})$;
- $\mathcal{T}^\dagger(\boldsymbol{R})E(\boldsymbol{R})\mathcal{T}(\boldsymbol{R})$.

Now, let's consider the situation where the gauge is appropriately chosen so that $\mathcal{T}(\boldsymbol{R})$ becomes a diagonal matrix, as shown in Eq. (C.39). This choice of gauge significantly reduces the computational cost of obtaining the matrix elements of $\tilde{H}^{\text{eff}}_{\boldsymbol{k}}(\boldsymbol{R})$. It is important to recall that the indices n and m denotes the band indices of the local solutions at the $\boldsymbol{\Gamma}$, $\boldsymbol{K}$ or $\boldsymbol{K}'$ point of the local moiré Brillouin zone.

$$[\mathcal{T}^\dagger(\boldsymbol{R})(-i\boldsymbol{\nabla}_{\boldsymbol{R}}\mathcal{T}(\boldsymbol{R}))]_{nm} = \boldsymbol{p}_n\delta_{nm} - i\boldsymbol{\nabla}_{\boldsymbol{R}}. \tag{3.89}$$

For the other terms, we have

$$\tilde{\boldsymbol{\Gamma}}_{nm}(\boldsymbol{R}) = \sum_{n'm'} \mathcal{T}^\dagger_{nn'}(\boldsymbol{R})\boldsymbol{\Gamma}_{n'm'}(\boldsymbol{R})\mathcal{T}_{m'm}(\boldsymbol{R}) = e^{-i(\boldsymbol{p}_n - \boldsymbol{p}_m)\cdot\boldsymbol{R}}\boldsymbol{\Gamma}_{nm}(\boldsymbol{R}), \tag{3.90}$$

$$\tilde{A}_{nm}(\boldsymbol{R}) = \sum_{n'm'} \mathcal{T}^\dagger_{nn'}(\boldsymbol{R})A_{n'm'}(\boldsymbol{R})\mathcal{T}_{m'm}(\boldsymbol{R}) = e^{-i(\boldsymbol{p}_n - \boldsymbol{p}_m)\cdot\boldsymbol{R}}A_{nm}(\boldsymbol{R}), \tag{3.91}$$

and

$$\tilde{E}_{nm}(\boldsymbol{R}) = \sum_{n'm'} \mathcal{T}^{\dagger}_{nn'}(\boldsymbol{R}) E_{n'm'}(\boldsymbol{R}) \mathcal{T}_{m'm}(\boldsymbol{R}) = e^{-i(\boldsymbol{p}_n - \boldsymbol{p}_m)\cdot \boldsymbol{R}} E_{nm}(\boldsymbol{R}). \tag{3.92}$$

The effective Schrödinger's equation is now written as:

$$\sum_m \tilde{H}^{\text{eff}}_{\boldsymbol{k},nm}(\boldsymbol{R}) f_m(\boldsymbol{R}) = \mathcal{E} f_n(\boldsymbol{R}). \tag{3.93}$$

The matrix elements of the transformed effective Hamiltonian are given by

$$\tilde{H}^{\text{eff}}_{\boldsymbol{k},nm}(\boldsymbol{R}) = \tilde{\boldsymbol{\Gamma}}_{nm}(\boldsymbol{R}) \cdot (\boldsymbol{k} + \boldsymbol{p}_n \delta_{nm} - i\boldsymbol{\nabla}_{\boldsymbol{R}}) + \tilde{A}_{nm}(\boldsymbol{R}) + \tilde{E}_{nm}(\boldsymbol{R}). \tag{3.94}$$

where every term in the Hamiltonian is periodic on the supermoiré lattice. Therefore, they can be expanded in Fourier series:

$$\tilde{\boldsymbol{\Gamma}}_{nm}(\boldsymbol{R}) = \sum_{\boldsymbol{Q} \in \text{SRL}} \tilde{\boldsymbol{\Gamma}}_{nm}(\boldsymbol{Q}) e^{i\boldsymbol{Q}\cdot\boldsymbol{R}}, \tag{3.95}$$

$$\tilde{A}_{nm}(\boldsymbol{R}) = \sum_{\boldsymbol{Q} \in \text{SRL}} \tilde{A}_{nm}(\boldsymbol{Q}) e^{i\boldsymbol{Q}\cdot\boldsymbol{R}}, \tag{3.96}$$

and

$$\tilde{E}_{nm}(\boldsymbol{R}) = \sum_{\boldsymbol{Q} \in \text{SRL}} \tilde{E}_{nm}(\boldsymbol{Q}) e^{i\boldsymbol{Q}\cdot\boldsymbol{R}}. \tag{3.97}$$

The periodic effective Hamiltonian defined on the supermoiré reciprocal lattice (SRL) is given by:

$$\begin{aligned} &\tilde{H}^{\text{eff}}_{\boldsymbol{k},nm}(\boldsymbol{Q}_1, \boldsymbol{Q}_2) \\ &= \sum_{\boldsymbol{Q} \in \text{SRL}} \delta_{\boldsymbol{Q}_1 + \boldsymbol{Q}, \boldsymbol{Q}_2} \left(\tilde{\boldsymbol{\Gamma}}_{nm}(\boldsymbol{Q}) \cdot (\boldsymbol{k} + \boldsymbol{p}_n \delta_{nm} - \boldsymbol{Q}_2) + \tilde{A}_{nm}(\boldsymbol{Q}) + \tilde{E}_{nm}(\boldsymbol{Q}) \right). \end{aligned} \tag{3.98}$$

To numerically solve Eq. (3.98), we need to specify two cutoffs. First, we require a cutoff for $\boldsymbol{Q}_1$ and $\boldsymbol{Q}_2$ to limit the total number of Fourier components of the wave function and thereby restrict the dimension of the Hamiltonian matrix. Since the effective model is periodic, the fast convergence can be achieved this cutoff increases.

The second cutoff is applied to $\boldsymbol{Q}$ to limit the number of Fourier components in the Hamiltonian itself. This cutoff determines the maximum distance between two momenta whose coupling is considered in the calculation. As will be shown in the subsequent chapter, a small radius for the second cutoff is enough to achieve convergence.

3.8 Effective model at low energy in the supermoiré scale

The indices n and m in Eq. (3.98) go through all the bands of the local models. Now we consider to limit the number of local bands taken into consideration because we are interested in finding the band structure corresponding to the supermoiré energy scale.

We can first obtain an intuition of the different orders of magnitude of the energy levels in the moiré and the supermoiré scale. The typical moiré energy is expressed as $E_{\text{moiré}} \sim \hbar v_F |\boldsymbol{q}|$, compared to the typical supermoiré energy $E_{\text{supermoiré}} \sim \hbar v_F |\delta \boldsymbol{q}|$. We can make a rough estimation with the twist angles $\theta_1 = \theta_2 = \theta = 2^\circ \equiv 0.035$ Rad. Since $|\boldsymbol{q}| = |\boldsymbol{K}_G|\theta$ and $|\delta \boldsymbol{q}| = |\boldsymbol{K}|\theta^2$ where $\boldsymbol{K}_G$ is the wave vector at the $\boldsymbol{K}$ point of the graphene Billouin zone, it is evident that

$$\frac{E_{\text{supermoiré}}}{E_{\text{moiré}}} = \theta = 0.035. \tag{3.99}$$

Taking $\hbar v_F |\boldsymbol{K}_G| = 9.905$ eV as a reference, we find that the typical energy scale associated with the supermoiré scale is an order of magnitude smaller than that of the moiré energy:

$$E_{\text{moiré}} \sim \hbar v_F |\boldsymbol{K}_G| \theta \sim 10^2 \text{ meV}, \tag{3.100}$$

and

$$E_{\text{supermoiré}} \sim \hbar v_F |\boldsymbol{K}_G| \theta^2 \sim 10 \text{ meV}. \tag{3.101}$$

This indicates that the energy separation between bands within the moiré Brillouin zone is much larger than the energy separation between bands within the supermoiré Brillouin zone.

Therefore, if we are primarily interested in the band structure associated with the supermoiré energy scale, we can limit the number of local bands taken into consideration. This can simplify the calculation and reduce the computational cost, as we only need to focus on a subset of bands relevant to the supermoiré physics. The specific number of bands to include will depend on the specific system and the desired level of accuracy in the calculation.

The band structures of the local Hamiltonians presented in Chapter 2 reveal that the majority of local eigenstates reside at energy levels that are significantly different from the typical supermoiré energy, with the exception of states near the zero energy level. These low-energy local states are predominantly concentrated around the $\boldsymbol{\Gamma}$, $\boldsymbol{K}$, and $\boldsymbol{K}'$ points of the local moiré Brillouin zone. The main contribution to the effective model arises from

these low-energy local states. This can be observed by reformulating Eq. (3.35) as follows:

$$f_n(\boldsymbol{R}) = \frac{1}{\mathcal{E} - E_n(\boldsymbol{R})} \sum_m \left(-i\boldsymbol{\Gamma}_{nm}(\boldsymbol{R}) \cdot \boldsymbol{\nabla}_{\boldsymbol{R}} f_m(\boldsymbol{R}) + A_{nm}(\boldsymbol{R}) f_m((\boldsymbol{R}))\right) \tag{3.102}$$

The wave function of the effective model is predominantly composed of components associated with the local states whose energies are closest to $\mathcal{E}$.

This enables us to significantly reduce the number of local bands involved in the effective model. In the case where $\theta_1/\theta_2 \sim 1$, two zero-energy states remain pinned at the $\boldsymbol{\Gamma}$ point. The Dirac point at the $\boldsymbol{K}$ (or $\boldsymbol{K}'$) point is only slightly gapped out when the C_{3z} symmetry is broken. Therefore, we can construct an effective model by considering the two lowest-energy states at either the local $\boldsymbol{\Gamma}$ or $\boldsymbol{K}$ point, resulting in a two-band effective model for each pair of local states.

The situation is slightly different when $\theta_1/\theta_2 \sim 1/2$. At the local $\boldsymbol{\Gamma}$ point, the Dirac point can be slightly gapped out due to the absence of particle-hole symmetry (PHS) for any $\boldsymbol{R}$. At the local $\boldsymbol{K}$ point, all four lowest-energy states need to be considered in the effective model. On the other hand, at the $\boldsymbol{K}'$ point, a large gap separates the two lowest-energy bands when the twist angles are not extremely small. Therefore, for the case of $\theta_1/\theta_2 \sim 1/2$, we can establish a two-band model based on the local $\boldsymbol{\Gamma}$ states, but we need to work with a four-band effective model based on the local $\boldsymbol{K}$ states.

The numerical solutions will be presented in the following chapter.

3.9 Summary

In this chapter, we have developed a theoretical framework for studying staircase twisted trilayer graphene (TTG) with twist angle ratios that are close to rational numbers. By decomposing the two sets of moiré vectors, we can separate the "fast" variation occurring at the moiré scale, comparable to the periodicity of TBG, from the "slow" variation occurring at the supermoiré scale, which spans even longer distances than the size of a moiré unit cell. This allows us to view the exact TTG model as a moiré TTG model modulated by a slowly varying phase factor. Consequently, the approximate TTG models we solved in the previous chapter can now be regarded as "local" models, under the assumption that the slow phase factor remains almost constant within the moiré unit cell. The results obtained in Chapter 2, with different phase factors, are equivalent to local solutions of the exact model. However, these local solutions have been obtained independently from each other. The motivation behind developing the effective theory is to address the following questions:

Can we characterize the global physical properties of TTG by taking the direct sum or average of the local solutions? If not, what changes if we find a solution at the supermoiré scale that not only locally resembles the local solutions but also reveals new features across the supermoiré length scale?

To tackle these questions, we revisited the formalism of the $\boldsymbol{k} \cdot \boldsymbol{p}$ method and were inspired to propose a carefully designed ansatz as the eigenfunction of the *exact* TTG model. The ansatz functions involve a linear combination of local functions decorated by a modulation function. The modulation function is intentionally chosen to be slowly varying at the supermoiré scale and nearly constant within the moiré scale. By substituting the ansatz wave function into the Schrödinger's equation of the exact Hamiltonian and integrating over the moiré unit cell, we obtained a new eigenvalue equation that only involves the modulation functions.

In order to handle the effective model, the gauge-fixing procedure is an essential prerequisite. This step is crucial for obtaining smooth and continuous matrix elements of the effective Hamiltonian as functions of the supermoiré coordinates $\boldsymbol{R}$. It should be noted that the expressions of the effective model will depend on the choice of gauge. However, the physical properties computed from the effective model are gauge invariant, as they should be. Using gauge-fixed states makes the calculation of $\boldsymbol{\nabla}_{\boldsymbol{R}} |\psi_n(\boldsymbol{R})\rangle$ more complicated compared to using perturbation theory directly. We have also developed the theory for computing $\boldsymbol{\nabla}_{\boldsymbol{R}} |\psi_n(\boldsymbol{R})\rangle$ for gauge-fixed states, which also provides a method for calculating the Berry connection using these gauge-fixed states.

Additionally, we have demonstrated various symmetries encoded in the effective model, which are closely related to the transformations of the local states under symmetry operations. We have confirmed that the effective model exhibits symmetries that are fully consistent with the exact model. The locally broken symmetries, namely $C_{2z}T$ and C_{3z}, are globally restored in the effective model. The particle-hole symmetry, which is absent in the exact model, appears as an auxiliary symmetry in the local models but is again broken in the effective model. Even when particle-hole symmetry is present in the local models everywhere for $\theta_1 \sim \theta_2$, it is still broken in the effective model. The presence of C_{2x} requires the twist angles to be strictly equal, which holds true both in the exact model and in the effective model.

Finally, we have shown that the effective model can be further simplified by considering only the local states near the zero energy level, as they make the major contribution to the effective model when focusing on the typical supermoiré energy scale.

Thus, we have conducted a thorough analysis of the effective model and established a

comprehensive toolbox for solving it. In the following chapter, we will present the numerical results obtained from the effective model.

Chapter 4

Numerical solutions of low-energy supermoiré effective models

In this chapter, we focus on numerically solving the effective model, primarily considering twist angle ratios close to 1 and $1/2$. We start by computing the matrix elements of the effective model on a discretized real-space grid within a supermoiré unit cell (SMUC). The grid points are defined as

$$\boldsymbol{R} \to \boldsymbol{R}_{i,j} = \frac{i}{N_1}\boldsymbol{a}_1^{MM} + \frac{j}{N_2}\boldsymbol{a}_2^{MM}, \tag{4.1}$$

where i and j range from 0 to $N-1$. Here, $\boldsymbol{a}_1^{MM}$ and $\boldsymbol{a}_2^{MM}$ are the generating vectors of the supermoiré Bravais lattice, and N_1 and N_2 represent the number of discrete points within a SMUC along $\boldsymbol{a}_1^{MM}$ and $\boldsymbol{a}_2^{MM}$, respectively. In practice, we usually choose $N_1 = N_2 = N$.

For any periodic function defined on the supermoiré lattice, expressed as $g(\boldsymbol{R}_{i,j}) = \sum_{\boldsymbol{Q}} \mathcal{G}(\boldsymbol{Q}) e^{i\boldsymbol{Q}\cdot\boldsymbol{R}_{i,j}}$, we compute its Fourier coefficients $\mathcal{G}(\boldsymbol{Q})$ using discrete Fourier transform. The calculation is given by:

$$\mathcal{G}(\boldsymbol{Q}) = \frac{1}{N^2}\sum_{i=1}^{N}\sum_{j=1}^{N} g(\boldsymbol{R}_{i,j}) e^{-i\boldsymbol{Q}\cdot\boldsymbol{R}_{i,j}}, \tag{4.2}$$

where $\boldsymbol{Q}$ represents a vector on the reciprocal supermoiré lattice with n_1 and n_2 as integers, given by $\boldsymbol{Q} = n_1\boldsymbol{G}_1^{MM} + n_2\boldsymbol{G}_2^{MM}$. Here, $\boldsymbol{G}_{1/2}^{MM}$ denotes the generating vectors of the reciprocal supermoiré lattice, satisfying the condition $\boldsymbol{G}_i^{MM}\boldsymbol{a}_j^{MM} = 2\pi\delta_{ij}$.

Convention of notations. To maintain clarity in the notations, we will introduce a convention for distinguishing between points in the local moiré Brillouin zone and in the

supermoiré Brillouin zone. As previously mentioned, we consider low-energy supermoiré models associated with the local $\boldsymbol{\Gamma}$ states and $\boldsymbol{K}(\boldsymbol{K}')$ states near the zero-energy level.

To avoid confusion, we will use subscript "M" for the Brillouin zone points in the local *moiré* models. Specifically, we will denote them as $\boldsymbol{\Gamma}_M$, $\boldsymbol{K}_M$, and $\boldsymbol{K}'_M$, while the points within the supermoiré Brillouin zone will be denoted without subscript as $\boldsymbol{\Gamma}$, $\boldsymbol{K}$, and $\boldsymbol{K}'$. Consequently, we will refer to the effective model based on the $\boldsymbol{\Gamma}_M/\boldsymbol{K}_M$ states as the $\boldsymbol{\Gamma}_M/\boldsymbol{K}_M$ effective model.

Utilization of symmetrized operators. To solve the effective model numerically, we will utilize symmetrized operators, even though the Hermiticity of the effective Hamiltonian has already been established. The use of symmetrized Hermitian operators offers significant advantages, especially in the two-band effective model, where the Hermitian matrices can be decomposed into linear combinations of Pauli matrices with real coefficients. These coefficients not only facilitate the implementation of computational codes but also enhance the physical interpretation of the results.

Throughout this chapter, the notation $-i\boldsymbol{\Gamma}(\boldsymbol{R})\cdot\boldsymbol{\nabla}_{\boldsymbol{R}}\circ$ refers to

$$\frac{1}{2}\left(-i\boldsymbol{\Gamma}\left(\boldsymbol{R}\right)\cdot\boldsymbol{\nabla}_{\boldsymbol{R}}\circ+\left(-i\boldsymbol{\Gamma}\left(\boldsymbol{R}\right)\cdot\boldsymbol{\nabla}_{\boldsymbol{R}}\circ\right)^{\dagger}\right),$$

and $A(\boldsymbol{R})$ refers to

$$\frac{1}{2}\left(A\left(\boldsymbol{R}\right)+A^{\dagger}\left(\boldsymbol{R}\right)\right).$$

In the two band effective models developed in this chapter, any 2×2 hermitian matrix, M_H, can be expanded as :

$$M_H(\boldsymbol{R})=d_0(\boldsymbol{R})\sigma_0+d_x(\boldsymbol{R})\sigma_x+d_y(\boldsymbol{R})\sigma_y+d_z(\boldsymbol{R})\sigma_z\equiv d_0(\boldsymbol{R})\sigma_0+\boldsymbol{d}(\boldsymbol{R})\cdot\boldsymbol{\sigma},\qquad(4.3)$$

where $\boldsymbol{d}(\boldsymbol{R})=[d_x(\boldsymbol{R}),d_y(\boldsymbol{R}),d_z(\boldsymbol{R})]^T$ and $\boldsymbol{\sigma}=[\sigma_x,\sigma_y,\sigma_z]^T$. The Fourier components of each coefficient, denoted as $\mathcal{F}[d_i](\boldsymbol{Q})$, can be computed using Eq. (4.2).

4.1 Nearly equal twist angles

In this section, we present the numerical solutions for the effective models with equal twist angles of 2.2°. The construction of the effective model will be based on the $\boldsymbol{\Gamma}_M$ and $\boldsymbol{K}_M$ states separately. The model solved here has equal twist angles. For the case where the angles are nearly equal, the procedures are exactly identical.

4.1.1 $\mathbf{\Gamma}_M$ effective model

The $\mathbf{\Gamma}_M$ effective model is developed from the two constantly degenerate states at the Dirac point $\mathbf{\Gamma}_M$. Consequently, it is a two-band model. Due to the inherent particle-hole symmetry, which holds irrespective of the supermoiré coordinates, the two local $\mathbf{\Gamma}_M$ states are always pinned at zero energy. As a result, the $E(\boldsymbol{R})$ matrix in the effective model becomes zero.

To fix the gauge, we select the gauge-fixing operator as σ_z, which is the Pauli matrix defined solely on the *sublattice* degrees of freedom. Initially, we project σ_z onto the 2-dimensional subspace and determine the two eigenstates, denoted as $|\psi_A(\boldsymbol{R})\rangle$ and $|\psi_B(\boldsymbol{R})\rangle$, associated with the projected σ_z operator. These eigenstates exhibit sublattice polarization.

To fix the global phase, we choose two reference kets: $|\boldsymbol{Q}=\mathbf{0}, A, l=0\rangle$ and $|\boldsymbol{Q}=\mathbf{0}, B, l=0\rangle$. We impose the conditions that both $\langle \boldsymbol{Q}=\mathbf{0}, A, l=0|\psi_A(\boldsymbol{R})\rangle$ and $\langle \boldsymbol{Q}=\mathbf{0}, B, l=0|\psi_B(\boldsymbol{R})\rangle$ are real and positive.

With the chosen gauge, we observe that the effective Hamiltonian exhibits exact periodicity: $H_{\text{eff}}(\boldsymbol{R}+\boldsymbol{a}_{1/2}^{MM}) = H_{\text{eff}}(\boldsymbol{R})$. Recalling the relationship between the gauge-fixed states computed at $\boldsymbol{R}$ and $\boldsymbol{R}+\boldsymbol{a}_{1/2}^{MM}$, given by $\left|\psi_n(\boldsymbol{R}+\boldsymbol{a}_{1/2}^{MM})\right\rangle = S\sum_{m=A,B}|\psi_n(\boldsymbol{R})\rangle\,\zeta_{mn}$, where $n\in\{A,B\}$, S is described by Eq. (C.25), and it acts solely on the moiré coordinates and the layer indices. Notably, S commutes with σ_z. As a consequence, ζ becomes a diagonal matrix, since $S\,|\psi_n(\boldsymbol{R})\rangle$ is directly an eigenstate of the σ_z operator projected into the zero-energy space of the local model at $\boldsymbol{R}+\boldsymbol{a}_{1/2}^{MM}$. Thus, ζ merely compensates for the phase difference between $S\,|\psi A/B(\boldsymbol{R})\rangle$ and $\left|\psi_{A/B}(\boldsymbol{R}+\boldsymbol{a}_{1/2}^{MM})\right\rangle$. By selecting the aforementioned reference kets, the global phases are automatically fixed due to the condition:

$$\left\langle \boldsymbol{Q}=0, A/B, l=0\middle|Ue^{i\hat{\boldsymbol{k}}\cdot\boldsymbol{r}_0}\middle|\psi_{A/B}(\boldsymbol{R})\right\rangle = \left\langle \boldsymbol{Q}=0, A/B, l=0\middle|\psi_{A/B}(\boldsymbol{R})\right\rangle \in \mathbb{R}^+. \quad (4.4)$$

No compensating phase is required in the diagonal entries of ζ, resulting in

$$H_{\text{eff}}(\boldsymbol{R}+\boldsymbol{a}_{1/2}^{MM}) = \zeta^\dagger H_{\text{eff}}(\boldsymbol{R})\zeta = H_{\text{eff}}(\boldsymbol{R}). \quad (4.5)$$

In Figure 4.1, we present the matrix elements of the effective Hamiltonian evaluated within a supermoiré unit cell, considering both twist angles to be 2.2°. The data confirms that $H_{\text{eff}}(\boldsymbol{R})$ is a smooth and continuous function of $\boldsymbol{R}$. Furthermore, the periodicity of the effective Hamiltonian is verified. To facilitate comparison, the data in Figure 4.1 are

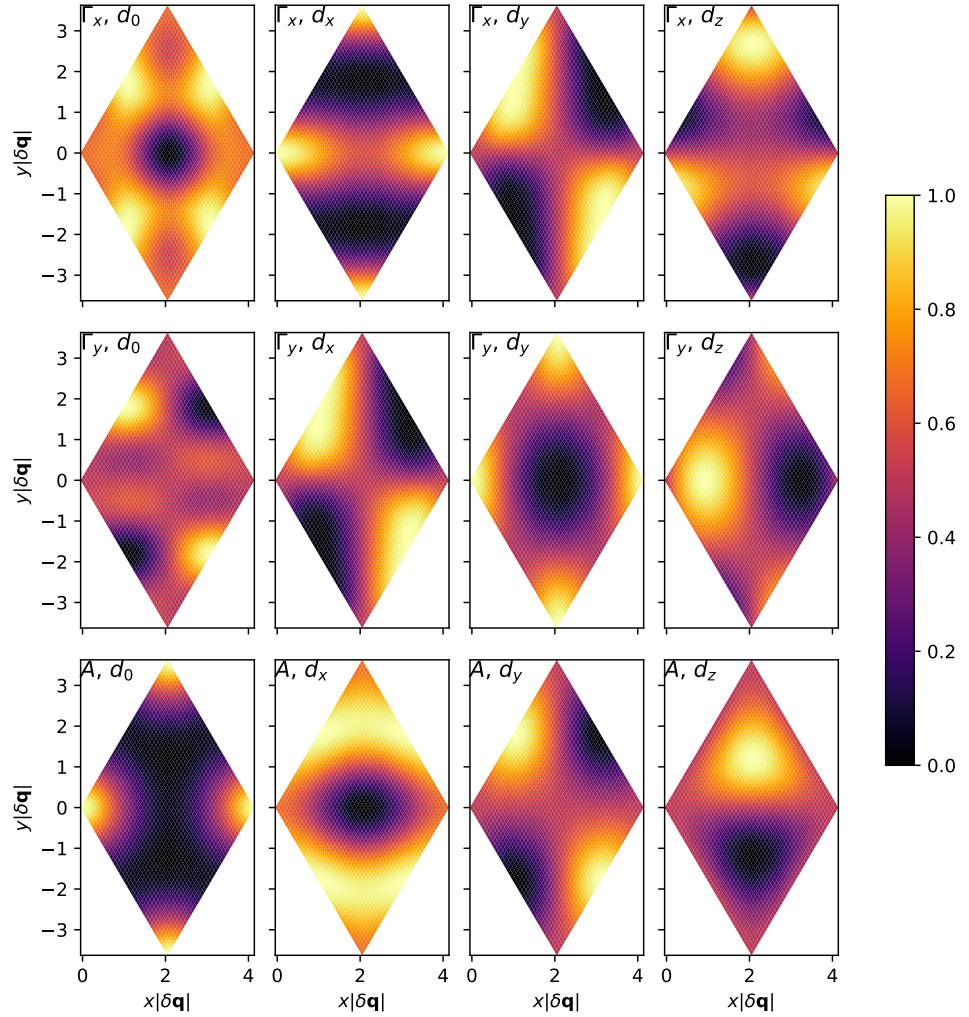

Figure 4.1: The matrix elements of the $\mathbf{\Gamma}_M$ effective model computed within a supermoiré unit cell for $\Gamma_x(\boldsymbol{R})$ (first row), $\Gamma_y(\boldsymbol{R})$ (second row) and $A(\boldsymbol{R})$ (third row), with the coefficients d_0, d_x, d_y and d_z arranged in the first, second, third and fourth columns, respectively. The variation of matrix elements is confirmed to be smooth and continuous. All matrix elements return to their original value after going over a supermoiré period. Data collected with $\theta_1 = \theta_2 = 2.2°$. To show more clearly the continuity and periodicity of each set of data within a supermoiré unit cell, the data in each subplot are normalized to the interval $[0, 1]$ using Eq. (4.6) so that the same color scale is employed for all color plots.

normalized using the transformation:

$$d_j(\boldsymbol{R}) \to \frac{d_j(\boldsymbol{R}) - \min(d_j)}{\max(d_j) - \min(d_j)}, \; j = 0, x, y, z, \tag{4.6}$$

ensuring that the values in each panel range between 0 and 1.

Figure 4.2 displays the Fourier coefficients of the data shown in Figure 4.1. It is clear from the plot that the dominant Fourier amplitudes are concentrated around the $\boldsymbol{Q} = \mathbf{0}$

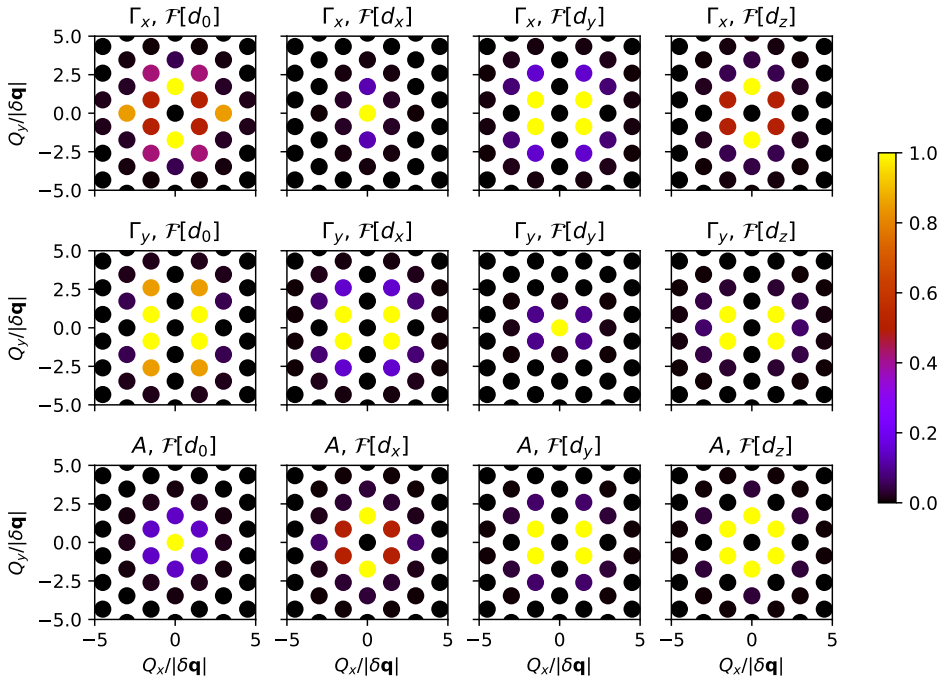

Figure 4.2: The absolute values of the Fourier coefficients of the data shown in Fig. 4.1. The arrangement of data in the panels corresponds to Fig. 4.1. The same normalization technique of data as in Fig. 4.1 is also performed on every set of data shwon in each subplot.

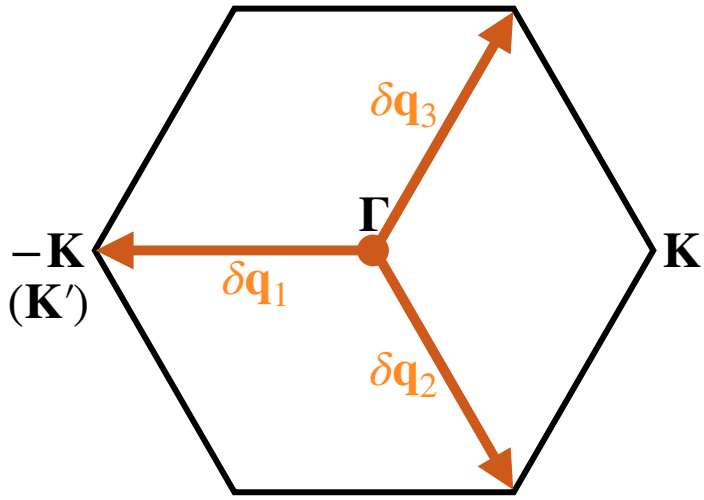

Figure 4.3: The supermoiré Brillouin zone. Band structure is calculated along the horizontal line $-\boldsymbol{K} - \boldsymbol{\Gamma} - \boldsymbol{K}$. The supermoiré vectors $\delta\boldsymbol{q}_j,\ j = 1, 2, 3$ are also shown.

component. As a result, we can safely choose a cutoff that is not excessively large for $\boldsymbol{Q}$ in Eq. (3.98). In practice, the cutoff for the Fourier components of the Hamiltonian was chosen as $3\sqrt{3}|\delta\boldsymbol{q}|$. This choice ensures that significant contributions from higher-order reciprocal lattice vectors are included while maintaining computational efficiency.

Once all the necessary data is prepared, the Hamiltonian matrix described in Eq. (3.98) can be constructed. The numerical diagonalization of this Hamiltonian matrix for each wave vector $\boldsymbol{k}$ within the supermoiré Brillouin zone enables the construction of the supermoiré band structure. In order to illustrate the band structure along a high symmetry line, we select the path $-\boldsymbol{K} - \boldsymbol{\Gamma} - \boldsymbol{K}$, as depicted in Fig. 4.3. This choice of path allows us to capture the key features of the band structure and identify any band crossings or gaps that may arise along this trajectory.

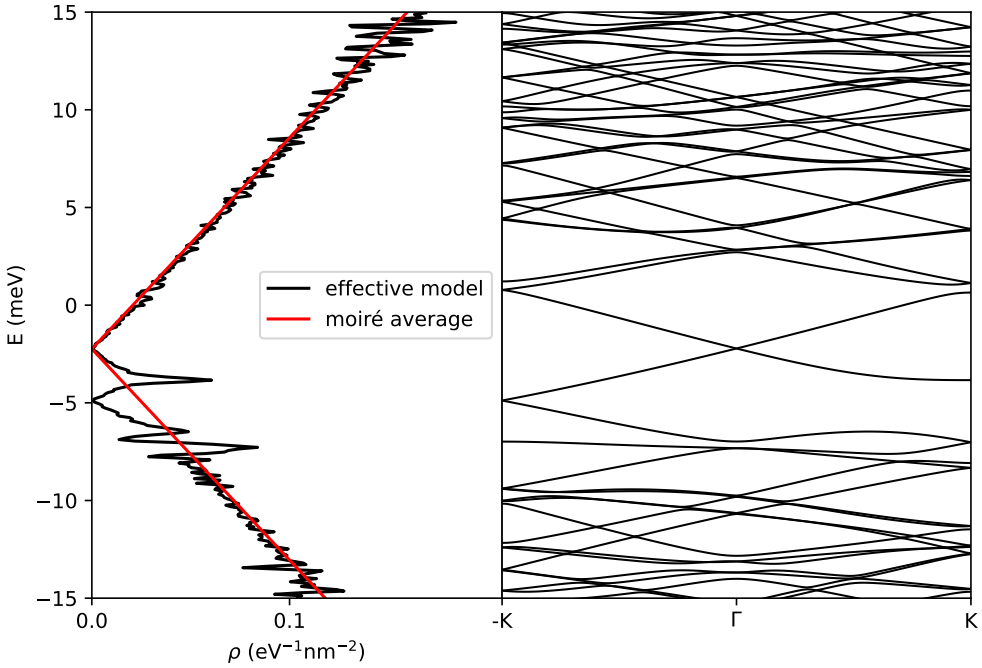

Figure 4.4: In the left panel, we observe the low-energy density of states of the $\boldsymbol{\Gamma}_M$ effective model. The black line represents the density of states computed from the effective model, while the red line corresponds to the profile of the average density of states of the local models. It is important to note that the average local density of states has been manually shifted to align the Dirac point with that of the effective model. This comparison allows us to assess the agreement between the low-energy states of the effective model and the average behavior of the local models. In the right panel, we present the band structure computed along the path $-\boldsymbol{K} - \boldsymbol{\Gamma} - \boldsymbol{K}$, which traverses the supermoiré Brillouin zone. This path provides insights into the energy dispersion and the formation of bands within the effective model. By analyzing the band structure, we can identify important features such as band crossings, band gaps, and the overall behavior of the energy levels along the selected trajectory.

Fig. 4.4 presents the band structure and the profiles of the density of states for the $\boldsymbol{\Gamma}_M$ effective model. The left panel displays the density of states (DOS) for both the effective model and the local models. The right panel shows the band structure along the $-\boldsymbol{K} - \boldsymbol{\Gamma} - \boldsymbol{K}$ route in the supermoiré Brillouin zone. The density of states, $\rho(\varepsilon)$, quantifies the number

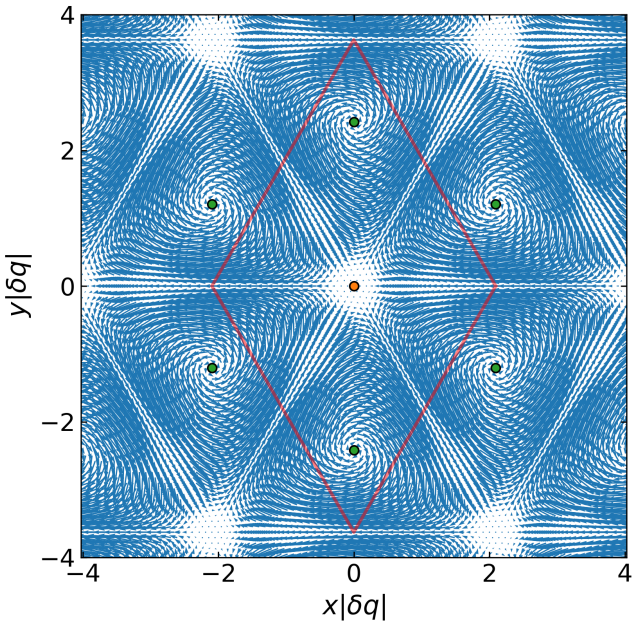

Figure 4.5: The vector field of $\boldsymbol{a}(\boldsymbol{R})$ on the $x-y$ plane. Red line depicts a supermoiré unit cell centered at $\boldsymbol{R}=\boldsymbol{0}$. The supermoiré coordinates restoring C_{3z} symmetry in the local models are also highlighted. The AAA stacked local model is marked with orange color, while the ABA/BAB stacked local models are shown in green.

of states per unit energy and per unit area at a given energy ε. In both the supermoiré models and the local models, the density of states is computed by summing over the bands and integrating over the wave vectors in the first Brillouin zone:

$$\rho(\varepsilon)=\sum_{n}\int_{\mathrm{BZ}}\frac{\mathrm{d}\boldsymbol{k}^2}{(2\pi)^2}\delta(\varepsilon-E_{n\boldsymbol{k}}), \tag{4.7}$$

where n goes over the band indices and $\boldsymbol{k}$ denotes the wave vectors within the first Brillouin zone.

By comparing the density of states profiles between the effective model and the local models, we can observe the differences and the supermoiré features that arise from the spatial variations in the moiré system. The effective model takes into account the long-range spatial variations, capturing the emergence of new energy bands and the formation of van Hove singularities, which are not present in the averaged density of states obtained from the local models.

This comparison highlights the importance of the effective model in capturing the global electronic properties and supermoiré effects that arise from the intricate interplay of the twist angles and the moiré pattern.

In the numerical evaluation of the density of states, the integral over the Brillouin zone is replaced by a discrete sum over the grid points in the Brillouin zone:

$$\int_{\mathrm{BZ}} \mathrm{d}\boldsymbol{k}^2 \longrightarrow \sum_i \delta\boldsymbol{k}^2,$$

where $\delta\boldsymbol{k}^2$ is the area of the discrete grid within the Brillouin zone. The Dirac delta function is approximated by the Kronecker delta symbol to match the discrete values of energy.

$$\delta(\varepsilon - E_{n\boldsymbol{k}}) \longrightarrow \frac{\delta_{\varepsilon, E_{n\boldsymbol{k}}}}{\delta\varepsilon},$$

where $\delta\varepsilon$ is the bin size of discrete values of ε. The numerical computation of the density of states is achieved by evaluating the following formula:

$$\rho(\varepsilon) = \sum_n \sum_i \frac{\delta\boldsymbol{k}^2}{(2\pi)^2} \frac{\delta_{\varepsilon, E_{n\boldsymbol{k}_i}}}{\delta\varepsilon}. \tag{4.8}$$

The summation $\sum_n \sum_i \delta_{\varepsilon, E_{n\boldsymbol{k}_i}}$ is in fact a histogram $\vartheta(\varepsilon)$. As a result, we have

$$\rho(\varepsilon) = \frac{\delta\boldsymbol{k}^2}{(2\pi)^2 \delta\varepsilon} \vartheta(\varepsilon). \tag{4.9}$$

The above formula can also be used for the computation of the density of states from local models. It suffices to perform the calculation for every supermoiré coordinate $\boldsymbol{R}$ to obtain the local density $\rho_{\mathrm{loc}}(\varepsilon, \boldsymbol{R})$. The average local density of states is given by

$$\bar{\rho}_{\mathrm{loc}}(\varepsilon) = \int_{\mathrm{SMUC}} \frac{\mathrm{d}\boldsymbol{R}^2}{\Omega}\, \rho_{\mathrm{loc}}(\varepsilon, \boldsymbol{R}), \tag{4.10}$$

where Ω is the area of the supermoiré unit cell.

Each local model exhibits a bare Dirac cone at the $\boldsymbol{\Gamma}_M$ point, which is pinned at $E = 0$ due to particle-hole symmetry. As a result, the average density of states shows a linear dependence on energy, with zero density at the Dirac point. In Fig. 4.4, we have manually adjusted the position of the average density profile (red line) to align its Dirac point with that of the effective model. The disparity between the two profiles is significant.

Firstly, it is worth noting that the breaking of particle-hole symmetry cannot be captured by local averaging. The effective model exhibits a broken particle-hole symmetry, evident from the shifted Dirac point away from zero energy and the asymmetric density profile around the Dirac point. The analytical proofs presented in the previous chapter also confirm this broken symmetry.

Secondly, the spectral weight of states in the effective model is clearly redistributed across different energy levels compared to the local average. Notably, the effective model exhibits distinct mini-band features. Although the presence of $C_{2z}T$ symmetry enforces a fully connected band structure, the depletion of density near the band touching point gives rise to an almost isolated band.

These observations emphasize the importance of considering the effective model, as it captures essential features that cannot be captured by local averaging alone. The broken symmetries and the redistribution of spectral weight are significant aspects that are elucidated by the effective model.

To gain insight into the redistribution of spectral weight and the emergence of mini-bands, we analyze the gauge field $A(\boldsymbol{R})$. By expanding the 2×2 matrix $A(\boldsymbol{R})$ as a linear combination of Pauli matrices, we obtain

$$A(\boldsymbol{R}) = a_0(\boldsymbol{R})\tau_0 + a_x(\boldsymbol{R})\tau_x + a_y(\boldsymbol{R})\tau_y + a_z(\boldsymbol{R})\tau_z = a_0(\boldsymbol{R})\tau_0 + \boldsymbol{a}\cdot\boldsymbol{\tau}, \tag{4.11}$$

where τ_i with $i = x, y, z, 0$ represent the Pauli matrices defined on the band indices to avoid confusion with the σ_i matrices defined on the sublattice degrees of freedom. The vector $\boldsymbol{a}(\boldsymbol{R}) = [a_x(\boldsymbol{R}), a_y(\boldsymbol{R}), a_z(\boldsymbol{R})]^T$ corresponds to an effective vector potential. Consequently, we recognize the presence of a pseudo-magnetic field in the effective model. This pseudo-Landau level effect redistributes the states across different energy levels and enhances the flatness of the bands, giving rise to the mini-band structure observed in the density of states.

In Fig. 4.5, we visualize the vector field encoded in $A(\boldsymbol{R})$ on the x-y plane. Notably, the vector field exhibits non-zero curl patterns as the vectors swirl around the ABA/BAB points, effectively restoring the C_{3z} symmetry observed in the local models.

4.1.2 $\boldsymbol{K}_M$ effective model

The $\boldsymbol{K}_M$ effective model has a non-zero $E(\boldsymbol{R})$ matrix that vanishes constantly in the $\boldsymbol{\Gamma}_M$ model.To solve the $\boldsymbol{K}_M$ effective model with equal twist angles of $2.2°$, we incorporate the $E(\boldsymbol{R})$ term, which was previously neglected in the $\boldsymbol{\Gamma}_M$ model. We employ the same gauge-fixing conditions as in the $\boldsymbol{\Gamma}_M$ model. Specifically, we select the two lowest-energy states at $\boldsymbol{K}_M$ to be the eigenstates of σ_z projected into their respective subspaces. We further impose that their scalar product with $|\boldsymbol{Q} = 0, A/B, l = 0\rangle$ is real and positive.

In Figs.4.6 and 4.7, we present the computed matrix elements and their Fourier coeffi-

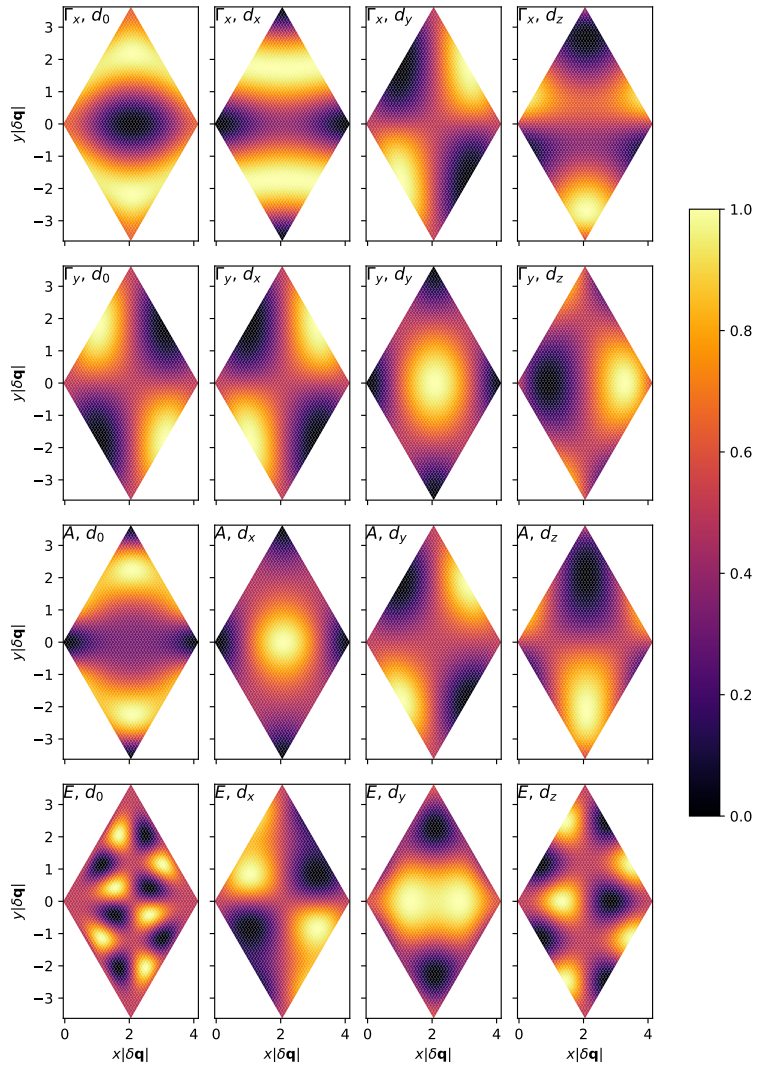

Figure 4.6: The matrix elements of the $\boldsymbol{K}_M$ effective model computed within a supermoiré unit cell for $\Gamma_x(\boldsymbol{R})$ (first row), $\Gamma_y(\boldsymbol{R})$ (second row), $A(\boldsymbol{R})$ (third row) and $E(\boldsymbol{R})$ (fourth row), with the coefficients d_0, d_x, d_y and d_z arranged in the first, second, third and fourth columns, respectively. The variation of matrix elements is confirmed to be smooth and continuous. All matrix elements return to their original value after going over a supermoiré period. Data collected with $\theta_1 = \theta_2 = 2.2°$. To show more clearly the continuity and periodicity of each set of data within a supermoiré unit cell, the data in each subplot are normalized to the interval $[0, 1]$ so that the same color scale is employed for all color plots.

cients, respectively. The data are normalized for better visibility. Fig.4.8 displays the low-energy band structure and density of states of the $\boldsymbol{K}_M$ effective model. Similar to the $\boldsymbol{\Gamma}_M$ effective model, the gauge field serves as a pseudo-magnetic field, leading to a redistribution of spectral weight among the states. This redistribution results in the observed mini-band characteristics in the density profile. It is important to note once again that this feature cannot be captured by a direct averaging of the moiré models.

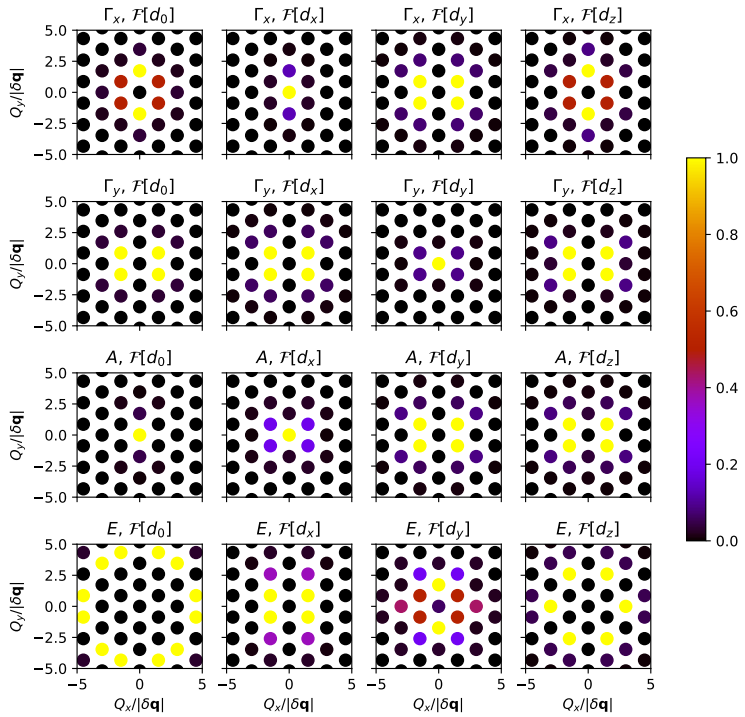

Figure 4.7: The absolute values of the Fourier coefficients of the data shown in Fig. 4.6. The arrangement of data in the panels corresponds to Fig. 4.6. All data are also normalized to $[0, 1]$ for better visibility.

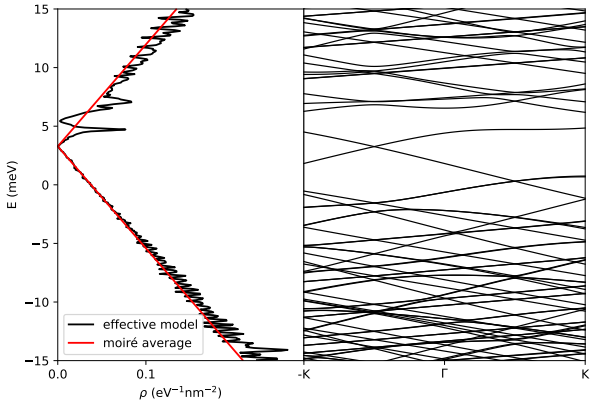

Figure 4.8: In the left panel, we shown The low-energy density of states of the $\boldsymbol{K}_M$ effective model. Black line show the density of states computed from the effective model. The red line show profile of the average density of local models. The average local density of states is shifted by hand to make the Dirac point coincide with that of the effective model. In the right panel, we present the band structure computed along the route $-\boldsymbol{K} - \boldsymbol{\Gamma} - \boldsymbol{K}$ transversing the supermoiré Brillouin zone.

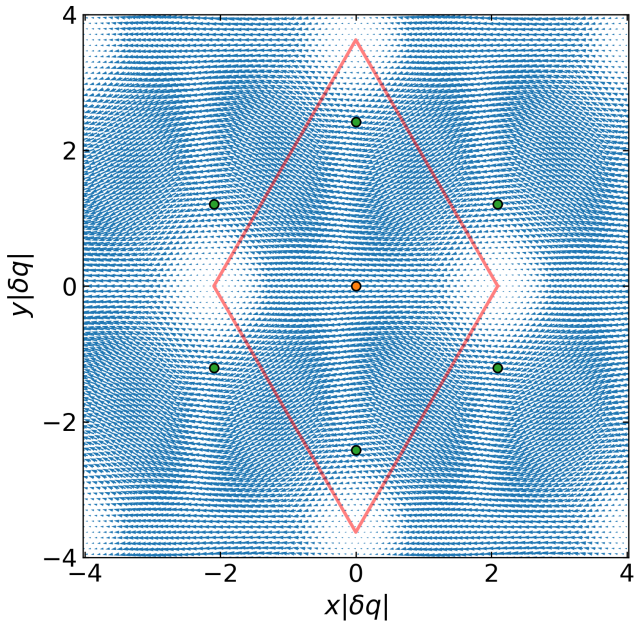

Figure 4.9: The vector field of $\boldsymbol{a}(\boldsymbol{R})$ on the $x-y$ plane computed for the $\boldsymbol{K}_M$ model. Red line depicts a supermoiré unit cell centered at $\boldsymbol{R} = \boldsymbol{0}$. The supermoiré coordinates restoring C_{3z} symmetry in the local models are also highlighted. The AAA stacked local model is marked with orange color, while the ABA/BAB stacked local models are shown in green.

4.1.3 Evolution with different twist angles

In Fig. 4.10, we present the evolution of the low-energy density of states profile with different twist angles. The profiles are obtained by applying the same procedures used in the previous sections for constructing and diagonalizing the effective models. As the twist angles vary, the density of states exhibits notable changes. The emergence of mini-bands and the redistribution of spectral weight are prominent features observed in the density profiles. These results demonstrate the strong dependence of the electronic properties on the twist angle in moiré systems.

The analysis of the low-energy density of states in twisted trilayer graphene with varying twist angles provides valuable insights into the electronic properties of the system. As the twist angles decrease, two main factors contribute to the enhancement of the low-energy density of states.

Firstly, at smaller twist angles, the interlayer hopping between the layers becomes stronger, leading to a suppression of the dispersion velocity near the Fermi level. This suppression of dispersion velocity results in an increased density of states, as observed in both the effective model and the local moiré models.

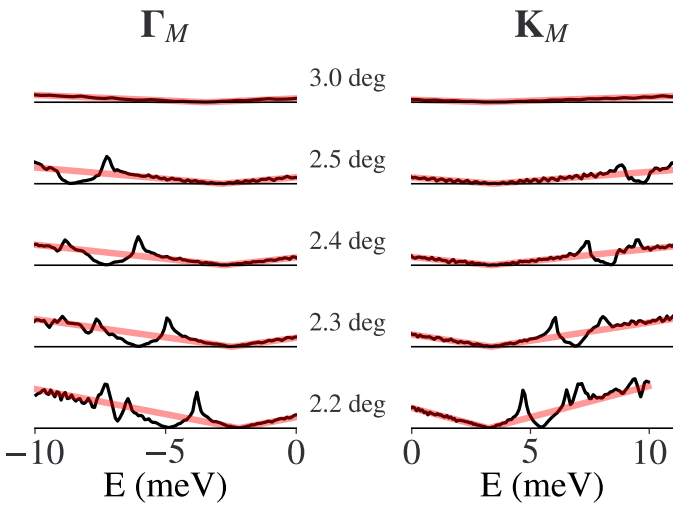

Figure 4.10: Black curves show the density of states of the $\boldsymbol{\Gamma}_M$ (left) and the $\boldsymbol{K}_M$ (right) effective models computed for different values of equal twist angles. The transparent red lines show the average density of states computed with local moiré models. They are shifted by hand to superpose their Dirac points with those of the effective models. The range of twist angles are chosen to be between $2.2°$ and $3°$.

Secondly, the presence of the gauge field in the effective model introduces a pseudo-magnetic field that further flattens the low-energy bands. This flattening effect gives rise to the appearance of high-density peaks in the density of states profiles, which are unique features of the effective model and cannot be captured by averaging over local models.

However, it should be noted that as the twist angles continue to decrease, a zero-velocity singularity emerges, indicating the breakdown of the effective theory. This singularity signifies the presence of fast variations in the effective wave function at the moiré scale, which violates the assumptions underlying the decoupling of physics at different scales.

Further discussions and analyses of this zero-velocity singularity will be presented at the end of this chapter, providing a comprehensive understanding of the limitations and challenges in describing twisted trilayer graphene systems with extremely small twist angles.

4.2 Effective model with $\theta_1/\theta_2 \simeq 1/2$

In this section, we investigate the numerical solutions to the effective model with a twist angle ratio of approximately $1/2$. As in the case of the equal-angle model, we construct the $\boldsymbol{\Gamma}_M$ effective model using the two lowest-energy states from each local solution. However, for the $\boldsymbol{K}_M$ effective model, we need to employ a four-band effective Hamiltonian. This is

because we have four low-energy states near the zero energy level at $\boldsymbol{K}_M$ point of the local model, as illustrated in Fig. 2.10.

4.2.1 $\boldsymbol{\Gamma}_M$ effective model

The procedure for constructing the $\boldsymbol{\Gamma}_M$ effective model with unequal twist angles is similar to that of the equal-angle case. We select the two lowest-energy states from each local model and fix their gauge using the gauge-fixing operator σ_z. The reference states chosen for gauge fixing are $|\boldsymbol{Q} = \boldsymbol{0}, A/B, l = 0\rangle$.

By decomposing the local Hamiltonian matrix as linear combinations of Pauli matrices defined on the band indices, we obtain the coefficients in real space, which are shown in Fig. 4.11. Additionally, we calculate their Fourier coefficients on the reciprocal lattice and present their amplitudes in Fig. 4.12. The data in both figures are normalized to the range $[0, 1]$ to improve visibility and facilitate comparison.

The computed band structure and density of states for the $\boldsymbol{\Gamma}_M$ model with unequal twist angles ($\theta_1 = 1.8°$ and $\theta_2 = 3.6°$) are displayed in Fig. 4.13. It is observed that the low-energy dispersion in this case is almost identical to the moiré average, indicating that the effect of the pseudo-magnetic field is substantially weaker compared to the case of equal twist angles. This observation is further supported by the vector fields encoded in the gauge field, as shown in Fig. 4.14. The lengths of the vectors, which represent the strength of the gauge field, are significantly smaller compared to the equal twist model. This indicates that the magnitude of the pseudo-magnetic field in the effective model is substantially weaker in the case of unequal twist angles. The vector field visualization helps us understand the spatial distribution and strength of the gauge field, providing insights into the underlying physics of the system.

4.2.2 $\boldsymbol{K}_M$ effective model

To develop the $\boldsymbol{K}_M$ effective model with unequal twist angles, we consider a four-band effective Hamiltonian due to the presence of four low-energy states near the $\boldsymbol{K}_M$ point of the local model. The gauge fixing procedure is updated accordingly by employing the fast-gauge fixing algorithm discussed in Chapter. 4.14. In this algorithm, we choose four reference states: $|\boldsymbol{Q} = 0, A/B, l = 0\rangle$ and $|\boldsymbol{Q} = \boldsymbol{q}_1, A/B, l = 1\rangle$. These reference states are polarized on the sublattices, resulting in sublattice-polarized gauge-fixed states.

To visualize the matrix elements of the four-band Hamiltonian on the supermoiré co-

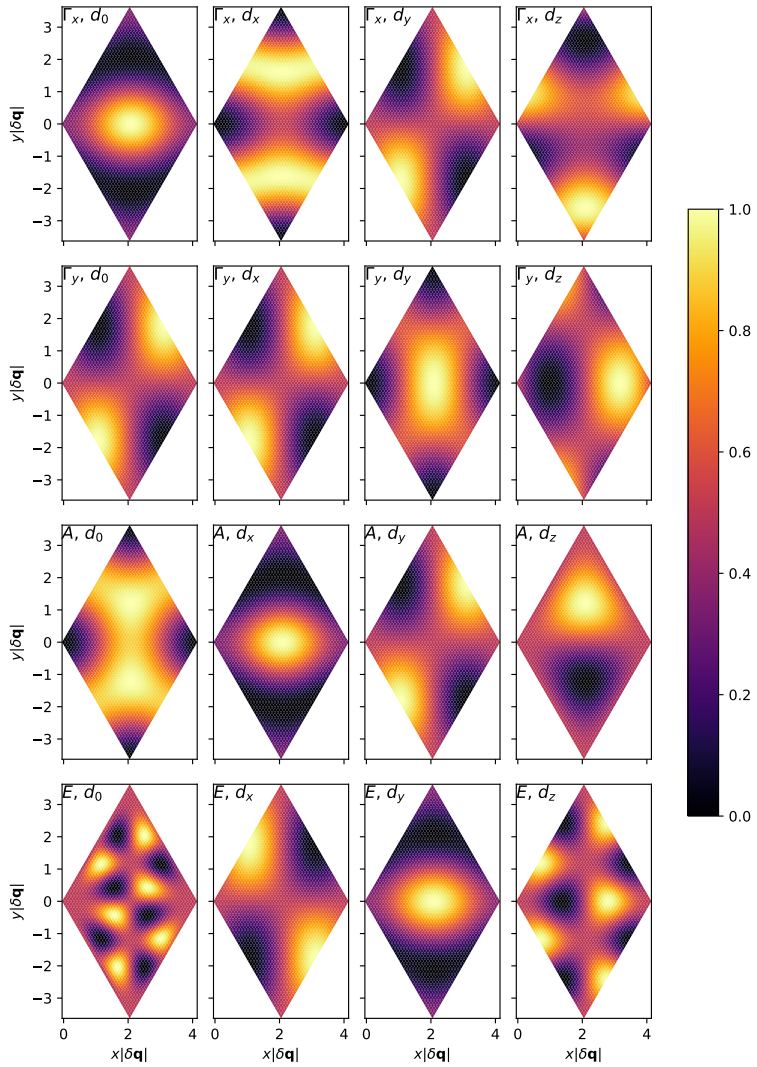

Figure 4.11: The matrix elements of the $\mathbf{\Gamma}_M$ effective model computed within a supermoiré unit cell, for $\Gamma_x(\boldsymbol{R})$ (first row), $\Gamma_y(\boldsymbol{R})$ (second row), $A(\boldsymbol{R})$ (third row) and $E(\boldsymbol{R})$ (fourth row), with the coefficients d_0, d_x, d_y and d_z arranged in the first, second, third and fourth columns, respectively, computed for twist angles $\theta_1 = 1.8°$ and $\theta_2 = 3.6°$. Data are normalized to $[0, 1]$ for better visibility. We confirm the smooth and continuous variation of all data with the supermoiré coordinates $\boldsymbol{R}$ as well as their periodicity.

ordinates, we refer you to the Appendix (Chapter D), where all 16 subplots for each 4×4 matrix are provided for clarity.

Finally, the band structure obtained from the $\boldsymbol{K}_M$ effective model is displayed in Fig. 4.15, providing insights into the low-energy dispersion characteristics of the system.

Once again, we observe the presence of mini-band features in Fig. 4.15, indicating the existence of a substantial pseudo-magnetic field arising from the gauge field. However, in the case of the $\boldsymbol{K}_M$ effective model with unequal twist angles, it is not possible to express

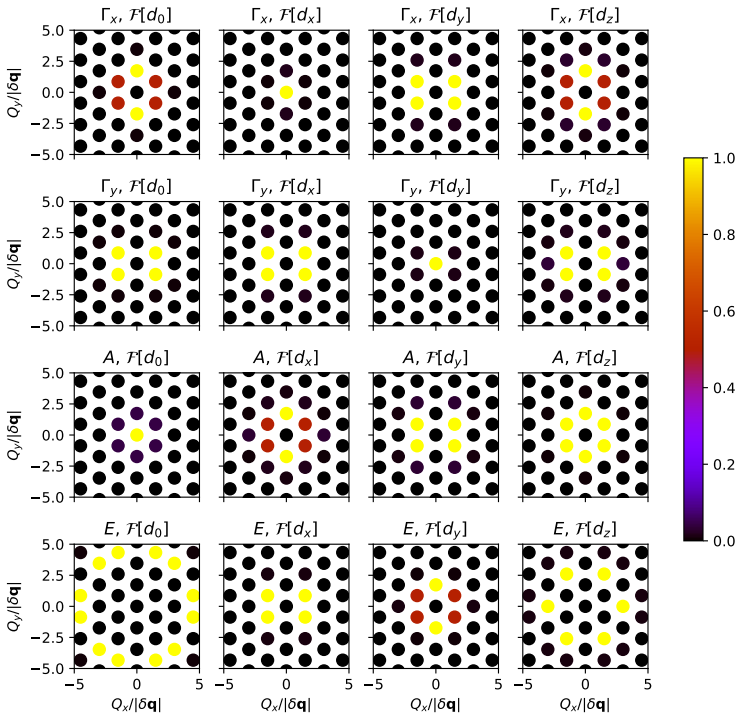

Figure 4.12: The Fourier amplitudes of all the data shown in Fig. 4.11. Every data set is normalized to $[0, 1]$.

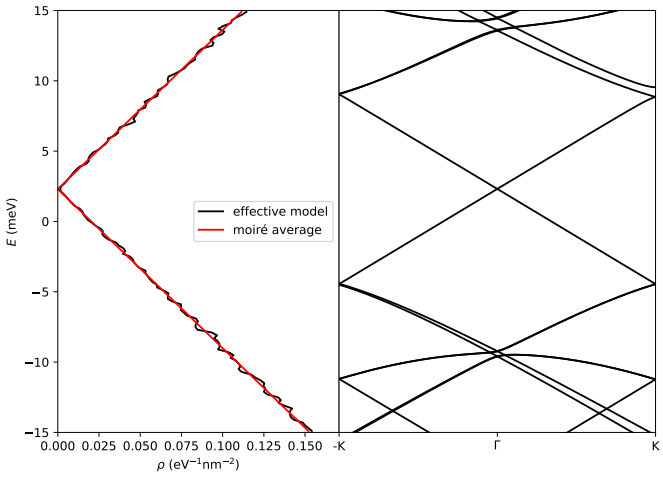

Figure 4.13: The band structure (right panel) and density of states (left panel) computed from the $\mathbf{\Gamma}_M$ effective model with $\theta_1 = 1.8°$ and $\theta_2 = 3.6°$.

the 4×4 Hamiltonian matrix as a scalar product between a vector $\boldsymbol{a}(\boldsymbol{R})$ and a vector of matrices. Consequently, the visual representation of the effective vector potential contained in $A(\boldsymbol{R})$ remains unclear.

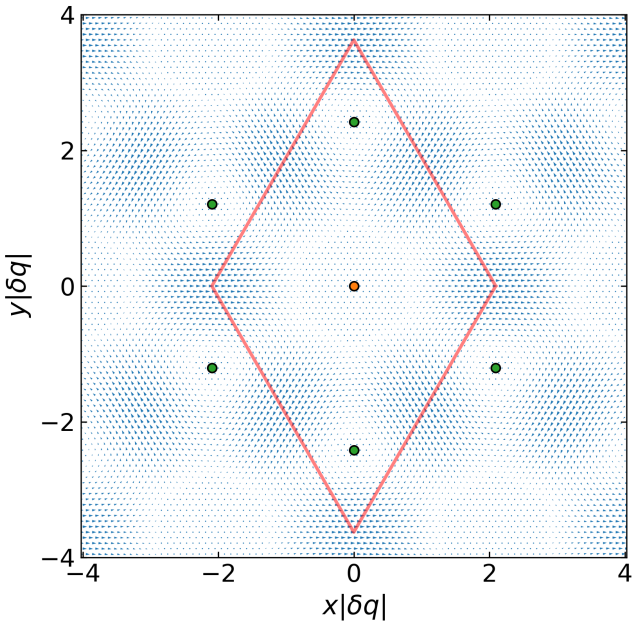

Figure 4.14: The a_x and a_y components of the gauge field extracted from the $\boldsymbol{\Gamma}_M$ effective model with $\theta_1 = 1.8°$ and $\theta_2 = 3.6°$.

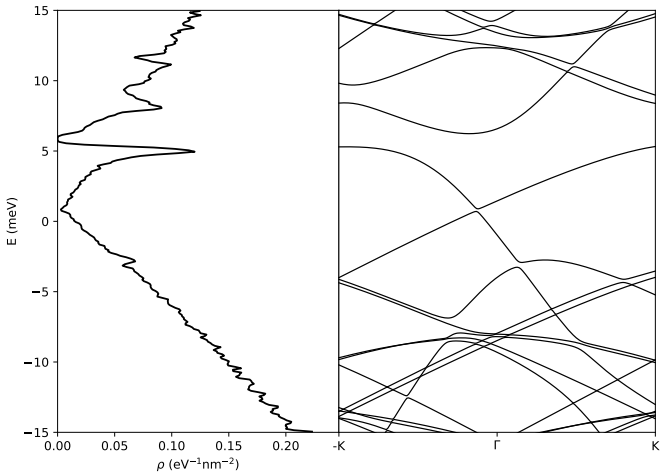

Figure 4.15: Low energy density of states (left panel) and band structure (right panel) given by the 4-band $\boldsymbol{K}_M$ effective model. Data collected for twist angles $\theta_1 = 1.8°$ and $\theta_2 = 3.6°$.

4.2.3 Evolution with different angles

In the previous sections, we provided detailed solutions of the effective model based on local states at $\boldsymbol{\Gamma}_M$ and $\boldsymbol{K}_M$ with twist angles of $1.8°$ and $3.6°$ respectively. By following the same procedures, we can compute the density of states and band structures for other

combinations of angles.

In the following analysis, we maintain a fixed ratio of $1/2$ between the angles and vary θ_1 from $1.6°$ to $2.1°$. The density of states obtained from the corresponding effective models is presented in Fig. 4.16.

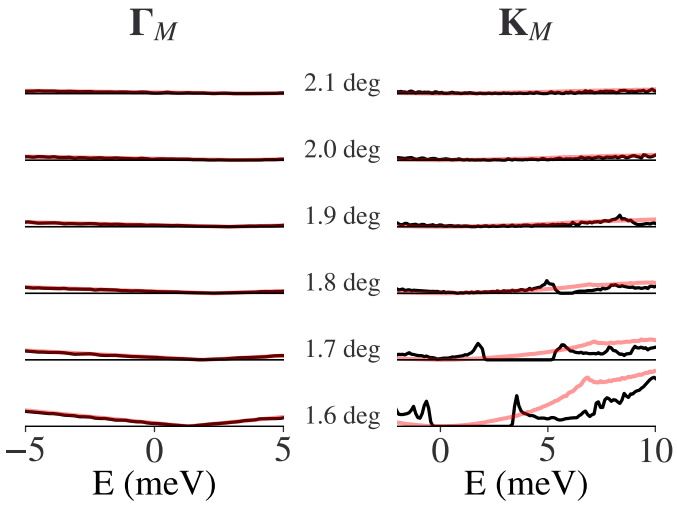

Figure 4.16: The black curves show the profiles of density of states of the effective models with $\theta_1 = \frac{\theta_2}{2}$ ranging from $1.6°$ to $2.1°$. The data of the $\boldsymbol{\Gamma}_M$ and $\boldsymbol{K}_M$ effective models are displayed in the left and right panels, respectively. Transparent red lines are the average density of states over local moiré models within a supermoiré unit cell, and are shifted by hand to align their Dirac points with those of the effective models.

4.3 Zero-velocity singularity

In both the effective models with equal and unequal twist angles, we have encountered a phenomenon known as the zero-velocity singularity when exploring small twist angles. These singularities occur when one of the components (characterized by the two singular values in Eq. (2.22)) vanishes at certain supermoiré coordinates. It is important to note that complete suppression of velocity is not necessary for the occurrence of the singularity.

The presence of the singularity manifests as difficulties in convergence and unstable low-energy band structures. In the left panel of Fig. 4.17, we present example density of states profiles for the effective models incorporating the zero-velocity singularity. These profiles were computed for both the $\boldsymbol{\Gamma}_M$ and $\boldsymbol{K}_M$ models with $\theta_1 = \theta_2 = 1.8°$. Despite the challenges in obtaining stable density of states and band structures with increasing momentum cutoff during the numerical solution, the profiles qualitatively demonstrate a significant enhancement of low-energy states.

In the right panel of Fig. 4.17, we plot the minimum velocity components within a supermoiré unit cell for different angles in the $\boldsymbol{\Gamma}_M$ and $\boldsymbol{K}_M$ models. It can be observed that the local minimum velocity generally decreases as the twist angle diminishes. When the angle falls below 2°, the zero-velocity singularity emerges. However, it is interesting to note that at certain angles smaller than 2°, the $\boldsymbol{K}_M$ velocity reemerges while the minimum $\boldsymbol{\Gamma}_M$ velocity remains zero.

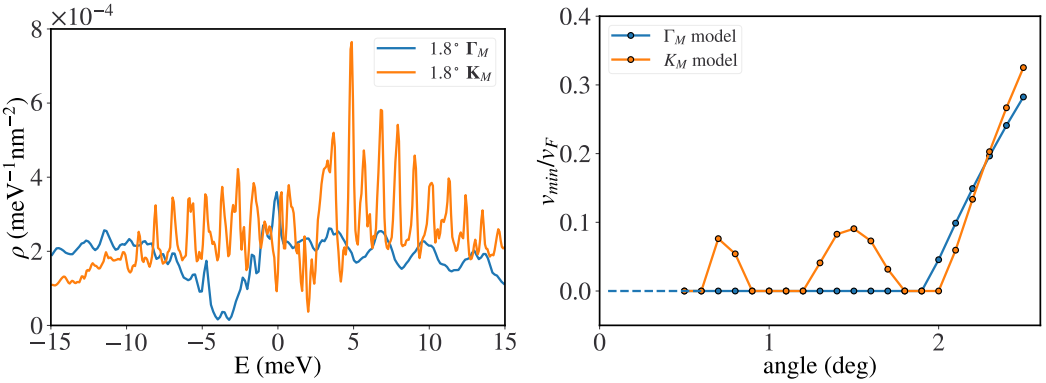

Figure 4.17: Left: The low-energy density of states with equal twist angles of 1.8°, computed from $\boldsymbol{\Gamma}_M$ (blue curve) and $\boldsymbol{K}_M$ (orange curve) effective models. The great enhancement of density of states at low-energy is qualitatively manifested. Right: The smallest velocity found within a supermoiré cell computed at different equal twist angles, for the $\boldsymbol{\Gamma}_M$ (blue curve) and $\boldsymbol{K}_M$ (orange curve) models.

In Fig. 4.18, we present the minimum velocity component of the Dirac cones at the $\boldsymbol{K}_M$ point for different values of $\theta_1 = \frac{1}{2}\theta_2$. These profiles correspond to density of states computations at certain angles where the $\boldsymbol{K}_M$ models are not affected by the singularity. It is evident that the high density of states coincides with small dispersion velocities. This observation supports the idea that the enhancement of density of states in twisted trilayer graphene arises from the suppression of dispersion velocity near the Fermi level.

In Fig. 4.19, we present the velocity components calculated locally using the singular-value decomposition for the Dirac cones at the $\boldsymbol{\Gamma}_M$ point of local models. It is evident that at small angles, the smaller velocity component, represented by the smaller singular value, can locally reach zero, leading to the singularity and the breakdown of the effective model's solution.

Furthermore, Fig. 4.19 also demonstrates that the two velocity components become equal at supermoiré coordinates where C_{3z} symmetry is restored. This implies that the local models exhibit isotropic Dirac cones at these specific supermoiré coordinates.

Now that we understand that reducing the velocity leads to an enhanced density of states, we can expect a significant increase in the density of states by further suppressing

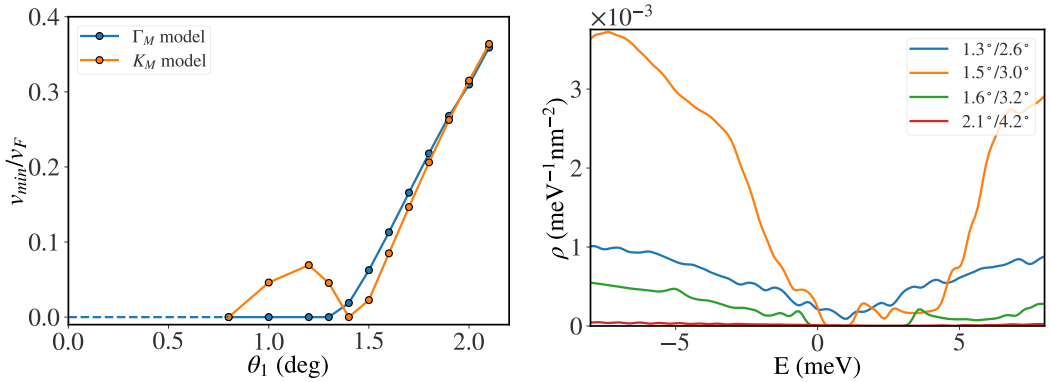

Figure 4.18: Left: the minimum velocity components at $\boldsymbol{\Gamma}_M$ (blue) and $\boldsymbol{K}_M$ (orange) for different values of $\theta_1 = \frac{1}{2}\theta_2$. Right: The density of states of the $\boldsymbol{K}_M$ effective model computed at several angles where the velocity of $\boldsymbol{K}_M$ does not touch zero. Comparing the plots of both sides, the remarkably high density of states emerges with small velocities.

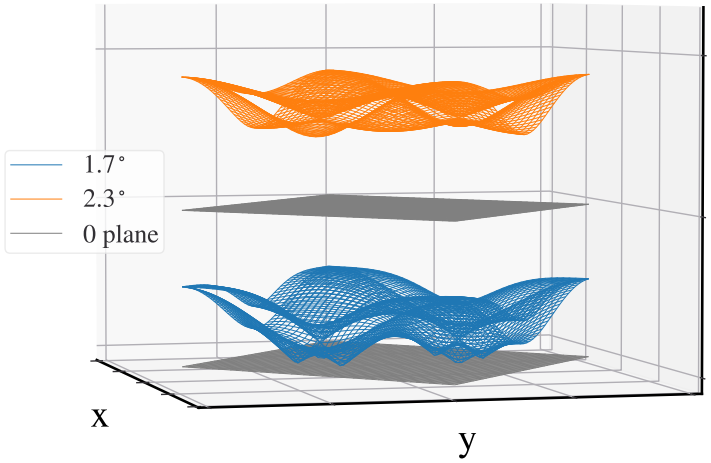

Figure 4.19: Velocity components of the Dirac cone in the local models across the supermoiré coordinates. Data collected for the $\boldsymbol{\Gamma}_M$ models with equal twist angles $1.7°$ (blue wired surface) and $2.2°$ (orange wired surface). The plane of zero value is shown in gray color.

the velocity until it locally vanishes.

4.3.1 1D Dirac model with space-dependent velocity

In the following, we will utilize an analytically solvable 1D Dirac model with a space-dependent velocity to illustrate the consequences of locally vanishing velocity. Let us consider the following 1D Hamiltonian:

$$\hat{h}(x) = \sqrt{v(x)} - i\frac{\mathrm{d}}{\mathrm{d}x}\sqrt{v(x)}, \tag{4.12}$$

where $v(x)$ is an *arbitrary* real function describing the space-dependent velocity. The Schrödinger's equation of the 1D Dirac Hamiltonian is given by:

$$\hat{h}(x)\varphi_\varepsilon(x) = \varepsilon\varphi_\varepsilon(x). \tag{4.13}$$

where ε denotes the eigenenergy. To solve Eq. (4.13), it is convenient to express the eigenfunction as:

$$\varphi_\varepsilon(x) = \frac{\mathcal{N}}{\sqrt{v(x)}} e^{i\phi_\varepsilon(x)}, \tag{4.14}$$

where $\mathcal{N}$ is a normalizing constant, and $\phi_\varepsilon(x)$ is a priori a complex function. Substituting this expression into the Schrödinger's equation yields a new equation involving $\phi_\varepsilon(x)$:

$$\frac{\mathrm{d}}{\mathrm{d}x}\phi_\varepsilon(x) = \frac{\varepsilon}{v(x)}. \tag{4.15}$$

Integrating this equation gives:

$$\phi_\varepsilon(x) = \varepsilon \int^x \mathrm{d}x' \, \frac{1}{v(x)}. \tag{4.16}$$

The wave function for states with eigenenergy ε is then given by:

$$\varphi_\varepsilon(x) = \frac{\mathcal{N}}{\sqrt{v(x)}} e^{i\varepsilon \int^x \mathrm{d}x' \, \frac{1}{v(x)}}. \tag{4.17}$$

From Eq. (4.17), we can extract two important messages when the velocity becomes extremely small near a certain location x_0:

1. The amplitude of the wave function becomes highly concentrated near the small-velocity site because $|\varphi_\varepsilon(x)| \propto 1/\sqrt{v(x)}$. This results in a highly localized wave function. When the velocity vanishes at x_0, the wave function collapses to a point-like function located at x_0. From the perspective of the supermoiré length scale, the localization on a supermoiré coordinate indicates that the state is governed by the moiré scale details. This breaks down the assumption of the effective model that decouples the moiré and supermoiré length scales.

2. The phase factor in the wave function becomes rapidly oscillating near x_0. This fast oscillation encodes high and even infinite momenta, even if the eigenenergy is small. This explains why the convergence of the effective model becomes challenging in the presence of zero-velocity singularities, regardless of the increased cutoff in momentum space. It would require an infinitely large cutoff to achieve convergence.

4.3.2 Explorable angles

The zero-velocity singularity problem highlights an implicit condition for the applicability of the supermoiré approach proposed in this thesis.

As we have previously learned, successful decoupling of moiré and supermoiré behaviors requires that $|\delta \boldsymbol{q}_j| \ll |\boldsymbol{q}_j|$, for $j = 1, 2, 3$. The geometrical decomposition described in Eq. (3.3) indicates that as the twist angles become smaller, the length differences between $|\delta \boldsymbol{q}_j|$ and $|\boldsymbol{q}_j|$ become larger.

However, the zero-velocity singularity poses a limit on the validity of the length scale separation as we approach smaller angles. When the twist angles become sufficiently small, the velocity component may locally vanish, leading to the importance of moiré-scale details in determining a supermoiré state. This imposes an implicit limitation on the application of the supermoiré approach.

Therefore, the application of our supermoiré approach is best suited for twist angles within certain ranges, avoiding both excessively large and excessively small angles.

In Fig. 4.20, we manually set the decoupling criterion to be $|\delta \boldsymbol{q}|/|\boldsymbol{q}| \leqslant 0.2$ and display the maximum density of states between -30 and 30 meV for twist angles with ratios close to 1, $1/2$, and 2. Data points are not shown if the criterion is not satisfied or if the zero-velocity singularity is present.

4.4 Summary

In this chapter, we have provided a detailed description of the protocols for numerically solving the effective model. The process begins with the geometrical decomposition of the original TBG moiré vectors, which allows us to decouple the moiré and supermoiré coordinates. Next, we solve the local moiré Hamiltonian at each supermoiré coordinate $\mathbf{R}$ to obtain the local states. To ensure the continuity and smoothness of these local states as functions of $\mathbf{R}$, we employ the gauge fixing procedures discussed in Chapter 3.4.2. Both gauge-fixing algorithms are used for the two-band effective models and the four-band effective model of $\mathbf{K}_M$ states.

By Fourier transforming the real-space matrix elements, we transfer the effective model to the reciprocal lattice. To facilitate the diagonalization of the effective Hamiltonian matrix and access the low-energy supermoiré states, we impose a cutoff on the size of the reciprocal lattice.

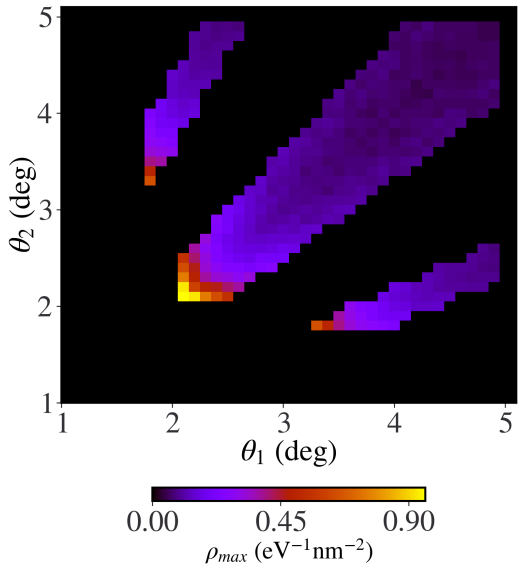

Figure 4.20: The maximum density of states computed for explorable angles with θ_1/θ_2 *near* 1, $1/2$ and 2, and for energy levels between -30 and 30 meV. Angles are limited between $1°$ and $5°$. Computation were performed for angles satisfying $|\delta \boldsymbol{q}|/|\boldsymbol{q}| \leqslant 0.2$.

However, we encountered convergence difficulties in the numerical solution when the twist angles became sufficiently small, mainly due to the emergence of zero-velocity singularities. To gain insights into the nature of these singularities, we performed an analytical study of a 1D Dirac model with space-dependent velocity. This analysis revealed that the zero-velocity singularity leads to wave function localization and rapidly changing phases. The former indicates the importance of moiré-scale details for the supermoiré state, while the latter explains the difficulty in achieving convergence in the numerical solution, as it would require an infinitely large momentum cutoff.

It should be noted that the exploration of the relationship between moiré details and supermoiré states goes beyond the scope of this research.

In summary, this chapter has presented a comprehensive numerical toolbox for solving the effective model, encompassing the retrieval of local states, gauge fixing, establishment, and diagonalization of the effective Hamiltonian.

Chapter 5

Conclusion

In most cases, twisted trilayer graphene (TTG) lacks the advantage of the mirror symmetry, which restores the periodic regime identical to TBG. As a result, TTG is generally considered a quasicrystal due to the incommensurability of the two TBG moiré patterns. Finding a general solution for the quasicrystal system remains challenging. To address this difficulty, we first demonstrate that by neglecting the non-colinearity between the moiré vectors of the two TBG moiré patterns, the TTG Hamiltonian can regain periodicity when the ratio between the twist angles is a rational number. This approximate model exhibits a periodicity comparable to that of the TBG moiré pattern and reveals the band structure and non-trivial topological properties in TTG. The moiré description is valid for a moderate distance, over which the supermoiré variation is not significant.

Next, we employ a geometrical decomposition of the exact moiré vectors to separate two distinct length scales: one comparable to the TBG moiré pattern and the other spanning a much longer range, known as the supermoiré period. This decomposition allows us to view the previous approximate TTG model as "local" models of the exact model located at different supermoiré coordinates. The exact model is then considered as the local models modulated by a phase factor that spans the supermoiré length scale.

The distinct length scales indicate that the supermoiré modulation varies much slower compared to the moiré potential, suggesting that the exact wave function of TTG should resemble the moiré states locally. Based on this intuition, we propose an ansatz for the exact wave function, which is written as a linear combination of local states decorated by a modulation function that varies slowly in the supermoiré scale.

By applying the ansatz, we can leverage the local solutions and integrate out the details within a moiré unit cell, resulting in a new effective Hamiltonian that only involves

the modulation functions. Solving the effective Hamiltonian yields the supermoiré states. However, solving the effective model requires necessary gauge-fixing procedures, which we discuss in detail. We explain the principles of gauge-fixing to obtain local states that vary smoothly and continuously as functions of the supermoiré coordinates, and we present two commonly used gauge-fixing methods.

The analysis of the translational symmetry of the effective model indicates that a proper choice of gauge greatly facilitates the solution of the effective model. To focus on the typical supermoiré energy scale, we consider only the local states closest to the zero energy level, which are located at the local $\boldsymbol{\Gamma}_M$ and $\boldsymbol{K}_M/\boldsymbol{K}'_M$ points. Based on their location in the moiré Brillouin zone, we construct the $\boldsymbol{\Gamma}_M$ and $\boldsymbol{K}_M$ effective models.

The numerical solutions of the effective model reveal distinct features compared to the direct averaging of the local models. The spectral weight of the states is redistributed over the energy levels in the effective model, which we confirm is due to the pseudo-magnetic field encoded in the gauge field term.

The theoretical approach proposed in this thesis offers a universal framework for addressing certain incommensurability problems that can be viewed as perturbed periodicities. In this work, the small deviations from the commensurable periodic lattice are caused by the non-colinearity between the two sets of moiré vectors and the slight difference in the ratio between angles from a rational number. The incommensurability gives rise to the supermoiré pattern treated within this framework, which is broadly applicable.

In experimental realizations of twisted multilayer graphene assemblies, the top and bottom graphene layers are typically deposited on hexagonal boron nitride (hBN) substrates. Even if the chemical bonds in graphene and hBN are perfectly aligned, their lengths differ: the B-N bond length in hBN is 1.44 Å, while the C-C bond length in a graphene single layer is 1.45 Å. The hBN lattice is neither commensurate with graphene nor with twisted bilayer graphene. In this context, the hBN substrate may potentially affect certain physical properties of the multilayer graphene systems under measurement, as it leads to band folding due to the supermoiré effects. However, the effect of the substrates has not been fully elucidated thus far, and the supermoiré effect of hBN on multilayer graphene, whether twisted or not, has mostly been ignored.

In a theoretical work by Grover et al. [101], the computation of local properties of TBG deposited on hBN is reported. These local properties are computed independently without coherence between each other. Our approach can provide additional information in this context. If a state spans the long supermoiré scale, we will be able to explore the global quantity as compared to incoherently summing up all the local quantities.

It is worth noting that the approach developed in this thesis is not limited to 2D multilayer graphene. We anticipate its usefulness in other scenarios where our theoretical and numerical toolbox can be applied. In general, it can be employed for Hamiltonians with fast and slow varying contributions denoted as $H(\boldsymbol{r}, \varpi(\boldsymbol{r}))$, where $\varpi(\boldsymbol{r})$ represents the slowly varying contributions. The periods of the two variations are not required to be commensurate. By assuming locally constant $\varpi(\boldsymbol{r})$, we can obtain the local solutions and construct a similar ansatz wave function by leveraging the local states, as demonstrated in the case of TTG. Injecting the ansatz wave function into the full model and integrating over the smaller unit cell leads to an effective Hamiltonian concerning the modulation functions of each local solution.

In relation to experiments, the results obtained from the effective model suggest that the supermoiré states exhibit physical properties that cannot be captured by averaging over local measurements. Experimentalists can measure the low-energy density of states over the supermoiré cell to observe how the spectral weight is redistributed by the pseudomagnetic field.

In summary, our approach provides a universal theoretical framework for addressing similar physical problems. The results obtained from the effective model shed new light on the experimentally detectable supermoiré properties.

Acknowledgment

The theoretical work presented in this thesis would not be possible without the careful and detailed guidance of my supervisor Prof. Christophe Mora. With his sharp physical intuition and strict rigorousness in theories, we were able to tackle a series of difficult problems, both expected or unexpected, during the work on this thesis.

I would like to express my gratitude also to Dr. Daniele Guerci who has also been deeply involved in this work. Although the time we physically worked together in Paris was short, it has been an unforgettable experience with extraordinary productivity and great inspirations. Our discussions were enthusiastic and fruitful, from which I have benefited a lot. This is a lifelong memory to be cherished.

I would like to thank my daughter, Chuyu Mao, my little pearl who has brought to us infinite joy and happiness, as well as sweet exhaust in countless nights.

Tons of thanks to my wife, Yuanzhao Chen, who has kept me company through my toughest days at the bottom of my life, and then over all my years of study in France. She has taken care of our life, either together or separated at the two ends of the continent. She has also devoted herself to raising our little naughty girl with me.

I thank my parents, my mother Huixia Chen and my father Zhaohua Mao, the most selfless parents in the world who have been supporting us in all aspects to the maximum of their capacity, both mentally and materially. They could have enjoyed a much cosier life in retirement if they had not been burdened by our life nine thousand kilometers away from home.

Appendices

Appendix A

Résumé substantiel en français

A.1 Introduction

Le succès de l'isolation du graphène monocouche a marqué le début d'une nouvelle ère de recherche sur la matière bidimensionnelle. Le graphène a attiré une attention considérable ces dernières années en raison de ses propriétés uniques. Les électrons dans une monocouche de graphène montrent une mobilité élevée sur une large gamme de températures. De plus, le graphène possède des conductivités électrique et thermique comparables à celles des métaux.

Cependant, la découverte expérimentale du graphène bicouche torsadé (TBG) en 2018 a ouvert un nouveau domaine de recherche scientifique sur les matériaux bidimensionnels, appelé "twistronique", qui fait l'objet d'une intense investigation jusqu'à ce jour. Le TBG est un système représentatif des hétérostructures de type van der Waals, où l'empilement de couches présentant des périodicités différentes donne lieu à ce célèbre motif moiré. Le potentiel moiré résultant de l'interaction entre les couches modifie significativement la surface de Fermi, ce qui entraîne une réduction significative de la mobilité des électrons dans le TBG. À certains angles "magiques", la vitesse de Fermi devient presque nulle et les bandes d'énergie autour du niveau de Fermi sont extrêmement aplaties. Les électrons qui se trouvent dans ces bandes plates du TBG aux angles magiques (MATBG) ont des implications importantes en termes de corrélation et de comportement collectif. Les expériences ont révélé l'existence de phases supraconductrices, de phases isolantes corrélées, de phases métalliques étranges, ainsi que d'autres phases exotiques.

Alors que la communauté scientifique continue à investir des efforts pour comprendre les mécanismes sous-jacents de ce riche mais complexe diagramme de phase, d'autres

hétérostructures bidimensionnelles sont également étudiées. Parmi tous les systèmes explorés jusqu'à présent, le graphène tricouche torsadé (TTG) émerge comme une plateforme prometteuse en raison de sa grande adaptabilité en termes de structure électronique et de diagramme de phase. Les expériences ont également confirmé la présence de phases exotiques similaires à celles du TBG dans le TTG. Avec une couche de graphène supplémentaire, la complexité du TTG est considérablement accrue par rapport au TBG. Dans le TTG, les deux motifs moirés non appariés du TBG créent un motif moiré secondaire, appelé supermoiré, au-dessus d'eux.

La majorité des travaux théoriques et expérimentaux antérieurs ont utilisé une configuration spéciale du TTG qui est symétrique par rapport à un plan passant par la couche médiane. Cette configuration permet d'obtenir une périodicité identique à celle du TBG avec le même angle de torsion. En effet, l'Hamiltonien du TTG avec une symétrie de miroir (mTTG) peut être transformé en un TBG effectif et en un cône de Dirac découplé. L'angle magique du mTTG correspond à celui où les deux bandes proches de l'énergie nulle redeviennent plates. Les expériences menées sur les mTTG ont également révélé l'existence de phases exotiques telles que les phases supraconductrices et les phases isolantes corrélées. Cependant, la configuration du TTG peut être plus complexe lorsque les couches supérieure et inférieure ne sont plus parfaitement alignées. Cela pose un problème complètement nouveau dans le TTG par rapport au TBG, à savoir la présence d'un motif moiré secondaire, ou supermoiré, en raison du décalage entre les deux motifs moirés.

Le motif supermoiré est difficile à étudier en raison de sa nature quasi-cristalline résultant de l'incommensurabilité des deux motifs moirés. Par conséquent, une périodicité est généralement absente dans un TTG avec deux angles de torsion arbitraires. Pour étudier cet effet de supermoiré, l'attention se porte sur la configuration hélicoïdale (sTTG, staircase TTG en anglais), où les couches supérieure et inférieure sont tournées dans des sens opposés.

Les premières tentatives pour résoudre le sTTG ont adopté une approximation importante en ignorant la non-colinéarité entre les deux ensembles de vecteurs moirés. Dans ce cas, lorsque le rapport des angles de torsion est un nombre rationnel, le système retrouve une périodicité moirée comparable à celle du TBG. Bien que de nombreuses propriétés du sTTG aient été révélées dans ce modèle moiré, l'impact du motif supermoiré a été entièrement ignoré en raison des approximations effectuées.

Inspiré par les résultats obtenus dans ce modèle approximatif, l'objectif est d'établir un cadre théorique permettant d'étudier l'effet supermoiré dans certaines conditions.

Cette thèse est donc structurée de la manière suivante. Le chapitre 1 commence par la

construction du modèle continu de Bistrizer-MacDonald pour le TBG, qui sert de base pour établir l'Hamiltonien continu du TTG. Dans le chapitre 2, le modèle continu du TTG est établi et la solution numérique de l'échelle moiré est présentée en appliquant les approximations nécessaires et en adoptant un rapport rationnel entre les angles. Le chapitre 3 présente l'établissement du cadre théorique permettant de créer le modèle effectif de l'échelle supermoiré. Enfin, dans le chapitre 4, les solutions numériques du modèle effectif limité à basse énergie sont présentées en détail.

A.2 Travail de thèse

A.2.1 Chapitre 1 – Graphène bicouche torsadé : bandes plates, angles magiques et symétries

Ce chapitre est dédié à la démonstration de la théorie du graphène bicouche torsadé (TBG), initialement proposée par Bistrizer et A. H. MacDonald (appelée modèle BM par la suite). Ce modèle prend en compte les niveaux d'énergie proches de la surface de Fermi dans chaque monocouche de graphène (c'est-à-dire les deux cônes de Dirac) couplés par un potentiel moiré.

Dans les travaux actuels, la démonstration du modèle BM commence généralement par un modèle de liaisons fortes décrivant l'aspect atomistique, puis le simplifie jusqu'à obtenir un modèle continu de BM. Contrairement à ces pratiques, nous construisons le modèle BM de manière différente et beaucoup plus simplifiée. Nous partons directement des deux cônes de Dirac initialement découplés. En prenant en compte les contraintes liées aux différentes symétries, nous montrons que la forme analytique du potentiel moiré qui couple les deux couches est déjà fixée et correspond à celle du modèle BM.

Les procédures de construction du modèle BM présentées dans ce chapitre partage la philosophie de la théorie des orbitales frontières de la chimie quantique proposée par Fukui Ken'ichi. Selon notre connaissance, la construction du modèle BM dans ce chapitre est la plus simple et la plus directe à ce jour.

Le modèle BM révèle que la physique à basse énergie du TBG peut toujours être décrite dans un régime périodique, quel que soit l'angle de torsion. Grâce à cette périodicité moiré, l'application du théorème de Bloch redevient possible. Les solutions numériques du modèle BM sont ainsi obtenues dans le réseau réciproque.

Dans la suite du chapitre, les structures de bande sont calculées pour différents angles.

En particulier, nous montrons l'existence de bandes entièrement plates autour du niveau de Fermi lorsque l'angle atteint certaines valeurs spécifiques, appelées angles magiques.

Les symétries importantes du TBG sont ensuite analysées en détail. Nous montrons la transformation des états sous les opérations de symétrie et expliquons la définition inhabituelle du point $\mathbf{\Gamma}$ dans la zone de Brillouin moiré, qui diffère du point $\boldsymbol{k} = \mathbf{0}$ car il est le centre des symétries.

Enfin, à la fin du chapitre, nous présentons l'effet des pseudo-niveaux de Landau dans le TBG en développant le modèle autour du point $\boldsymbol{r} = \mathbf{0}$. Cet effet d'un champ pseudo-magnétique explique partiellement l'origine des bandes entièrement plates.

A.2.2 Chapitre 2 – Graphène tricouche torsadé : modèle et solution à l'échelle moiré

Dans ce chapitre, nous démontrons la solution moiré du graphène tricouche torsadé (TTG) en adoptant l'approximation de la colinéarité entre les vecteurs moirés et un rapport rationnel des angles de torsion. Cette approximation permet de ramener le modèle du TTG à nouveau dans le régime périodique, ce qui facilite les résolutions numériques.

Nous commençons par la construction simple de l'hamiltonien du TTG en adoptant les potentiels moirés du TBG pour coupler les couches adjacentes. Nous mettons particulièrement l'accent sur certaines conséquences importantes liées à l'ajout d'une couche supplémentaire par rapport au TBG, notamment le fait que le TTG n'est plus indépendant des facteurs de phase. Cela rend le TTG plus ajustable dans le sens où les facteurs de phase peuvent également modifier les structures de bande et la symétrie du système.

Dans un premier temps, nous présentons brièvement le TTG avec la symétrie de miroir (mTTG). En transformant explicitement l'hamiltonien initial en un hamiltonien effectif du TBG, dont l'amplitude du couplage intercouche est amplifiée par un facteur $\sqrt{2}$, et un cône de Dirac découplé, en reportant l'hamiltonien sur les bases des états propres de la symétrie de miroir. Les solutions numériques pour les mTTGs ne sont pas démontrées car ses procédures sont essentiellement identiques à celles du TBG.

Nous abordons ensuite le traitement du TTG hélicoïdal (sTTG). Nous montrons la non-colinéarité entre les vecteurs moirés dans ce modèle original. En ignorant légèrement la déviation par rapport à la colinéarité parfaite, nous obtenons à nouveau un hamiltonien périodique dont la périodicité est comparable à celle du TBG.

Nous présentons ensuite les solutions numériques pour deux cas typiques où les angles

sont égaux et où le rapport des angles vaut $1/2$. Les résultats montrent que les structures de bande dépendent des deux angles. L'analyse des symétries montre que les symétries peuvent être distinctes dans ces deux cas.

Nous avons également recherché, dans la limite chirale avec des angles égaux, les bandes entièrement plates, ainsi que la topologie non triviale qui leur est associée.

A.2.3 Chapitre 3 – Théorie effective supermoiré : formalisme, jauge et symétries

Ce chapitre démontre les travaux théoriques du cœur dans cette thèse. Nous montrons en détail la construction de la théorie effective du sTTG.

Nous commençons par vérifier les symétries du modèle original sans aucune approximation, et trouvons que les symétries présentes sont $C_{2z}T$ et C_{3z}. Contrairement au modèle approximatif, la symétrie particule-trou est constamment brisée. Nous attendons que le modèle effectif développé possède des symétries cohérentes avec le modèle initial.

Pour établir la théorie effective, on commence par une décomposition géométrique des vecteurs moirés du modèle initial. Cela permet d'obtenir deux ensembles de vecteurs appartenant aux échelles distinctes, l'échelle moiré et celle supermoiré. L'Hamiltonien du sTTG est réécrit en explicitant un potentiel moiré modulé par une variation de phase lente à travers de l'échelle supermoiré. Puisque la modulation est lente, elle peut être considérée comme étant constante dans une cellule moirée. Si on traite le sTTG localement en adoptant les facteurs de phase constants, on revient aux solutions des modèles moirés du chapitre précédent.

Inspiré par l'intuition que les états du modèle exactes doivent localement ressembler les états obtenus par les modèles locaux, on propose alors une forme ansatz des fonctions d'onde du modèles exact, figurant une combinaison linéaire des fonctions d'onde locales habillées des fonctions de modulation qui varient lentement à l'échelle supermoirée. On injecte ensuite les fonctions d'onde ansatz dans l'équation de Schrödinger de l'Hamiltonien exacte, et intègre sur une cellule moirée. Nous obtenons ainsi une nouvelle équation qui concerne uniquement les fonctions de modulation. C'est un Hamiltonien effectif défini sur les bases des fonctions de modulation.

La forme des fonctions d'onde exacte nécessite de fixer la jauge des états locaux afin que les variations des fonctions de modulation, des fonctions d'onde locaux et de l'Hamiltonien effectif soient lisse and continue. On montre dans ce chapitre les principes pour fixer la

jauge et propose deux protocoles que nous avons utilisés dans notre pratique.

L'hamiltonien effectif décrit un fermion relativiste ayant une vitesse dépendante de l'espace. Il est couplé à un champ de jauge qui provient d'une connexion de Berry non abélienne. Dans le chapitre suivant, nous démontrons que ce champ de jauge joue le rôle d'un pseudo-champ magnétique. Cela entraîne l'apparition de l'effet Hall anormal dans les sTTGs.

La forme de l'Hamiltonien effectif dépend évidemment du choix de jauge. Alors que les propriétés physiques doivent être indépendantes de jauge. On vérifie que le changement de jauge conduit à une transformation unitaire de l'Hamiltonien effectif. Cela signifie que les propriétés physiques du modèle effectif sont en effet invariantes du choix de jauge.

Pour étudier les symétries du modèle effectif, on révèle un critère des états locaux permettant de vérifier la présence ou l'absence des symétries dans l'Hamiltonien effectif, sans se soucier de l'expression explicite des symétries du modèle effectif qui dépend aussi du choix de jauge.

La symétrie de translation est un cas particulier, car nous avons besoin de son expression exacte pour obtenir la forme explicite des fonctions de Bloch. Nous avons étudié les conditions sous lesquelles l'opérateur de translation par une période moiré s'exprime en une forme diagonale et simple.

A la fin du chapitre, on justifie qu'un état du niveau d'énergie typique supermoiré est dominé par les états locaux provenant des bandes les plus proches de l'énergie nulle. On réduit ainsi la dimension de l'Hamiltonien effectif à 2 ou 4.

Tous les travaux théoriques de ce chapitre établissent un cadre complet pour traiter le modèle de TTG dans le contexte d'une périodicité perturbée. Cela nous permet de procéder à la solution numérique du modèle effectif.

A.2.4 Chapitre 4 – Solution numérique du modèle supermoiré effectif à basse énergie

Ce chapitre se consacre à présenter en détail les données obtenues à chaque étape pour établir le modèle effectif et résoudre le problème. Les résultats obtenus sont également présentés. Deux types de TTG ont été résolus : avec un rapport d'angles de torsion d'environ 1 et 1/2.

Tout d'abord, nous résolvons le sTTG avec $\theta_1/\theta_2 \approx 1$. En fonction de la localisation

des états locaux dans la zone de Brillouin du modèle local, soit au point $\boldsymbol{\Gamma}_M$ soit au point $\boldsymbol{K}_M$, nous établissons deux modèles effectifs. Les états locaux sont obtenus en résolvant numériquement les modèles locaux définis sur des coordonnées supermoirées discrétisées. Pour chaque solution, nous fixons la jauge des états en effectuant une rotation dans le sous-espace des états choisis, de manière à obtenir deux nouveaux états qui diagonalisent l'opérateur σ_z projeté dans ce sous-espace. Pour fixer la phase globale des états locaux, nous choisissons deux états de référence et imposons que les éléments diagonaux de la matrice de recouvrement entre les états de référence et les états locaux soient réels et positifs. Une fois la jauge des états locaux fixée, nous pouvons calculer les éléments de la matrice de l'Hamiltonien effectif sur les coordonnées supermoirées. Pour résoudre le problème, une transformation de Fourier est nécessaire, ce qui ramène le modèle au réseau réciproque supermoiré. En diagonalisant l'Hamiltonien effectif transformé sur le réseau réciproque supermoiré, nous obtenons les états supermoirés et calculons la densité d'états.

Pour le sTTG avec $\theta_1/\theta_2 \approx 1/2$, les procédures sont identiques à celles décrites précédemment pour le modèle effectif basé sur les états locaux au point $\boldsymbol{\Gamma}_M$. Cependant, pour établir le modèle effectif basé sur les états locaux provenant du point $\boldsymbol{K}_M$, nous devons prendre en compte 4 états car ils sont tous les états les plus proches de l'énergie nulle. Cela modifie légèrement les procédures de fixation de la jauge. Nous avons alors utilisé un algorithme rapide pour fixer la jauge en utilisant 4 états de référence. La décomposition en valeurs singulières nous permet d'obtenir rapidement les états locaux avec les jauges fixées.

Dans ce chapitre, nous avons également présenté en détail les données pour montrer que la variation du modèle effectif sur les coordonnées supermoirées est lisse et continue. Les structures de bandes et les profils de densité d'états sont également présentés. L'évolution de la densité d'états en fonction des angles de torsion est également examinée.

Nos résultats mettent en évidence une redistribution significative des états dans les niveaux d'énergie en raison de la présence du champ de jauge. Ce champ de jauge engendre un effet similaire à celui d'un pseudo-champ magnétique. En comparant les profils de densité d'états obtenus à partir de la moyenne des modèles locaux, nous démontrons que les caractéristiques supermoirées ne peuvent être capturées par une simple moyenne incohérente des modèles locaux.

Un défi inattendu apparaît lorsque nous explorons le modèle effectif dans le régime des petits angles de torsion. Lorsque les angles de torsion deviennent petits, la vitesse du modèle effectif peut localement disparaître. Cela entraîne une singularité qui empêche la convergence de la solution numérique. Nous avons étudié cette singularité en utilisant un modèle 1D résoluble analytiquement. Les fonctions d'onde analytiques montrent une

divergence au point où la vitesse s'annule. La singularité de la vitesse localement nulle signifie que la physique d'un état supermoiré contient également d'importantes variations à l'échelle moiré. Malgré leurs longueurs distinctes, l'échelle moiré et l'échelle supermoiré sont à nouveau couplées aux petits angles de torsion, ce qui remet en question la validité de notre approche effective qui suppose une séparation des deux échelles.

A.2.5 Chapitre 5 – Conclusion

Dans le dernier chapitre, nous présentons un résumé des travaux effectués dans cette thèse. Nous commençons par dériver de manière simple et concise le modèle de Bistrizer-MacDonald pour le TBG. Ensuite, nous développons le modèle continu du TTG basé sur la description du modèle BM pour le couplage entre les couches adjacentes.

Dans un premier temps, nous résolvons le TTG hélicoïdal (sTTG) en utilisant l'approximation de la colinéarité entre les vecteurs moirés et un rapport rationnel des angles de torsion. Ce modèle sTTG approximatif peut être résolu dans le régime périodique moiré. Toutefois, afin d'étudier les cas où le rapport des angles présente une légère déviation par rapport à une valeur propre et où la non-colinéarité entre les vecteurs moirés intervient, nous développons un cadre théorique pour traiter le sTTG en le considérant comme un problème de périodicité perturbée. Nos résultats révèlent des caractéristiques supermoirées qui ne peuvent pas être capturées par la simple moyenne des modèles locaux.

Dans ce chapitre, nous discutons également des perspectives de recherche future. Cette approche n'est pas limitée aux seuls systèmes de graphène multicouche torsadé. D'autres systèmes physiques présentant deux périodicités légèrement décalées peuvent être étudiés dans ce cadre.

En relation avec les expériences, notre théorie permettra de mieux comprendre les effets du substrat en nitrure de bore hexagonal sur lequel les échantillons de graphène multicouche sont déposés.

Appendix B

Gauge invariance of effective model

In this appendix, we present a detailed demonstration of the gauge invariance of the effective model. The computation is performed term by term, ensuring a thorough analysis of each component.

We can examine how the effective Hamiltonian is transformed term by term. The transformed local energy matrix $E'_{nm}(\boldsymbol{R})$ is given by:

$$\begin{aligned} E'_{nm}(\boldsymbol{R}) =& \langle \varphi'_n(\boldsymbol{R})|H(\boldsymbol{R})|\varphi_m(\boldsymbol{R})\rangle = \sum_{n'm'} \xi^\dagger_{nn'}(\boldsymbol{R}) \langle \varphi_{n'}(\boldsymbol{R})|H(\boldsymbol{R})|\varphi_{m'}(\boldsymbol{R})\rangle \xi_{m'n}(\boldsymbol{R}) \\ =& \sum_{n'm'} \xi^\dagger_{nn'}(\boldsymbol{R}) E_{n'm'}(\boldsymbol{R}) \xi_{m'm}(\boldsymbol{R}). \end{aligned} \tag{B.1}$$

Similarly, the transformed velocity matrix $\boldsymbol{\Gamma}'_{nm}(\boldsymbol{R})$ is given by:

$$\boldsymbol{\Gamma}'_{nm}(\boldsymbol{R}) = \langle \varphi'_n(\boldsymbol{R})|\boldsymbol{\sigma}|\varphi'_m(\boldsymbol{R})\rangle = \sum_{n'm'} \xi^\dagger_{nn'}(\boldsymbol{R}) \langle \varphi_{n'}(\boldsymbol{R})|\boldsymbol{\sigma}|\varphi_{m'}\rangle \xi_{m'm}(\boldsymbol{R}). \tag{B.2}$$

The transformation of the gauge potential $A(\boldsymbol{R})$ is given by:

$$\begin{aligned} A'(\boldsymbol{R})_{nm}(\boldsymbol{R}) =& \langle \varphi'_n(\boldsymbol{R})|-i\boldsymbol{\nabla}_{\boldsymbol{R}}\cdot\boldsymbol{\sigma}|\varphi'_m(\boldsymbol{R})\rangle \\ =& \sum_{n'm'} \xi^\dagger_{nn'}(\boldsymbol{R}) \langle \varphi_{n'}(\boldsymbol{R})|-i\boldsymbol{\sigma}\cdot\boldsymbol{\nabla}_{\boldsymbol{R}}|\varphi_{m'}(\boldsymbol{R})\rangle \xi_{m'm}(\boldsymbol{R}) \\ & - i\xi^\dagger_{nn'}(\boldsymbol{R}) \langle \varphi_{n'}(\boldsymbol{R})|\boldsymbol{\sigma}|\varphi_{m'}(\boldsymbol{R})\rangle \cdot (\boldsymbol{\nabla}_{\boldsymbol{R}}\xi_{m'm}(\boldsymbol{R})) \\ =& \sum_{n'm'} \xi^\dagger_{nn'}(\boldsymbol{R}) A_{n'm'}(\boldsymbol{R}) \xi_{m'm} - i\sum_{n'm'} \xi^\dagger_{nn'}(\boldsymbol{R}) \boldsymbol{\Gamma}_{nm}\cdot(\boldsymbol{\nabla}_{\boldsymbol{R}}\xi_{m'm}(\boldsymbol{R})) \end{aligned} \tag{B.3}$$

At first sight, it seems that the unitary transformation only applies to the velocity term $\boldsymbol{\Gamma}(\boldsymbol{R})$ and not to the full kinetic term $-i\boldsymbol{\Gamma}(\boldsymbol{R})\cdot\boldsymbol{\nabla}_{\boldsymbol{R}}$. However, upon closer inspection, we find that the extra terms in the transformation of the velocity term and the gauge potential have opposite signs and cancel out when added together. Given that

$$\begin{aligned}
&\sum_{n'm'}\xi^{\dagger}_{nn'}(\boldsymbol{R})[-i\boldsymbol{\Gamma}'_{nm}\cdot\boldsymbol{\nabla}_{\boldsymbol{R}}\circ]\xi_{m'm}(\boldsymbol{R})\\
&=-i\{\sum_{n'm'}\xi^{\dagger}_{nn'}(\boldsymbol{R})\boldsymbol{\Gamma}_{nm}\varphi_{m'}(\boldsymbol{R})\xi_{m'm}(\boldsymbol{R})\}\cdot\boldsymbol{\nabla}_{\boldsymbol{R}}\circ-i\sum_{n'm'}\xi^{\dagger}_{nn'}(\boldsymbol{R})\boldsymbol{\Gamma}_{nm}\cdot(\boldsymbol{\nabla}_{\boldsymbol{R}}\xi_{m'm}(\boldsymbol{R}))\\
&=-i\boldsymbol{\Gamma}'_{nm}(\boldsymbol{R})\cdot\boldsymbol{\nabla}_{\boldsymbol{R}}\circ-i\sum_{n'm'}\xi^{\dagger}_{nn'}(\boldsymbol{R})\boldsymbol{\Gamma}_{nm}\cdot(\boldsymbol{\nabla}_{\boldsymbol{R}}\xi_{m'm}(\boldsymbol{R})),
\end{aligned}\tag{B.4}$$

we have

$$\begin{aligned}
&-i\boldsymbol{\Gamma}'_{nm}\cdot\boldsymbol{\nabla}_{\boldsymbol{R}}\circ\\
&=\sum_{n'm'}\xi^{\dagger}_{nn'}(\boldsymbol{R})[-i\boldsymbol{\Gamma}_{nm}\cdot\boldsymbol{\nabla}_{\boldsymbol{R}}]\xi_{m'm}(\boldsymbol{R})+i\sum_{n'm'}\xi^{\dagger}_{nn'}(\boldsymbol{R})\boldsymbol{\Gamma}_{nm}\cdot(\boldsymbol{\nabla}_{\boldsymbol{R}}\xi_{m'm}(\boldsymbol{R})).
\end{aligned}\tag{B.5}$$

As a result, we obtain

$$-i\boldsymbol{\Gamma}'(\boldsymbol{R})\cdot\boldsymbol{\nabla}_{\boldsymbol{R}}\circ+A'(\boldsymbol{R})=\xi^{\dagger}(\boldsymbol{R})\{-i\boldsymbol{\Gamma}(\boldsymbol{R})\cdot\boldsymbol{\nabla}_{\boldsymbol{R}}\circ+A(\boldsymbol{R})\}\xi(\boldsymbol{R}).\tag{B.6}$$

Appendix C

Symmetries of effective model

C.1 General principle

Now, let's examine the effective Hamiltonian at the coordinate $\boldsymbol{s}(\boldsymbol{R})$. We find:

$$\begin{aligned}\boldsymbol{\Gamma}_{nm}(\boldsymbol{s}(\boldsymbol{R})) &= \langle\psi_n(\boldsymbol{s}(\boldsymbol{R}))|\boldsymbol{\sigma}|\psi_m(\boldsymbol{s}(\boldsymbol{R}))\rangle \\ &= \sum_{n'm'} \zeta^{\dagger}_{nn'}(\boldsymbol{R})\,\langle\psi_{n'}(\boldsymbol{R})|S^{\dagger}\boldsymbol{\sigma}S|\psi_{m'}(\boldsymbol{R})\rangle\,\zeta_{m'm}(\boldsymbol{R}),\end{aligned} \tag{C.1}$$

and

$$\begin{aligned}&A_{nm}(\boldsymbol{s}(\boldsymbol{R})) = -i\,\langle\psi_n(\boldsymbol{s}(\boldsymbol{R}))|\boldsymbol{\nabla}_{\boldsymbol{s}(\boldsymbol{R})}\cdot\boldsymbol{\sigma}|\psi_m(\boldsymbol{s}(\boldsymbol{R}))\rangle \\ &= \sum_{n'm'} -i\zeta^{\dagger}_{nn'}(\boldsymbol{R})\,\langle\psi_{n'}(\boldsymbol{R})\big|S^{\dagger}\boldsymbol{\sigma}\cdot S\big|\boldsymbol{\nabla}_{\boldsymbol{s}(\boldsymbol{R})}\psi_{m'}(\boldsymbol{R})\rangle\,\zeta_{m'm}(\boldsymbol{R}) \\ &\quad - i\sum_{n'm'}\zeta^{\dagger}_{nn'}(\boldsymbol{R})\,\langle\psi_{n'}(\boldsymbol{R})|S^{\dagger}\boldsymbol{\sigma}S|\psi_{m'}(\boldsymbol{R})\rangle\cdot(\boldsymbol{\nabla}_{\boldsymbol{s}(\boldsymbol{R})}\zeta_{m'm}(\boldsymbol{R})).\end{aligned} \tag{C.2}$$

The onsite energy term $E(\boldsymbol{s}(\boldsymbol{R}))$ can be expressed as:

$$\begin{aligned}E_{nm}(\boldsymbol{s}(\boldsymbol{R})) &= \langle\psi_n(\boldsymbol{s}(\boldsymbol{R}))|\hat{H}_{\text{local}}(\boldsymbol{s}(\boldsymbol{R}))|\psi_m(\boldsymbol{s}(\boldsymbol{R}))\rangle \\ &= \sum_{n'm'}\zeta^{\dagger}_{nn'}(\boldsymbol{R})\,\langle\psi_{n'}(\boldsymbol{R})|S^{\dagger}\hat{H}_{\text{local}}(\boldsymbol{s}(\boldsymbol{R}))S|\psi_{m'}(\boldsymbol{R})\rangle\,\zeta_{m'm}(\boldsymbol{R}) \\ &= \sum_{n'm'}\zeta^{\dagger}_{nn'}(\boldsymbol{R})\,\langle\psi_{n'}(\boldsymbol{R})|\hat{H}_{\text{local}}(\boldsymbol{R})|\psi_{m'}(\boldsymbol{R})\rangle\,\zeta_{m'm}(\boldsymbol{R}) \\ &= \sum_{n'm'}\zeta^{\dagger}_{nn'}(\boldsymbol{R})E_{n'm'}(\boldsymbol{R})\zeta_{m'm}(\boldsymbol{R})\end{aligned} \tag{C.3}$$

The transformation of $E(\boldsymbol{R})$ in Eq. (C.3) indicates that the only possible unitary transformation on the effective Hamiltonian is $\zeta(\boldsymbol{R})$. Therefore, for a symmetry to be valid, it is required that:

$$S^{\dagger}(\boldsymbol{\nabla}_{\boldsymbol{s}(\boldsymbol{R})}) \cdot \boldsymbol{\sigma} S = S^{\dagger}\boldsymbol{\sigma} S \cdot \boldsymbol{\nabla}_{\boldsymbol{s}(\boldsymbol{R})} = \boldsymbol{\sigma} \cdot \boldsymbol{\nabla}_{\boldsymbol{R}}. \tag{C.4}$$

Once Eq. (3.66) is satisfied, Eq. (C.1) immediately leads to

$$\begin{aligned}
&- i\boldsymbol{\Gamma}_{nm}(\boldsymbol{s}(\boldsymbol{R})) \cdot \boldsymbol{\nabla}_{\boldsymbol{s}(\boldsymbol{R})} \circ \\
&= -i \sum_{n'm'} \zeta^{\dagger}_{nn'}(\boldsymbol{R}) \left\langle \psi_{n'}(\boldsymbol{R}) | S^{\dagger}\boldsymbol{\sigma} S | \psi_{m'}(\boldsymbol{R}) \right\rangle \cdot \boldsymbol{\nabla}_{\boldsymbol{s}(\boldsymbol{R})} \circ \zeta_{m'm}(\boldsymbol{R}) \\
&\quad + i \sum_{n'm'} \zeta^{\dagger}_{nn'}(\boldsymbol{R}) \left\langle \psi_{n'}(\boldsymbol{R}) | S^{\dagger}\boldsymbol{\sigma} S | \psi_{m'}(\boldsymbol{R}) \right\rangle \cdot (\boldsymbol{\nabla}_{\boldsymbol{s}(\boldsymbol{R})} \zeta_{m'm}(\boldsymbol{R})) \\
&= -i \sum_{n'm'} \zeta^{\dagger}_{nn'}(\boldsymbol{R}) \left\langle \psi_{n'}(\boldsymbol{R}) | \boldsymbol{\sigma} | \psi_{m'}(\boldsymbol{R}) \right\rangle \cdot \boldsymbol{\nabla}_{\boldsymbol{R}} \circ \zeta_{m'm}(\boldsymbol{R}) \\
&\quad + i \sum_{n'm'} \zeta^{\dagger}_{nn'}(\boldsymbol{R}) \left\langle \psi_{n'}(\boldsymbol{R}) | \boldsymbol{\sigma} | \psi_{m'}(\boldsymbol{R}) \right\rangle \cdot (\boldsymbol{\nabla}_{\boldsymbol{R}} \zeta_{m'm}(\boldsymbol{R})) \\
&= \sum_{n'm'} \zeta^{\dagger}_{nn'}(\boldsymbol{R}) - i\boldsymbol{\Gamma}_{n'm'}(\boldsymbol{R}) \cdot \boldsymbol{\nabla}_{\boldsymbol{R}} \circ \zeta_{m'm}(\boldsymbol{R}) \\
&\quad + i \sum_{n'm'} \zeta^{\dagger}_{nn'}(\boldsymbol{R}) \left\langle \psi_{n'}(\boldsymbol{R}) | \boldsymbol{\sigma} | \psi_{m'}(\boldsymbol{R}) \right\rangle \cdot (\boldsymbol{\nabla}_{\boldsymbol{R}} \zeta_{m'm}(\boldsymbol{R})).
\end{aligned} \tag{C.5}$$

and

$$\begin{aligned}
A_{nm}(\boldsymbol{s}(\boldsymbol{R})) = &\sum_{n'm'} \zeta^{\dagger}_{nn'}(\boldsymbol{R}) A_{n'm'}(\boldsymbol{R}) \zeta_{m'm}(\boldsymbol{R}) \\
&- i \sum_{n'm'} \zeta^{\dagger}_{nn'}(\boldsymbol{R}) \left\langle \psi_{n'}(\boldsymbol{R}) | \boldsymbol{\sigma} | \psi_{m'}(\boldsymbol{R}) \right\rangle \cdot (\boldsymbol{\nabla}_{\boldsymbol{R}} \zeta_{m'm}(\boldsymbol{R})).
\end{aligned} \tag{C.6}$$

Again, the extra term cancels out in the sum of $-i\boldsymbol{\Gamma}(\boldsymbol{s}(\boldsymbol{R})) \cdot \boldsymbol{\nabla}_{\boldsymbol{s}(\boldsymbol{R})}$ and $A(\boldsymbol{s}(\boldsymbol{R}))$.

With Eqs. (3.64) and (3.66) being valid simultaneously, the effective Hamiltonian verifies

$$H_{\text{eff}}(\boldsymbol{s}(\boldsymbol{R})) = \zeta^{\dagger}(\boldsymbol{R}) H_{\text{eff}}(\boldsymbol{R}) \zeta(\boldsymbol{R}). \tag{C.7}$$

This is a symmetry of the effective model because $\boldsymbol{R}$ is now the real space coordinates of the wave functions instead of a parameter.

It is now clear that the symmetry of the effective model is closely related to the transform of the local Hamiltonian under symmetry operators. The exact unitary transform of the effective Hamiltonian under a valid symmetry operation, $\zeta(\boldsymbol{R})$, depends on the symmetry and also the choice of gauge for local states.

In addition, the gauge invariance can be regarded as a special case of symmetry where

$S = \mathbb{1}$ and $\boldsymbol{s}(\boldsymbol{R}) = \boldsymbol{R}$.

C.2 Translational symmetry

As demonstrated in Chapter 2, the phase factors have a period of π for equal twist angles and $2\pi/3$ for $\theta_1/\theta_2 = 1/2$ or 2. The periodicity of phase factors reflects a corresponding periodicity on the supermoiré coordinates. Here, we generalize the discussion of the phase period and deduce the size of the supermoiré periodic unit cell.

For the local models it is ways possible to gauge out the first phase factor so that $\phi_1(\boldsymbol{R}) = 0$. Let us massage the forms of $T_{12}(\boldsymbol{r}, -\boldsymbol{\phi})$ and $T_{23}(\boldsymbol{r}, \boldsymbol{\phi})$:

$$\begin{aligned} T_{12}(\boldsymbol{r}, -\boldsymbol{\phi}) &= e^{-i\phi_1} e^{-ip\boldsymbol{q}_1\cdot\boldsymbol{r}} (T_1 + T_2 e^{ip\boldsymbol{b}_1\cdot\boldsymbol{r}} e^{-i(\phi_2-\phi_1)} + T_3 e^{ip\boldsymbol{b}_2\cdot\boldsymbol{r}} e^{-i(\phi_3-\phi_1)}); \\ T_{23}(\boldsymbol{r}, \boldsymbol{\phi}) &= e^{i\phi_1} e^{-iq\boldsymbol{q}_1\cdot\boldsymbol{r}} (T_1 + T_2 e^{iq\boldsymbol{b}_1\cdot\boldsymbol{r}} e^{i(\phi_2-\phi_1)} + T_3 e^{iq\boldsymbol{b}_2\cdot\boldsymbol{r}} e^{i(\phi_3-\phi_1)}), \end{aligned} \tag{C.8}$$

where $\boldsymbol{b}_1$ and $\boldsymbol{b}_2$ are the base vectors generating the moiré reciprocal lattice, given by

$$\begin{aligned} \boldsymbol{b}_1 &= \boldsymbol{q}_1 - \boldsymbol{q}_2; \\ \boldsymbol{b}_2 &= \boldsymbol{q}_1 - \boldsymbol{q}_3. \end{aligned} \tag{C.9}$$

Correspondingly, the Bravais lattice generator vectors are $\boldsymbol{a}_1$ and $\boldsymbol{a}_2$ satisfying $\boldsymbol{a}_i \cdot \boldsymbol{b}_j = 2\pi\delta_{ij}$.

To find the period ϕ_T in the phase factors, we expect that ϕ_T can be canceled simultaneously in $T_{12}(\boldsymbol{r}, -\boldsymbol{\phi})$ and $T_{23}(\boldsymbol{r}, \boldsymbol{\phi})$ by shifting the origin of the $\boldsymbol{r}$ coordinates to $\boldsymbol{r}_0$.

If ϕ_2 is shifted by to $\phi_2 + \phi_T$ with the convention $\phi_T > 0$, then the phase period needs to satisfy

$$\begin{cases} p\boldsymbol{b}_1 \cdot \boldsymbol{r}_0 = \phi_T + 2N\pi \\ p\boldsymbol{b}_2 \cdot \boldsymbol{r}_0 = 0 \\ q\boldsymbol{b}_1 \cdot \boldsymbol{r}_0 = -\phi_T + 2M\pi \\ q\boldsymbol{b}_2 \cdot \boldsymbol{r}_0 = 0 \end{cases}, \tag{C.10}$$

where $N, M \in \mathbb{Z}$. It is immediate that

$$\phi_T = 2\pi \frac{pM - qN}{p + q}. \tag{C.11}$$

The period in phase is defined by the smallest *non-zero* ϕ_T. Consequently we gave

$$\boldsymbol{b}_1 \cdot \boldsymbol{r}_0 = 2\pi \frac{M + N}{p + q}, \tag{C.12}$$

leading to

$$\boldsymbol{r}_0 = \frac{M+N}{p+q}\boldsymbol{a}_1. \tag{C.13}$$

Then to explore the phase period along ϕ_3, we need to solve the equations:

$$\begin{cases} p\boldsymbol{b}_1 \cdot \boldsymbol{r}_0 = 0 \\ p\boldsymbol{b}_2 \cdot \boldsymbol{r}_0 = \phi_T + 2N\pi \\ q\boldsymbol{b}_1 \cdot \boldsymbol{r}_0 = 0 \\ q\boldsymbol{b}_2 \cdot \boldsymbol{r}_0 = -\phi_T + 2M\pi \end{cases}. \tag{C.14}$$

The value of ϕ_T in Eq. (C.11) also satisfies the above equations. But $\boldsymbol{r}_0$ now satisfies

$$\boldsymbol{b}_2 \cdot \boldsymbol{r}_0 = 2\pi\frac{M+N}{p+q}, \tag{C.15}$$

which leads to

$$\boldsymbol{r}_0 = \frac{M+N}{p+q}\boldsymbol{a}_2. \tag{C.16}$$

In summary, the phase period is given by the smallest non-zero value of Eq. (C.11), i.e.

$$\phi_T(p,q) = 2\pi \overset{+}{\min}(\frac{pM-qN}{p+q}). \tag{C.17}$$

In fact, since p and q cannot be even numbers at the same time as they are coprime numbers, the smallest positive value of $pM - qN$ has to be 1. Finally we have

$$\phi_T(p,q) = \frac{2\pi}{p+q}. \tag{C.18}$$

The results can be verified by comparing them with the findings in the previous chapter. In the case where the angles are equal, specifically when $p = q = 1$, the minimum positive value of the period is $\phi_T(1,1) = \pi$. Furthermore, when the ratio of θ_1 to θ_2 is $1/2$ and we have $p = 1$ and $q = 2$, it leads to $\phi_T(1,2) = 2\pi/3$. Both of these results align coherently with the conclusions presented here.

We can express the phase differences in Eq. (C.8) in terms of the supermoiré coordinates as follows:

$$\begin{aligned} \phi_2 - \phi_1 &= (\delta\boldsymbol{q}_2 - \delta\boldsymbol{q}_1)\cdot\boldsymbol{R} = \boldsymbol{b}_1^{MM}\cdot\boldsymbol{R} \\ \phi_3 - \phi_1 &= (\delta\boldsymbol{q}_3 - \delta\boldsymbol{q}_1)\cdot\boldsymbol{R} = \boldsymbol{b}_2^{MM}\cdot\boldsymbol{R} \end{aligned}, \tag{C.19}$$

Here, we introduce the notation $\boldsymbol{b}_1^{MM} = \delta\boldsymbol{q}_2 - \delta\boldsymbol{q}_1$ and $\boldsymbol{b}_2^{MM} = \delta\boldsymbol{q}_3 - \delta\boldsymbol{q}_1$ to represent the

generating vectors of the supermoiré reciprocal lattice. These vectors define the supermoiré Bravais lattice base vectors $\boldsymbol{a}_i^{MM}$, where $i = 1, 2$, and satisfy the relation $\boldsymbol{a}_i^{MM} \cdot \boldsymbol{b}_j^{MM} = 2\pi\delta ij$.

A phase shift along ϕ_2 by $2\pi/(p+q)$ corresponds to a displacement of $\boldsymbol{R}$ by $\boldsymbol{a}_1^{MM}$, which generates a phase shift of $\boldsymbol{b}_1^{MM} \cdot \boldsymbol{a}_1^{MM}/(p+q) = 2\pi/(p+q)$. This explains why the vectors $\delta\boldsymbol{q}_j$ in Eq. (3.3) are divided by $p+q$. Otherwise, the resulting supermoiré period would be $(p+q)$ times larger than the smallest value.

Similarly, shifting the phase along ϕ_3 is equivalent to displacing $\boldsymbol{R}$ by $\boldsymbol{a}_2^{MM}$. Therefore, $\boldsymbol{a}_1^{MM}$ and $\boldsymbol{a}_2^{MM}$ represent the supermoiré periods over which the spectrum of the local model is restored to its original form. The supermoiré lattice in real space is, therefore, a triangular lattice defined by $\boldsymbol{a}_1^{MM}$ and $\boldsymbol{a}_2^{MM}$.

In general, the supermoiré periodicity of the local Hamiltonian can be expressed as:

$$H_{\text{local}}(\boldsymbol{r} - \boldsymbol{r}_0; \boldsymbol{\phi}(\boldsymbol{R} + \boldsymbol{a}_{1/2}^{MM})) = U H_{\text{local}}(\boldsymbol{r}; \boldsymbol{\phi}(\boldsymbol{R}))U^\dagger. \tag{C.20}$$

It remains to fix the form of the unitary matrix U that compensates for the extra global phase factor along with in $T_{12}(\boldsymbol{r}; \boldsymbol{\phi}(\boldsymbol{R}))$ and $T_{23}(\boldsymbol{r}; \boldsymbol{\phi}(\boldsymbol{R}))$ caused by the shift of coordinates both in $\boldsymbol{r}$ and $\boldsymbol{R}$. Given that

$$T_{12}(\boldsymbol{r} - \boldsymbol{r}_0, -\boldsymbol{\phi}(\boldsymbol{R} + \boldsymbol{a}_{1/2}^{MM})) = e^{i\varphi_{12}} T_{12}(\boldsymbol{r}; -\boldsymbol{\phi}(\boldsymbol{R}))$$

and

$$T_{23}(-(\boldsymbol{r} - \boldsymbol{r}_0), -\phi(\boldsymbol{R} + \boldsymbol{a}_{1/2}^{MM})) = e^{i\varphi_{23}} T_{23}(-\boldsymbol{r}; -\boldsymbol{\phi}(\boldsymbol{R}))$$

with

$$\varphi_{12} = \boldsymbol{q}_1 \cdot \boldsymbol{r}_0 - \frac{\delta q_1 \cdot \boldsymbol{a}_{1/2}^{MM}}{p+q} = \frac{2\pi}{3(p+q)} \left(1 - p\,(N+M)\right), \tag{C.21}$$

and

$$\varphi_{23} = -\boldsymbol{q}_1 \cdot \boldsymbol{r}_0 - \frac{\delta q_1 \cdot \boldsymbol{a}_{1/2}^{MM}}{p+q} = \frac{2\pi}{3(p+q)} \left(1 + q\,(N+M)\right). \tag{C.22}$$

They lead to

$$U = \begin{pmatrix} e^{-i\varphi_{12}} & & \\ & 1 & \\ & & e^{-i\varphi_{23}} \end{pmatrix}_{\text{layer}} = \begin{pmatrix} \ddots & & \\ & e^{i\phi_l} & \\ & & \ddots \end{pmatrix}_{\text{layer}} \tag{C.23}$$

with

$$\phi_l = \begin{cases} -\varphi_{12} & \text{if } l = 1 \\ 1 & \text{if } l = 1 \\ -\varphi_{23} & \text{if } l = -1 \end{cases} \tag{C.24}$$

U cancels out the extra global phase in front of the interlayer hopping potentials due to the shift of both moiré and supermoiré coordinates. With the shift of the moiré coordinates taken into account, the translational symmetry operator is expressed as

$$S = U e^{i\hat{\boldsymbol{k}}_{\boldsymbol{r}} \cdot \boldsymbol{r}_0}, \tag{C.25}$$

where $\hat{\boldsymbol{k}}_{\boldsymbol{r}} = -i\boldsymbol{\nabla}_{\boldsymbol{r}}$ acts on the moiré coordinates only. Then the validity of Eq. (3.66) in terms of the translational symmetry is obvious. Because U acts on the layer degree of freedom and $e^{i\hat{\boldsymbol{k}}_{\boldsymbol{r}} \cdot \boldsymbol{r}_0}$ operates only on the $\boldsymbol{r}$ degree of freedom, $U e^{i\hat{\boldsymbol{k}}_{\boldsymbol{r}} \cdot \boldsymbol{r}_0}$ trivially commutes with $\boldsymbol{\sigma}$, giving

$$U^\dagger e^{-i\hat{\boldsymbol{k}}_{\boldsymbol{r}} \cdot \boldsymbol{r}_0} \boldsymbol{\sigma} \cdot \boldsymbol{\nabla}_{\boldsymbol{R}} e^{i\hat{\boldsymbol{k}}_{\boldsymbol{r}} \cdot \boldsymbol{r}_0} U = \boldsymbol{\sigma} \cdot \boldsymbol{\nabla}_{\boldsymbol{R}}. \tag{C.26}$$

The effective Hamiltonian is periodic in the sense that

$$H_{\text{eff}}(\boldsymbol{R} + \boldsymbol{a}_{1/2}^{mm})) = \zeta_{\mathcal{T}}^\dagger H_{\text{eff}}(\boldsymbol{R}) \zeta_{\mathcal{T}}, \tag{C.27}$$

where $\zeta_{\mathcal{T}}$ is the unitary matrix relating two gauge-fixed local states whose supermoiré coordinates differ by a supermoiré period $\boldsymbol{a}_1^{MM}$ or $\boldsymbol{a}_2^{MM}$:

$$\left|\psi_n(\boldsymbol{R} + \boldsymbol{a}_{1/2}^{mm})\right\rangle = e^{i\hat{\boldsymbol{k}}_{\boldsymbol{r}} \cdot \boldsymbol{r}_0} U \sum_m \left|\psi_m(\boldsymbol{R})\right\rangle \zeta_{\mathcal{T}mn}. \tag{C.28}$$

Eq. (C.27) directly enables the application of the Bloch's theorem. The eigenfunctions of $H_{\text{eff}}(\boldsymbol{R})$, noted $\boldsymbol{F}_{\boldsymbol{k}}(\boldsymbol{R})$, has translational symmetry on the supermoiré coordinates manifested by

$$\boldsymbol{F}_{\boldsymbol{k}}(\boldsymbol{R} + \boldsymbol{a}_{1/2}^{MM}) = e^{i\boldsymbol{k} \cdot \boldsymbol{a}_{1/2}^{MM}} \zeta_{\mathcal{T}}^\dagger \boldsymbol{f}_{\boldsymbol{k}}(\boldsymbol{R}), \tag{C.29}$$

where $\boldsymbol{k}$ is a wave vector inside the *supermoiré* Brillouin zone, and the Bloch function defined by

$$\boldsymbol{f}_{\boldsymbol{k}}(\boldsymbol{R}) = [f_1(\boldsymbol{R}), \cdots, f_N(\boldsymbol{R})]^T \tag{C.30}$$

is a completely periodic functions by a translation of supermoiré lattice vector:

$$\boldsymbol{f}_{\boldsymbol{k}}(\boldsymbol{R} + \boldsymbol{a}_{1/2}^{MM}) = \boldsymbol{f}_{\boldsymbol{k}}(\boldsymbol{R}). \tag{C.31}$$

$\boldsymbol{f}_{\boldsymbol{k}}(\boldsymbol{R})$ can therefore be expanded on the discrete Fourier bases on the supermoiré reciprocal

lattice (SRL):

$$\boldsymbol{f_k}(\boldsymbol{R}) = \sum_{\boldsymbol{Q}\in \mathrm{SRL}} \boldsymbol{f_k}(\boldsymbol{Q}) e^{-i\boldsymbol{Q}\cdot\boldsymbol{R}}. \tag{C.32}$$

The final form of the wave function of the effective model is

$$\boldsymbol{F_k}(\boldsymbol{R}) = e^{i\boldsymbol{k}\cdot\boldsymbol{R}} \mathcal{T}(\boldsymbol{R}) \boldsymbol{f_k}(\boldsymbol{R}), \tag{C.33}$$

where $\mathcal{T}(\boldsymbol{R})$ is a unitary matrix satisfying

$$\mathcal{T}(\boldsymbol{R} + \boldsymbol{a}_{1/2}^{MM}) = \zeta_{\mathcal{T}}^{\dagger} \mathcal{T}(\boldsymbol{R}). \tag{C.34}$$

Knowing the exact form of $\mathcal{T}(\boldsymbol{R})$ is therefore crucial for the implementation of the solution of the effective model. To express $\mathcal{T}(\boldsymbol{R})$, it is then imperative to find out the exact expression of $\zeta_{\mathcal{T}}$.

Note that when the gauge-fixing operator $\hat{O}$ is chosen to act fully on the *sublattice* degrees of freedom, such as σ_z, the diagonal condition in Eq.(3.70) is immediately satisfied for ζ_t. Hence, we have $\zeta_{\mathcal{T}nm} = e^{i\phi_n}\delta_{nm}$. With this, Eq.(C.28) can be written as:

$$\left|\psi_n(\boldsymbol{R} + \boldsymbol{a}_{1/2}^{MM})\right\rangle = e^{i\hat{\boldsymbol{k}}_{\boldsymbol{r}}\cdot\boldsymbol{r}_0} U \left|\psi_n(\boldsymbol{R})\right\rangle e^{i\phi_n}. \tag{C.35}$$

To determine $\zeta_{\mathcal{T}nm}$, i.e., $e^{i\phi_n}$, we can utilize the second gauge-fixing condition that $\langle g_n|\psi_n(\boldsymbol{R})\rangle \in \mathbb{R}^+$ and $\left\langle g_n\middle|\psi_n(\boldsymbol{R} + \boldsymbol{a}_{1/2}^{MM})\right\rangle \in \mathbb{R}^+$ must both be true simultaneously.

In general a reference state can be expanded on the natural bases $\{|\boldsymbol{Q}, \alpha, l\rangle\}$ that define the local TTG model:

$$|g_n\rangle = \sum_{\boldsymbol{Q},\alpha,l} g_n^{\boldsymbol{Q},\alpha,l} |\boldsymbol{Q}, \alpha, l\rangle \tag{C.36}$$

where $\boldsymbol{Q}, \alpha$ and l represent the momentum, sublattice and layer degrees of freedom, respectively. It leads to

$$\begin{aligned} \left\langle g_n\middle|\psi_n(\boldsymbol{R} + \boldsymbol{a}_{1/2}^{MM})\right\rangle =& \ \langle g_n| e^{i\boldsymbol{k}_{\boldsymbol{r}}\cdot\boldsymbol{r}_0} U |\psi_n(\boldsymbol{R})\rangle \, e^{i\phi_n} \\ =& \ e^{i\phi_n} \sum_{\boldsymbol{Q},\alpha,l} g_n^{\boldsymbol{Q},\alpha,l*} e^{i\boldsymbol{Q}\cdot\boldsymbol{r}_0} e^{i\phi_l} u_n^{\boldsymbol{Q},\alpha,l}(\boldsymbol{R}) \in \mathbb{R}^+, \end{aligned} \tag{C.37}$$

where we have also used the expansion $|\psi_n(\boldsymbol{R})\rangle = \sum_{\boldsymbol{Q},\alpha,l} u_n^{\boldsymbol{Q},\alpha,l}(\boldsymbol{R}) |\boldsymbol{Q}, \alpha, l\rangle$. The phase ϕ_n can be determined as:

$$\phi_n = -\arg\Big(\sum_{\boldsymbol{Q},\alpha,l} g_n^{\boldsymbol{Q},\alpha,l*} e^{i\boldsymbol{Q}\cdot\boldsymbol{r}_0} e^{i\phi_l} u_n^{\boldsymbol{Q},\alpha,l}(\boldsymbol{R})\Big). \tag{C.38}$$

Then the matrix $\mathcal{T}(\boldsymbol{R})$ can be written as a diagonal matrix:

$$\mathcal{T}(\boldsymbol{R}) = \begin{pmatrix} \ddots & & \\ & e^{i\tau_n(\boldsymbol{R})} & \\ & & \ddots \end{pmatrix}, \tag{C.39}$$

where $\mathcal{T}(\boldsymbol{R})$ is carefully designed so that:

$$\tau_n(\boldsymbol{R} + \boldsymbol{a}_{1/2}^{MM}) = \phi_n(\boldsymbol{R}). \tag{C.40}$$

The ϕ_n calculated above depends on the local wave function at $\boldsymbol{R}$ and is therefore a function of $\boldsymbol{R}$, which complicates the computation of $\mathcal{T}(\boldsymbol{R})$.

Now we demonstrate that by making specific choices of reference states $|g_n\rangle$, we can greatly simplify the computation by ensuring that ϕ_n does not depend on $\boldsymbol{R}$. This will allow us to obtain a simple expression for $\mathcal{T}(\boldsymbol{R})$.

Once again, we observe that $e^{i\hat{\boldsymbol{k}}_{\boldsymbol{r}}\cdot\boldsymbol{r}_0}U$ affects only the $\boldsymbol{r}$ and layer degrees of freedom, while $\hat{\boldsymbol{k}}_{\boldsymbol{r}}$ measures the moiré momentum. Consequently, if we choose $|g_n\rangle$ to be a pure state in terms of momentum and layer degrees of freedom, for instance:

$$|g_n\rangle = g_n(A)\,|\boldsymbol{Q}, A, l\rangle + g_n(B)\,|\boldsymbol{Q}, B, l\rangle\,, \tag{C.41}$$

with $|g_n(A)|^2 + |g_n(B)|^2 = 1$, we immediately obtain:

$$\left\langle g_n \middle| \psi_n(\boldsymbol{R} + \boldsymbol{a}_{1/2}^{MM}) \right\rangle = e^{i\phi_n} e^{i\boldsymbol{Q}\cdot\boldsymbol{r}_0} e^{i\phi_l} \left\langle g_n | \psi_n(\boldsymbol{R}) \right\rangle. \tag{C.42}$$

Since $\langle g_n|\psi_n(\boldsymbol{R})\rangle$ is real and positive due to gauge fixing, ϕ_n only needs to compensate for $\boldsymbol{Q}\cdot\boldsymbol{r}_0 + \phi_l$, i.e.:

$$\phi_n = -\boldsymbol{Q}\cdot\boldsymbol{r}_0 - \phi_l. \tag{C.43}$$

With this choice, ϕ_n becomes a constant once the gauge of local states is fixed. Consequently, the diagonal entries of $\mathcal{T}(\boldsymbol{R})$ are given by:

$$\tau_n(\boldsymbol{R}) = e^{i\boldsymbol{p}_n\cdot\boldsymbol{R}}, \tag{C.44}$$

where $\boldsymbol{b}_1^{MM} = \delta\boldsymbol{q}_2 - \delta\boldsymbol{q}_1$ and $\boldsymbol{b}_2^{MM} = \delta\boldsymbol{q}_3 - \delta\boldsymbol{q}_1$ are the generating vectors of the supermoiré reciprocal lattice. Here, we have introduced:

$$\boldsymbol{p}_n = \frac{\phi_n}{2\pi}(\boldsymbol{b}_1^{MM} + \boldsymbol{b}_2^{MM}). \tag{C.45}$$

C.3 C_{3z} symmetry

For a local Hamiltonian $H_{\text{local}}(\boldsymbol{r};\boldsymbol{\phi}(\boldsymbol{R}))$ that does not necessarily has C_{3z} symmetry, when transformed by $C_{3z}=e^{2i\pi\sigma_z/3}$, its moiré coordinate is sent to $\boldsymbol{r}\to\hat{R}_{2\pi/3}\boldsymbol{r}$. We can confirm that its supermoiré coordinate is similarly sent to $\boldsymbol{R}\to\hat{R}_{2\pi/3}\boldsymbol{R}$. This can be observed by examining the interlayer hopping potential, such as $T_{12}(\boldsymbol{r};-\boldsymbol{\phi}(\boldsymbol{R}))$:

$$\begin{aligned}
&e^{2i\pi\sigma_z/3}T_{12}(\boldsymbol{r};-\boldsymbol{\phi}(\boldsymbol{R}))e^{-2i\pi\sigma_z/3}\\
&=e^{2i\pi\sigma_z/3}(T_1e^{-i\boldsymbol{q}_1\cdot\boldsymbol{r}}e^{-i\delta\boldsymbol{q}_1\cdot\boldsymbol{R}/(p+q)}+T_2e^{-i\boldsymbol{q}_2\cdot\boldsymbol{r}}e^{-i\delta\boldsymbol{q}_2\cdot\boldsymbol{R}/(p+q)}+T_3e^{-i\boldsymbol{q}_3\cdot\boldsymbol{r}}e^{-i\delta\boldsymbol{q}_3\cdot\boldsymbol{R}/(p+q)})e^{-2i\pi\sigma_z/3}\\
&=T_2e^{-i\boldsymbol{q}_1\cdot\boldsymbol{r}}e^{-i\delta\boldsymbol{q}_1\cdot\boldsymbol{R}/(p+q)}+T_3e^{-i\boldsymbol{q}_2\cdot\boldsymbol{r}}e^{-i\delta\boldsymbol{q}_2\cdot\boldsymbol{R}/(p+q)}+T_1e^{-i\boldsymbol{q}_3\cdot\boldsymbol{r}}e^{-i\delta\boldsymbol{q}_3\cdot\boldsymbol{R}/(p+q)}\\
&=T_{12}(\hat{R}_{2\pi/3}\boldsymbol{r};-\boldsymbol{\phi}(\hat{R}_{2\pi/3}\boldsymbol{R})).
\end{aligned}\tag{C.46}$$

Similarly, it can be found that

$$e^{2i\pi\sigma_z/3}T_{23}(\boldsymbol{r};\boldsymbol{\phi}(\boldsymbol{R}))e^{-2i\pi\sigma_z/3}=T_{23}(\hat{R}_{2\pi/3}\boldsymbol{r};\boldsymbol{\phi}(\hat{R}_{2\pi/3}\boldsymbol{R})).$$

The transformed $T_{12}(\boldsymbol{r};-\boldsymbol{\phi}(\boldsymbol{R}))$ and $T_{23}(\boldsymbol{r};\boldsymbol{\phi}(\boldsymbol{R}))$ are independent of the ratio of the twist angles. The hint from their transformation is that the $\boldsymbol{s}_{C_{3z}}(\boldsymbol{R})$ for C_{3z} symmetry is given by:

$$\boldsymbol{s}_{C_{3z}}(\boldsymbol{R})=\hat{R}_{2\pi/3}\boldsymbol{R}.\tag{C.47}$$

Now we verify Eq. (3.66). To compute $e^{2i\pi\sigma_z/3}\boldsymbol{\sigma}e^{-2i\pi\sigma_z/3}$, it is convenient to use the expressions:

$$e^{i\theta/2}\sigma_xe^{-i\theta/2}=\cos(\theta)\sigma_x-\sin(\theta)\sigma_y,\tag{C.48}$$

and

$$e^{i\theta/2}\sigma_ye^{-i\theta/2}=\sin(\theta)\sigma_x+\cos(\theta)\sigma_y.\tag{C.49}$$

Then lead to

$$e^{2i\pi\sigma_z/3}\sigma_xe^{-2i\pi\sigma_z/3}=\cos(2\pi/3)\sigma_x+\sin(2\pi/3)\sigma_y,\tag{C.50}$$

and

$$e^{2i\pi\sigma_z/3}\sigma_ye^{-2i\pi\sigma_z/3}=-\sin(2\pi/3)\sigma_x+\cos(2\pi/3)\sigma_y.\tag{C.51}$$

where

$$\boldsymbol{\nabla}_{\hat{R}_\theta\boldsymbol{R}}\circ=\hat{R}_\theta^{-1}\boldsymbol{\nabla}_{\boldsymbol{R}}\circ\,.\tag{C.52}$$

Therefore, we obtain

$$\begin{aligned}
&e^{2i\pi\sigma_z/3}\boldsymbol{\sigma}e^{-2i\pi\sigma_z/3}\cdot\boldsymbol{\nabla}_{\hat{R}_{2\pi/3}\boldsymbol{R}}\circ \\
&=\begin{bmatrix}\sigma_x & \sigma_y\end{bmatrix}\begin{bmatrix}\cos(2\pi/3) & -\sin(2\pi/3)\\ \sin(2\pi/3) & \cos(2\pi/3)\end{bmatrix}\begin{bmatrix}\cos(2\pi/3) & \sin(2\pi/3)\\ -\sin(2\pi/3) & \cos(2\pi/3)\end{bmatrix}\begin{bmatrix}\partial_x\circ\\ \partial_y\circ\end{bmatrix} \\
&=\boldsymbol{\sigma}\cdot\boldsymbol{\nabla}_{\boldsymbol{R}}\circ,
\end{aligned} \tag{C.53}$$

where $\partial_{x/y}\circ$ acts also only on the modulation functions of the ansatz wave functions and we have used

$$\hat{R}^{-1}_{2\pi/3}=\begin{bmatrix}\cos(2\pi/3) & \sin(2\pi/3)\\ -\sin(2\pi/3) & \cos(2\pi/3)\end{bmatrix}. \tag{C.54}$$

As a result, both the symmetry criteria are satisfied and C_{3z} symmetry is hence verified in the effective model, transforming the effective Hamiltonian in such a way that

$$\zeta^{\dagger}_{C_{3z}}(\boldsymbol{R})H_{\text{eff}}(\boldsymbol{R})\zeta_{C_{3z}}(\boldsymbol{R})=H_{\text{eff}}(\hat{R}_{2\pi/3}\boldsymbol{R}). \tag{C.55}$$

The exact form of $\zeta_{C_{3z}}(\boldsymbol{R})$ depends on the gauge choice and does not have a universal expression.

C.4 C_{2x} symmetry.

If the ratio θ_1/θ_2 in the local models is significantly different from 1, it is not possible to find two local Hamiltonians at different supermoiré coordinates connected by the C_{2x} operation. Therefore, the existence of C_{2x} symmetry is limited to the effective model with (almost) equal twist angles. We will show later that strict equality of angles is necessary for C_{2x} to hold in the effective model. Recalling that

$$C_{2x}=\sigma_x\otimes\begin{pmatrix}&&1\\&1&\\1&&\end{pmatrix}_{\text{layer}}.$$

we can explicitly calculate $C_{2x}H(\boldsymbol{r};\boldsymbol{\phi}(\boldsymbol{R}))C^{\dagger}_{2x}$ to find that $T_{12}(\boldsymbol{r};\boldsymbol{\phi}(\boldsymbol{R}))$ is transformed to

$$\begin{aligned}
&T_{12}(\boldsymbol{r};-\boldsymbol{\phi}(\boldsymbol{R})) \\
&=T_1e^{i\boldsymbol{q}_1\cdot\boldsymbol{r}}e^{-i\delta\boldsymbol{q}_1\cdot\boldsymbol{R}/(p+q)}+T_3e^{i\boldsymbol{q}_2\cdot\boldsymbol{r}}e^{-i\delta\boldsymbol{q}_2\cdot\boldsymbol{R}/(p+q)}+T_2e^{i\boldsymbol{q}_3\cdot\boldsymbol{r}}e^{-i\delta\boldsymbol{q}_3\cdot\boldsymbol{R}/(p+q)} \\
&\equiv T_{12}(\hat{M}_x\boldsymbol{r};\boldsymbol{\phi}(\hat{M}_{\delta\boldsymbol{q}_1}\boldsymbol{R}))
\end{aligned} \tag{C.56}$$

where $\hat{M}_x$ reflects a coordinate to its mirror image with respect to a mirror plane perpendicular to the xy-plane and passing through the x-axis. $\hat{M}_{\delta \boldsymbol{q}_1}$ is a mirror plane passing through the origin of coordinates, parallel to the vector $\delta \boldsymbol{q}_1$. The transformation of $T_{23}(\boldsymbol{r}; \boldsymbol{\phi}(\boldsymbol{R}))$ under C_{2x} is the same: $T_{23}(\boldsymbol{r}; \boldsymbol{\phi}(\boldsymbol{R})) \to T_{23}(\hat{M}_x \boldsymbol{r}; \boldsymbol{\phi}(\hat{M}_{\delta \boldsymbol{q}_1} \boldsymbol{R}))$. This establishes that, for $\theta_1 \approx \theta_2$, the local Hamiltonians transform under C_{2x} as

$$C_{2x} H_{\text{local}}(\boldsymbol{r}; \boldsymbol{\phi}(\boldsymbol{R})) C_{2x}^{\dagger} = H_{\text{local}}(\hat{M}_x \boldsymbol{r}; \boldsymbol{\phi}(\hat{M}_{\delta \boldsymbol{q}_1} \boldsymbol{R})). \tag{C.57}$$

When C_{2x} acts on $\boldsymbol{\sigma} \cdot \boldsymbol{\nabla}_{\boldsymbol{R}} \circ$, we have

$$\sigma_x \boldsymbol{\sigma} \sigma_x \cdot \hat{M}_{\delta \boldsymbol{q}_1}^{-1} \boldsymbol{\nabla}_{\boldsymbol{R}} \circ = [\sigma_x, -\sigma_y] \cdot \hat{M}_{\delta \boldsymbol{q}_1}^{-1} \boldsymbol{\nabla}_{\boldsymbol{R}} \circ \tag{C.58}$$

which, in general, is *not* equal to $\boldsymbol{\sigma} \cdot \boldsymbol{\nabla}_{\boldsymbol{R}} \circ$. The equality holds only if $\hat{M}_{\delta \boldsymbol{q}_1} = \hat{M}_x$, which implies that $\hat{M}_x^{-1} \boldsymbol{\nabla}_{\boldsymbol{R}} \circ = \boldsymbol{e}_x \partial_x - \boldsymbol{e}_y \partial_y$. Then we have

$$\sigma_x \boldsymbol{\sigma} \sigma_x \cdot \hat{M}_y^{-1} \boldsymbol{\nabla}_{\boldsymbol{R}} \circ = \boldsymbol{\sigma} \cdot \boldsymbol{\nabla}_{\boldsymbol{R}} \circ.$$

In other words, the validity of C_{2x} in the effective model requires $\delta \boldsymbol{q}_1$ to be along the x-axis. According to the geometric decomposition described in Eq. (3.3), the only $\delta \boldsymbol{q}_1$ that satisfies this requirement is when θ_1 and θ_2 are *exactly* equal. For a ratio θ_1/θ_2 that is close but not exactly equal to 1, the local Hamiltonians and local states do not differ from those with $\theta_1/\theta_2 = 1$. However, the orientation of $\delta \boldsymbol{q}_1$ in the two cases is not identical, resulting in a valid C_{2x} symmetry only for $\theta_1/\theta_2 = 1$ and not for $\theta_1/\theta_2 \approx 1$ with $\theta_1/\theta_2 \neq 1$.

C.5 $C_{2z}T$ symmetry

The discussion on $C_{2z}T$ symmetry in local models reveals that the local models only restore $C_{2z}T$ symmetry when they are the periodic counterparts of the zero-phase Hamiltonian. To globally restore $C_{2z}T$ in the effective model, it is crucial that two local models at different supermoiré coordinates are connected by $C_{2z}T$. Under $C_{2z}T$ transformation, a local model $H_{\text{local}}(\boldsymbol{r}; \boldsymbol{\phi}(\boldsymbol{R}))$ transforms as follows:

$$\sigma_x {H_{\text{local}}}^*(\boldsymbol{r}; \boldsymbol{\phi}(\boldsymbol{R})) \sigma_x = H_{\text{local}}(-\boldsymbol{r}, \boldsymbol{\phi}(-\boldsymbol{R})). \tag{C.59}$$

This implies that the local Hamiltonian has identical spectra at $\boldsymbol{R}$ and $-\boldsymbol{R}$. Specifically, if

$$H_{\text{local}}(\boldsymbol{r}; \boldsymbol{\phi}(\boldsymbol{R})) \Psi_{n\boldsymbol{k}}(\boldsymbol{r}; \boldsymbol{R}) = E_{n\boldsymbol{k}}(\boldsymbol{R}) \Psi_{n\boldsymbol{k}}(\boldsymbol{r}; \boldsymbol{R}),$$

then we have:

$$H_{\text{local}}(\boldsymbol{r};\boldsymbol{\phi}(-\boldsymbol{R}))\sigma_x\Psi^*_{n\boldsymbol{k}}(-\boldsymbol{r};\boldsymbol{R}) = E(\boldsymbol{R})\sigma_x\Psi^*_{n\boldsymbol{k}}(-\boldsymbol{r};\boldsymbol{R}).$$

By working with gauge-fixed states, we find that

$$\Psi_{n\boldsymbol{k}}(\boldsymbol{r};-\boldsymbol{R}) = \sum_m \sigma_x\Psi^*_{m\boldsymbol{k}}(-\boldsymbol{r};\boldsymbol{R})\zeta^*_{mn}(\boldsymbol{R}), \tag{C.60}$$

or equivalently, by taking the complex conjugate on both sides,

$$\Psi^*_{n\boldsymbol{k}}(\boldsymbol{r};-\boldsymbol{R}) = \sum_m \sigma_x\Psi_{m\boldsymbol{k}}(-\boldsymbol{r};\boldsymbol{R})\zeta_{mn}(\boldsymbol{R}). \tag{C.61}$$

Since the complex conjugation is explicitly involved in $C_{2z}T$ symmetry, it is more convenient to perform the calculation explicitly on the $C_{2z}T$ transform of the effective model.

For the velocity term, we have:

$$\begin{aligned}
\boldsymbol{\Gamma}^*_{nm}(-\boldsymbol{R}) &= \sum_{\alpha\beta}\sum_l \int_{MUC} \mathrm{d}\boldsymbol{r}^2\ \psi^{\alpha,l}_n(\boldsymbol{r};-\boldsymbol{R})\boldsymbol{\sigma}^{\alpha\beta *}\psi^{\beta,l*}_m(\boldsymbol{r};-\boldsymbol{R}) \\
&= \sum_{n'm'}\sum_{\alpha\beta}\sum_{\alpha'\beta'}\sum_l \int_{MUC} \mathrm{d}\boldsymbol{r}^2\ \zeta^* n'n(\boldsymbol{R})\psi^{\alpha,l*}_{n'}(-\boldsymbol{r};-\boldsymbol{R})\sigma_x^{\alpha\alpha'}\boldsymbol{\sigma}^{\alpha'\beta'*}\sigma_x^{\beta'\beta}\psi^{\beta,l*}_{m'}(\boldsymbol{r};-\boldsymbol{R})\zeta_{m'm}(\boldsymbol{R}) \\
&= \sum_{n'm'}\zeta^\dagger_{nn'}(\boldsymbol{R})\sum_{\alpha\beta}\sum_l \psi^{\alpha,l*}_{n'}(-\boldsymbol{r};-\boldsymbol{R})\boldsymbol{\sigma}^{\alpha\beta}\psi^{\beta,l*}_{m'}(\boldsymbol{r};-\boldsymbol{R})\zeta_{m'm}(\boldsymbol{R}) \\
&\equiv \sum_{n'm'}\zeta^\dagger_{nn'}(\boldsymbol{R})\boldsymbol{\Gamma}_{n'm'}\zeta_{m'm}(\boldsymbol{R}).
\end{aligned} \tag{C.62}$$

The transform of the gauge field term is given by:

$$\begin{aligned}
A^*(-\boldsymbol{R})_{nm} &= \sum_{\alpha\beta}\sum_l \int_{MUC} \mathrm{d}\boldsymbol{r}^2\ \psi^{\alpha,l}_n(\boldsymbol{r};-\boldsymbol{R})(-i)\boldsymbol{\sigma}^{\alpha\beta *}\cdot(\boldsymbol{\nabla}_{\boldsymbol{R}}\psi^{\beta,l*}_m(\boldsymbol{r};-\boldsymbol{R})) \\
&= \sum_{n'm'}\sum_{\alpha\beta}\sum_{\alpha'\beta'}\int_{MUC} \mathrm{d}\boldsymbol{r}^2\ \zeta^\dagger_{nn'}(\boldsymbol{R})\psi^{\alpha,l*}_{n'}(-\boldsymbol{r};-\boldsymbol{R})\sigma_x(-i)\boldsymbol{\sigma}^{\alpha\beta *}\cdot\boldsymbol{\nabla}_{\boldsymbol{R}}\psi^{\beta,l*}_{m'}(\boldsymbol{r};-\boldsymbol{R})\zeta_{m'm}(\boldsymbol{R}) \\
&= \sum_{n'm'}\sum_{\alpha\beta}\sum_l \int_{MUC} \mathrm{d}\boldsymbol{r}^2\ \zeta^\dagger_{nn'}(\boldsymbol{R})\psi^{\alpha,l*}_{n'}(-\boldsymbol{r};-\boldsymbol{R})(-i)\boldsymbol{\sigma}^{\alpha\beta}\cdot(\boldsymbol{\nabla}_{\boldsymbol{R}}\psi^{\beta,l*}_{m'}(\boldsymbol{r};-\boldsymbol{R}))\zeta_{m'm}(\boldsymbol{R}) \\
&\quad + \sum_{n'm'}\sum_{\alpha\beta}\sum_l \int_{MUC} \mathrm{d}\boldsymbol{r}^2\ \zeta^\dagger_{nn}(\boldsymbol{R})\psi^{\alpha,l*}_{n'}(-\boldsymbol{r};-\boldsymbol{R})(-i)\boldsymbol{\sigma}^{\alpha\beta}\psi^{\beta,l*}_{m'}(\boldsymbol{r};-\boldsymbol{R}))\cdot(\boldsymbol{\nabla}_{\boldsymbol{R}}\zeta_{m'm}(\boldsymbol{R})) \\
&= \sum_{n'm'}\zeta^\dagger_{nn'}(\boldsymbol{R})A_{n'm'}(R)\zeta_{m'm}(\boldsymbol{R}) + \zeta^\dagger_{nn'}(\boldsymbol{R})\boldsymbol{\Gamma}_{n'm'}(\boldsymbol{R})\cdot\boldsymbol{\nabla}_{\boldsymbol{R}}\zeta_{m'm}(\boldsymbol{R})
\end{aligned} \tag{C.63}$$

The extra term $\zeta^\dagger(\boldsymbol{R})\boldsymbol{\Gamma}(\boldsymbol{R})\cdot\boldsymbol{\nabla}_{\boldsymbol{R}}\zeta(\boldsymbol{R})$ disappears when we calculate the sum $(-i\boldsymbol{\Gamma}^*(-\boldsymbol{R})\cdot\boldsymbol{\nabla}_{-\boldsymbol{R}}+A(-\boldsymbol{R}))^*$.

The onsite energy term obviously satisfies

$$E^*_{nm}(-\boldsymbol{R})=\sum_{n'm'}\zeta^\dagger_{nn'}(\boldsymbol{R})E_{n'm'}\zeta_{m'm}(\boldsymbol{R}). \tag{C.64}$$

Now we can conclude that the effective Hamiltonian also possesses $C_{2z}T$ symmetry as it verifies

$$H_{\text{eff}}{}^*(-\boldsymbol{R})=\zeta^\dagger(\boldsymbol{R})H_{\text{eff}}(\boldsymbol{R})\zeta(\boldsymbol{R}). \tag{C.65}$$

We remark that $C_{2z}T$ is locally broken almost everywhere except at the origin of the supermoiré coordinates but globally restored in the TTG model.

Appendix D

Matrix elements of the 4-band $\boldsymbol{K}_M$ model

In this appendix, we provide an enumeration of the matrix elements for each 4×4 matrix of the $\boldsymbol{K}_M$ effective model at every supermoiré coordinate, along with their Fourier transformations. Since the matrix elements are complex numbers, we display their amplitudes as functions of $\boldsymbol{R}$. Additionally, we present the amplitudes of the Fourier coefficients on the supermoiré reciprocal lattice.

All the data presented in this appendix are computed using twist angles of $1.8°$ and $3.6°$. To enhance visibility, each dataset is normalized to the range $[0, 1]$, as explained earlier.

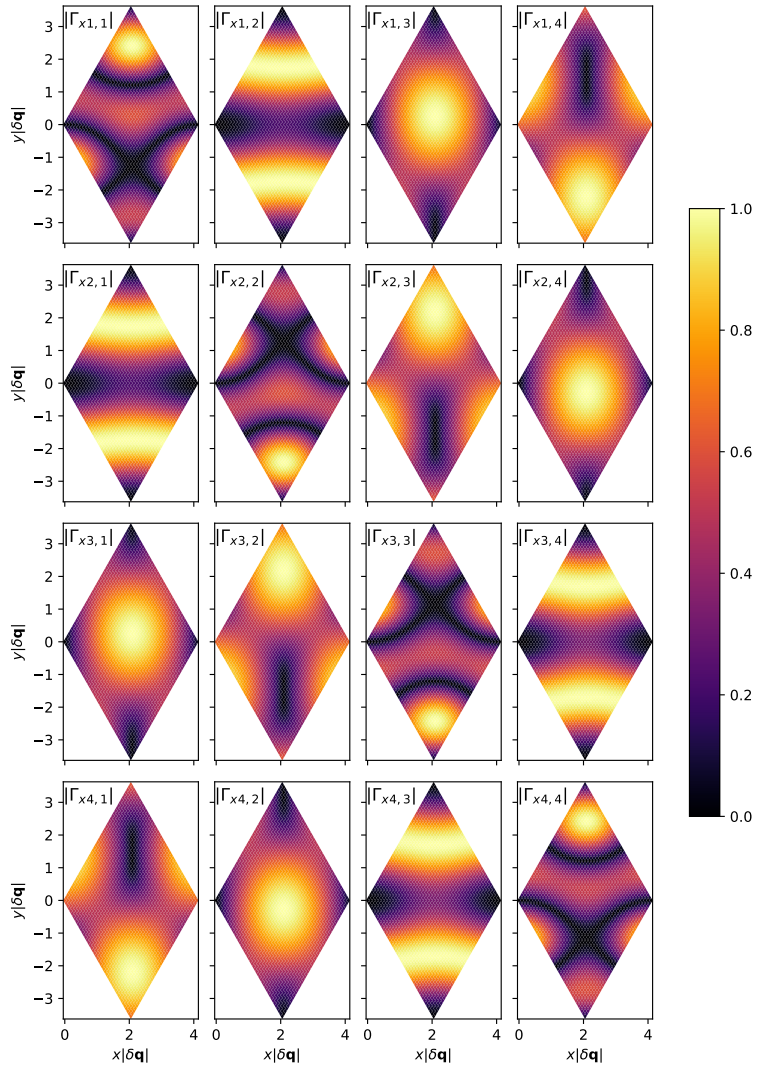

Figure D.1: The normalized data of matrix elements $|\Gamma_{x\ i,j}(\boldsymbol{R})|$ from the $\boldsymbol{K}_M$ effective model with twist angles being 1.8° and 3.6°.

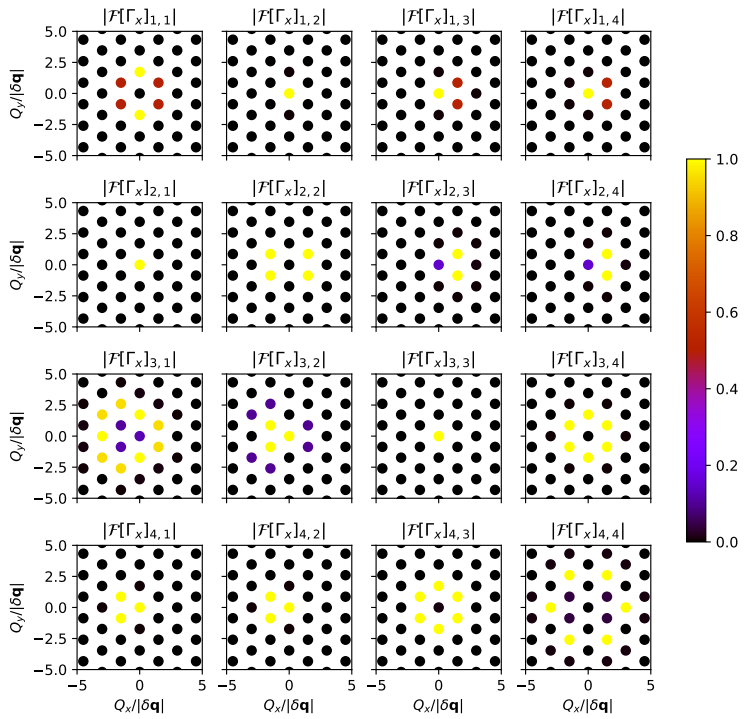

Figure D.2: The normalized Fourier coefficients of $\Gamma_{x\ i,j}$ on the supermoiré reciprocal lattice from the $\boldsymbol{K}_M$ effective model with twist angles being $1.8°$ and $3.6°$.

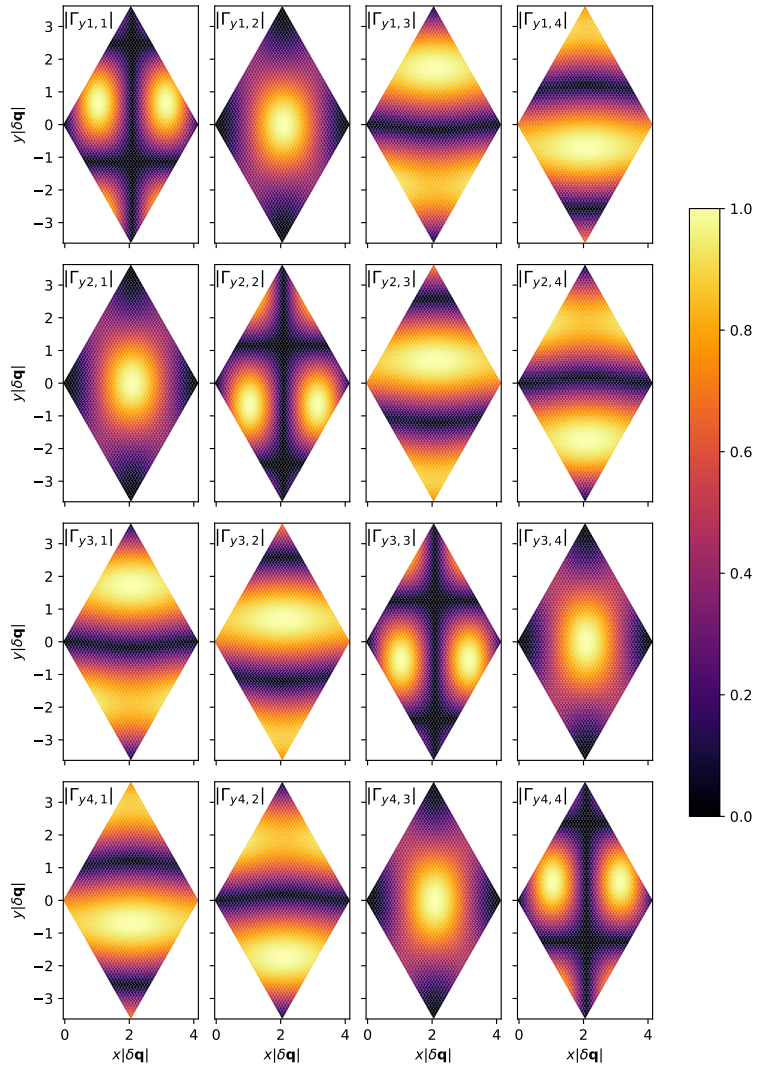

Figure D.3: The normalized data of matrix elements $|\Gamma_{y\ i,j}(\boldsymbol{R})|$ from the $\boldsymbol{K}_M$ effective model with twist angles being 1.8° and 3.6°.

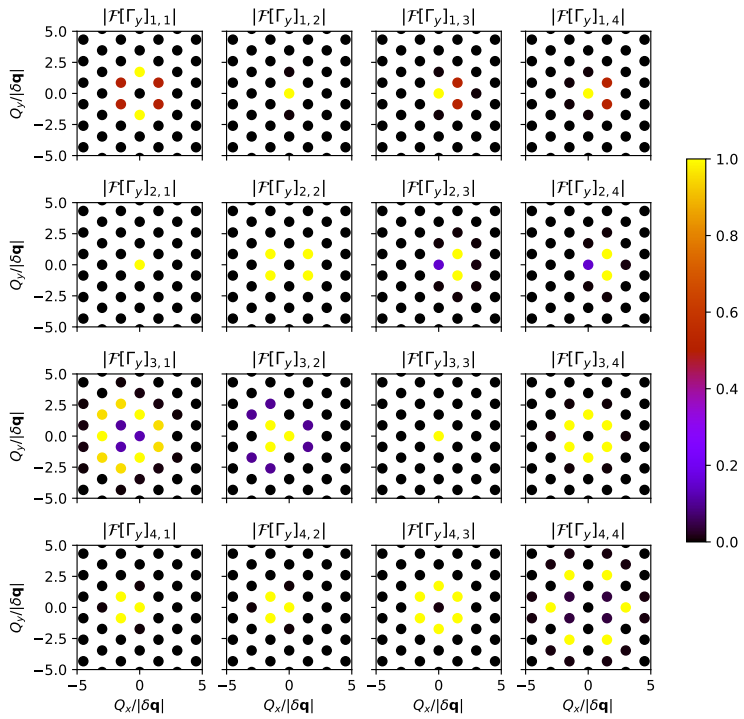

Figure D.4: The normalized Fourier coefficients of $\Gamma_{y\ i,j}$ on the supermoiré reciprocal lattice from the $\boldsymbol{K}_M$ effective model with twist angles being $1.8°$ and $3.6°$.

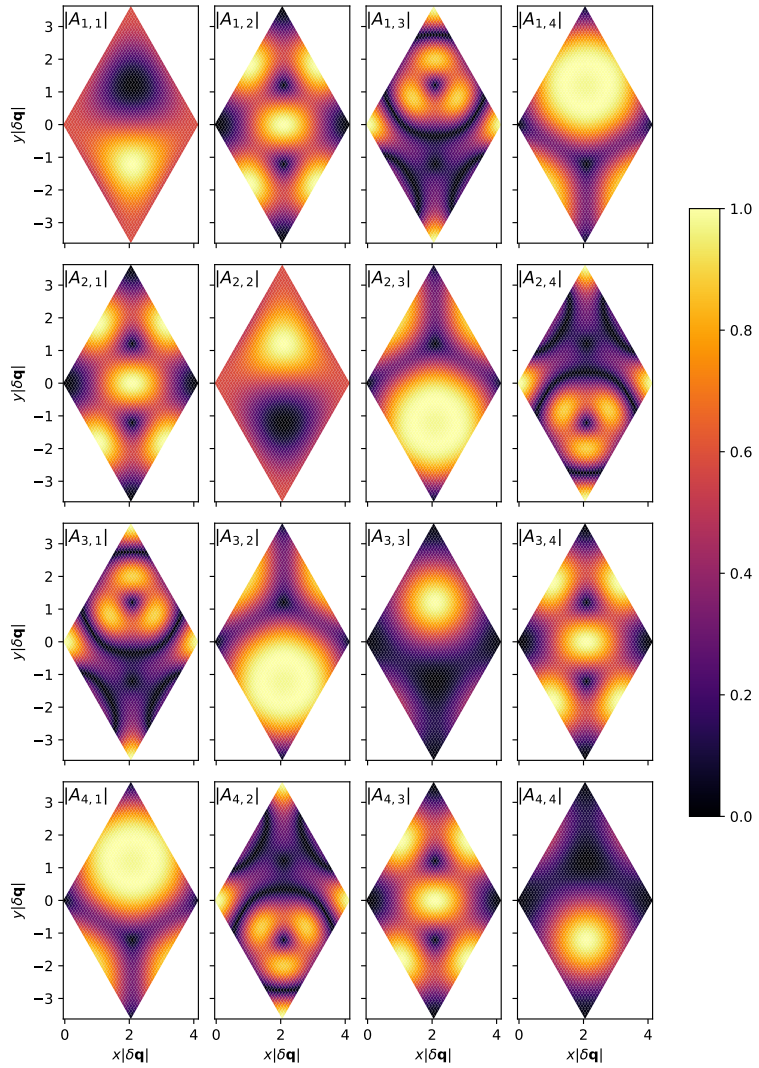

Figure D.5: The normalized data of matrix elements $|A_{i,j}(\boldsymbol{R})|$ from the $\boldsymbol{K}_M$ effective model with twist angles being 1.8° and 3.6°.

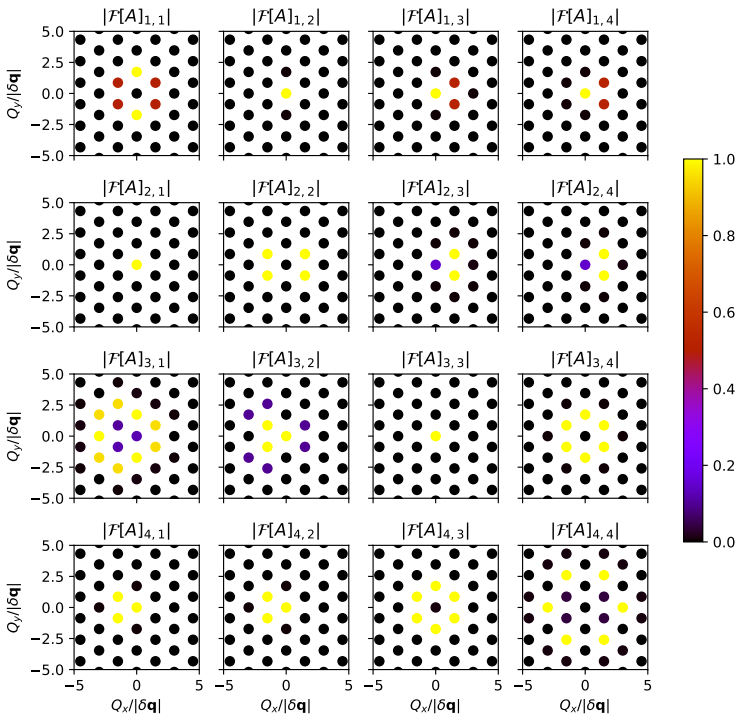

Figure D.6: The normalized Fourier coefficients of $A_{i,j}$ on the supermoiré reciprocal lattice from the $\boldsymbol{K}_M$ effective model with twist angles being $1.8°$ and $3.6°$.

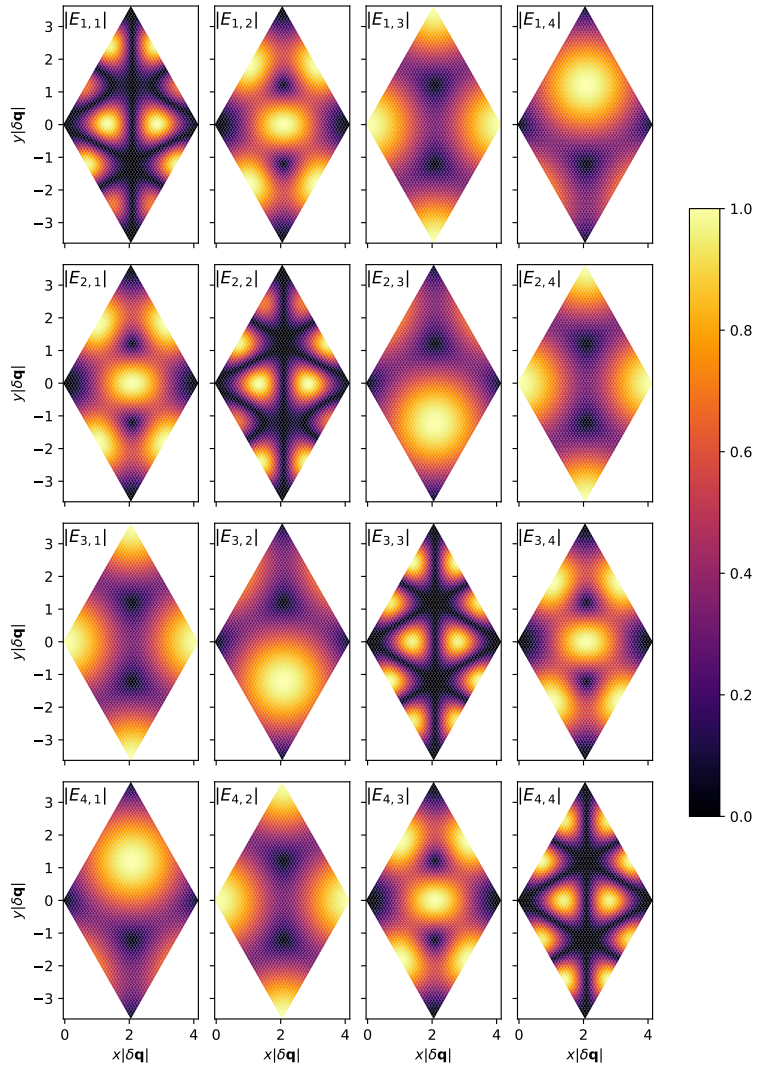

Figure D.7: The normalized data of matrix elements $|E_{i,j}(\boldsymbol{R})|$ from the $\boldsymbol{K}_M$ effective model with twist angles being 1.8° and 3.6°.

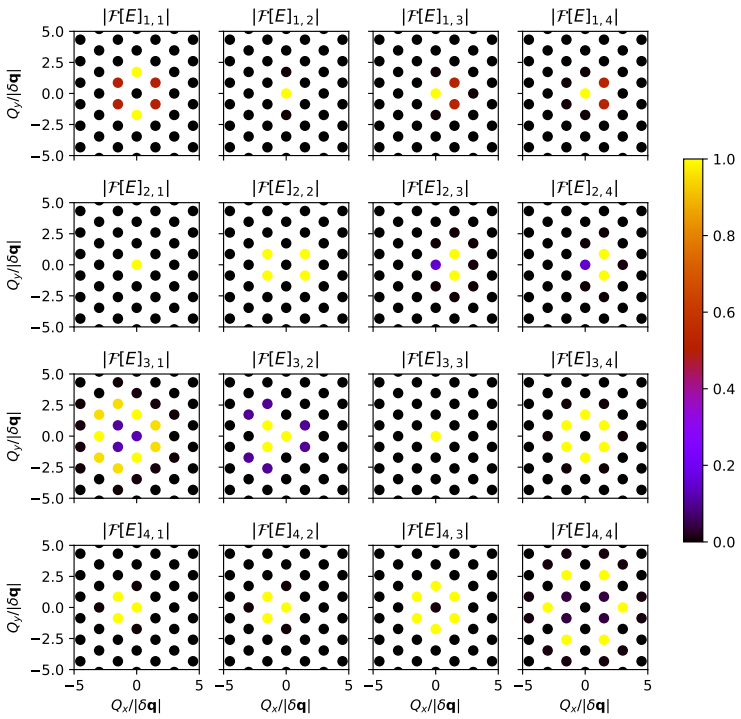

Figure D.8: The normalized Fourier coefficients of $E_{i,j}$ on the supermoiré reciprocal lattice from the $\boldsymbol{K}_M$ effective model with twist angles being $1.8°$ and $3.6°$.

Bibliography

1. Novoselov, K. S. *et al.* Electric Field Effect in Atomically Thin Carbon Films. *Science* **306,** 666–669 (2004).
2. Geim, A. K. & Novoselov, K. S. The rise of graphene. *Nature materials* **6,** 183–191 (2007).
3. Novoselov, K. S. *et al.* Two-dimensional gas of massless Dirac fermions in graphene. *nature* **438,** 197–200 (2005).
4. Morozov, S. V. *et al.* Giant Intrinsic Carrier Mobilities in Graphene and Its Bilayer. *Phys. Rev. Lett.* **100,** 016602 (1 2008).
5. Kashuba, A. B. Conductivity of defectless graphene. *Phys. Rev. B* **78,** 085415 (8 2008).
6. Balandin, A. A. *et al.* Superior thermal conductivity of single-layer graphene. *Nano letters* **8,** 902–907 (2008).
7. Gu, Q., Xing, D. & Sun, J. Superconducting single-layer T-graphene and novel synthesis routes. *Chinese Physics Letters* **36,** 097401 (2019).
8. Guo, H.-M. & Franz, M. Topological insulator on the kagome lattice. *Phys. Rev. B* **80,** 113102 (11 2009).
9. Li, S., Xing, J., Tao, J., Yang, H. & Wen, H.-H. Superconductivity in Ba2/3Pt3B2 with the Kagome lattice. *Annals of Physics* **358,** 248–254 (2015).
10. Gui, X. & Cava, R. J. LaIr3Ga2: a superconductor based on a kagome lattice of Ir. *Chemistry of Materials* **34,** 2824–2832 (2022).
11. Superconductivity from repulsive interactions on the kagome lattice. *Physical Review B* **106,** 174514 (Nov. 2022).
12. Jiang, K. *et al.* Kagome superconductors AV_3Sb_5(A= K, Rb, Cs). *National Science Review* **10,** nwac199 (2023).
13. Zhou, H. *et al.* Isospin magnetism and spin-polarized superconductivity in Bernal bilayer graphene. *Science* **375,** 774–778 (2022).
14. Pantaleón, P. A. *et al.* Superconductivity and correlated phases in non-twisted bilayer and trilayer graphene. *Nature Reviews Physics,* 1–12 (2023).
15. De Gail, R., Goerbig, M. O., Guinea, F., Montambaux, G. & Castro Neto, A. H. Topologically protected zero modes in twisted bilayer graphene. *Phys. Rev. B* **84,** 045436 (4 July 2011).

16. Lopes dos Santos, J. M. B., Peres, N. M. R. & Castro Neto, A. H. Graphene Bilayer with a Twist: Electronic Structure. *Phys. Rev. Lett.* **99,** 256802 (25 2007).

17. Morell, E. S., Correa, J., Vargas, P., Pacheco, M. & Barticevic, Z. Flat bands in slightly twisted bilayer graphene: Tight-binding calculations. *Physical Review B* **82,** 121407 (2010).

18. Bistritzer, R. & MacDonald, A. H. Moiré bands in twisted double-layer graphene. *Proceedings of the National Academy of Sciences* **108,** 12233–12237 (2011).

19. Bistritzer, R. & MacDonald, A. Moiré butterflies in twisted bilayer graphene. *Physical Review B* **84,** 035440 (2011).

20. Cao, Y. *et al.* Unconventional superconductivity in magic-angle graphene superlattices. *Nature* **556,** 43–50 (2018).

21. Cao, Y. *et al.* Correlated insulator behaviour at half-filling in magic-angle graphene superlattices. *Nature* **556,** 80–84 (2018).

22. Yankowitz, M. *et al.* Tuning superconductivity in twisted bilayer graphene. *Science* **363,** 1059–1064 (2019).

23. Lu, X. *et al.* Superconductors, orbital magnets and correlated states in magic-angle bilayer graphene. *Nature* **574,** 653–657 (2019).

24. Stepanov, P. *et al.* Untying the insulating and superconducting orders in magic-angle graphene. *Nature* **583,** 375–378 (2020).

25. Liu, X. *et al.* Tuning electron correlation in magic-angle twisted bilayer graphene using Coulomb screening. *Science* **371,** 1261–1265 (2021).

26. Arora, H. S. *et al.* Superconductivity in metallic twisted bilayer graphene stabilized by WSe2. *Nature* **583,** 379–384 (2020).

27. Jiang, Y. *et al.* Charge order and broken rotational symmetry in magic-angle twisted bilayer graphene. *Nature* **573,** 91–95 (2019).

28. Cao, Y. *et al.* Nematicity and competing orders in superconducting magic-angle graphene. *Science* **372,** 264–271 (2021).

29. Oh, M. *et al.* Evidence for unconventional superconductivity in twisted bilayer graphene. *Nature* **600,** 240–245 (2021).

30. Xie, Y. *et al.* Spectroscopic signatures of many-body correlations in magic-angle twisted bilayer graphene. *Nature* **572,** 101–105 (2019).

31. Sharpe, A. L. *et al.* Emergent ferromagnetism near three-quarters filling in twisted bilayer graphene. *Science* **365,** 605–608 (2019).

32. Saito, Y. *et al.* Hofstadter subband ferromagnetism and symmetry-broken Chern insulators in twisted bilayer graphene. *Nature Physics* **17,** 478–481 (2021).

33. Serlin, M. *et al.* Intrinsic quantized anomalous Hall effect in a moiré heterostructure. *Science* **367,** 900–903 (2020).

34. Lin, J.-X. *et al.* Spin-orbit–driven ferromagnetism at half moiré filling in magic-angle twisted bilayer graphene. *Science* **375,** 437–441 (2022).

35. Sharpe, A. L. *et al.* Evidence of orbital ferromagnetism in twisted bilayer graphene aligned to hexagonal boron nitride. *Nano Letters* **21,** 4299–4304 (2021).

36. Wong, D. *et al.* Cascade of electronic transitions in magic-angle twisted bilayer graphene. *Nature* **582,** 198–202 (2020).

37. Zondiner, U. *et al.* Cascade of phase transitions and Dirac revivals in magic-angle graphene. *Nature* **582,** 203–208 (2020).

38. Nuckolls, K. P. *et al.* Strongly correlated Chern insulators in magic-angle twisted bilayer graphene. *Nature* **588,** 610–615 (2020).

39. Pierce, A. T. *et al.* Unconventional sequence of correlated Chern insulators in magic-angle twisted bilayer graphene. *Nature Physics* **17,** 1210–1215 (2021).

40. Xie, Y. *et al.* Fractional Chern insulators in magic-angle twisted bilayer graphene. *Nature* **600,** 439–443 (2021).

41. Das, I. *et al.* Symmetry-broken Chern insulators and Rashba-like Landau-level crossings in magic-angle bilayer graphene. *Nature Physics* **17,** 710–714 (2021).

42. Wu, S., Zhang, Z., Watanabe, K., Taniguchi, T. & Andrei, E. Y. Chern insulators, van Hove singularities and topological flat bands in magic-angle twisted bilayer graphene. *Nature materials* **20,** 488–494 (2021).

43. Polshyn, H. *et al.* Large linear-in-temperature resistivity in twisted bilayer graphene. *Nat. Phys.* **15,** 1011–1016 (2019).

44. Wu, F., Hwang, E. & Das Sarma, S. Phonon-induced giant linear-in-T resistivity in magic angle twisted bilayer graphene: Ordinary strangeness and exotic superconductivity. *Phys. Rev. B* **99,** 165112 (16 Apr. 2019).

45. Cao, Y. *et al.* Strange Metal in Magic-Angle Graphene with near Planckian Dissipation. *Phys. Rev. Lett.* **124,** 076801 (7 Feb. 2020).

46. Jaoui, A. *et al.* Quantum critical behaviour in magic-angle twisted bilayer graphene. *Nature Physics* **18,** 1–6 (2022).

47. Park, J. M., Cao, Y., Watanabe, K., Taniguchi, T. & Jarillo-Herrero, P. Flavour Hund's coupling, Chern gaps and charge diffusivity in moiré graphene. *Nature* **592,** 43–48 (2021).

48. Xie, M. & MacDonald, A. H. Weak-Field Hall Resistivity and Spin-Valley Flavor Symmetry Breaking in Magic-Angle Twisted Bilayer Graphene. *Phys. Rev. Lett.* **127,** 196401 (19 Nov. 2021).

49. Potasz, P., Xie, M. & MacDonald, A. H. Exact Diagonalization for Magic-Angle Twisted Bilayer Graphene. *Phys. Rev. Lett.* **127,** 147203 (14 Sept. 2021).

50. Bistritzer, R. & MacDonald, A. H. Moiré bands in twisted double-layer graphene. *Proc. Nat. Acad. Sci.* **108,** 12233–12237 (2011).

51. Bernevig, B. A., Song, Z.-D., Regnault, N. & Lian, B. Twisted bilayer graphene. I. Matrix elements, approximations, perturbation theory, and a $k \cdot p$ two-band model. *Phys. Rev. B* **103,** 205411 (20 May 2021).

52. Song, Z.-D., Lian, B., Regnault, N. & Bernevig, B. A. Twisted bilayer graphene. II. Stable symmetry anomaly. *Phys. Rev. B* **103,** 205412 (2021).

53. Bernevig, B. A., Song, Z.-D., Regnault, N. & Lian, B. Twisted bilayer graphene. III. Interacting Hamiltonian and exact symmetries. *Phys. Rev. B* **103,** 205413 (20 May 2021).

54. Lian, B. *et al.* Twisted bilayer graphene. IV. Exact insulator ground states and phase diagram. *Phys. Rev. B* **103,** 205414 (20 May 2021).

55. Bernevig, B. A. *et al.* Twisted bilayer graphene. V. Exact analytic many-body excitations in Coulomb Hamiltonians: Charge gap, Goldstone modes, and absence of Cooper pairing. *Phys. Rev. B* **103,** 205415 (20 May 2021).

56. Xie, F. *et al.* Twisted bilayer graphene. VI. An exact diagonalization study at nonzero integer filling. *Phys. Rev. B* **103,** 205416 (20 May 2021).

57. Song, Z.-D. & Bernevig, B. A. Magic-Angle Twisted Bilayer Graphene as a Topological Heavy Fermion Problem. *Phys. Rev. Lett.* **129,** 047601 (4 July 2022).

58. Zhou, G.-D. & Song, Z.-D. *Kondo Phase in Twisted Bilayer Graphene – A Unified Theory for Distinct Experiments* 2023. arXiv: 2301.04661 [cond-mat.str-el].

59. Song, Z. *et al.* All Magic Angles in Twisted Bilayer Graphene are Topological. *Phys. Rev. Lett.* **123,** 036401 (3 July 2019).

60. Tang, Y. *et al.* Simulation of Hubbard model physics in WSe2/WS2 moiré superlattices. *Nature* **579,** 353–358 (2020).

61. Shen, C. *et al.* Correlated states in twisted double bilayer graphene. *Nature Physics* **16,** 520–525 (2020).

62. Cao, Y. *et al.* Tunable correlated states and spin-polarized phases in twisted bilayer–bilayer graphene. *Nature* **583,** 215–220 (2020).

63. Liu, X. *et al.* Tunable spin-polarized correlated states in twisted double bilayer graphene. *Nature* **583,** 221–225 (2020).

64. He, M. *et al.* Symmetry breaking in twisted double bilayer graphene. *Nature Physics* **17,** 26–30 (2021).

65. Liu, Z., Abouelkomsan, A. & Bergholtz, E. J. Gate-Tunable Fractional Chern Insulators in Twisted Double Bilayer Graphene. *Phys. Rev. Lett.* **126,** 026801 (2 Jan. 2021).

66. Chen, S. *et al.* Electrically tunable correlated and topological states in twisted monolayer–bilayer graphene. *Nature Physics* **17,** 374–380 (2021).

67. Xu, S. *et al.* Tunable van Hove singularities and correlated states in twisted monolayer–bilayer graphene. *Nature Physics* **17,** 619–626 (Feb. 2021).

68. Park, J. M. *et al.* Robust superconductivity in magic-angle multilayer graphene family. *Nature Materials* **21,** 877–883 (2022).

69. Hao, Z. *et al.* Electric field-tunable superconductivity in alternating-twist magic-angle trilayer graphene. *Science* **371,** 1133–1138 (2021).

70. Lei, C., Linhart, L., Qin, W., Libisch, F. & MacDonald, A. H. Mirror symmetry breaking and lateral stacking shifts in twisted trilayer graphene. *Phys. Rev. B* **104,** 035139 (3 July 2021).

71. Park, J. M., Cao, Y., Watanabe, K., Taniguchi, T. & Jarillo-Herrero, P. Tunable strongly coupled superconductivity in magic-angle twisted trilayer graphene. *Nature* **590,** 249–255 (2021).

72. Liu, X., Zhang, N. J., Watanabe, K., Taniguchi, T. & Li, J. Isospin order in superconducting magic-angle twisted trilayer graphene. *Nature Physics* **18,** 522–527 (2022).

73. Cao, Y., Park, J. M., Watanabe, K., Taniguchi, T. & Jarillo-Herrero, P. Pauli-limit violation and re-entrant superconductivity in moiré graphene. *Nature* **595,** 526–531 (2021).

74. Gonzàlez, J. & Stauber, T. Ising superconductivity induced from spin-selective valley symmetry breaking in twisted trilayer graphene. *Nature Communications* **14,** 2746 (2023).

75. Zhang, Y. *et al.* Promotion of superconductivity in magic-angle graphene multilayers. *Science* **377,** 1538–1543 (2022).

76. Amorim, B. & Castro, E. V. *Electronic spectral properties of incommensurate twisted trilayer graphene* 2018. arXiv: 1807.11909 [cond-mat.mes-hall].

77. Chen, G. *et al.* Evidence of a gate-tunable Mott insulator in a trilayer graphene moiré superlattice. *Nature Physics* **15,** 237–241 (2019).

78. Kim, H. *et al.* Evidence for unconventional superconductivity in twisted trilayer graphene. *Nature* **606,** 494–500 (2022).

79. Turkel, S. *et al.* Orderly disorder in magic-angle twisted trilayer graphene. *Science* **376,** 193 (2022).

80. Carr, S. *et al.* Ultraheavy and ultrarelativistic dirac quasiparticles in sandwiched graphenes. *Nano Letters* **20,** 3030–3038 (2020).

81. Shen, C. *et al.* Dirac spectroscopy of strongly correlated phases in twisted trilayer graphene. *Nature Materials* **22,** 316–321 (2023).

82. Yankowitz, M. Unravelling the magic of twisted trilayer graphene. *Nature Materials,* 1–2 (2023).

83. Christos, M., Sachdev, S. & Scheurer, M. S. Correlated Insulators, Semimetals, and Superconductivity in Twisted Trilayer Graphene. *Phys. Rev. X* **12,** 021018 (2 Apr. 2022).

84. Xie, F., Regnault, N., C ălug ăru, D., Bernevig, B. A. & Lian, B. Twisted symmetric trilayer graphene. II. Projected Hartree-Fock study. *Phys. Rev. B* **104,** 115167 (11 Sept. 2021).

85. C ălug ăru, D. *et al.* Twisted symmetric trilayer graphene: Single-particle and many-body Hamiltonians and hidden nonlocal symmetries of trilayer moiré systems with and without displacement field. *Phys. Rev. B* **103,** 195411 (19 May 2021).

86. Guerci, D., Simon, P. & Mora, C. Higher-order Van Hove singularity in magic-angle twisted trilayer graphene. *Phys. Rev. Research* **4,** L012013 (1 Feb. 2022).

87. Zhang, X. *et al.* Correlated Insulating States and Transport Signature of Superconductivity in Twisted Trilayer Graphene Superlattices. *Phys. Rev. Lett.* **127,** 166802 (16 Oct. 2021).

88. Mora, C., Regnault, N. & Bernevig, B. A. Flatbands and Perfect Metal in Trilayer Moiré Graphene. *Phys. Rev. Lett.* **123,** 026402 (2 July 2019).

89. Popov, F. K. & Tarnopolsky, G. *Magic Angles In Equal-Twist Trilayer Graphene* 2023. arXiv: 2303.15505 [cond-mat.str-el].

90. Guerci, D., Mao, Y. & Mora, C. *Chern mosaic and ideal flat bands in equal-twist trilayer graphene* 2023. arXiv: 2305.03702 [cond-mat.mes-hall].

91. Zhu, Z., Carr, S., Massatt, D., Luskin, M. & Kaxiras, E. Twisted trilayer graphene: A precisely tunable platform for correlated electrons. *Phys. Rev. Lett.* **125,** 116404 (2020).

92. Uri, A. *et al. Superconductivity and strong interactions in a tunable moiré quasiperiodic crystal* 2023. arXiv: 2302.00686 [cond-mat.mes-hall].

93. EN Adams, I. Motion of an electron in a perturbed periodic potential. *Phys. Rev.* **85,** 41 (1952).

94. Luttinger, J. M. & Kohn, W. Motion of Electrons and Holes in Perturbed Periodic Fields. *Phys. Rev.* **97,** 869–883 (4 Feb. 1955).

95. Bastard, G. Superlattice band structure in the envelope-function approximation. *Phys. Rev. B* **24,** 5693–5697 (10 Nov. 1981).

96. Bastard, G. Theoretical investigations of superlattice band structure in the envelope-function approximation. *Phys. Rev. B* **25,** 7584 (1982).

97. Smith, D. L. & Mailhiot, C. Theory of semiconductor superlattice electronic structure. *Rev. Mod. Phys.* **62,** 173–234 (1 Jan. 1990).

98. Tarnopolsky, G., Kruchkov, A. J. & Vishwanath, A. Origin of Magic Angles in Twisted Bilayer Graphene. *Phys. Rev. Lett.* **122,** 106405 (10 Mar. 2019).

99. Mao, Y., Guerci, D. & Mora, C. Supermoiré low-energy effective theory of twisted trilayer graphene. *Phys. Rev. B* **107,** 125423 (12 Mar. 2023).

100. Marzari, N., Mostofi, A. A., Yates, J. R., Souza, I. & Vanderbilt, D. Maximally localized Wannier functions: Theory and applications. *Rev. Mod. Phys.* **84,** 1419–1475 (4 Oct. 2012).

101. Grover, S. *et al.* Chern mosaic and Berry-curvature magnetism in magic-angle graphene. *Nature Physics* **18,** 885–892. ISSN: 1745-2481 (Aug. 2022).